

## **INFORMATION TO USERS**

This manuscript has been reproduced from the microfilm master. UMI films the text directly from the original or copy submitted. Thus, some thesis and dissertation copies are in typewriter face, while others may be from any type of computer printer.

**The quality of this reproduction is dependent upon the quality of the copy submitted.** Broken or indistinct print, colored or poor quality illustrations and photographs, print bleedthrough, substandard margins, and improper alignment can adversely affect reproduction.

In the unlikely event that the author did not send UMI a complete manuscript and there are missing pages, these will be noted. Also, if unauthorized copyright material had to be removed, a note will indicate the deletion.

Oversize materials (e.g., maps, drawings, charts) are reproduced by sectioning the original, beginning at the upper left-hand corner and continuing from left to right in equal sections with small overlaps.

Photographs included in the original manuscript have been reproduced xerographically in this copy. Higher quality 6" x 9" black and white photographic prints are available for any photographs or illustrations appearing in this copy for an additional charge. Contact UMI directly to order.

ProQuest information and Learning  
300 North Zeeb Road, Ann Arbor, MI 48106-1346 USA  
800-521-0600

**UMI<sup>®</sup>**



UNIVERSITY OF ALBERTA  
THEORETICAL ANALYSIS AND EXPERIMENTAL INVESTIGATION OF THE  
PERFORMANCE OF OZONE BUBBLE COLUMNS

BY  
MOHAMED GAMAL EL-DIN ©

A THESIS  
SUBMITTED TO THE FACULTY OF GRADUATE STUDIES AND RESEARCH IN  
PARTIAL FULFILLMENT OF THE REQUIREMENTS FOR THE DEGREE OF  
DOCTOR OF PHILOSOPHY  
IN  
ENVIRONMENTAL ENGINEERING

DEPARTMENT OF CIVIL & ENVIRONMENTAL ENGINEERING

EDMONTON, ALBERTA

FALL, 2001



**National Library  
of Canada**

**Acquisitions and  
Bibliographic Services**

**395 Wellington Street  
Ottawa ON K1A 0N4  
Canada**

**Bibliothèque nationale  
du Canada**

**Acquisitions et  
services bibliographiques**

**395, rue Wellington  
Ottawa ON K1A 0N4  
Canada**

*Your file Votre référence*

*Our file Notre référence*

**The author has granted a non-exclusive licence allowing the National Library of Canada to reproduce, loan, distribute or sell copies of this thesis in microform, paper or electronic formats.**

**The author retains ownership of the copyright in this thesis. Neither the thesis nor substantial extracts from it may be printed or otherwise reproduced without the author's permission.**

**L'auteur a accordé une licence non exclusive permettant à la Bibliothèque nationale du Canada de reproduire, prêter, distribuer ou vendre des copies de cette thèse sous la forme de microfiche/film, de reproduction sur papier ou sur format électronique.**

**L'auteur conserve la propriété du droit d'auteur qui protège cette thèse. Ni la thèse ni des extraits substantiels de celle-ci ne doivent être imprimés ou autrement reproduits sans son autorisation.**

0-612-68934-4

**Canada**

UNIVERSITY OF ALBERTA  
RELEASE FORM

NAME OF AUTHOR: MOHAMED GAMAL EL-DIN  
TITLE OF THESIS: THEORETICAL ANALYSIS AND EXPERIMENTAL  
INVESTIGATION OF THE PERFORMANCE OF  
OZONE BUBBLE COLUMNS

DEGREE FOR WHICH  
THIS THESIS  
HAS PRESENTED: DOCTOR OF PHILOSOPHY

YEAR THIS DEGREE  
GRANTED: FALL 2001

Permission is hereby granted to THE UNIVERSITY OF ALBERTA LIBRARY to reproduce single copies of this thesis and to lend or sell such copies for private, scholarly or scientific research purposes only.

The author reserves other publication rights, and neither the thesis nor extensive extracts from it may be printed or otherwise reproduced without the author's written permission.

(signed) Mohamed I

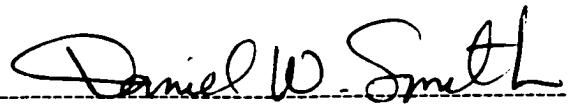
PERMANENT ADDRESS:

611E Michener Park  
Edmonton, Alberta  
Canada  
T6H 5A1

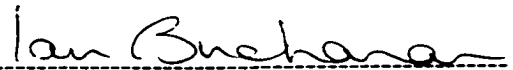
Date October 1, 2001

UNIVERSITY OF ALBERTA  
FACULTY OF GRADUATE STUDIES AND RESEARCH

The undersigned certify that they have read, and recommended to the faculty of Graduate Studies and Research, for acceptance, a thesis entitled: **THEORETICAL ANALYSIS AND EXPERIMENTAL INVESTIGATION OF THE PERFORMANCE OF OZONE BUBBLE COLUMNS** submitted by: Mohamed Gamal El-Din in partial fulfillment of the requirement for the degree of **DOCTOR OF PHILOSOPHY IN ENVIRONMENTAL ENGINEERING**.



Dr. Daniel W. Smith-Supervisor



Dr. Ian D. Buchanan



Dr. Tong Yu



Dr. Nallamuthu Rajaratnam



Dr. Jerry Leonard



Dr. Nihar Biswas (External Examiner)

Date 1 Oct 2001

## **DEDICATION**

This work is dedicated to my family who had a great influence on my life. My mother, Dr. Nadia El-Safory who has taught me that every thing is possible with hard work. My father, Mr. Galal Gamal El-Din, who has always encouraged me to seek more knowledge and has always been there for me when I needed him. My brother, Mr Ahmed Gamal El-Din, with whom I shared all the good and bad times throughout this journey.

## **ABSTRACT**

The transient Back flow cell model (BFCM) has been presented as an alternative approach to describe the hydrodynamics of ozone bubble columns. Compared to the traditionally used models, transient BFCM provided a more flexible, reliable, and accurate tool to describe the backmixing in the liquid phase.

The two-phase steady-state axial dispersion model (2P-ADM) and BFCM have been developed for describing the performance of ozone bubble columns. Although, the 2P-ADM and BFCM have proven to be adequate for modeling the ozonation process, the BFCM was easier to formulate and solve.

A modified steady-state non-isobaric one-phase axial dispersion model (1P-ADM) has been developed. The 1P-ADM is composed of a single non-homogeneous linear second-order ordinary differential that was solved analytically. Compared to 2PADM, the 1P-ADM has provided reliable predictions of the dissolved and gaseous ozone concentrations.

An impinging-jet bubble column, that utilized two venturi injectors, has been tested for the ozone mass transfer applications. The venturi injectors created impinging gas-liquid jets in the ambient fluid and that caused an increase in the turbulence produced in the ambient fluid and therefore, the gas-liquid mass transfer rates increased. The 1P-ADM was applied to analyze the measured dissolved and gaseous ozone concentrations.

Excellent conformity between the measured and the predicted concentrations was observed. Therefore, the 1P-ADM model has proven to be an efficient, adequate, and easy-to-use tool for describing the ozonation in the impinging-jet bubble column.

Compared to conventional diffuser ozone bubble columns, the impinging-jet design has provided comparable reduction efficiencies of the impurities present in Kraft pulp mill effluents. However, the impinging-jet bubble column was more effective due to its smaller reactor volume and lower off-gas ozone concentrations.

A 2-D laser particle dynamics analyzer was used to measure the characteristics of the gas bubbles in the impinging-jet bubble column using clean deionized water and ozonated Kraft pulp mill effluent as the test liquid. The count mean bubble diameter ( $d_B$ ) and Sauter mean bubble diameter ( $d_S$ ) were smaller than those obtained in conventional bubble columns and that has led to a significant increase in the specific bubbles' interfacial area and gas hold-up.

## **ACKNOWLEDGEMENT**

I would like to express my sincere and great appreciation to Dr. Daniel W. Smith for his guidance, support, encouragement, and patience throughout my research program. I also would like to thank him for encouraging me to attend many technical conferences and gave me the opportunity to submit and publish a number of papers.

I also want to express my great appreciation and thanks to my great brother and friend Mr. Ahmed Gamal El-Din who has been always there when I needed him and with whom I shared great discussions throughout my research program. He also has provided me with great suggestions and thoughts throughout the preparation of my thesis.

A special thank you to my great collogue and friend Mr. Kevin McCullum for his help during some of my experimental laboratory work. I also appreciate the suggestions and fruitful discussions he has shared with me throughout my research program.

I would to thank all the technical staff at the Environmental Engineering Laboratory at the University of Alberta for their great assistance during the laboratory program. Especially, Mr. Nick Chernuka, Mrs. Maria Demeter, and Mrs. Debra Long. I also appreciate the assistance by Mr. Garry Solonynko during the setting-up of the experimental apparatus.

The financial support throughout the research project was provided to Dr. Daniel W. Smith by the Sustainable Forest Management (SFM) network and the Natural Sciences and Engineering Research Council of Canada (NSERC) is greatly appreciated.

Finally a special thank you to my parents and my brother for their guidance, encouragement, understanding, and sacrifices during the course of the long journey of my graduate studies.

## TABLE OF CONTENTS

CHAPTER 1.	GENERAL INTRODUCTION.....	1
1.1	BACKGROUND .....	1
1.2	FUNDAMENTALS OF THE OZONATION PROCESS.....	6
1.2.1	Backmixing Process.....	6
1.2.2	Ozone Auto-Decomposition Process .....	6
1.2.3	Mass Transfer Process .....	8
1.2.3.1	Mass Transfer Without Chemical Reactions .....	8
1.2.3.2	Mass Transfer With Chemical Reactions .....	8
1.3	Practical ASPECTS OF OZONE CONTACTORS .....	10
1.3.1	Types of Ozone Contactors.....	10
1.3.2	Designing Ozone Contactors .....	12
1.4	OBJECTIVES AND SCOPES OF THE RESEARCH PROGRAM.....	13
1.5	REFERENCES .....	16
CHAPTER 2.	DEVELOPMENT OF TRANSIENT BACK FLOW CELL MODEL (BFCM) FOR BUBBLE COLUMNS* .....	20
2.1	INTRODUCTION .....	20
2.2	TRACER TESTS.....	21
2.3	THEORY .....	23
2.3.1	Axial Dispersion Model.....	23
2.3.2	Transient Continuous-Flow-Stirred-Tank-Reactors In-Series Model ...	26
2.4	Transient Back Flow Cell Model (BFCM) .....	27
2.4.1	Development of the Transient BFCM.....	27
2.4.2	Numerical Simulations of the Transient BFCM .....	33
2.4.2.1	Numerical Solution Technique .....	33
2.4.2.2	Results.....	34
2.5	TESTING OF THE TRANSIENT BFCM.....	43
2.5.1	Experimental Study.....	43
2.5.2	Data Analysis Technique .....	43
2.5.3	Results.....	45

2.6	CONCLUSIONS.....	49
2.7	REFERENCES .....	50
CHAPTER 3.	<b>OZONE MASS TRANSFER IN WATER TREATMENT: MASS TRANSFER MODELING OF OZONE BUBBLE COLUMNS*</b> .....	52
3.1	INTRODUCTION .....	52
3.2	THEORETICAL BACKGROUND.....	53
3.3	DEVELOPMENT OF THE BACK FLOW CELL MODEL (BFCM)..	56
3.3.1	Transient BFCM .....	56
3.3.2	Steady-State BFCM.....	59
3.4	RESULTS AND DISCUSSION .....	63
3.4.1	Transient BFCM .....	63
3.4.2	Steady-state BFCM.....	64
3.5	CONCLUSIONS.....	67
3.6	REFERENCES .....	68
CHAPTER 4.	<b>TWO-PHASE NON-ISOBARIC AXIAL DISPERSION MODELS FOR MODELING THE OZONATION PROCESS DYNAMICS–I. MODELS DEVELOPMENT</b> .....	70
4.1	INTRODUCTION .....	70
4.1.1	Ozonation Process Dynamics .....	70
4.1.2	Bubble Column Parameters .....	70
4.1.3	Dispersion Models for Two-Phase Flows.....	71
4.2	PROCESSES FUNDAMENTALS .....	72
4.2.1	Slow-Chemical-Reaction-Kinetics-Regime Systems .....	72
4.2.2	Fast-Chemical-Reaction-Kinetics-Regime Systems.....	74
4.3	DEVELOPMENT OF THE TWO-PHASE AXIAL DISPERSION MODEL (2P-ADM) EQUATIONS .....	76
4.3.1	Considering the Gas-Phase Dispersion.....	77
4.3.1.1	Wastewater Treatment Conditions.....	77
4.3.1.2	Boundary Conditions .....	81
4.3.2	Special Conditions of the Two-Phase Axial Dispersion Model (2P-ADM).....	83

4.3.2.1	Consideration of the Gas-Phase Dispersion (Water Treatment Conditions).....	83
4.3.2.2	Neglecting the Gas-Phase Dispersion.....	83
4.4	NUMERICAL SOLUTION TECHNIQUE.....	85
4.4.1	2P-ADM With Gas-Phase Dispersion (Wastewater Treatment Conditions).....	86
4.4.2	2P-ADM With Gas-Phase Dispersion (Water Treatment Conditions)..	89
4.4.3	2P-ADM without gas phase dispersion.....	89
4.5	CONCLUSIONS.....	90
4.6	REFERENCES .....	91
CHAPTER 5.	TWO-PHASE NON-ISOBARIC AXIAL DISPERSION MODELS FOR MODELING THE OZONATION PROCESS DYNAMICS–II. NUMERICAL ANALYSES AND EXPERIMENTAL VERIFICATION* .....	93
5.1	INTRODUCTION .....	93
5.2	NUMERICAL SIMULATIONS AND SENSITIVITY ANALYSES... 94	
5.2.1	Numerical Solution Techniques of the 2P-ADM Equations.....	94
5.2.2	Operating Conditions for Water Treatment Applications.....	95
5.2.3	Operating Conditions for Wastewater Treatment Applications.....	96
5.2.4	Operating Conditions for Model Testing (Water Treatment Applications).....	97
5.3	RESULTS AND DISCUSSION .....	98
5.3.1	Counter-Current Flow Mode (Water Treatment Applications) .....	98
5.3.2	Co-Current Flow Mode (Water Treatment Applications) .....	108
5.3.3	Counter-Current and Co-Current Flow Modes (Wastewater Treatment Applications) .....	112
5.3.4	Model Testing for Water Treatment Applications.....	115
5.4	CONCLUSIONS.....	117
5.5	REFERENCES .....	118

<b>CHAPTER 6.</b>	<b>THEORETICAL ANALYSIS AND EXPERIMENTAL VERIFICATION OF OZONE MASS TRANSFER IN BUBBLE COLUMNS*</b>	<b>119</b>
6.1	INTRODUCTION	119
6.2	THEORETICAL BACKGROUND	121
6.3	OUTLINE OF THE MATHEMATICAL MODELS AND THE NUMERICAL SOLUTIONS TECHNIQUES	124
6.3.1	Axial Dispersion Model (ADM)	124
6.3.2	Back Flow Cell Model (BFCM)	126
6.4	OPERATING CONDITIONS FOR MODELS TESTING AND NUMERICAL ANALYSES	129
6.4.1	Water Treatment	129
6.4.2	Wastewater Treatment	130
6.5	RESULTS AND DISCUSSION	131
6.5.1	Water Treatment: Initial Testing of the Models	131
6.5.2	Wastewater Treatment	133
6.6	CONCLUSIONS	139
6.7	REFERENCES	140
<b>CHAPTER 7.</b>	<b>DESIGNING OZONE BUBBLE COLUMNS: A SPREADSHEET APPROACH TO AXIAL DISPERSION MODEL*</b>	<b>142</b>
7.1	INTRODUCTION	142
7.2	DISPERSION MODELS FOR TWO-PHASE FLOWS	145
7.2.1	Process Fundamentals	145
7.2.2	Mass Transfer Process with Chemical Reactions	147
7.2.3	Two-Phase Axial Dispersion Model (2P-ADM)	149
7.2.4	Development of the One-Phase Axial Dispersion Model (1P-ADM)	151
7.3	OPERATING CONDITIONS FOR THE MODEL SIMULATIONS AND TESTING	158
7.3.1	Water Treatment Conditions	158
7.3.2	Wastewater Treatment Conditions	158

7.4	RESULTS AND DISCUSSION.....	160
7.4.1	Theoretical Analyses of the 1P-ADM Predictions.....	160
7.4.1.1	Water Treatment Applications: Counter-Current Flow Mode.....	160
7.4.1.1	Water Treatment Applications: Co-Current Flow Mode.....	164
7.4.1.2	Wastewater Treatment Applications: Counter-Current and Co-Current Flow Modes .....	168
7.4.2	Initial Model Testing for Water Treatment Conditions .....	171
7.5	CONCLUSIONS.....	174
7.6	REFERENCES .....	175
CHAPTER 8.	DEVELOPMENT OF DESIGN PARAMETERS OF AN IMPINGING-JET BUBBLE COLUMN* .....	178
8.1	INTRODUCTION .....	178
8.2	OUTLINE OF THE MODIFIED NON-ISOBARIC ONE-PHASE AXIAL DISPERSION MODEL (1P-ADM) .....	181
8.3	EXPERIMENTAL AND DATA ANALYSES METHODS.....	186
8.3.1	Bench Tests: Ozone Auto-Decomposition kinetics Study.....	186
8.3.2	Pilot-Scale Tests: Ozone Mass Transfer Study.....	188
8.3.3	Data Analysis Method for the Kinetics Study .....	193
8.3.4	Data Analysis Method for the Mass Transfer Study.....	193
8.4	EXPERIMENTAL RESULTS.....	194
8.4.1	Bench Tests: Ozone Auto-Decomposition Kinetics Study.....	194
8.4.2	Pilot-Scale Tests: Ozone Mass Transfer Study.....	196
8.5	DEVELOPMENT OF PROCESS-PARAMETER CORRELATIONS .....	200
8.5.1	Correlations of the Mass Transfer Coefficient.....	201
8.5.2	Correlations of the Backmixing Coefficient .....	209
8.5.3	Correlations of the Gas-phase-Concentration-Decrease Exponent.....	212
8.6	CONCLUSIONS.....	214
8.7	REFERENCES .....	215

<b>CHAPTER 9.</b>	<b>MAXIMIZING THE ENHANCED OZONE OXIDATION OF KRAFT PULP MILL EFFLUENTS IN AN IMPINGING-JET BUBBLE COLUMN*</b>	<b>219</b>
9.1	INTRODUCTION	219
9.2	FUNDAMENTALS OF THE OZONATION PROCESS	222
9.3	THE MODIFIED NON-ISOBARIC ONE-PHASE AXIAL DISPERSION MODEL (1P-ADM)	222
9.4	EXPERIMENTAL METHODS	223
9.4.1	Bench Tests: Ozone Auto-Decomposition Kinetics Study	223
9.4.2	Pilot-Scale Tests: Continuous-Flow Mode/Ozonation of Water and Pulp Mill Effluent	224
9.4.3	Pilot-Scale Tests: Semibatch-Flow Mode/Ozonation of Pulp mill Effluent	227
9.4.4	Pulp Mill Effluent Characterization	227
9.5	RESULTS AND DISCUSSION	228
9.5.1	Bench Tests: Ozone Auto-Decomposition Kinetics	228
9.5.2	Pilot-Scale Tests: Ozone Mass Transfer in Water	230
9.5.3	Ozone Mass Transfer in Pulp Mill Effluent: Gas Absorption Dynamics	232
9.5.4	Ozone Oxidation Efficiencies	237
9.6	CONCLUSIONS	241
9.7	REFERENCES	243
<b>CHAPTER 10.</b>	<b>COMPARING DIFFERENT DESIGNS AND SCALES OF BUBBLE COLUMNS FOR THEIR EFFECTIVENESS IN TREATING KRAFT PULP MILL EFFLUENTS*</b>	<b>246</b>
10.1	INTRODUCTION	246
10.2	EXPERIMENTAL METHODS	248
10.2.1	Extra-Coarse-Bubble Diffuser Ozone Contactor	248
10.2.2	Impinging-Jet Ozone Contactor	249
10.2.2.1	Continuous-Flow Mode	249
10.2.2.2	Semibatch-Flow Mode	252

10.2.3	Fine-Bubble Diffuser Ozone Contactor.....	252
10.2.4	Characterization of the Pulp Mill Wastewater.....	252
10.3	<b>RESULTS AND DISCUSSION.....</b>	<b>253</b>
10.3.1	Ozonation Treatment Efficiencies .....	253
10.3.1.1	Extra-Coarse-Bubble Diffuser Ozone Contactor .....	253
10.3.1.2	Impinging-Jet Ozone Contactor.....	255
10.3.2	Ozone Gas Absorption Dynamics.....	259
10.3.3	Modeling of the Ozonation Treatment Efficiencies.....	264
10.3.4	Scale-Up of the Ozonation Process.....	269
10.4	<b>CONCLUSIONS.....</b>	<b>272</b>
10.5	<b>REFERENCES .....</b>	<b>273</b>
CHAPTER 11.	<b>Measurements of the Size, Rise Velocity, and Specific Interfacial Area of Bubbles in an Impinging-Jet Bubble Column*.....</b>	<b>275</b>
11.1	<b>INTRODUCTION .....</b>	<b>275</b>
11.2	<b>MEASUREMENT METHODS.....</b>	<b>277</b>
11.2.1	Particle Dynamics Analyzer .....	277
11.2.1.1	Operating Principle .....	277
11.2.1.2	Principle of the Bubble Rise Velocity Measurement.....	277
11.2.1.3	Principle of the Bubble Size and Concentration Measurements.....	278
11.2.1.4	PDA System Configuration and Operational Settings Adjustment .....	280
11.2.2	Digital Photographic Measurements of the Bubble Size and the Bubble Rise Velocity .....	280
11.2.3	Experimental Set-Up for the Photographic and the PDA Studies .....	282
11.2.4	Experimental Set-Up for the Ozonation of Kraft Pulp Mill Effluent ..	283
11.3	<b>RESULTS AND DISCUSSION.....</b>	<b>285</b>
11.3.1	Digital Photographic Measurements.....	285
11.3.2	Particle Dynamics Analyzer Measurements .....	287
11.3.2.1	Deionized Water .....	287
11.3.2.2	Kraft pulp mill effluent .....	297
11.4	<b>Conclusions.....</b>	<b>305</b>
11.5	<b>REFERENCES .....</b>	<b>307</b>

<b>CHAPTER 12. GENERAL CONCLUSIONS AND RECOMMENDATIONS.....</b>	<b>309</b>
<b>12.1 GENERAL OVERVIEW .....</b>	<b>309</b>
<b>12.2 CONCLUSIONS.....</b>	<b>311</b>
<b>12.3 RECOMMENDATIONS.....</b>	<b>317</b>
<b>APPENDIX A. CURRICULUM VITAE.....</b>	<b>319</b>

## LIST OF TABLES

Table 3.1	Operating conditions for the co-current flow mode.....	64
Table 3.2	Operating conditions for the counter-current flow mode.....	65
Table 5.1	Operating conditions for the counter-current flow mode (water treatment). ....	97
Table 5.2	Operating conditions for the co-current flow mode (water treatment). ....	98
Table 6.1	Mathematical representation of the ADM (Gamal El-Din and Smith, 2000).....	125
Table 6.2	Mathematical representation of the BFCM (Gamal El-Din and Smith, 2000).....	127
Table 6.3	Dimensionless parameters pertaining to the ADM and the BFCM. ....	129
Table 6.4	Operating conditions for the co-current and counter-current flow modes (water treatment). ....	130
Table 7.1	Dimensionless parameters that are used to describe the 1P-ADM and the 2P-ADM.....	150
Table 7.2	Mathematical representation of the 2P-ADM for water and wastewater treatment applications. ....	151
Table 7.3	Coefficients of the exponential model used for the prediction of the gaseous ozone profiles. ....	153
Table 7.4	Operating conditions for the counter-current flow mode (water treatment). ....	159
Table 7.5	Operating conditions for the co-current flow mode (water treatment). ..	160
Table 8.1	Dimensionless parameters pertaining to the 1P-ADM. ....	184
Table 8.2	Mathematical representation of the 1P-ADM differential equation and boundary conditions. ....	184
Table 8.3	Main Average characteristics of the deionized water. ....	187
Table 8.4	Operating conditions of the pilot-scale ozone mass transfer experiments. ....	192
Table 9.1	Average characteristics of the deionized water. ....	224

<b>Table 9.2</b>	<b>Average characteristics of the pulp mill effluent.....</b>	<b>228</b>
<b>Table 10.1</b>	<b>Average characteristics of the raw pulp mill effluent.....</b>	<b>251</b>
<b>Table 10.2</b>	<b>Regression parameters for the modeling of the induced reduction efficiencies of color, AOX, COD, and TOC.....</b>	<b>268</b>
<b>Table 10.3</b>	<b>A comparison between three different scales and designs of ozone contactors in terms of the color, AOX, COD, and TOC reduction efficiencies.....</b>	<b>270</b>
<b>Table 11.1</b>	<b>PDA system configuration and operational settings.....</b>	<b>281</b>
<b>Table 11.2</b>	<b>Kraft pulp mill effluent average characteristics.....</b>	<b>283</b>

## LIST OF FIGURES

Figure 2.1	Theoretical RTD curves for the transient ADM under closed-closed or closed-open boundary conditions. ....	25
Figure 2.2	Theoretical RTD curves for the transient CFSTR's in-series model. ....	26
Figure 2.3	Transient BFCM schematic for non-reactive tracer for a co-current flow conditions. ....	28
Figure 2.4	Theoretical RTD's for $N_{BFCM} = 10$ at the bottom sampling port. ....	35
Figure 2.5	Theoretical RTD's for $N_{BFCM} = 10$ at the top sampling port. ....	35
Figure 2.6	Effect of $Pe_L$ and $N_{BFCM}$ on the theoretical RTD's at the middle sampling port for $Pe_L = 1.0$ . ....	36
Figure 2.7	Effect of $Pe_L$ and $N_{BFCM}$ on the theoretical RTD's at the top sampling port for $Pe_L = 1.0$ . ....	37
Figure 2.8	Effect of $Pe_L$ and $N_{BFCM}$ on the theoretical RTD's at the middle sampling port for $Pe_L = 40.0$ . ....	37
Figure 2.9	Effect of $Pe_L$ and $N_{BFCM}$ on the theoretical RTD's at the top sampling port for $Pe_L = 40.0$ . ....	38
Figure 2.10	Comparison between the transient BFCM, ADM, and CFSTR's in-series model on the theoretical RTD's for $Pe_L = 1.0$ and $N_{BFCM} = N_{FCSTR} = 10$ . ....	39
Figure 2.11	Comparison between the transient BFCM, ADM, and CFSTR's in-series model on the theoretical RTD's for $Pe_L = 20.0$ and $N_{BFCM} = N_{FCSTR} = 10$ . ....	39
Figure 2.12	Comparison between the transient BFCM, ADM, and CFSTR's in-series model on the theoretical RTD's for $Pe_L = 1.0$ and $N_{BFCM} = N_{FCSTR} = 20$ . ....	40
Figure 2.13	Comparison between the transient BFCM, ADM, and CFSTR's in-series model on the theoretical RTD's for $Pe_L = 20.0$ and $N_{BFCM} = N_{FCSTR} = 20$ . ....	41
Figure 2.14	Theoretical RTD's for $N_{BFCM} = 20.0$ and variable $Pe_L$ along the column height ( $j = 1$ to $4$ ). ....	42

Figure 2.15	Theoretical RTD's for $N_{BFCM} = 20.0$ and variable $Pe_L$ along the column height ( $j = 5$ to $20$ ). .....	42
Figure 2.16	Experimental and predicted RTD's in a counter-current flow mode.....	44
Figure 2.17	Experimental and predicted RTD's in a co-current flow mode.....	45
Figure 2.18	Comparison between the transient BFCM and the regression model predictions of back flow ratios.....	47
Figure 2.19	Comparison between the transient BFCM, ADM, and CFSTR's model in predicting the RTD's in a co-current bubble column. ....	47
Figure 3.1	BFCM schematic for co-current flow conditions in bubble columns.....	56
Figure 3.2	Theoretical RTD at the bottom sampling port. ....	63
Figure 3.3	Theoretical RTD at the top sampling port. ....	64
Figure 3.4	Steady-state BFCM testing for co-current flow mode.....	65
Figure 3.5	Steady-state BFCM testing for counter-current flow mode.....	66
Figure 4.1	Schematic representation of the co-current axial dispersion model. ....	77
Figure 4.2	Computational upwind finite difference scheme. ....	85
Figure 5.1	$Pe_L$ and $Pe_G$ effects on the 2P-ADM predicted dissolved ozone concentration profiles in the counter-current flow mode and for water treatment applications ( $(Pe_L = 1.0, 2.5, 5.0, 10.0, 20.0,$ and $\infty)$ and $(Pe_G = 12.4/124.0, 30.9/309.0, 61.8/618.0, 123.7/1237.0, 247.3/2473.0,$ and $\infty)$ ). ....	99
Figure 5.2	$Pe_L$ and $Pe_G$ effects on the 2P-ADM predicted gaseous ozone concentration and superficial gas velocity profiles in the counter-current flow mode and for water treatment applications ( $(Pe_L = 1.0, 2.5, 5.0, 10.0, 20.0,$ and $\infty)$ and $(Pe_G = 12.4/124.0, 30.9/309.0, 61.8/618.0, 123.7/1237.0, 247.3/2473.0,$ and $\infty)$ ). ....	100
Figure 5.3	$k_L a$ effects on the 2P-ADM predicted dissolved ozone concentration profiles in the counter-current flow mode and for water treatment applications ( $k_L a = 1.0 \times 10^{-3}, 3.0 \times 10^{-3}, 5.0 \times 10^{-3}, 7.0 \times 10^{-3}, 1.0 \times 10^{-2}, 1.5 \times 10^{-2},$ and $2.0 \times 10^{-2} \text{ s}^{-1}$ ). ....	101
Figure 5.4	$k_L a$ effects on the 2P-ADM predicted gaseous ozone concentration and superficial gas velocity profiles in the counter-current flow mode	

	and for water treatment applications ( $k_{La} = 1.0 \times 10^{-3}$ , $3.0 \times 10^{-3}$ , $5.0 \times 10^{-3}$ , $7.0 \times 10^{-3}$ , $1.0 \times 10^{-2}$ , $1.5 \times 10^{-2}$ , and $2.0 \times 10^{-2} \text{ s}^{-1}$ ). .....	102
Figure 5.5	$D_a$ effects on the 2P-ADM predicted dissolved ozone concentration profiles in the counter-current flow mode and for water treatment applications ( $D_a = 0.0000$ , $0.0505$ , $0.0831$ , $0.1010$ , $0.5050$ , $1.0000$ , $3.0000$ , and $6.0000$ ). .....	103
Figure 5.6	$D_a$ effects on the 2P-ADM predicted gaseous ozone concentration and superficial gas velocity profiles in the counter-current flow mode and for water treatment applications ( $D_a = 0.0000$ , $0.0505$ , $0.0831$ , $0.1010$ , $0.5050$ , $1.0000$ , $3.0000$ , and $6.0000$ ). .....	104
Figure 5.7	$P_T$ or $\alpha$ effects on the 2P-ADM predicted dissolved ozone concentration profiles in the counter-current flow mode and for water treatment applications ( $P_T = 101.3$ , $303.9$ , $506.5$ , $709.1$ , $1013.0$ , and $\infty$ kPa).....	105
Figure 5.8	$P_T$ or $\alpha$ effects on the 2P-ADM predicted gaseous ozone concentration and superficial gas velocity profiles in the counter-current flow mode and for water treatment applications ( $P_T = 101.3$ , $303.9$ , $506.5$ , $709.1$ , $1013.0$ , and $\infty$ kPa).....	107
Figure 5.9	$k_{La}$ effects on the 2P-ADM predicted dissolved ozone concentration profiles in the co-current flow mode and for water treatment applications ( $k_{La} = 1.0 \times 10^{-3}$ , $3.0 \times 10^{-3}$ , $5.0 \times 10^{-3}$ , $7.0 \times 10^{-3}$ , $1.0 \times 10^{-2}$ , $1.5 \times 10^{-2}$ , and $2.0 \times 10^{-2} \text{ s}^{-1}$ ). .....	110
Figure 5.10	$k_{La}$ effects on the 2P-ADM predicted gaseous ozone concentration and superficial gas velocity profiles in the co-current flow mode and for water treatment applications ( $k_{La} = 1.0 \times 10^{-3}$ , $3.0 \times 10^{-3}$ , $5.0 \times 10^{-3}$ , $7.0 \times 10^{-3}$ , $1.0 \times 10^{-2}$ , $1.5 \times 10^{-2}$ , and $2.0 \times 10^{-2} \text{ s}^{-1}$ ). .....	111
Figure 5.11	$D_a$ and $M$ effects on the 2P-ADM predicted dissolved ozone concentration profiles in the counter and co-current flow mode and for wastewater treatment applications ( $D_a = 89$ and $M = 0.037$ to $D_a = 8900000$ and $M = 11.659$ ). .....	113

Figure 5.12	$k_{La}$ effects on the 2P-ADM predicted gaseous ozone concentration and superficial gas velocity profiles in the counter and co-current flow modes and for wastewater treatment applications ( $k_{La} = 1.0 \times 10^{-3}, 3.0 \times 10^{-3}, 5.0 \times 10^{-3}, 7.0 \times 10^{-3}, 1.0 \times 10^{-2}, 1.5 \times 10^{-2},$ and $2.0 \times 10^{-2} \text{ s}^{-1}$ ). .....	114
Figure 5.13	Comparison between the predicted and the measured dissolved ozone concentration profiles in a counter-current fine-bubble diffuser ozone bubble column for water treatment applications.....	115
Figure 5.14	Comparison between the predicted and the measured dissolved ozone concentration profiles in a co-current fine-bubble diffuser ozone bubble column for water treatment applications. ....	116
Figure 6.1	Reaction kinetics regimes for ozone absorption process (adapted from Zhou and Smith, 1997).....	120
Figure 6.2	Schematic representation of the co-current ADM. ....	124
Figure 6.3	Schematic representation of the co-current BFCM. ....	126
Figure 6.4	Comparison between the predicted and the measured dissolved ozone concentrations in a co-current bubble column for water treatment applications. ....	132
Figure 6.5	Comparison between the predicted and the measured dissolved ozone concentrations in a counter-current bubble column for water treatment applications. ....	132
Figure 6.6	Effect of $Pe_L$ on the dissolved ozone profiles in the co-current flow mode for wastewater treatment applications ( $(Pe_L = 1.0, 2.5, 5.0, 10.0, 20.0,$ and $\infty)$ , $D_a = 89, k_{La} = 5.0 \times 10^{-3} \text{ s}^{-1}, M = 0.037,$ $\alpha = 0.48,$ and $y_0 = 0.00675$ ). .....	134
Figure 6.7	Effects of $Pe_L$ on the gaseous ozone and the superficial gas velocity profiles in the co-current flow mode for wastewater treatment applications ( $(Pe_L = 1.0, 2.5, 5.0, 10.0, 20.0,$ and $\infty)$ , $D_a = 89, k_{La} = 5.0 \times 10^{-3} \text{ s}^{-1}, M = 0.037, \alpha = 0.48,$ and $y_0 = 0.00675$ ). .	135
Figure 6.8	Effect of $k_{La}$ on the dissolved ozone profiles in the co-current flow mode for wastewater treatment applications ( $(k_{La} = 1.0 \times 10^{-3},$	

	3.0 x 10 <sup>-3</sup> , 5.0 x 10 <sup>-3</sup> , 7.0 x 10 <sup>-3</sup> , 1.0 x 10 <sup>-2</sup> , 1.5 x 10 <sup>-2</sup> , and 2.0 x 10 <sup>-2</sup> s <sup>-1</sup> ), Pe <sub>L</sub> = 5.0, D <sub>a</sub> = 89, M = 0.037, α = 0.48, and y <sub>0</sub> = 0.00675).....	136
Figure 6.9	Effects of k <sub>L</sub> a on the gaseous ozone and the superficial gas velocity profiles in the co-current flow mode for wastewater treatment applications ((k <sub>L</sub> a = 1.0 x 10 <sup>-3</sup> , 3.0 x 10 <sup>-3</sup> , 5.0 x 10 <sup>-3</sup> , 7.0 x 10 <sup>-3</sup> , 1.0 x 10 <sup>-2</sup> , 1.5 x 10 <sup>-2</sup> , and 2.0 x 10 <sup>-2</sup> s <sup>-1</sup> ), Pe <sub>L</sub> = 5.0, D <sub>a</sub> = 89, M = 0.037, α = 0.48, and y <sub>0</sub> = 0.00675).....	137
Figure 7.1	Reaction kinetics regimes for ozone absorption process (adapted from Zhou and Smith, 1997).....	144
Figure 7.2	Schematic representation of the co-current ADM. ....	149
Figure 7.3	Typical gaseous ozone profiles in bubble columns for water and wastewater treatment conditions. ....	152
Figure 7.4	Pe <sub>L</sub> effects on the concentration profiles in the counter-current flow mode and water treatment applications. ....	161
Figure 7.5	k <sub>L</sub> a effects on the concentration profiles in the counter-current flow mode and water treatment applications. ....	162
Figure 7.6	D <sub>a</sub> effects on the concentration profiles in the counter-current flow mode and water treatment applications. ....	162
Figure 7.7	Pe <sub>L</sub> effects on the concentration profiles in the co-current flow mode and water treatment applications.....	164
Figure 7.8	k <sub>L</sub> a effects on the concentration profiles in the co-current flow mode and water treatment applications.....	166
Figure 7.9	D <sub>a</sub> effects on the concentration profiles in the co-current flow mode and water treatment applications.....	167
Figure 7.10	Pe <sub>L</sub> effects on the concentration profiles in the wastewater treatment applications. ....	169
Figure 7.11	k <sub>L</sub> a effects on the concentration profiles in the wastewater treatment applications. ....	169
Figure 7.12	D <sub>a</sub> and M effects on the concentration profiles in the wastewater treatment applications. ....	170

Figure 7.13	Comparison between the predicted and the experimental dissolved ozone concentrations in an ozone bubble column under water treatment conditions for the counter-current flow mode. ....	172
Figure 7.14	Comparison between the predicted and the experimental dissolved ozone concentrations in an ozone bubble column under water treatment conditions for the co-current flow mode.....	172
Figure 8.1	Schematic representation of the 1P-ADM. ....	182
Figure 8.2	Schematic of the headspace-free reactor.....	186
Figure 8.3	Schematics of the pilot-scale impinging-jet bubble column and the configuration of the Mazzei <sup>®</sup> injector (model 384). ....	189
Figure 8.4	Typical ozone auto-decomposition kinetics in deionized water. ....	194
Figure 8.5	The effect of water temperature on the ozone auto-decomposition rate constant. ....	195
Figure 8.6	Typical dimensionless dissolved ozone concentration profiles in the impinging-jet bubble column operated in a gas-injection mode...	197
Figure 8.7	Typical dimensionless dissolved ozone concentration profiles in the impinging-jet bubble column operated in a gas-ejection mode. ...	197
Figure 8.8	Effects of the $u_G$ and $u_L$ on the gas bubble diameters and concentrations in the injection mode. ....	205
Figure 8.9	Comparison of the $k_L a$ correlations for gas sparging under positive pressure in various types of bubble columns. ....	207
Figure 8.10	Comparison of the $k_L a$ correlations for gas sparging under negative pressure in various types of bubble columns.....	208
Figure 8.11	Comparison between the 1P-ADM and the non-linear regression correlations of $k_L a$ . ....	208
Figure 8.12	Comparison between the 1P-ADM and the non-linear regression correlations of $D_L$ . ....	211
Figure 8.13	Comparison between the 1P-ADM and the linear regression correlations of $a_1$ . ....	212
Figure 9.1	Schematic of the floating-lid headspace-free reactor.....	223
Figure 9.2	Schematic of the experimental set-up of the pilot-scale	

	impinging-jet bubble column.....	226
Figure 9.3	The effect of water temperature on the ozone auto-decomposition kinetics in deionized water.....	230
Figure 9.4	A comparison between the $k_{La}$ 's predicted using the 1P-ADM and the non-linear regression analyses. ....	232
Figure 9.5	The effect of ozonation on $E_{kLa}$ values.....	234
Figure 9.6	The effect of ozonation on E values. ....	235
Figure 9.7	The effect of the ozone contact time on the amounts of the applied, utilized, and exhausted ozone.....	236
Figure 9.8	A comparison between the measured and the predicted off-gas ozone concentrations.....	237
Figure 9.9	The ozonation treatment reduction efficiencies of color, AOX, TOC, and COD. ....	238
Figure 9.10	The ozonation effects on the biodegradability of pulp mill effluents.....	240
Figure 10.1	Schematic of the experimental set-up of the extra-coarse-bubble diffuser ozone contactor.....	248
Figure 10.2	Schematic of the experimental set-up of the pilot-scale impinging-jet ozone contactor. ....	250
Figure 10.3	Reduction efficiencies of color, AOX, COD, and TOC in the extra-coarse-bubble diffuser ozone contactor.....	254
Figure 10.4	The effect of ozonation on the $BOD_5$ of the pulp mill wastewater treated in the extra-coarse-bubble diffuser ozone contactor.....	255
Figure 10.5	Reduction efficiencies of color, AOX, COD, and TOC in the impinging-jet ozone contactor operated in a semibatch-flow mode.....	257
Figure 10.6	Reduction efficiencies of color, AOX, COD, and TOC in the impinging-jet ozone contactor operated in a continuous-flow mode.....	257
Figure 10.7	The effect of ozonation on the $BOD_5$ of the pulp mill wastewater treated in the impinging-jet ozone contactor. ....	258
Figure 10.8	The effect of ozonation on the off-gas ozone concentration profiles in three different ozone contactors operated in a semibatch-flow mode. ....	260

Figure 10.9	The effect of ozonation on the off-gas to the feed-gas ozone concentrations' ratio in the impinging-jet ozone contactor operated in a continuous-flow mode.....	261
Figure 10.10	The effect of ozonation on the E values in three different ozone contactors operated in a semibatch-flow mode.....	263
Figure 10.11	The effect of ozonation on the $ESt_G$ values in three different ozone contactors operated in a semibatch-flow mode. ....	263
Figure 10.12	The effect of ozonation on the $BOD_5/COD$ ratio of the treated Kraft pulp mill wastewater in the impinging-jet ozone contactor.....	264
Figure 10.13	The effect of ozonation on the color/COD ratio of the treated Kraft pulp mill wastewater in the impinging-jet ozone contactor.....	265
Figure 10.14	The effect of ozonation on the AOX/COD ratio of the treated Kraft pulp mill wastewater in the impinging-jet ozone contactor.....	266
Figure 10.15	The effect of ozonation on the TOC/COD ratio of the treated Kraft pulp mill wastewater in the impinging-jet ozone contactor.....	266
Figure 10.16	A comparison between the predicted and the measured reduction efficiencies of AOX. ....	269
Figure 11.1	Components of the particle dynamics analyzer set-up. ....	279
Figure 11.2	Schematic of the experimental set-up of the pilot-scale impinging-jet bubble column.....	282
Figure 11.3	Schematic of the ozonation system set-up. ....	284
Figure 11.4	A digital image of the air bubbles at $u_L = 7.7 \times 10^{-3} \text{ ms}^{-1}$ and $u_G = 1.0 \times 10^{-3} \text{ ms}^{-1}$ . ....	286
Figure 11.5	A digital image of the air bubbles at $u_L = 7.7 \times 10^{-3} \text{ ms}^{-1}$ and $u_G = 7.8 \times 10^{-3} \text{ ms}^{-1}$ . ....	286
Figure 11.6	A digital image of the air bubbles at $u_L = 1.9 \times 10^{-2} \text{ ms}^{-1}$ and $u_G = 8.7 \times 10^{-4} \text{ ms}^{-1}$ . ....	287
Figure 11.7	Definition of angle $\phi$ . ....	287
Figure 11.8	Effects of $u_G$ and $u_L$ on $d_B$ and $d_S$ in deionized water. ....	288
Figure 11.9	A typical plot of the count-based bubble size distribution in deionized water at high $u_G$ and low $u_L$ . ....	289

Figure 11.10	A typical plot of the volume-based bubble size distribution in deionized water at high $u_G$ and low $u_L$ .....	290
Figure 11.11	A typical plot of the surface area-based bubble size distribution in deionized water at high $u_G$ and low $u_L$ .....	291
Figure 11.12	A typical plot of the count-based bubble size distribution in deionized water at low $u_G$ and low $u_L$ .....	292
Figure 11.13	Effects of $u_G$ and $u_L$ on $C_B$ in deionized water.....	292
Figure 11.14	Effects of $u_G$ and $u_L$ on the gas-phase axial turbulence % in deionized water.....	293
Figure 11.15	Typical probability density distributions of the gas-phase $u$ and $v$ in deionized water.....	295
Figure 11.16	Effects of $u_G$ and $u_L$ on $u$ in deionized water.....	296
Figure 11.17	Effects of $u_G$ and $u_L$ on $\epsilon_G$ in deionized water.....	297
Figure 11.18	Effects of $u_G$ and $u_L$ on $a$ in deionized water.....	297
Figure 11.19	Effects of $u_G$ and $u_L$ on $d_B$ and $d_S$ in raw Kraft pulp mill effluent.....	299
Figure 11.20	Effects of $\Delta O_3$ on $d_B$ and $d_S$ in Kraft pulp mill effluent.....	300
Figure 11.21	Effects of $u_G$ and $u_L$ on $C_B$ in raw Kraft pulp mill effluent.....	301
Figure 11.22	Effects of $u_G$ and $u_L$ on $\epsilon_G$ in raw Kraft pulp mill effluent.....	302
Figure 11.23	Effects of $u_G$ and $u_L$ on $a$ in raw Kraft pulp mill effluent.....	302
Figure 11.24	A typical plot of the count-based bubble size distribution in raw Kraft pulp mill effluent at low $u_G$ and low $u_L$ .....	303
Figure 11.25	A typical plot of the count-based bubble size distribution in raw Kraft pulp mill effluent at high $u_G$ and low $u_L$ .....	304
Figure 11.26	A typical plot of the count-based bubble size distribution in raw Kraft pulp mill effluent at low $u_G$ and high $u_L$ .....	304

## LIST OF SYMBOLS

$A'$ to $E'$	dimensionless linear regression coefficients in Equation 8.20
$a'$	input parameter of the 1P-ADM defined in Equations 7.17 and 8.11, $\text{mgL}^{-1}$
$A$	gas bubbles' surface area, $\text{m}^2$
$a$	gas bubbles' specific interfacial area, $\text{m}^{-1}$
$a_1$	dimensionless empirical coefficient of the gas-phase mole fraction decrease along column height
$A_j$ to $N_j$	dimensionless coefficients in the algebraic equations of the 2P-ADM
AOX	absorbable organic halides, $\text{mgL}^{-1}$
$b'$	input parameter of the 1P-ADM defined in Equations 7.18 and 8.12, $\text{mgL}^{-1}$
$\text{BOD}_5$	biochemical oxygen demand, $\text{mgL}^{-1}$
$C_0^*$	instantaneously-mixed tracer concentration in the first cell in the transient BFCM or transient CFSTR's in-series model, $\text{mgL}^{-1}$
$C_B$	gas bubbles concentration, $\#\text{bubblesL}^{-1}$
$C_G$	gas-phase ozone concentration, $\text{mgL}^{-1}$
$C_{G,\text{in}}$	feed-gas ozone concentration, $\text{mgL}^{-1}$
$C_{G,\text{off}}$	off-gas (i.e., exhaust-gas) ozone concentration, $\text{mgL}^{-1}$
$C_i$	recorded tracer concentration at time step ( $\Delta t_i$ ), $\text{mgL}^{-1}$
$C_j$	tracer concentration in cell number "j" in the transient BFCM, $\text{mgL}^{-1}$
$C_L$	instantaneous dissolved ozone concentration, $\text{mgL}^{-1}$
$C_{L,\text{measured}}$	measured tracer concentration, $\text{mgL}^{-1}$
$C_{L,\text{predicted}}$	predicted tracer concentration, $\text{mgL}^{-1}$
$C_{L,\ell}$	dissolved ozone concentration at depth ( $\ell$ ), $\text{mgL}^{-1}$
$C_L^*$	equilibrium dissolved ozone concentration, $\text{mgL}^{-1}$

$C_{L,\ell}^*$	equilibrium dissolved ozone concentration at depth ( $\ell$ ), $\text{mgL}^{-1}$
$C_0 = C_t$	instantaneous tracer concentration, $\text{mgL}^{-1}$
$C_0$	tracer concentration in the influent to the reactor, $\text{mgL}^{-1}$
COD	chemical oxygen demand, $\text{mgL}^{-1}$
$D$	bubble column diameter, m
$D_a$	dimensionless Damköhler number
$D_G$	gas-phase axial dispersion coefficient, $\text{m}^2\text{s}^{-1}$
$D_L$	liquid-phase axial dispersion coefficient, $\text{m}^2\text{s}^{-1}$
$D_{O_2}$	oxygen gas diffusivity in the liquid phase, $\text{m}^2\text{s}^{-1}$
$D_{O_3}$	ozone gas diffusivity in the liquid phase, $\text{m}^2\text{s}^{-1}$
$D_1$	dimensionless input parameter of the 1P-ADM defined in Equations 7.29 and 8.8
$d_B$	count mean diameter of gas bubbles, $\mu\text{m}$
$d_S$	Sauter (i.e., volume-to-surface area) mean diameter of gas bubbles, $\mu\text{m}$
$E$	dimensionless enhancement factor
$E(\theta)$	dimensionless residence time density function, as a function of the dimensionless time ( $\theta$ )
$E(t)$	residence time density function, as a function of the time ( $t$ ), $\text{s}^{-1}$
$E_1$	dimensionless input parameter of the 1P-ADM defined in Equations 7.30 and 8.9
$Ek_{La}$	enhanced overall mass transfer coefficient, $\text{s}^{-1}$
$Est_L$	dimensionless enhanced liquid-phase Stanton number
$f_j$	dimensionless correction factor for the volume of cell number “j” in the transient BFCM
$f_{Z,j}$	dimensionless correction factor for the dimensionless distance ( $Z$ ) for cell number “j” in the transient BFCM
$g$	gravitational acceleration, $\text{ms}^{-2}$
$G/L$	dimensionless gas-to-liquid flowrate ratio ( $= Q_G/Q_L$ )
$h_{c,j}$	height of cell number “j” in the transient BFCM, m

<b>H</b>	Henry's law constant, $\text{kPaLmg}^{-1}$
<b>H<sub>a</sub></b>	dimensionless Hatta number
<b>I</b>	diffusive flux of the dissolved mass, $\text{molm}^{-2}\text{s}^{-1}$
<b>k<sub>L</sub></b>	local mass transfer coefficient, $\text{ms}^{-1}$
<b>k<sub>L</sub>a</b>	overall mass transfer coefficient, $\text{s}^{-1}$
<b>k<sub>w</sub></b>	specific ozone utilization rate constant, $\text{s}^{-1}$
<b>K<sub>0</sub></b>	dimensionless input parameter of the 1P-ADM defined in Equations 7.27 and 8.6
<b>K<sub>1</sub></b>	dimensionless input parameter of the 1P-ADM defined in Equations 7.28 and 8.7
<b>k<sub>1</sub></b>	empirical ozone auto-decomposition rate constant, $\text{s}^{-1}$
<b>k<sub>2</sub></b>	empirical ozone auto-decomposition rate constant, $\text{s}^{-1}$
<b>k<sub>3</sub></b>	empirical ozone auto-decomposition rate constant, $\text{Lmg}^{-1}$
<b>L</b>	total height of the bubble column, m
<b>ℓ</b>	axial distance (i.e., axial coordinate) along the column height, m
<b>M</b>	dimensionless enhancement factor
<b>M</b>	mass of the injected tracer, kg
<b>N</b>	dimensionless input parameter of the 1P-ADM defined in Equations 7.31 and 8.10
<b>N</b>	total number of the time steps in the numerical simulation of the transient BFCM
<b>N</b>	total number of elements used in the finite difference scheme in the solution of the 2P-ADM
<b>N<sub>BFCM</sub></b>	number of cells in the transient BFCM
<b>N<sub>CFSTR</sub></b>	number of cells in the transient CFSTR's in-series model
<b>P</b>	liquid hydrostatic pressure, kPa
<b>Pe</b>	dimensionless Peclet number
<b>Q'<sub>B,j</sub></b>	back flowrate for cell number "j" in the transient BFCM, $\text{m}^3\text{s}^{-1}$
<b>Q<sub>B,j</sub></b>	exchange flowrate for cell number "j" in the transient BFCM, $\text{m}^3\text{s}^{-1}$

$Q_{G,0}$	feed-gas flowrate flowing into the first cell in the steady-state BFCM, $m^3 s^{-1}$
$Q_{G,j}$	gas flowrate flowing out of cell number “j” in the steady-state BFCM, $m^3 s^{-1}$
$Q_L$	liquid flowrate, $m^3 s^{-1}$
$r'_j$	dimensionless back-flow ratio of cell number “j” in the transient BFCM
$r_j$	dimensionless exchange-flow ratio of cell number “j” in the transient BFCM
R	Universal gas constant, $atmLmole^{-1}K^{-1}$
$Re_j$	dimensionless jet Reynolds number
St	dimensionless Stanton number
T	fluid temperature, °C or °K
t	ozone contact time, s
$t_i$	acquisition time of the tracer data, s
$t_m$	mean of the residence time distribution (RTD), s
TOC	total organic carbon, $mgL^{-1}$
u	instantaneous bubble rise velocity, $ms^{-1}$
$u_G$	superficial gas velocity = feed-gas flowrate/cross-sectional area of the bubble column (cross-sectional area of the straight section in case of the impinging-jet bubble column), $ms^{-1}$
$u_L$	superficial liquid velocity = liquid flowrate/cross-sectional area of the bubble column (cross-sectional area of the straight section in case of the impinging-jet bubble column), $ms^{-1}$
$V_{c,j}$	volume of cell number “j” in the transient BFCM, $m^3$
V	total volume of the bubble column, $m^3$
$V_c$	average cell volume in the transient BFCM, $m^3$
$V_L$	effective reactor volume, $m^3$

<b>X</b>	<b>dimensionless dissolved ozone concentration in the liquid phase</b>
<b>Y</b>	<b>dimensionless ozone concentration in the gas phase</b>
<b><math>Y_j</math></b>	<b>normalized tracer concentration in cell number “j” in the transient BFCM</b>
<b>y</b>	<b>dimensionless ozone molar fraction in the gas phase</b>
<b><math>y_z</math></b>	<b>ozone molar fraction in the gas phase at dimensionless axial co-ordinate (Z)</b>
<b><math>y_\ell</math></b>	<b>ozone molar fraction in the gas phase at depth <math>\ell</math></b>
<b>Z</b>	<b>dimensionless distance (i.e., axial coordinate) along the column height</b>
<b><math>Z_{j,act}</math></b>	<b>actual dimensionless distance of cell number “j” in the transient BFCM</b>
<b><math>Z_{j,avg}</math></b>	<b>average dimensionless distance of cell number “j” in the transient BFCM</b>

### **Greek Letters**

<b><math>\Delta O_3</math></b>	<b>amount of the utilized ozone, <math>\text{mgL}^{-1}</math></b>
<b><math>\Delta t_i</math></b>	<b>time step during the acquisition of the tracer data, s</b>
<b><math>\Delta Z</math></b>	<b>dimensionless numerical spatial step in the numerical solution of the 2P ADM</b>
<b><math>\Delta \theta</math></b>	<b>dimensionless time step during the acquisition of the tracer data</b>
<b><math>\alpha</math></b>	<b>non-linear regression parameter in Equations 8.15 and 8.17</b>
<b><math>\alpha_1</math></b>	<b>input parameter of the 1P-ADM defined in Equations 7.20 and 8.11, <math>\text{mgL}^{-1}</math></b>
<b><math>\beta</math></b>	<b>non-linear regression parameter in Equations 8.15 and 8.17</b>
<b><math>\beta_1</math></b>	<b>input parameter of the 1P-ADM defined in Equations 7.21 and 8.12, <math>\text{mgL}^{-1}</math></b>
<b><math>\epsilon</math></b>	<b>dimensionless fluid-phase hold-up</b>

$\theta$	dimensionless temperature correction factor in van't Hoff-Arrhenius relationship
$\lambda_1$	dimensionless input parameter of the IP-ADM defined in Equations 7.34 and 8.4
$\lambda_2$	dimensionless input parameter of the IP-ADM defined in Equations 7.34 and 8.5
$\theta$	dimensionless time in the modeling of the hydrodynamics of the bubble column
$\rho$	liquid density, $\text{kgm}^{-3}$
$\sigma_\theta^2$	variance of the RTD as a function of the dimensionless time ( $\theta$ )
$\sigma_t^2$	variance of the RTD as a function of time ( $t$ ), $\text{s}^2$
$\tau$	mean theoretical hydraulic retention time of the bubble column, s
$\psi$	rate of gas absorption into the liquid phase, $\text{mgL}^{-1}\text{s}^{-1}$
$\gamma$	non-linear regression parameter in Equation 8.17

### Subscripts

0	bottom of the bubble column, i.e., at $Z = 0$
act	actual
avg	average
B	back or exchange flow
BFCM	back flow cell model
c	cell
CFSTR	continuous-flow-stirred-tank reactors model
G	gas phase
i	number of the time step during the acquisition of the tracer data
in	feed-gas
inf	influent
j	cell number in the BFCM

<b>j</b>	<b>identifier of the element number in the finite difference scheme used to solve the 2P-ADM (<math>N + 1 \geq j \geq -1</math>)</b>
<b>L</b>	<b>liquid phase</b>
<b>m</b>	<b>mean</b>
<b>N</b>	<b>number of the top element in the finite difference scheme of the 2P-ADM</b>
<b>N+1</b>	<b>number of the imaginary element in the finite difference scheme of the 2P ADM</b>
<b>O<sub>2</sub></b>	<b>oxygen gas</b>
<b>O<sub>3</sub></b>	<b>ozone gas</b>
<b>out</b>	<b>off-gas</b>
<b>T</b>	<b>top of the bubble column</b>
<b>t</b>	<b>time</b>
<b>T</b>	<b>top of the column, i.e., at <math>Z = 1</math></b>
<b>-1</b>	<b>number of the imaginary element beneath the bottom of the column</b>

## CHAPTER 1. GENERAL INTRODUCTION

### 1.1 BACKGROUND

Most of the models that dealt with ozone contactors were directed to the water treatment applications with very little done to model the ozonation process for wastewater treatment. Most of the models are two-phase flow (i.e., gas-liquid) models that are applied to predict the dissolved and the gaseous ozone profiles along bubble columns. In order to simplify the design process of ozone bubble columns, many of those models were based on one of the following two liquid-phase flow regimes: (1) complete mixing or; (2) plug flow (Alvarez-Cuenca *et al.*, 1980; Alvarez-Cuenca *et al.*, 1981; Chang and Chian, 1981; Laplanche *et al.*, 1991; Hull *et al.*, 1992; Lev and Regli, 1992). Although, the actual flow pattern in bubble columns is usually closer to being mixed flow rather than plug flow, but still not completely mixed flow (Zhou, 1995). Very few studies were conducted using the type of models that consider the backmixing process in the liquid-phase flow. One of those studies was the one conducted by Zhou *et al.* (1994), in which, they modeled the performance of ozone bubble columns by using the two-phase axial dispersion model, or referred to as the 2P-ADM, and an elaborate numerical technique was needed to solve the model equations. The 2P-ADM demonstrated excellent capability of predicting the dissolved ozone profiles in ozone contactors.

The design of ozone bubble columns usually encounter two major sources of uncertainties: (1) the complications and unreliable methods used in measuring and estimating the operating parameters of bubble columns; and (2) the application of the pertinent design model, particularly, when designing an ozonation treatment facility for a complex chemical systems such as the effluents produced from the pulping and bleaching processes. Although constructing ozone contactors is an easy task, optimizing their operations is not as simple. The operating parameters of ozone contactors are interrelated and thus, they cause difficulty in the design, operation, and scale-up. Therefore, reliable and accurate methods of measuring and estimating such parameters should be applied.

A number of processes occur simultaneously during the ozonation process. Those processes are: the convection and the backmixing processes of the liquid and gas phases flowing through the contacting chamber; the ozone gas mass transfer process; the ozone auto-decomposition process, and the competitive reactive processes of the constituents in water and wastewater with dissolved ozone (Zhou *et al.*, 1994). Besides those processes, the contactor configuration, the operating conditions, and the water or wastewater quality influence the overall performance of the ozonation process. For any ozonation system, it is crucial to quantify the dissolved ozone to achieve reliable rational design and optimum operation of ozone contactors. Meanwhile, quantifying the gaseous ozone, i.e., the ozone off-gas leaving the contactor, is essential for achieving optimum and reliable design of the off-gas destruction facilities.

Several studies have been conducted to study the fundamentals of the processes that control the performance of ozone contactors in water treatment over the past decades with a fewer number of studies aimed at investigating the ozone mass transfer mechanisms and the effect of chemical reactions on the rate of ozone absorption when treating industrial wastewater. Kraft pulp mill effluents are characterized by their high concentrations of color, AOX (absorbable organic halides), COD (chemical oxygen demand), and TOC (total organic carbon). Recently, the color and AOX-causing contaminants have become the center of attention as a result of their high resistance towards conventional biological treatment processes. In order to comply with the more stringent effluent discharge regulations, the focus of the pulp mill effluent treatment industry has shifted from the conventional biological treatment processes to other treatment alternatives (Haberl *et al.*, 1991; Zhou and Smith, 1997). Ozonation has emerged as a very promising technology for treating pulp mill effluents due to its high reduction efficiencies of color and AOX-causing compounds (Bauman and Lutz, 1974; Zhou and Smith, 1997). Ozone can selectively react with the chromophoric (color-causing) and halogenated (AOX-causing) functional groups through fast oxidation reactions as a result of these compounds' electrophilic nature (Bauman and Lutz, 1974). They observed that the color reduction efficiency was dependent mainly on the amount of the utilized ozone ( $\Delta O_3$ ), but to some extent it was also dependent on the wastewater

initial characteristics in terms of color, COD, pH, and dissolved and suspended solids' concentrations.

Ozone contactors that utilize bubble diffusers are the most common practice used for treating water and wastewater. In water treatment applications, ozonation is limited by the mass transfer process as it is considered the controlling process that dictates the overall performance of ozone contactors (Zhou *et al.*, 1994; Gamal El-Din and Smith, 2000). In order to achieve higher treatment levels in ozone contactors, the configuration and the design of the contacting unit and the type of the gas absorber need to be modified in an attempt to achieve higher turbulent mixing in the liquid phase. According to the theory of surface renewal proposed by Danckwerts (1970), an increase in the mixing intensity will cause the liquid film at the gas-liquid interface to be renewed at a higher rate leading to a higher local mass transfer coefficient ( $k_L$ ). The ozone gas-absorption in water treatment is assumed to follow the slow-reaction kinetics regime (Zhou *et al.*, 1994; Gamal El-Din and Smith, 2000). Since the ozone gas diffusivity in the liquid phase is much smaller than that in the gas phase, the gas diffusion through the liquid film becomes the rate-limiting step of the mass transfer process (Valentin, 1967). High turbulent shear stresses will also cause the liquid film to become thinner, and as a result, the ozone gas will diffuse through the liquid film at a higher rate causing  $k_L$  to increase. Higher turbulent shear stresses will also cause the gas bubbles to become smaller. As a result, the gas bubbles' specific interfacial area (gas bubbles' surface area/bubbly bed volume) will increase leading to higher overall mass transfer coefficient ( $k_{La}$ ).

In the study of Witze (1974), when two axisymmetrical circular turbulent air jets (i.e., having the same nozzle diameter and momentum) intersected at an angle of  $180^\circ$ , the resultant jet behaved like a radial jet which grew at about three times the rate of a single radial jet. As a result of the impingement, higher turbulent shear stresses were developed in the ambient fluid and a region of backflow was observed. Guo and Sharp (1996) studied the characteristics of radial jets and mixing under buoyant conditions. They observed that the turbulence intensity increased with the width of the orifice. Unger and Muzzio (1999) investigated the effect of a jet impingement at an intersecting angle of

90° on the mixing characteristics. It was observed that efficient and homogeneous mixing occurred at jets' Reynolds numbers ( $Re_j$ 's) greater than 300. Fitzgerald and Holley (1979) used two turbulent jets intersecting at an angle of 90° to investigate the resultant effects on the mixing behaviour. They observed more uniform and improved mixing across the annular tube.

Many researchers have attempted to improve the performance of bubble columns by maximizing the rate of physical gas absorption process. These attempts included: adding internal baffles (Catros, 1986), utilizing perforated plates (Chen *et al.*, 1986), inducing internal liquid circulation in air-lift reactors (Lewis and Davidson, 1985), and utilizing motionless mixers (Wang and Fan, 1978). Many researchers utilized gas injectors in order to improve the mass transfer process. Wachsmann *et al.* (1984) studied the mass transfer process using an injection-type nozzle. Gas was introduced under positive and negative pressures. They observed remarkable increase in the overall mass transfer coefficient ( $k_L a$ ) due to the generation of bubbles that had a large specific interfacial area. They also observed that the values of  $k_L a$  in the gas-injection mode varied from those in the gas-ejection mode. Thalasso *et al.* (1995) used a venturi-type injector to increase the gas transfer rates and that led to an improvement in the performance of the bioreactor that they investigated. Under gas injection mode, they observed an increase in  $k_L a$  as the liquid superficial velocity ( $u_L$ ) and the gas superficial velocity ( $u_G$ ) increased. In a gas-liquid spouted vessel, gas was absorbed under positive pressure into the liquid-phase flow (Nishikawa *et al.*, 1977). It was observed that as  $u_G$  and  $u_L$  increased,  $k_L a$  increased and  $k_L a$  was more dependent on  $u_G$  than on  $u_L$ . Wang and Fan (1978) studied the mass transfer process in bubble columns packed with motionless mixers. They observed that  $k_L a$  was dependent on  $u_G$  and  $u_L$  and as  $u_G$  and  $u_L$  increased,  $k_L a$  increased. Huynh *et al.* (1991) studied the mass transfer process in an upward venturi-bubble column combination. They correlated  $k_L a$  with  $u_G$  and  $u_L$  for the bubble/venturi combination. As  $u_G$  and  $u_L$  increased,  $k_L a$  increased. The increase in  $u_G$  could have caused an increase in the gas bubbles' specific interfacial area while the increase in  $u_L$  could have resulted in an increase in the liquid shear stresses (Huynh *et al.*, 1991).

Gas hold-up ( $\epsilon_G$ ) is one of the important variables that characterize the hydrodynamics of the gas-liquid, i.e., the two-phase flows, in bubble columns. It is defined as the fraction of the dispersed volume occupied by the gas bubbles.  $\epsilon_G$  can affect the performance of bubble columns in two ways: (1) it provides the fractional volume of the gas phase and therefore, its residence time inside the reactor; and (2) in conjunction with the knowledge of the Sauter mean (i.e., volume-to-surface area mean) bubble diameter, it allows the determination of the and the gas bubbles' specific interfacial area (Jamialahmadi and Müller-Steinhagen, 1992). With the knowledge of gas hold-up and Sauter mean diameter, the gas bubbles' specific interfacial area can be determined. Zhou and Smith (2000) investigated the effects of gas flowrates on the gas bubbles' specific interfacial area using a 2D-Laser particle dynamics analyzer. They observed a proportional increase in the gas bubbles' specific interfacial area with the increase in  $u_G$  as a result of the linear increase in the gas hold-up. The same phenomenon was also reported by Roustan *et al.* (1996).

The use of computational fluid dynamics (CFD) has grown over the past decade since it can offer detailed predictions of the behaviour and the characteristics of multiphase flows such as gas-liquid flow in bubble columns. CFD can lead to significant improvements in the area of scale-up of bubble columns. In order to achieve successful application of CFD in the scale-up process, a better understanding of the fundamentals of the gas-liquid flow phenomena has to be provided. Gas-liquid flows are complex in their nature and their behaviour can vary substantially depending on the design, configuration, and operating conditions of the bubble columns. It is very hard to conduct experimental measurements inside gas-liquid flows because of their sensitive nature to any disturbances caused by intrusive measuring devices such as electric probes (Mudde *et al.*, 1998). As a result, the use of non-intrusive measurement techniques such as laser Doppler anemometry and Phase Doppler anemometry measurement systems can provide great tools for characterization and better understanding of the local rather than the global flow phenomena (Mudde *et al.*, 1998).

## 1.2 FUNDAMENTALS OF THE OZONATION PROCESS

A number of processes occur simultaneously during the ozonation process. Those processes are: the convection and the backmixing processes of the liquid and gas phases flowing through the contacting chamber; the ozone gas mass transfer process; the ozone auto-decomposition process, and the competitive reactive processes of the constituents in water and wastewater with dissolved ozone (Zhou *et al.*, 1994).

### 1.2.1 Backmixing Process

There are several models that account for backmixing in the liquid phase. Among those models that are available for predicting the performance of bubble columns, is the axial dispersion model (ADM). In the ADM, a diffusion-like process is assumed and superimposed on a plug flow (Levenspiel, 1972). An empirical Fick's law is applied by replacing the molecular diffusion coefficient by the axial dispersion coefficient ( $D_L$ ) as the mixing parameter:

$$\text{Diffusive mass flux} = -D_L \frac{\partial C_L}{\partial l} \quad [1.1]$$

where:  $C_L$  = dissolved ozone concentration ( $\text{mgL}^{-1}$ ) and  $D_L$  = axial dispersion coefficient ( $\text{m}^2\text{s}^{-1}$ ). In the  $D_L$ , the effects of the non-uniform velocity profile (shear dispersion), the molecular, and eddy diffusivities are lumped together. Equation 1.1 can be also applied to describe the backmixing process in the gas phase.

### 1.2.2 Ozone Auto-Decomposition Process

The overall ozone auto-decomposition rate is influenced by the concentration and the history of the ozonation process and this ozone auto-decomposition process could be represented by a modified pseudo-first-order rate expression (Yurteri and Gurol, 1988; Oke *et al.*, 1998). In the experimental study of Oke *et al.* (1998), it was shown that the

commonly used first-order kinetics expression with a constant reaction rate constant was inadequate in describing the ozone auto-decomposition process especially in situations where the initial ozone demand was significant. It was demonstrated that the reaction rate constant was continuously decreasing along the course of ozonation as a result of the changes in the water characteristics. As a result, an exponentially decreasing function was proposed as a better alternative to describe the ozone auto-decomposition kinetics (Oke *et al.*, 1998). In that expression, the reaction rate constant was replaced by a variable referred to as the specific ozone utilization rate constant ( $k_w$ ) that is a function of the utilized ozone dose ( $\Delta O_3$ ):

$$\frac{dC_L}{dt} = -k_w C_L = -(k_1 + k_2 e^{-k_3 \Delta O_3}) C_L \quad [1.2]$$

where:  $C_L$  = instantaneous dissolved ozone concentration ( $\text{mgL}^{-1}$ ),  $k_w$  = specific ozone utilization rate constant ( $\text{s}^{-1}$ ),  $k_1$  = empirical non-linear regression constant ( $\text{s}^{-1}$ ),  $k_2$  = empirical non-linear regression constant ( $\text{s}^{-1}$ ),  $k_3$  = empirical non-linear regression constant ( $\text{Lmg}^{-1}$ ),  $t$  = reaction time (s), and  $\Delta O_3$  = amount of the utilized ozone ( $\text{mgL}^{-1}$ ).  $k_1$ ,  $k_2$ , and  $k_3$  are empirical constants that can be obtained by applying non-linear regression analysis to the kinetics data and they are also characteristics of the water to be treated.

According to Equation 1.2, as the amount of the utilized ozone increases along the course of ozonation,  $k_w$  will decrease. At the beginning of the ozonation, i.e., when the amount of the utilized ozone is zero,  $k_w$  is equal to  $k_1 + k_2$  as the ozone auto-decomposition process is only attributed to the initial ozone demand. In the study of Oke *et al.* (1998) and for clean deionized water, the initial ozone demand was practically equal to zero and therefore,  $k_w$  could be assumed constant during the course of the ozonation.

### 1.2.3 Mass Transfer Process

#### 1.2.3.1 Mass Transfer Without Chemical Reactions

The two-film model is usually used to describe the absorption of ozone gas from the gas phase into the liquid phase. Assuming that no chemical reactions between the dissolved gas and any constituents, that can be present in the liquid phase, occur during the mass transfer process, the gas-absorption rate ( $\psi$ ) is defined as:

$$\psi = k_L a (C_L^* - C_L) \quad [1.3]$$

where:  $\psi$  = gas-absorption rate ( $\text{mgL}^{-1}\text{s}^{-1}$ ),  $k_L$  = local liquid mass transfer coefficient ( $\text{ms}^{-1}$ ),  $a$  = gas bubbles' specific interfacial area ( $\text{m}^{-1}$ ),  $C_L^*$  = concentration of the dissolved ozone in equilibrium with the bulk ozone gas ( $\text{mgL}^{-1}$ ), and  $C_L$  = concentration of the dissolved ozone in the bulk liquid ( $\text{mgL}^{-1}$ ). Due to the fact that ozone gas diffuses much faster in the gas phase than in the liquid phase, the mass transfer in the liquid phase is assumed to be the rate-controlling step. Consequently, the overall mass transfer coefficient ( $k_L a$ ) is considered to entirely consist of the local mass transfer coefficient in the liquid phase.

#### 1.2.3.2 Mass Transfer With Chemical Reactions

Chemical reactions occur during the ozonation of wastewater. In such applications, the dimensionless squared Hatta number ( $H_a^2 = M$ ) is often applied to compare between the amount of dissolved gas that reacts at the gas-liquid interface or in the liquid film near the interface and the amount of dissolved gas that reaches the bulk liquid in an unreacted state:

$$H_a^2 = E^2 = M = \frac{D_{O_3} k_w}{k_L^2} \quad [1.4]$$

where:  $H_a = E = \sqrt{M}$  = dimensionless Hatta number,  $k_L$  = local mass transfer coefficient ( $\text{ms}^{-1}$ ),  $D_{O_3}$  = molecular diffusivity of ozone gas in water ( $\text{m}^2\text{s}^{-1}$ ), and  $k_w$  = specific ozone utilization rate constant ( $\text{s}^{-1}$ ). For pseudo-first-order irreversible reactions, the location of those reactions that take place during the gas absorption process could be classified into two categories (Kramers and Westertrep, 1963; Kaštánek *et al.*, 1993). Reactions would take place in the bulk of the liquid or at the gas-liquid interface and/or in the liquid film near the interface at  $H_a < 0.03$  and  $H_a > 5.00$ , respectively (Kramers and Westertrep, 1963; Kaštánek *et al.*, 1993). Although, generally for bubble columns it can also be assumed that at that at  $H_a > 3.00$ , reactions would still be fast enough to occur predominantly at the gas-liquid interface and/or in the liquid film near the interface (Kaštánek *et al.*, 1993). Therefore, reactions would simultaneously take place in both regions at  $0.03 < H_a < 3.00$ . Equation 1.4 is only applicable in situations where two conditions have to be satisfied: (1)  $\sqrt{M} \gg 1$ ; and (2) fast or instantaneous irreversible first-order reactions with no bulk liquid concentration where the driving force for the mass transfer process will be maximized (Danckwerts, 1970). As a result, Equation 1.3 becomes:

$$\psi = Ek_L a C_L^* \quad [1.5]$$

where:  $Ek_L a$  = enhanced overall mass transfer coefficient ( $\text{s}^{-1}$ ). Zhou and Smith (1999) proposed that for wastewater ozonation, both the ozone auto-decomposition and its reactions with the organic and inorganic constituents in wastewater could be lumped together in a first-order rate constant ( $k_w$ ). Danckwerts (1970) proposed the following equation for the conditions when  $M > 0$  and  $C_L > 0$ :

$$\psi = k_L a \sqrt{1+M} \left( C_L^* - \frac{C_L}{1+M} \right) \quad [1.6]$$

When  $M \gg 1$  and  $C_L$  approaches zero (i.e.,  $C_L \cong 0$ ), Equation 1.6 reduces to Equation 1.5. The effects of chemical reactions on the local mass transfer coefficient for an

irreversible first-order reaction could be neglected and the gas absorption could be dealt with as pure physical absorption when  $M$  approaches zero (Danckwerts, 1970). Therefore, this assumption is valid when:

$$H_3^2 = E^2 = M = \frac{D_{O_3} k_w}{k_L^2} \ll 1 \quad [1.7]$$

$k_w$  was reported to be  $4.7 \times 10^{-4} \text{ s}^{-1}$  for the deionized water tested by Zhou (1995). Yurteri and Gurol (1988) reported that  $k_w$  was in the order of  $2.8 \times 10^{-3} \text{ s}^{-1}$  for the tested raw surface water. The diffusivity of ozone in water was determined by the Wilke-Chang formula to be  $1.74 \times 10^{-9} \text{ m}^2 \text{ s}^{-1}$  (at  $20 \text{ }^\circ\text{C}$ ) which is comparable to the value of  $1.71 \times 10^{-9} \text{ m}^2 \text{ s}^{-1}$  obtained using the equation recommended by Johnson and Davis (1996).  $k_L$  was reported to be in the order of  $3.1 \times 10^{-4} \text{ ms}^{-1}$  for clean water and in the order of  $1.9 \times 10^{-4} \text{ ms}^{-1}$  for water containing organic substances (Beltrán *et al.*, 1997). Substituting for these typical values of  $D$ ,  $k_w$ , and  $k_L$  into Equation 1.4 yields squared-Hatta numbers of  $8.5 \times 10^{-6}$  and  $1.4 \times 10^{-4}$  for the deionized and the surface water, respectively. Based on these small Hatta numbers, it can be concluded that the chemical reactions that occur during the course of clean or surface water ozonation has negligible effect on the local mass transfer coefficient and hence, Equation 1.3 will be applied for ozone absorption without any modification.

### 1.3 PRACTICAL ASPECTS OF OZONE CONTACTORS

#### 1.3.1 Types of Ozone Contactors

Several designs of ozone contactors have been used in water and wastewater ozone treatment applications (Langlais *et al.* 1991). The type of ozone contactor, to be used in a specific ozone treatment application, would depend on the goal of the treatment process. Several designs of ozone contactors have been used in the ozone treatment industry. Those designs included:

- (1) conventional diffuser contactors;
  - (1.a) fine diffuser

- (1.b) coarse diffuser
- (1.c) extra-coarse diffuser
- (2) turbine mixer contactors;
  - (2.a) positive gas pressure
  - (2.b) negative gas pressure (aspirator)
- (3) side stream gas injector followed by gas-liquid separators;
  - (3.a) positive gas pressure
  - (3.b) negative gas pressure
- (4) packed bubble columns;
- (5) spray chambers;
- (6) deep U tube contactors
- (7) porous plate diffuser contactors; and
- (8) submerged static radial turbine contactors

Among those several designs, the conventional fine-diffuser contactor design is the most widely applied practice in both North America and Europe (Zhou, 1995). Based on the gas and liquid flow patterns, conventional diffuser contactors can be further generalized into three types (Zhou, 1995):

- (1) counter-current pattern, where the liquid phase flows downwards in an opposite direction to that of the rising gas bubbles;
- (2) co-current pattern, where both the liquid and gas phases flow upwards; and
- (3) reactive pattern, where no ozone gas is introduced while the liquid phase can still have a residual ozone concentration.

The first two flow patterns allow for dissolving the ozone gas from the gas phase into the liquid phase, while the reactive pattern provides the opportunity for further contact between the residual ozone and the different constituents present in the liquid phase.

Ozone contacting facilities are usually divided into several chambers, ranging from two to six chambers in series and there are usually practical limits to the number of chambers due to the cost of installing baffles and the buildup of the headloss (Zhou,

1995). Most of the conventional fine bubble contactors, in both North America and Europe, utilize two or three chambers for the ozone contacting and reaction purposes (Zhou, 1995).

### 1.3.2 Designing Ozone Contactors

In designing ozone contactors, some challenges can be experienced as a result of some distinct properties of ozone gas (Zhou, 1995). Most of the available commercial ozone generators can produce a ozone concentration in the gas phase ( $\geq 10\%$  w/w) and that will limit the driving force available for the mass transfer process. This is a result of the low dissolved ozone concentration that is in equilibrium with the bulk ozone gas due to the low solubility of ozone gas in water. Second, ozone is an unstable gas and can react with a variety of constituents present in the liquid phase (Zhou, 1995). Ozone reactions are complex in nature and therefore, it does not allow for a reliable prediction of the ozone consumption rate (Zhou, 1995). Also, the knowledge of scaling-up of an ozonation treatment system has not been well understood because of the complexity of ozone chemistry and the lack of reliable process design parameters (Zhou and Smith, 1997).

If the ozonation process involves mass-transfer-limited reactions such as the oxidation of the color or AOX-causing organic compounds, it is crucial to maximize the ozone mass transfer process. Alternatively, if the ozonation process involves chemical-reaction-rate-limited reactions, such as in during disinfection, it is recommended to maintain a desired residual ozone concentration for a specified time period. Therefore, a series of multiple chambers was suggested. A sufficient amount of ozone should be applied to achieve a high dissolved ozone concentration in the first chamber to satisfy the initial ozone demand. Then, additional ozone should be applied at a lower dose in the subsequent chambers to maintain the required residual concentration.

The hydrodynamic behaviour of ozone contactors has been recently identified as another key-design component (Lev and Regli, 1992). In typical full-scale diffuser contactors with two chambers in series, the liquid-phase backmixing was equivalent to

that in reactor composed of two to five CFSTR's (continuous-flow-stirred-tank-reactors) in-series (Roustan *et al.*, 1993). They concluded that the liquid-phase backmixing depends on the water and gas flowrates as well as the geometry and the configuration of ozone contactors. Regarding the hydrodynamics of the gas phase and due to the large buoyancy of the gas bubbles, it usually assumed that the backmixing in the gas phase is negligible (Zhou *et al.*, 1994). As a result, the gas-phase is assumed to flow in perfect plug flow regime. However, this assumption is usually valid in ozone contactors and bubble columns with large aspect ( $L/D$ ) ratios. Deckwer (1976) suggested that the performance of bubble columns could be affected by the gas phase dispersion in columns with diameters greater than 500 mm. As a result, the need for proper designs and configurations of ozone contactors has become the focus of the ozone treatment industry. Designing and configuring ozone contactors properly will lead to high and efficient ozone mass transfer rates and will ensure that the required retention times, for the intended ozone treatments, are satisfied. In order to design ozone contactors properly, accurate and reliable models are needed. Those models can be also useful for the on-line process control. Those models should be developed such that they take into consideration the various processes that occur simultaneously during the ozonation process.

#### 1.4 OBJECTIVES AND SCOPES OF THE RESEARCH PROGRAM

As discussed earlier, the performance of ozone contactors is controlled by the combined effects of the hydrodynamics, ozone mass transfer, and ozone reactions with the constituents that can be present in the liquid phase. Although great advancements in the area of ozone treatment have been achieved, there is still a great demand for:

- (1) more efficient and compact designs of ozone contactors that can provide higher treatment levels in more compact contactors and thus, the cost of the treatment process will be lowered;
- (2) the development of reliable ozonation process parameters that can be used to predict the performance of the ozone treatment; and

- (3) the development of a rational design approach that integrates the variables that affect the performance of the ozonation process and therefore, it can be used in the design and on-line process control of ozone contactors.

The main scope of this research project was to design a new compact ozone contactor that can provide higher treatment levels than those in the conventional ozone contactor designs.

This research program was designed to achieve several objectives. Those objectives included:

- (1) development of a reliable, accurate, and simple-to-use model (transient back flow cell model (BFCM)) that can be used for modeling the hydrodynamics of ozone contactors (Chapter 2);
- (2) development of models (steady-state two-phase axial dispersion model (2P-ADM) and steady-state BFCM)) that integrate the various processes that occur simultaneously during the ozonation process and therefore, those models can be used for the design and on-line process control of ozone contactors (Chapters 3,4, and 5);
- (3) comparing the steady-state 2P-ADM with the steady-state BFCM in terms of their predictions of the performance of ozone contactors (Chapter 6);
- (4) development of a simpler version of the axial dispersion model or referred to as the one-phase axial dispersion model (1P-ADM) and comparing its predictions of the performance of ozone contactors with those of the 2P-ADM (Chapter 7);
- (5) modeling the ozone mass transfer process in the new design of ozone contactors or referred to as the impinging-jet bubble column for ozone treatment applications in water and wastewater (Chapters 8 and 9);
- (6) comparing the performance of the impinging-jet bubble column with two other conventional ozone contactors for their performance during the ozonation of Kraft pulp mill effluents (Chapter 10); and

- (7) conducting a phase Doppler anemometry (PDA) study to characterize the gas phase in terms of the bubble size, the bubble size distribution, the bubble rise velocity, the axial and radial mixing intensities in the impinging-jet bubble column during the treatment of water and Kraft pulp mill effluent (Chapter 11).

As a result, a number of models were developed first to describe the hydrodynamics and the overall ozonation process for water and wastewater treatment applications. Then, those models were initially tested using some existing experimental data that was obtained in a conventional fine-diffuser ozone bubble column.

The second step of this research work involved designing a new compact ozone contactor that can provide higher treatment levels than those in the conventional ozone contactor designs. For that purpose, an impinging-jet ozone bubble column was designed and constructed. This ozone bubble column was used for ozone applications in water and wastewater treatment. One of the previously developed models, was used for describing the performance of the impinging-jet ozone bubble column when used for water treatment applications.

The third step of this research work involved treating Kraft pulp mill effluents in the impinging-jet ozone bubble column for further exploration of the advantages of using this new ozone bubble column design over the common conventional designs of ozone bubble columns when used for treating highly reactive wastewaters such as Kraft pulp mill effluents.

The last step of this research work involved the use of a laser Doppler system for characterizing the gas bubbles produced in the impinging-jet bubble column in both water and Kraft pulp mill effluents. This study will lead to further understanding of the ozone mass transfer process during water and wastewater treatment applications.

## 1.5 REFERENCES

1. Alvarez-Cuenca, M. and M.A. Nerenberg, "Oxygen Mass Transfer in Bubble Columns Working at Large Gas and Liquid Flow Rates", *AIChE J.* 27(1): 66-73 (1981).
2. Alvarez-Cuenca, M., C.G.J. Baker, and M.A. Bergougnou, "Oxygen Mass Transfer in Bubble Columns", *Chem. Eng. Sci.* 35: 1121-1127 (1980).
3. Bauman, H.D. and L.R. Lutz, "Ozonation of a Kraft Mill Effluent", *Tappi J.* 57(5): 116-119 (1974).
4. Beltrán, F.J., J.F. García-Araya, and J.M. Encinar, "Henry and Mass Transfer Coefficients in the Ozonation of Wastewaters", *Ozone Sci. & Eng.* 19: 281-296 (1997).
5. Catros, A., "*Hydrodynamics and Mass Transfer in Three-Phase Fluidized Beds with Baffles: Ph.D. Thesis* (London, ON, Canada: University of Western Ontario, 1986).
6. Chang, B.-J. and E.S.K. Chian, "A Model Study of Ozone-Sparged Vessels for the Removal of Organics from Water", *Wat. Res.* 15: 929-936 (1981).
7. Chen, B.H., N.S. Yang, and A.F. McMillan, "Gas Hold-Up and Pressure Drop for Air-Water Flow Through Plate Bubble Columns", *Can. J. Chem. Eng.* 64: 387-399 (1986).
8. Danckwerts, P.V., *Gas-Liquid Reactions* (NY, USA: McGraw-Hill, Inc., 1970).
9. Deckwer, W.-D., "Non-Isobaric Bubble Columns With Variable Gas Velocity", *Chem. Eng. Sci.* 31: 309-317 (1976).
10. Fitzgerald, S.D. and E.R. Holley, *Research Report No. 144* (Urbana, IL, USA: Water Resources Centre, University of Illinois, 1979).
11. Gamal El-Din, M. and D.W. Smith, "Designing Ozone Bubble Columns: A Spreadsheet Approach to Axial Dispersion Model", *Proc. of IOA/PAG Conf.: Advances in Ozone Technology*, Orlando, FL, USA, 2000.
12. Guo, Z.-R. and J.J. Sharp, "Characteristics of Radial Jets and Mixing Under Buoyant Conditions", *J. Hydr. Eng., ASCE* 122: 495-502 (1996).

13. Haberl, R., R. Urban, R. Gehringer, and R. Szinovata, "Treatment of Pulp-Bleaching Wastewaters by Activated Sludge, Precipitation, Ozonation, and Irradiation", *Wat. Sci. & Technol.* 24: 229-239 (1991).
14. Hull, C.S., P.C. Singer, K. Saravanan, and C.T. Miller, "Ozone Mass Transfer and Reaction: Completely Mixed Systems", *Proc. of the Annual AWWA Conf.: Water Quality*, Vancouver, BC, Canada, 1992.
15. Huynh, L.X., C.L. Briens, J.F. Large, A. Catros, J.R. Bernard, and M.A. Bergougou, "Hydrodynamics and Mass Transfer in an Upward Venturi/Bubble Column Combination", *Can. J. Chem. Eng.* 69: 711-722 (1991).
16. Jamialahmadi, M. and H. Müller-Steinhagen, "Effect of Superficial Gas Velocity on Bubble Size, Terminal Bubble Rise Velocity and Gas Hold-Up in Bubble Columns", *Develop. Chem. Eng.* 1: 16-31 (1992).
17. Johnson, P.N. and R.A. Davis, "Diffusivity of Ozone in Water", *J. Chem. Eng. Data* 41: 1485-1487 (1996).
18. Kaštánek, J., J. Zahradník, J. Kratochvíl, and J. Čermák, *Chemical Reactors for Gas-Liquid Systems* (Chichester, England: Ellis Horwood, 1993).
19. Kramers, H. and K.R. Westerterp, *Elements of Chemical Reactor Design and Operation* (NY, USA: Academic Press, Inc., 1963).
20. Langlais, B., D.A. Reckhow, and D.R. Brink, *Ozone in Water Treatment: Application and Engineering* (MI, USA: Lewis Publishers, Inc., 1991).
21. Laplanche, A., N. Le Sauze, G. Martin, and B. Langlais, "Simulation of Ozone Transfer in Water: Comparison with a Pilot Unit", *Ozone Sci. & Eng.* 13(5): 13, 535-558 (1991).
22. Levenspiel, O., *Chemical Reaction Engineering, 2<sup>nd</sup> ed.* (NY, USA: John Wiley and Sons, Inc., 1972).
23. Lev, O. and S. Regli, "Evaluation of Ozone Disinfection Systems: Characteristic Contact Time T", *J. Environ. Eng., ASCE* 118(2): 268-285 (1992).
24. Lewis, D.A. and J.F. Davidson, "Mass Transfer in a Recirculation Bubble Column", *Chem. Eng. Sci.* 40: 2013-2017 (1985).
25. Mudde, R.F., J.S. Groen, and H.E.A. Van Den Akker, "Application of LDA to Bubbly Flows", *Nuc. Eng. & Des.* 184: 329-338 (1998).

26. Nishikawa, M., K. Kosaka, and K. Hashimoto, "Gas Absorption in Gas-Liquid or Solid-Gas-Liquid Spouted Vessel", *Proc. 2<sup>nd</sup> Pacific Chem. Eng. Congress*, Denver, CO, USA, 1977.
27. Oke, N.J., D.W. Smith, and H. Zhou, "An Empirical Analysis of Ozone Decay Kinetics in Natural Waters", *Ozone Sci. & Eng.* 20: 361-379 (1998).
28. Roustan, M., R.Y. Wang, and D. Wolbert, "Modeling Hydrodynamics and Mass Transfer Parameters in a Continuous Ozone Bubble Column", *Ozone Sci. & Eng.* 18: 99-115 (1996).
29. Roustan M., C. Beck, O. Wable, J. P. Duguet, and J. Mallevalle, "Modeling Hydraulics of Ozone Contactors", *Ozone Sci. & Eng.* 15: 213-226 (1993).
30. Thalasso, F., H. Naveau, and E.-J. Nyns, "Design and Performance of a Bioreactor Equipped with a Venturi Injector for High Gas Transfer Rates", *Chem. Eng. J.* 57: B1-B5 (1995).
31. Unger, D.R. and F. Muzzio, "Laser-Induced Fluorescence Technique for the Quantification of Mixing in Impinging Jets", *AIChE J.* 45: 2477-2486 (1999).
32. Valentin, F.H.H., *Absorption in Gas-Liquid Dispersions: Some Aspects of Bubble Technology*, Donald M.B. (Ed.). (London, England: E. & F.N. Spon Ltd., 1967).
33. Wachsmann, U., N. Rübiger, and A. Vogelwohl, "The Compact Reactor-A Newly Developed Loop Reactor with a High Mass Transfer Performance", *Ger. Chem. Eng.* 7: 39-44 (1984).
34. Wang, K.B. and L.T. Fan, "Mass Transfer in Bubble Columns Packed with Motionless Mixers", *Chem. Eng. Sci.* 33: 945-952 (1978).
35. Witze, P.O., *A Study of Impinging Axisymmetric Turbulent Flows: The Wall Jet, The Radial and Opposing Free Jets: Ph.D. Thesis* (Davis, CA, USA.: University of California, Davis, 1974).
36. Yurteri, C. and M.D. Gurol, "Ozone Consumption in Natural Waters: Effects of Background Organic Matter, pH and Carbonate Species", *Ozone Sci. & Eng.* 10: 277-290 (1988).
37. Zhou, H. and D.W. Smith, "Ozone Mass Transfer in Water and Wastewater Treatment: Experimental Observations Using a 2D-Laser Particle Dynamics Analyzer", *Wat. Res.* 34: 909-921 (2000).

38. Zhou, H. and D.W. Smith, "Applying Mass Transfer Theory to Study the Kinetics of Fast Ozone Reactions in Pulp Mill Effluents", *Proc. of the 14<sup>th</sup> Ozone World Congress*, Detroit, MI, USA, 1999.
39. Zhou, H. and D.W. Smith, "Process Parameter Development for Ozonation of Kraft Pulp Mill Effluents", *Wat. Sci. & Technol.* 35(2-3): 251-259 (1997).
40. Zhou, H., *Investigation of Ozone Disinfection Kinetics and Contactor Performance Modeling: Ph.D. Thesis* (Edmonton, AB, Canada: University of Alberta, 1995).
41. Zhou, H., D.W. Smith, and S.J. Stanley, "Modeling of Dissolved Ozone Concentration Profiles in Bubble Columns", *J. Environ. Eng., ASCE* 120(4): 821-840 (1994).

## **CHAPTER 2. DEVELOPMENT OF TRANSIENT BACK FLOW CELL MODEL (BFCM) FOR BUBBLE COLUMNS\***

### **2.1 INTRODUCTION**

Water and wastewater ozonation is usually conducted by dissolving the on-site generated ozone gas in the liquid phase. This is often achieved by using an ozone bubble column as the reacting chamber where ozone gas is bubbled through the liquid phase by utilizing conventional bubble diffusers, turbine mixers, negative pressure gas ejectors, positive pressure gas injectors, etc. In all these different bubble columns' designs there are number of processes that occur simultaneously. These processes are convection and backmixing of the liquid and gas phases flowing through the contacting chamber, ozone gas mass transfer from the gas phase to the liquid phase, ozone decay, and competitive reactions with the constituents in water and wastewater with the dissolved ozone (Zhou *et al.*, 1994).

The rates of the individual phase transport and transformation processes, contactor configuration, operating conditions, and water or wastewater quality influence the overall performance of any ozonation system. Backmixing of the gas phase is another important hydrodynamic property to be considered for the modeling, the design, and the optimization of the bubble columns' performance (Zahradník and Fialová, 1996).

Backmixing in the liquid phase flowing through bubble columns has been studied by several investigators to better understand the mixing behavior of bubble columns (Ohki and Inoune, 1970; Deckwer *et al.*, 1973; Hikita and Kikukawa, 1974; Chianese *et al.*, 1981; Ogawa *et al.*, 1982; Houzelot *et al.*, 1985; Le Sauze *et al.*, 1992). Therefore, the topic of gas and liquid phase backmixing in two-phase (i.e., gas-liquid) flows has received major attention in the chemical engineering field. Especially with regard to the gas phase backmixing, several investigators studied the effect of gas phase backmixing in bubble columns (Reith *et al.*, 1968; Deckwer, 1976; Van Vuuren, 1988; Kawagoe *et al.*, 1989; Wachi and Nojima, 1990; Shetty *et al.*, 1992; Zahradník and Fialová, 1996).

---

A version of this chapter has been published. Gamal El-Din, M. and D.W. Smith, *Ozone Sci. & Eng.* 23(4): 313-326 (2001).

In bubble columns with diameters larger than 140 mm, the gas phase dispersion is higher due to the occurrence of eddies at larger scales. In bubble columns with diameters less than 140 mm and large aspect ratios ( $L/D \gg 1$ ), the gas-phase dispersion coefficient is less than the liquid-phase dispersion coefficient by an order of magnitude (Reith *et al.*, 1968). Based on the theoretical calculations of Deckwer (1976), the gas-phase backmixing could be neglected in bubble columns with diameters of less than 500 mm. Therefore, the gas phase could be considered in the plug flow regime. Thus, it is essential to adequately and accurately characterize these fundamental processes and determine the variables that control and dictate the overall performance of any ozonation system.

## 2.2 TRACER TESTS

Two types of tracer tests have been widely used to characterize the backmixing process in non-ideal flow conditions in a chemical reactor: pulse or stimulus-input tests and step-input tests. The results from these two types of tracer inputs are interrelated and can provide similar information on the residence time distribution of the fluid elements inside a chemical reactor (Levenspiel, 1972). In a pulse-input test, a pulse or stimulus of non-reactive tracer is introduced into the fluid influent line just upstream of the contactor inlet at time zero. As the injection time is minimized compared to the hydraulic theoretical retention time of the reactor (few seconds compared to few minutes), the pulse input can be assumed to be an ideal pulse, and therefore, it can be represented by the Dirac  $\delta$  function. Simultaneously with the tracer injection, the concentrations of the tracer inside the reactor at different points along the reactor height and at the effluent exit point from the reactor are continuously recorded till the tracer is recovered. That can be confirmed by the residence time density (RTD) curve returning back to the background level of the tracer in the tested liquid. The measured concentrations (after being corrected for the background tracer level in the tested water, i.e., the background noise) are then normalized to produce a curve with an area of unity above the time axis. This curve represents the RTD function ( $E(t)$ ) that is described mathematically as:

$$\int_0^{\infty} E(t) \cdot dt = 1 \quad [2.1]$$

where:  $t_m$  = mean residence time of the RTD (s) and  $E(t)$  = residence time density function ( $s^{-1}$ ). The RTD curve is often characterized by the mean residence time ( $t_m$ ) and the variance ( $\sigma_t^2$ ) (Levenspiel, 1972). Respectively, the mean and the variance represent the location and the spread of the RTD. Mathematically, they can be calculated from the discrete pulse-input tracer test data as follows:

$$t_m = \frac{\sum C_i t_i \Delta t_i}{\sum C_i \Delta t_i} \quad [2.2]$$

and

$$\sigma_t^2 = \frac{\sum C_i t_i^2 \Delta t_i}{\sum C_i \Delta t_i} - t_m^2 \quad [2.3]$$

where:  $t_i$  = data acquisition time (s),  $\Delta t_i$  = time step (s),  $C_i$  = recorded tracer concentration at time step ( $\Delta t_i$ ) ( $mgL^{-1}$ ), and  $\sigma_t^2$  = variance of the RTD as a function of time ( $s^2$ ). The results can then be used to estimate the traditional mixing parameters: the dimensionless Peclet number ( $Pe_L$ ) and the equivalent number of the continuous-flow-stirred-tank-reactors (CFSTR) in-series ( $N_{CFSTR}$ ). With respect to the sampling points inside the reactor, the boundary conditions can be considered as closed-open conditions and for the sampling point at the effluent exit point, the boundary conditions can be considered as closed-closed conditions (Levenspiel, 1972). For the closed-open boundary conditions:

$$\sigma_\theta^2 = \frac{\sigma_t^2}{\tau^2} = \frac{2}{Pe_L} + \frac{3}{Pe_L^2} = \frac{1}{N_{CFSTR}} \quad [2.4]$$

where:  $\tau$  = theoretical hydraulic retention time of the bubble column (s) and  $\sigma_{\theta}^2$  = variance of the RTD as a function of the dimensionless time ( $\theta$ ). And for the closed-closed boundary conditions:

$$\sigma_{\theta}^2 = \frac{\sigma_t^2}{\tau^2} = \frac{2}{Pe_L} - \frac{2}{Pe_L^2} (1 - e^{-Pe_L}) = \frac{1}{N_{CFSTR}} \quad [2.5]$$

If potassium chloride or sodium chloride is used as the tracer material, the dissolved electrolytes can have an effect on the surface tension of the solution resulting in change in the bubble sizes and the bubbles' coalescence. At high dissolved electrolyte concentrations ( $> 5,000 \text{ mgL}^{-1}$ ), the bubble rise velocity and the bubbles' coalescence decrease resulting in higher gas hold-up and thus, causes the dispersion number  $\left(\frac{1}{Pe_L}\right)$  to decrease. This effect can be ignored if the dissolved electrolyte concentrations are low ( $< 1,000$  to  $2,000 \text{ mgL}^{-1}$ ) (Jamialahmadi and Müller-Steinhagen, 1990). Since tap water or deionized water could contain traces of these electrolytes, the recorded experimental RTD must be corrected for those traces by obtaining the base line RTD for the tested water. Therefore, the background noise can be eliminated. Comparing the theoretical RTD curves with the corrected-experimental RTD curves and using a minimization technique to reduce the summation of the squared residuals (SSR) between the two curves, the mixing parameters can be accurately determined.

## 2.3 THEORY

### 2.3.1 Axial Dispersion Model

Assuming that the liquid phase is in axial dispersion regime, i.e., a diffusion-like process is assumed and is superimposed on a plug flow regime (Levenspiel, 1972), the transient axial dispersion model (transient ADM) for a pulse-input can be mathematically described as:

$$\frac{\partial C_t}{\partial t} = D_a \frac{\partial^2 C_t}{\partial \ell^2} - u_L \frac{\partial C_t}{\partial \ell} \quad [2.6]$$

where:  $\ell$  = distance along the column height (m),  $t$  = measurement time (s),  $D_a$  = axial dispersion coefficient of the liquid phase ( $m^2s^{-1}$ ),  $C_t$  = instantaneous tracer concentration ( $mgL^{-1}$ ), and  $u_L$  = superficial liquid velocity ( $ms^{-1}$ ). For a bubble column of a total height,  $L$  (m), Equation 2.6 can be written in a dimensionless form as follows:

$$\frac{\partial C_\theta}{\partial \theta} = \frac{1}{Pe_L} \frac{\partial^2 C}{\partial Z^2} - \frac{\partial C}{\partial Z} \quad [2.7]$$

where:

$$Pe_L = \frac{u_L L}{D_a \epsilon_L} \quad [2.8]$$

$$\theta = \frac{t}{\tau} \quad [2.9]$$

and

$$Z = \frac{\ell}{L} \quad [2.10]$$

where:  $L$  = total column height (m),  $Z$  = dimensionless distance along the column height,  $C_0 = C_t$  = instantaneous tracer concentration ( $mgL^{-1}$ ),  $\theta$  = dimensionless time, and  $\epsilon_L$  = dimensionless liquid-phase hold-up. For small Peclet numbers ( $Pe_L < 100$ ) and for both the closed-closed and the closed-open boundary conditions, the analytical solution of Equation 2.7 is not available (Levenspiel, 1972). Therefore, Levenspiel (1972) suggested that the analytical solution of Equation 2.7 that can be obtained for small deviations from plug flow conditions ( $Pe_L > 100$ ) at any given boundary conditions can still be applied to

the closed-closed and the closed-open boundary conditions for situations where  $Pe_L$  is slightly less than 100. As a result, the theoretical RTD for a pulse-input tracer test under those operating and boundary conditions, can be represented by:

$$\text{theoretical } E_\theta = \frac{1}{2\sqrt{\frac{\pi}{Pe_L}}} \exp\left[-Pe_L \frac{(1-\theta)^2}{4}\right] \quad [2.11]$$

and

$$\text{experimental } E_\theta = \frac{V}{M} C_\theta \quad [2.12]$$

where:  $E_\theta$  = dimensionless residence time density function as a function of the dimensionless time ( $\theta$ ),  $V$  = volume of the bubble column ( $m^3$ ), and  $M$  = mass of the injected tracer (kg).

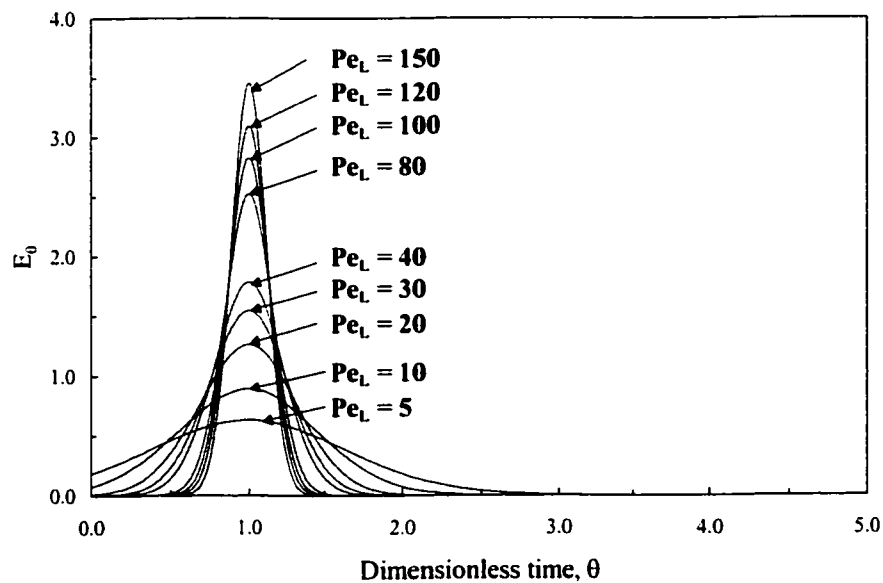


Figure 2.1 Theoretical RTD curves for the transient ADM under closed-closed or closed-open boundary conditions.

The theoretical RTD curves for such cases are shown in Figure 2.1. At low  $Pe_L$  ( $Pe_L \ll 100$ ), the pulse response is broad and it passes the measurement point slowly enough that it changes and spreads causing the  $E_\theta$  curve to be non-symmetrical. As shown in Figure 2.1, as the  $Pe_L$  approaches 100 or exceeds 100, the RTD narrows as the liquid flow approaches plug flow conditions.

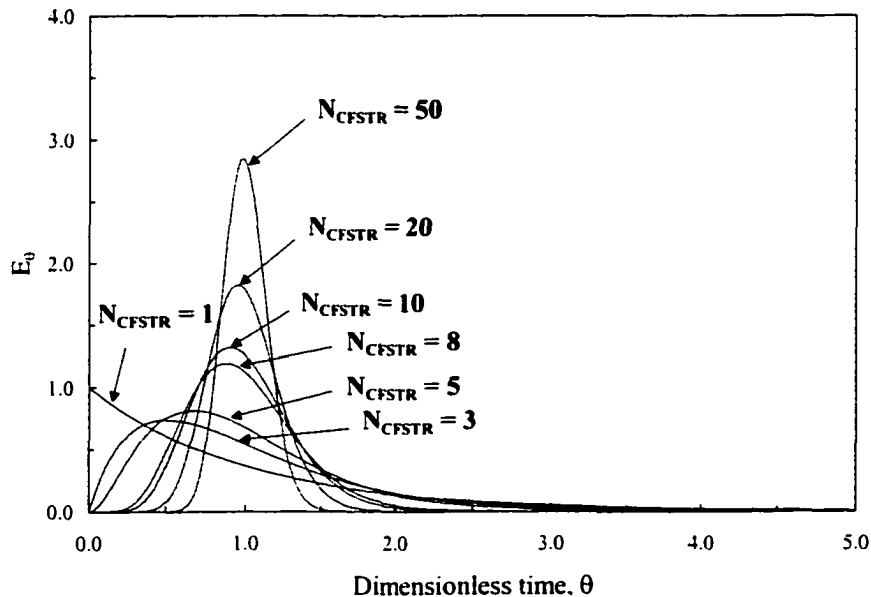


Figure 2.2 Theoretical RTD curves for the transient CFSTR's in-series model.

### 2.3.2 Transient Continuous-Flow-Stirred-Tank-Reactors In-Series Model

For a transient continuous-flow-stirred-tank-reactors (transient CFSTR's) in-series model, the theoretical RTD for a pulse-input tracer test can be represented by:

$$E_\theta = \frac{N_{CFSTR} (N_{CFSTR} \theta)^{N_{CFSTR} - 1}}{(N_{CFSTR} - 1)!} \quad [2.13]$$

The CFSTR's in-series model is usually more reliable than the ADM for the flow conditions where the dispersion numbers are large (Levenspiel, 1972). The theoretical RTD curves, for CFSTR's in-series model, are shown in Figure 2.2. Despite being

appropriate to describe the hydrodynamic behavior of tall bubble columns that have large aspect ratios, the ADM and the CFSTR's in-series model have limitations when they are used to describe the hydrodynamics of full-scale ozone contactors.

## 2.4 TRANSIENT BACK FLOW CELL MODEL (BFCM)

### 2.4.1 Development of the Transient BFCM

Transient BFCM hypothesizes both back flow and exchange flow to characterize the axial dispersion in the liquid phase (Zhou, 1995). Figure 2.3 represents a transient BFCM schematic for co-current flow conditions in bubble columns. It consists of two series of completely mixed cells, one series representing the liquid phase and the other representing the gas phase and each has a number of cells equals  $N_{\text{BFCM}}$ . As shown in Figure 2.3, it is assumed that the mixing parameter  $Pe_L$  varies along the reactor height. Three different distinct regions of mixing have been considered, which is usually the case in tall bubble columns with aspect ratio  $(L/D) \gg 1$ . In tall bubble columns and as the liquid flow passes through the reactor, the  $Pe_L$  will increase as the backmixing decreases along the column height from that in the intense mixing zone near the column entrance. In full-scale industrial ozone multi-chamber reactors, the aspect ratio is usually not very large. Because of the complex nature of such systems, the shape of the overflow structure, the presence of intermediate baffles, and the shape and location of the gas diffusers should be considered along with the aspect ratio in characterizing the hydrodynamic behavior of those systems.

The assumptions that govern the transient BFCM are as follows: (1) back flow occurs only in the liquid phase; (2) backflow is negligible in the gas phase due to the large buoyancy of gas bubbles and large reactor aspect ratio, i.e., the gas phase is assumed to be in a plug flow regime; (3) the ozone bubble column is operated at constant liquid and gas flowrates; (4) no mass transfer and chemical decay should be considered for the inert tracer; and (5) gas hold-up and bubbles' interfacial area are constant along the column height. In order to ensure that the gas phase flow conditions are close to be in a plug flow regime, the number of mixed cells ( $N_{\text{BFCM}}$ ) has to be equal to or greater than

10. Although, in some situations, the number of cells that are needed to model bubble columns of small aspect ratios are less than 10, the assumption that the gas phase is in plug flow regime could still be moderately valid due to the large buoyancy of gas bubbles.

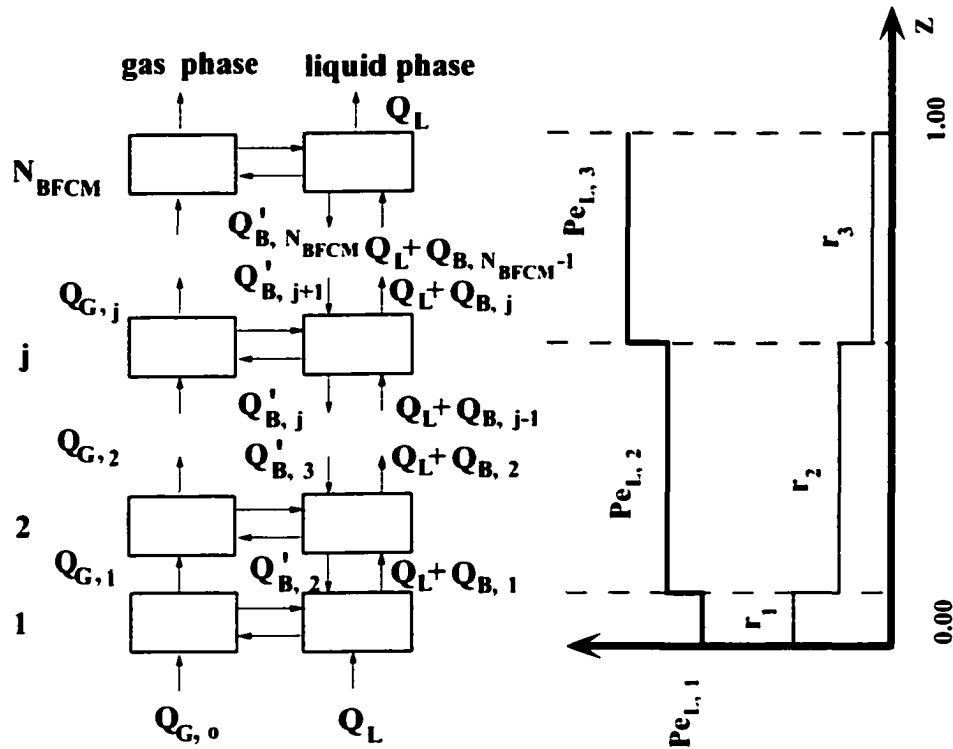


Figure 2.3 Transient BFCM schematic for non-reactive tracer for a co-current flow conditions.

Variable cell volume along the reactor length is considered in the model development to obtain a model that can be used to describe the hydrodynamics in ozone contactors of multiple chambers that have variable dimensions. By employing the mass balance with respect to the inert tracer around the cell number "1", the mathematical relationship for the transient BFCM can be written as follows:

$$Q_L C_0 + Q'_{B,2} C_2 - (Q_L + Q_{B,1}) C_1 = \frac{dC_1}{dt} V_c f_1 \quad [2.14]$$

where:  $C_0$  = tracer concentration in the influent to the first cell in the reactor ( $\text{mgL}^{-1}$ ),  $C_1$  = tracer concentration in the first cell in the reactor ( $\text{mgL}^{-1}$ ),  $C_2$  = tracer concentration in the second cell in the reactor ( $\text{mgL}^{-1}$ ),  $Q_L$  = liquid flowrate ( $\text{m}^3\text{s}^{-1}$ ),  $Q_{B,j}$  = exchange flowrate for cell number "1" ( $\text{m}^3\text{s}^{-1}$ ),  $Q'_{B,2}$  = back flowrate for cell number "2" ( $\text{m}^3\text{s}^{-1}$ ),  $V_c$  = average cell volume ( $\text{m}^3$ ) and it is equal to the total volume of the bubble column ( $V$ ) divided by the number of cells ( $N_{\text{BFCM}}$ ), and  $f_1$  = dimensionless correction factor for the volume of cell number "1". Dividing Equation 2.14 by  $V_c C_0^*$  where:

$$C_0^* = \frac{M}{V_c} = \frac{M}{\frac{V}{N_{\text{BFCM}}}} \quad [2.15]$$

and

$$f_1 = \frac{V_{c,j}}{\frac{V}{N_{\text{BFCM}}}} \quad [2.16]$$

where:  $C_0^*$  = instantaneously-mixed tracer concentration in the first cell ( $\text{mgL}^{-1}$ ),  $M$  = mass of the injected tracer (kg),  $N_{\text{BFCM}}$  = number of cells in-series in the transient BFCM, and  $V_{c,j}$  = volume of cell number "j" ( $\text{m}^3$ ). Then, substituting in the resultant equation for:

$$r_1 = \frac{Q_{B,1}}{Q_L} \quad [2.17]$$

and

$$r'_2 = \frac{Q'_{B,2}}{Q_L} \quad [2.18]$$

where:  $r_1$  = dimensionless exchange-flow ratio for cell number "1" and  $r'_2$  = dimensionless back-flow ratio for cell number "2". As a result:

$$\frac{dY_1}{dt} = -\frac{1+r_1}{f_1\tau/N_{\text{BFCM}}} Y_1 + \frac{r'_2}{f_1\tau/N_{\text{BFCM}}} Y_2 \quad [2.19]$$

where:

$$Y_j = \frac{C_j}{C_0} = \frac{E_{\theta,j}}{N_{\text{BFCM}}} \quad [2.20]$$

and

$$Z_{j,\text{act}} = f_{z,j} Z_{j,\text{avg}} = f_{z,j} \frac{j-0.5}{N_{\text{BFCM}}} = \frac{\left( \left[ \sum_{j=1}^{j-1} h_{c,j} \right] + h_{c,j}/2 \right)}{L} \quad [2.21]$$

where:  $Y_j$  = normalized tracer concentration in cell number "j" in the transient BFCM,  $f_{z,j}$  = dimensionless correction factor for the dimensionless distance (Z) for cell number "j",  $h_{c,j}$  = height of cell number "j" (m),  $Z_{j,\text{act}}$  = actual dimensionless distance of cell number "j",  $Z_{j,\text{avg}}$  = average dimensionless distance of cell number "j", and  $j$  = cell number in the transient BFCM. Following the same procedure used to derive Equation 2.19, one can obtain the transient BFCM equations for the cells from  $j = 2$  to  $j = N_{\text{BFCM}}$  as follows:

for  $1 < j < N_{\text{BFCM}}$ :

$$\frac{dY_j}{dt} = \frac{1+r_{j-1}}{f_j\tau/N_{\text{BFCM}}} Y_{j-1} - \frac{1+r'_j+r_j}{f_j\tau/N_{\text{BFCM}}} Y_j + \frac{r'_{j+1}}{f_j\tau/N_{\text{BFCM}}} Y_{j+1} \quad [2.22]$$

and for  $j = N_{\text{BFCM}}$ :

$$\frac{dY_{N_{\text{BFCM}}}}{dt} = \frac{1 + r_{N_{\text{BFCM}}-1}}{f_{N_{\text{BFCM}}} \tau / N_{\text{BFCM}}} Y_{N_{\text{BFCM}}-1} - \frac{1 + r'_{N_{\text{BFCM}}}}{f_{N_{\text{BFCM}}} \tau / N_{\text{BFCM}}} Y_{N_{\text{BFCM}}} \quad [2.23]$$

where:

$$r_1 = \frac{1}{\text{Pe}_{L,1}} - 0.5 \quad [2.24]$$

$$r_2 = \frac{j-1}{\text{Pe}_{L,2}} - 0.5 \quad [2.25]$$

$$r_3 = \frac{N_{\text{BFCM}} - j}{\text{Pe}_{L,3}} - 0.5 \quad [2.26]$$

By employing a liquid-flow balance on each cell from  $j = 1$  to  $j = N_{\text{BFCM}}$ , one can obtain:

$$Q_{B,1} = Q'_{B,2} = r_1 Q_L \quad \text{for } j = 1 \quad [2.27]$$

$$Q_{B,2} = Q'_{B,3} = r_2 Q_L \quad \text{for } j = 2 \quad [2.28]$$

$$Q_{B,j} = Q'_{B,j+1} = r_2 Q_L \quad \text{for } 3 \leq j \leq j-1 \quad [2.29]$$

$$Q'_{B,j} = Q_{B,j-1} = r_2 Q_L \quad \text{for } 3 \leq j \leq j \quad [2.30]$$

where:  $j$  = number of the cell at which the  $\text{Pe}_L$  changes from  $\text{Pe}_{L,2}$  to  $\text{Pe}_{L,3}$ .

$$Q_{B,j} = Q'_{B,j+1} = r_3 Q_L \quad \text{for } j \leq j \leq N_{\text{BFCM}}-1 \quad [2.31]$$

$$Q'_{B,j+2} = Q_{B,j+1} = r_3 Q_L \quad \text{for } j+1 \leq j \leq N_{\text{BFCM}}-1 \quad [2.32]$$

and

$$Q'_{B,N_{\text{BFCM}}} = Q_{B,N-1_{\text{BFCM}}} = r_3 Q_L \quad \text{for } j = N_{\text{BFCM}} \quad [2.33]$$

The transient BFCM and the transient ADM describe the backmixing of the liquid phase using different mixing parameters  $Pe_L$ ,  $N_{\text{BFCM}}$ , and  $r'$ . These parameters are interrelated by the following equation:

$$r' = \frac{N_{\text{BFCM}}}{Pe_L} - 0.5 \quad [2.34]$$

Equation 2.34 is an approximate relationship between the two models based on ignoring the  $\left(\partial^3 C / \partial Z^3\right)$  and higher-order terms in the Taylor series when the differential equation representing the transient ADM is transformed into a finite-difference equation (Mecklenburgh and Hartland, 1968). The term  $r'$  in Equation 2.34 refers to the backmixing between stages whilst the 0.5 refers to the perfect mixing within each stage.

These two effects are added together to give the total backmixing effect  $\left(N_{\text{BFCM}} / Pe_L\right)$  (Mecklenburgh and Hartland, 1975). Stagewise systems may rather be said to consist of finite regions of perfect mixing connected by regions of zero volume but with finite backmixing (Hartland and Mecklenburgh, 1968). This means that a series of stages will always inherent backmixing although if there is no interstage backmixing (when  $r' = 0$ ) (Mecklenburgh and Hartland, 1975). For this situation:

$$Pe_L = 2N_{\text{BFCM}} \quad [2.35]$$

In the transient BFCM, ideal plug flow conditions exist if  $r' = -0.5$ , although, this ideal situation can not exist in nature (Mecklenburgh and Hartland, 1975).

## 2.4.2 Numerical Simulations of the Transient BFCM

### 2.4.2.1 Numerical Solution Technique

Equations 2.19, 2.22, and 2.23, are  $N_{\text{BFCM}}$  differential equations in  $N_{\text{BFCM}}$  unknowns ( $Y_j$ 's). Those differential equations can be solved numerically by applying an explicit technique for the time discretization. This explicit technique allows the transformation of the equations from their differential form into an algebraic form. Solving the  $N_{\text{BFCM}}$  algebraic equations simultaneously at time step "n+1" allows for  $Y_j^{n+1}$  values to be determined as functions of  $Y_j^n$  values at time step "n" for  $j = 1$  to  $j = N_{\text{BFCM}}$  as follows:

for  $j = 1$ :

$$\frac{dY_1^{n+1}}{dt} = \frac{Y_1^{n+1} - Y_1^n}{\Delta t} = \frac{Y_1^{n+1} - Y_1^n}{\tau\Delta\theta} = -\frac{1+r_1}{f_1\tau/N_{\text{BFCM}}} Y_1^n + \frac{r'_2}{f_1\tau/N_{\text{BFCM}}} Y_2^n \quad [2.36]$$

for  $1 < j < N_{\text{BFCM}}$ :

$$\frac{dY_j^{n+1}}{dt} = \frac{Y_j^{n+1} - Y_j^n}{\Delta t} = \frac{Y_j^{n+1} - Y_j^n}{\tau\Delta\theta} = \frac{1+r_{j-1}}{f_j\tau/N_{\text{BFCM}}} Y_{j-1}^n - \frac{1+r'_j+r_j}{f_j\tau/N_{\text{BFCM}}} Y_j^n + \frac{r'_{j+1}}{f_j\tau/N_{\text{BFCM}}} Y_{j+1}^n \quad [2.37]$$

and for  $j = N_{\text{BFCM}}$ :

$$\begin{aligned} \frac{dY_{N_{\text{BFCM}}}^{n+1}}{dt} &= \frac{Y_{N_{\text{BFCM}}}^{n+1} - Y_{N_{\text{BFCM}}}^n}{\Delta t} = \frac{Y_{N_{\text{BFCM}}}^{n+1} - Y_{N_{\text{BFCM}}}^n}{\tau\Delta\theta} \\ &= \frac{1+r_{N_{\text{BFCM}}-1}}{f_{N_{\text{BFCM}}}\tau/N_{\text{BFCM}}} Y_{N_{\text{BFCM}}-1}^n - \frac{1+r'_{N_{\text{BFCM}}}}{f_{N_{\text{BFCM}}}\tau/N_{\text{BFCM}}} Y_{N_{\text{BFCM}}}^n \end{aligned} \quad [2.38]$$

The initial condition for this system of equations is as follows:

at  $t = 0$  :

$$Y_1 = 1$$

$$Y_j = 0 \text{ for } 1 < j < N_{\text{BFCM}}$$

The Dirac  $\delta$  function representing the ideal pulse tracer input is represented numerically by an assumption of  $Y_1 = 1$  at  $t = 0$  as an ideal instantaneous and complete mixing of the injected mass of the tracer is assumed to take place at  $t = 0$  in cell number "1". The system of Equations 2.36 to 2.38 was solved for a wide range of simulated operating conditions. These conditions included: (1) a wide range of the completely mixed cells in-series ( $N_{\text{BFCM}} = 6$  to 20); (2) a wide range of Peclet numbers ( $Pe_L = 1.0$  to 40.0); (3) Peclet number was assumed to be constant along the column height unless otherwise it was mentioned that it varied along the column height; and (4) constant cell volume and cross-sectional area were assumed along the column height.

#### 2.4.2.2 Results

The effect of Peclet number ( $Pe_L$ ) on the theoretical RTD for  $N_{\text{BFCM}}$  equal to 10 are shown in Figures 2.4 and 2.5, in which the RTD is presented in terms of  $Y_j$  that is related to  $E_{0,j}$  as shown in Equation 2.20. At the bottom sampling port and as  $Pe_L$  increases, the RTD narrows as observed before for the ADM theoretical RTD's as a result of the liquid-phase flow conditions being approaching a plug flow regime. At the top sampling port and as the  $Pe_L$  increases, the RTD narrows and becomes more symmetrical, and the peak of the RTD increases. Similar trends to those observed in Figures 2.4 and 2.5 were observed at the middle sampling port with higher peaks of the RTD,s than those predicted at the top sampling port. Generally, the peak of the RTD gets smaller and the RTD becomes more symmetrical as the sampling ports get closer to the effluent exit point from the reactor as a result of the liquid phase flow conditions are approaching more towards a plug flow regime.

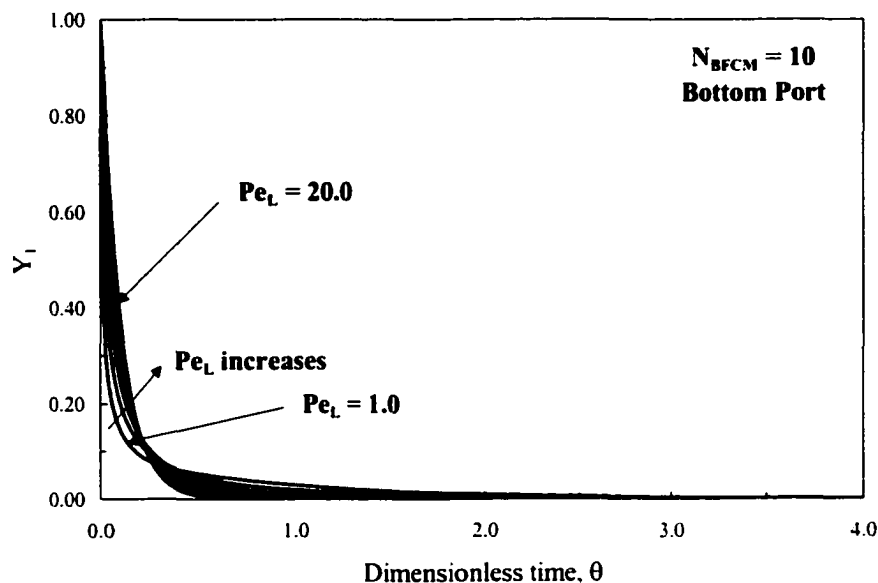


Figure 2.4 Theoretical RTD's for  $N_{BFCM} = 10$  at the bottom sampling port.

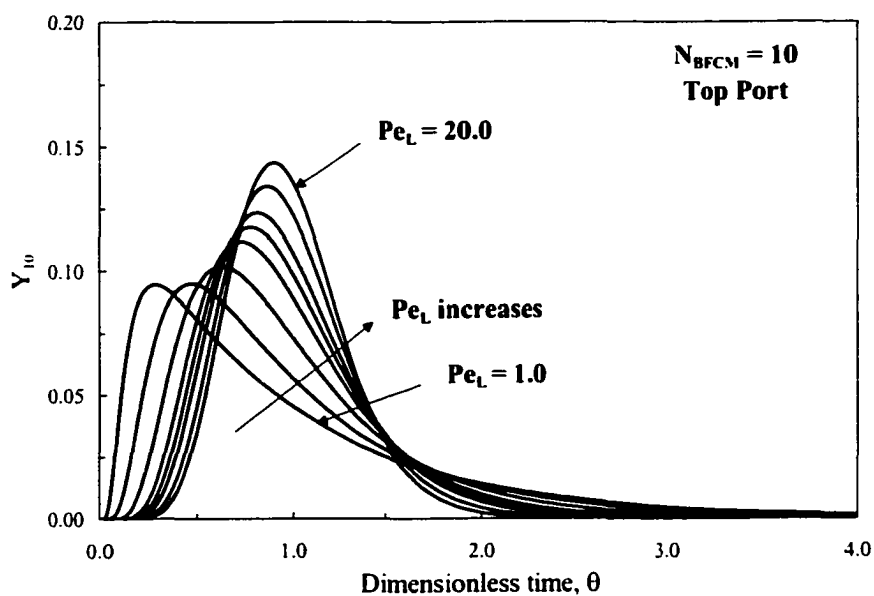


Figure 2.5 Theoretical RTD's for  $N_{BFCM} = 10$  at the top sampling port.

Figures 2.6 to 2.9 depict the effects of the  $N_{BFCM}$  and the  $Pe_L$  on the theoretical RTD at the middle and the top sampling ports. For an  $N_{BFCM}$  equal to or less than 14, not all the  $Pe_L$  range was applicable for model simulations because at high  $Pe_L$ ,  $r'$  approached  $-0.5$  and therefore, that produced unstable solution of the transient BFCM

equations, i.e., an oscillating solution. The  $-0.5$  is the extreme limit of the model that corresponds to an ideal plug flow mode that does not exist in nature. The dimensionless time step used in those model simulations was set equal to 0.008. Attempts to reduce that dimensionless time step below 0.008 were done in order to obtain solutions for the cases of high  $Pe_L$  and low  $N_{BFCM}$ , but still no success was achieved. This could be explained by the fact that as  $Pe_L$  increases, larger  $N_{BFCM}$  ( $N_{BFCM}$  larger than 10) is needed to describe the hydrodynamics of bubble columns as the liquid flow approaches plug flow conditions.

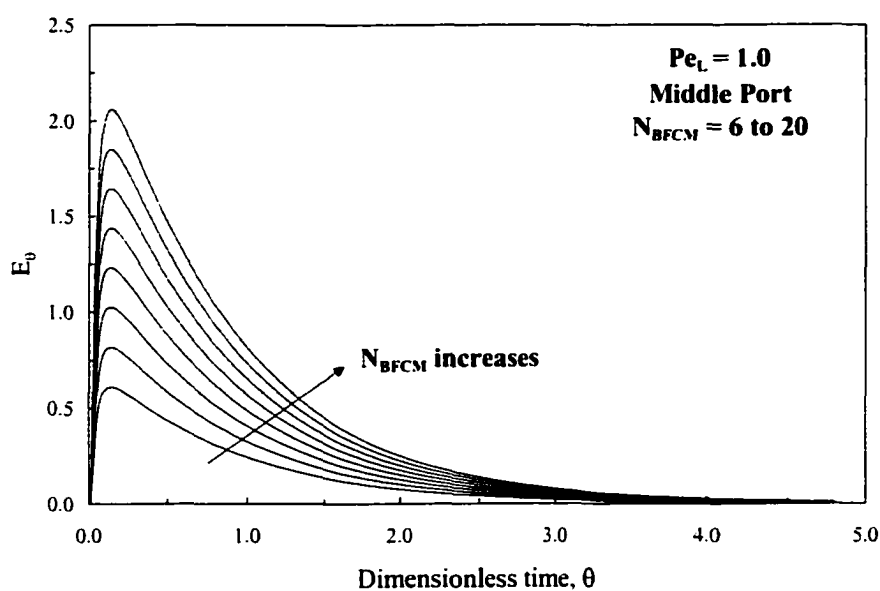


Figure 2.6 Effect of  $Pe_L$  and  $N_{BFCM}$  on the theoretical RTD's at the middle sampling port for  $Pe_L = 1.0$ .

Figures 2.6 and 2.7 show that varying the  $N_{BFCM}$  from 6 to 20 at  $Pe_L = 1.0$  causes the peaks of the RTD's to increase which contradicts with what Zhou (1995) has reported. All the peaks almost occur at the same point of dimensionless time with a slight shift and all the RTD's are broad and non-symmetrical. This suggests that as the pulse-input slowly passes the sampling port it spreads. This is usually the case for bubble columns that have small aspect ratios. As the  $Pe_L$  increases to 40.0, i.e., the liquid phase

is approaching plug flow conditions, we start to observe symmetrical RTD's at different  $N_{\text{BFCM}}$  ( $14 \leq N_{\text{BFCM}} \leq 20$ ) as shown in Figures 2.8 and 2.9.

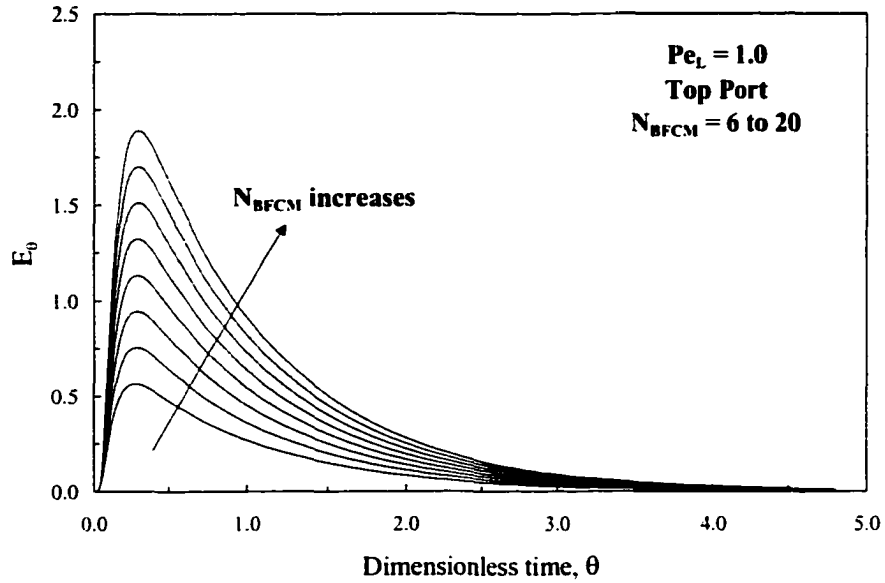


Figure 2.7 Effect of  $Pe_L$  and  $N_{\text{BFCM}}$  on the theoretical RTD's at the top sampling port for  $Pe_L = 1.0$ .

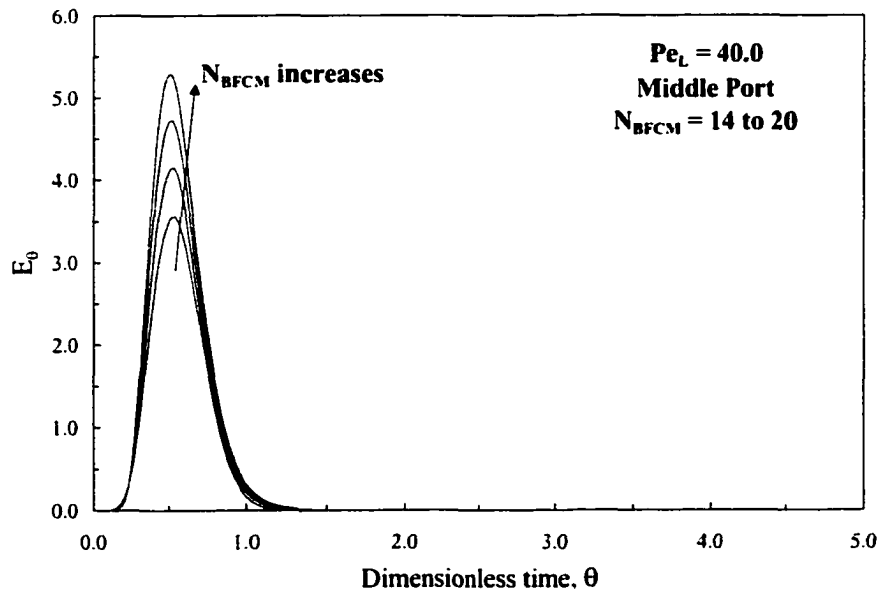


Figure 2.8 Effect of  $Pe_L$  and  $N_{\text{BFCM}}$  on the theoretical RTD's at the middle sampling port for  $Pe_L = 40.0$ .

Interestingly, at both the middle and the top sampling ports, the RTD's are spread with almost the same width, but the increase in the peak as  $N_{\text{BFCM}}$  increases from 14 to 20, is higher than that at  $Pe_L = 1.0$ . For  $N_{\text{BFCM}} < 10$ , the assumption of the gas phase being in a plug flow regime might not be very accurate, although it can still be moderately valid due to the large buoyancy of the gas bubbles. Therefore, those cases for  $N_{\text{BFCM}} < 10$  were included in the model simulations for the sake of comparison.

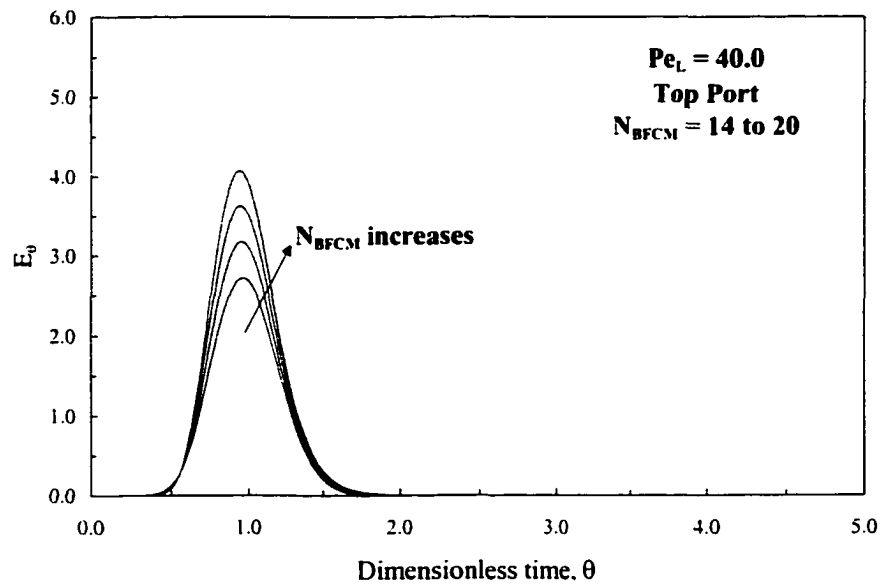


Figure 2.9 Effect of  $Pe_L$  and  $N_{\text{BFCM}}$  on the theoretical RTD's at the top sampling port for  $Pe_L = 40.0$ .

Comparisons between the transient BFCM, ADM, and CFSTR's in-series model for predicting the RTD's for  $Pe_L = 1.0$  and  $20.0$  at the middle and the top sampling ports respectively, are shown in Figures 2.10 to 2.13. For 10 cells in-series and  $Pe_L = 1.0$ , the transient ADM predicts lower peak of the RTD compared to the one predicted by the transient BFCM. This can be explained by the  $Pe_L$  being very small and therefore, the assumption that the flow conditions are slightly deviated from the ideal plug flow conditions is not satisfied which makes the transient ADM not adequate for predicting the liquid phase backmixing under those flow conditions.

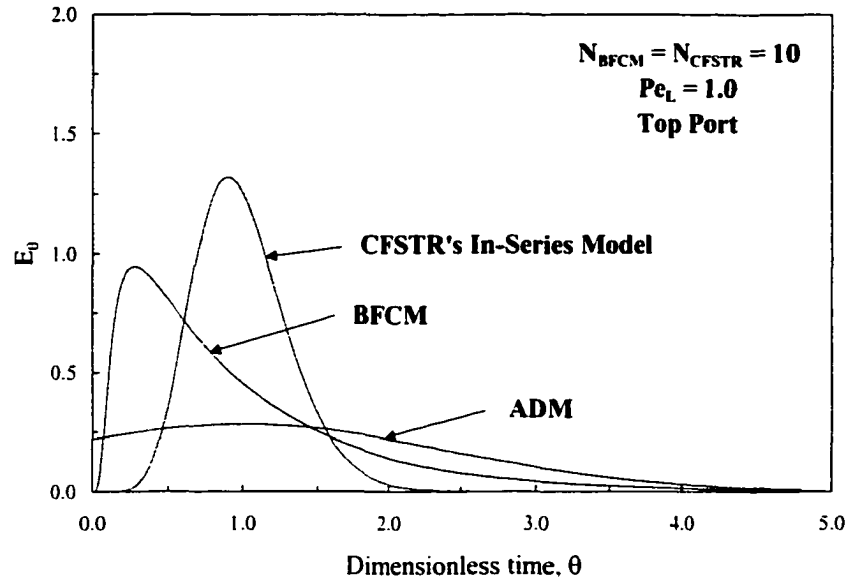


Figure 2.10 Comparison between the transient BFCM, ADM, and CFSTR's in-series model on the theoretical RTD's for  $Pe_L = 1.0$  and  $N_{BFCM} = N_{CFSTR} = 10$ .

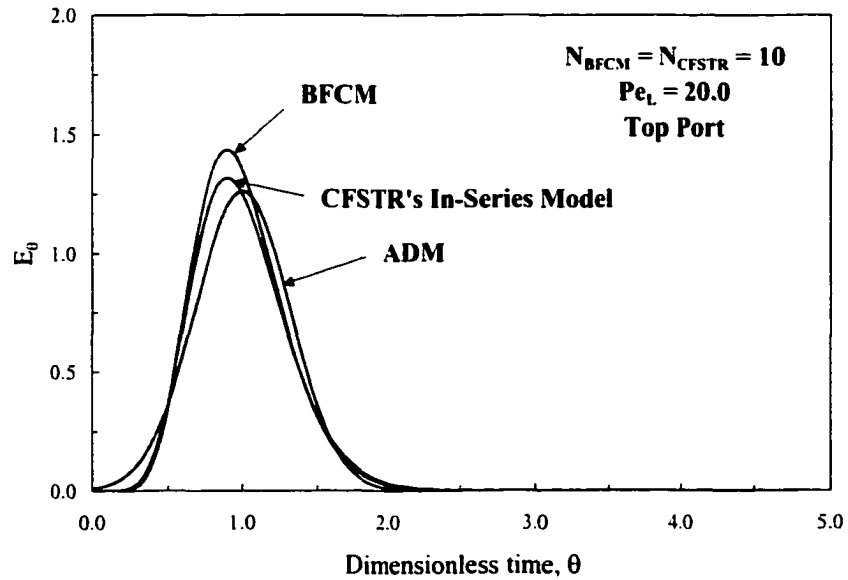


Figure 2.11 Comparison between the transient BFCM, ADM, and CFSTR's in-series model on the theoretical RTD's for  $Pe_L = 20.0$  and  $N_{BFCM} = N_{CFSTR} = 10$ .

At the same  $Pe_L$ , the transient CFSTR's in-series model predicts higher peak of the RTD compared to the transient BFCM and the predicted RTD is symmetrical rather than

being non-symmetrical which is usually the case when tracer tests are conducted in bubble column reactors. This can be explained by the fact that the transient CFSTR's in-series model does not account for the backmixing between the cells which is large at this low  $Pe_L$ . At  $Pe_L = 20.0$ , all three models predict symmetrical RTD's that have almost identical spreads and peaks as the backmixing ratio in the transient BFCM gets smaller at this high  $Pe_L$ .

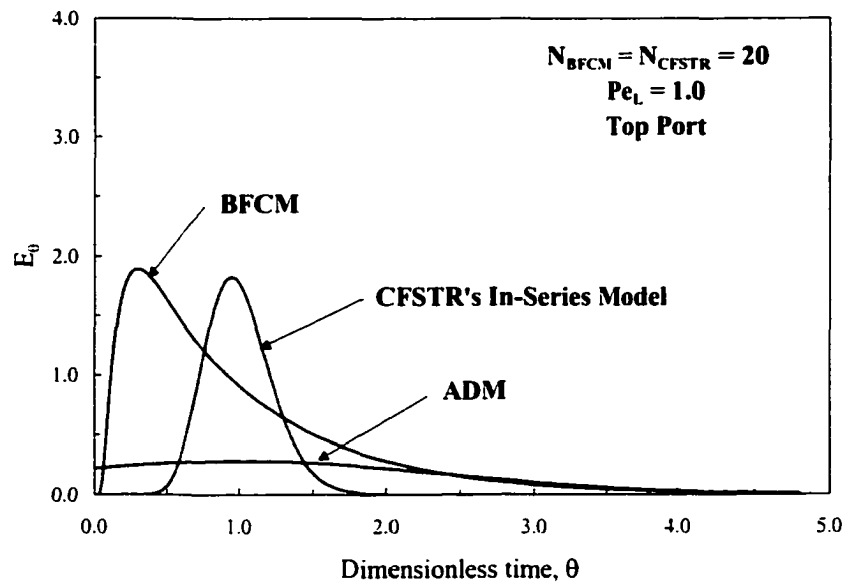


Figure 2.12 Comparison between the transient BFCM, ADM, and CFSTR's in-series model on the theoretical RTD's for  $Pe_L = 1.0$  and  $N_{BFCM} = N_{CFSTR} = 20$ .

At  $Pe_L = 1.0$ , Figure 2.12 depicts a similar trend to the one observed in Figure 2.10 except that the RTD predicted by the transient CFSTR's in-series model has a slightly lower peak than the one predicted by the transient BFCM. The large number of cells in-series ( $N_{BFCM} = 20$ ) at this very small  $Pe_L$  could have caused an increase in the RTD peak suggesting that the effect of the  $N_{BFCM}$  on the peak of the RTD is larger than the effect of the backmixing. As shown in Figure 2.13, as the  $Pe_L$  increases to 20.0 for the same number of cells ( $N_{CFSTR} = 20$ ), the transient CFSTR's in-series model and the transient ADM predict lower peak of the RTD compared to the one predicted by the transient BFCM. This can be explained by the transient BFCM performance being closer to plug

flow conditions than the performances of the transient ADM and the transient CFSTR's in-series model.

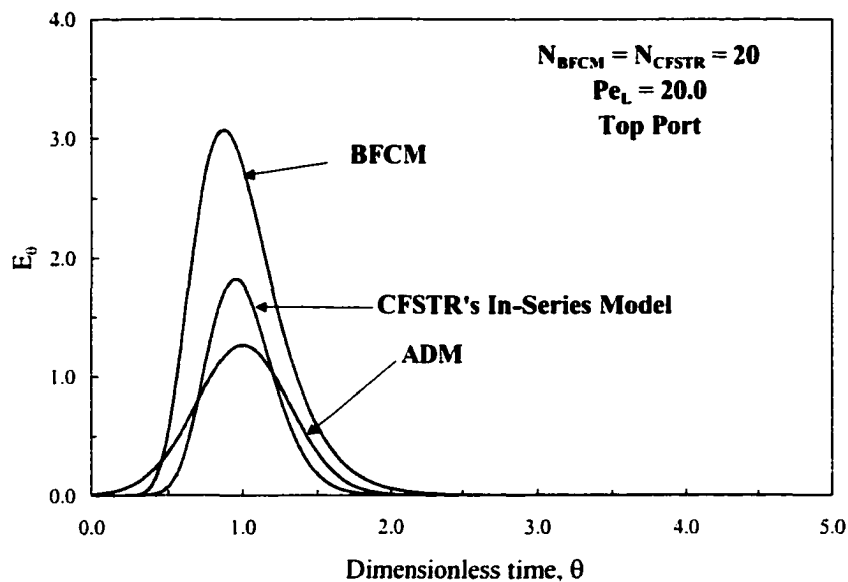


Figure 2.13 Comparison between the transient BFCM, ADM, and CFSTR's in-series model on the theoretical RTD's for  $Pe_L = 20.0$  and  $N_{\text{BFCM}} = N_{\text{CFSTR}} = 20$ .

Figures 12.4 and 2.15 show the theoretical RTD's for a situation where the  $Pe_L$  varies along the column height as in tall bubble columns.  $Pe_L$  was assumed to equal 0.40 from  $Z = 0.00$  to 0.05, 6.67 from  $Z = 0.05$  to 0.53, and 9.00 from  $Z = 0.53$  to 1.00. As shown and as the sampling port moves along the reactor height, i.e., as the cell number increases, the RTD's peak gets smaller and the RTD becomes more symmetrical, but still skewed to the left.

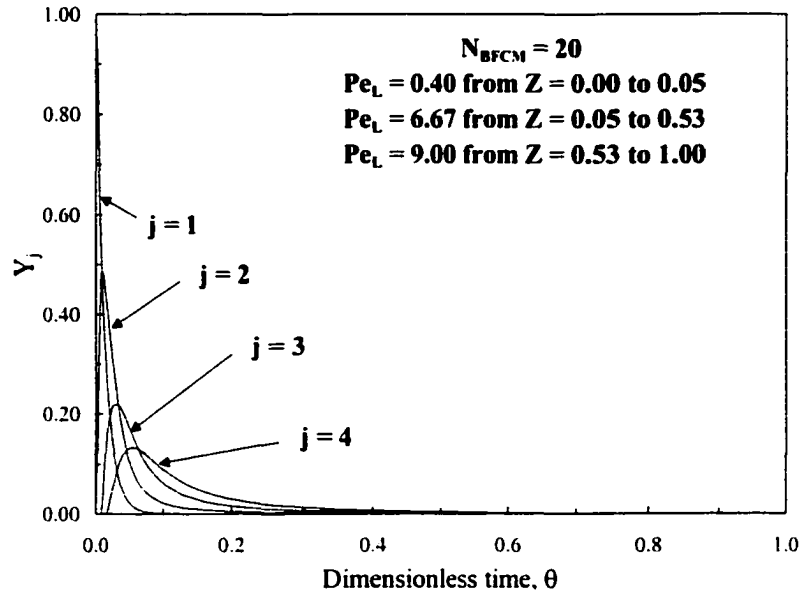


Figure 2.14 Theoretical RTD's for  $N_{BFCM} = 20.0$  and variable  $Pe_L$  along the column height ( $j = 1$  to  $4$ ).

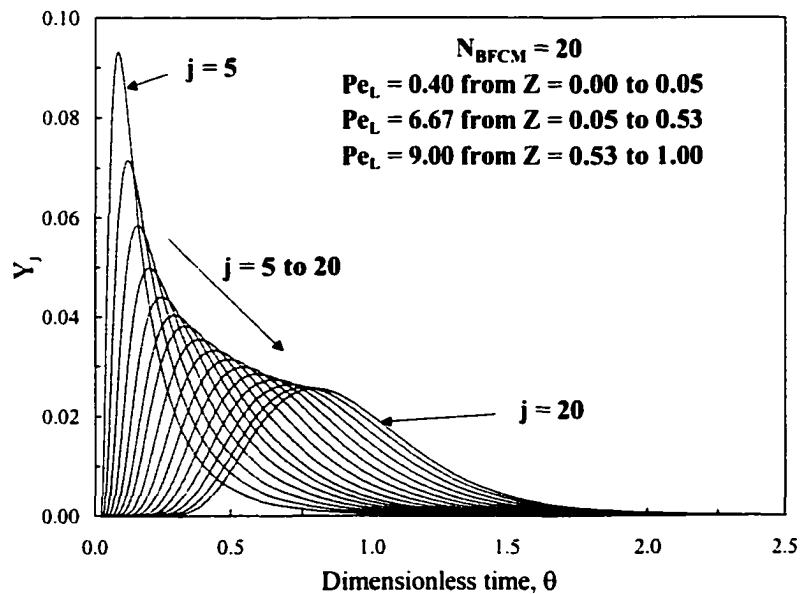


Figure 2.15 Theoretical RTD's for  $N_{BFCM} = 20.0$  and variable  $Pe_L$  along the column height ( $j = 5$  to  $20$ ).

## 2.5 TESTING OF THE TRANSIENT BFCM

### 2.5.1 Experimental Study

The experimental tracer data of Zhou (1995) was used for testing the applicability of the transient BFCM to describe the hydrodynamics in a fine-diffuser bubble column. The experimental set-up used in the study conducted by Zhou (1995) consisted of a glass bubble column with an inside diameter of 100 mm and a total column height of 2,000 mm. The water depth was maintained constant at 1,750 mm using an overflow weir. The tracer samples were collected from six sampling ports equally spaced along the column height as well as from the effluent exit line. The fine-bubble diffuser used in this bubble column was a 25 mm spherical fused crystalline aluminum stone that was elevated 5 mm from the bottom of the reactor to allow for good mixing between the gas bubbles and the liquid phase. The weir placed at the top of the column had 8 mm holes faced downward at the bottom of the headspace cap. This configuration helped minimizing the occurrence of swamp flows at the column exit (Zhou, 1995) and therefore, it could be concluded that the backmixing along the column height was uniform. The contactor was operated at two different flow modes: (1) the counter-current and (2) the co-current flow modes. The system was run for about eight turnovers to insure stable and steady-state operations before a Rhodamine WT tracer was injected upstream of the water inlet point into the column. The concentration of the Rhodamine in the collected samples ranged from 0 to  $10^{-2}$  mgL<sup>-1</sup> and was measured using the fluorescence method. In this experimental study, the theoretical hydraulic retention time ranged from 120 to 390 s and the gas-to-liquid flowrate (G/L) ratio ranged from 0.04 to 0.73.

### 2.5.2 Data Analysis Technique

Since the bubble column had a constant cross-sectional area, the cell volume was set constant along the column height and the cell volume correction factor, represented by Equation 2.16, was equal to 1. Also, since a uniform backmixing can be assumed along the column height due to the reactor configuration,  $Pe_L$  was assumed to be constant along the column height. As a result, the exchange-flow ratio ( $r$ ) was equal to the back-flow

ratio ( $r'$ ) and both were constant along the column height. The solutions of the transient BFCM equations were obtained using a spreadsheet program that was developed with a user-specified tolerance set equal to  $10^{-4}$ . The target cell in this spreadsheet program was the summation of squared residuals (SSR) of the tracer concentrations. The minimization technique was used to minimize the SSR by changing the back-flow ratio ( $r'$ ) according to the following equation:

$$SSR(r') = \sum (C_{L,\text{experimental}} - C_{L,\text{predicted}})^2 \quad [2.39]$$

where:  $C_{L,\text{measured}}$  = measured tracer concentration ( $\text{mgL}^{-1}$ ) and  $C_{L,\text{predicted}}$  = predicted tracer concentration ( $\text{mgL}^{-1}$ ). During the transient BFCM testing, a minimum SSR was always achieved as a result of having no problems with respect to the divergence of the model equations to reach a final solution. The initial “guess value” of the  $Pe_L$  was calculated using Equation 2.24 where  $r = r'$ .  $Pe_L$  was calculated using the tracer data of Zhou (1995) and by applying Equations 2.4 and 2.5 for the closed-open and closed-closed boundary conditions, respectively. After examining a different number of cells ( $N_{\text{BFCM}}$ ) for the transient BFCM analyses, it was found that 10 cells gave the lowest SSR's.

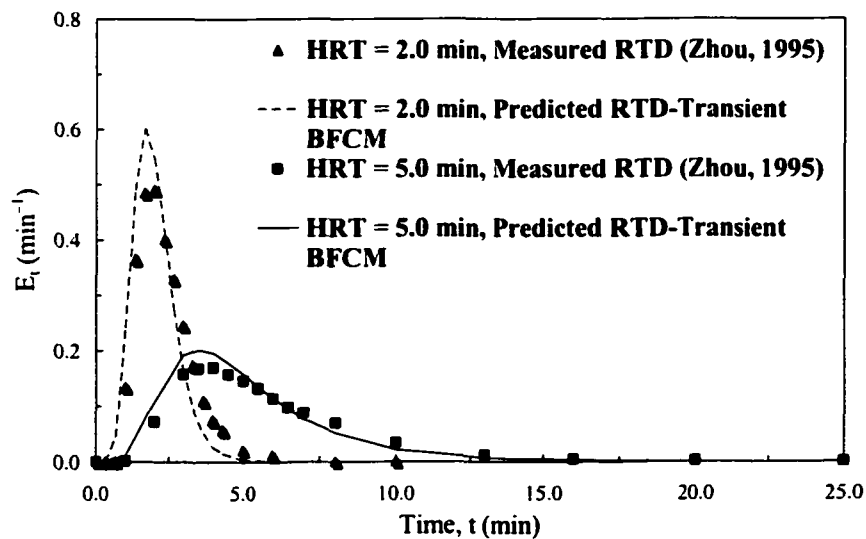


Figure 2.16 Experimental and predicted RTD's in a counter-current flow mode.

### 2.5.3 Results

The transient BFCM predictions of the RTD curves at the reactor exit point in the bubble column for the counter-current and the co-current flow modes are shown in Figures 2.16 and 2.17, respectively. Under a small hydraulic retention time of 120 s, the RTD curves were symmetrical. As the hydraulic retention time increased, tailing effects were observed and the RTD's were more asymmetrical rather than symmetrical. There were slight differences between the observed and the predicted RTD's in the two operating modes with the counter-current flow mode exhibiting higher backmixing. Examining the predicted back-flow ratios yielded findings that are in agreement with the literature. As the gas flowrate increased, the back-flow ratios increased in both the counter and the co-current flow modes. An explanation of this phenomenon is that as the gas flowrate increases, the bubbles' sizes increase and as a result, the circulation induced by the gas flow inside the bubble column will increase causing the backmixing to increase. By contrast, as the liquid flowrate increased, the back-flow ratios decreased as a result of the liquid flow being closer to plug flow conditions.

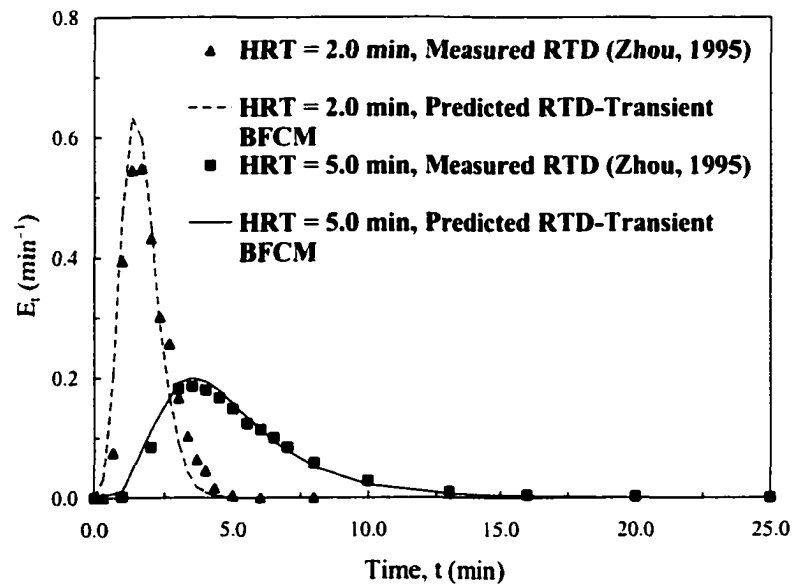


Figure 2.17 Experimental and predicted RTD's in a co-current flow mode.

Linear regression analyses of the predicted back-flow ratios obtained using the transient BFCM were conducted in order to obtain relationships that can be used to predict the back-flow (i.e., exchange-flow) ratios under different operating conditions in terms of the liquid flowrates, the gas flowrates, and the counter-current versus the co-current flow modes. Zhou (1995) proposed a generalized model for both the counter-current and the co-current flow modes in which  $\log(r+0.5)$  was correlated to  $\log(u_G)$  and  $\log(u_L)$ . The log of  $(r+0.5)$  was chosen for the proposed model for better comparison with the previous studies in the literature. This generalized model can be expressed as follows:

$$\log(r + 0.5) = a + b \cdot \log(u_G) + c \cdot \log(u_L) \quad [2.40]$$

Zhou (1995) used the pooled data of the counter-current and the co-current flow modes to obtain the regression constants  $a$ ,  $b$ , and  $c$ . They were determined to be 2.45, 0.40, and  $-1.03$ , respectively, with a correlation coefficient ( $r$ ) equal to 0.96. In another attempt to model the back-flow ratio as a function of the gas and liquid flowrates, the data of the counter-current flow mode was analyzed separately from the data of the co-current flow mode. The proposed model predicted higher back-flow ratios under the counter-current flow mode at the same gas and liquid flowrates. The regression analyses produced regression constants ( $a$ ,  $b$ , and  $c$ ) of  $-1.06$ ,  $0.34$ , and  $-0.95$ , respectively, for the counter-current flow mode with a correlation coefficient equal to 1.00. For the co-current flow mode, the regression constants ( $a$ ,  $b$ , and  $c$ ) were  $-1.64$ ,  $0.36$ , and  $-1.21$ , respectively, with a correlation coefficient equal to 0.99. It can be concluded that the gas flowrate has similar effect on the back-flow ratio in the counter-current and the co-current flow modes while the liquid flowrate has higher effect on the back-flow ratio in the co-current flow mode. Figure 2.18 depicts the transient BFCM predictions of the back-flow ratios versus the predictions of the proposed regression model (Equation 2.40). An excellent correlation between the two sets of back-flow ratios is evident.

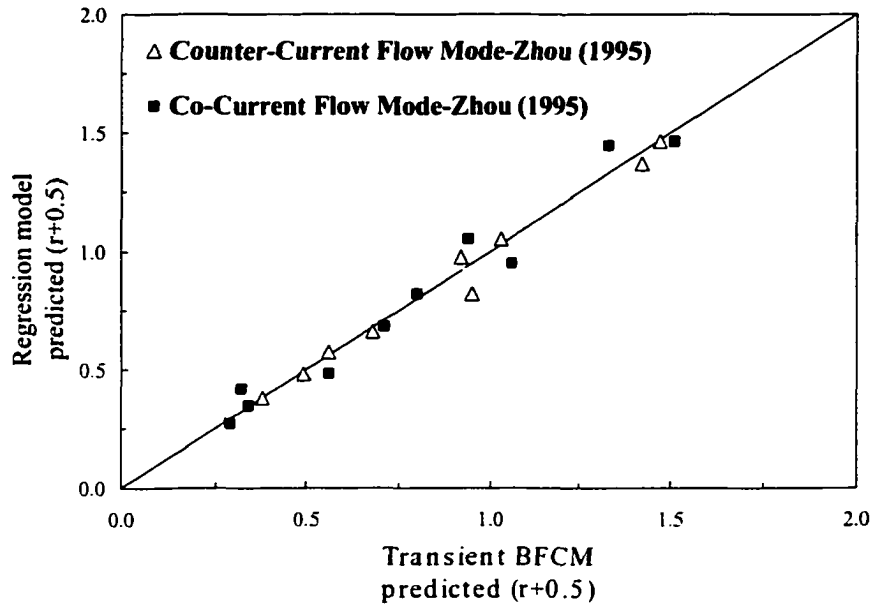


Figure 2.18 Comparison between the transient BFCM and the regression model predictions of back flow ratios.

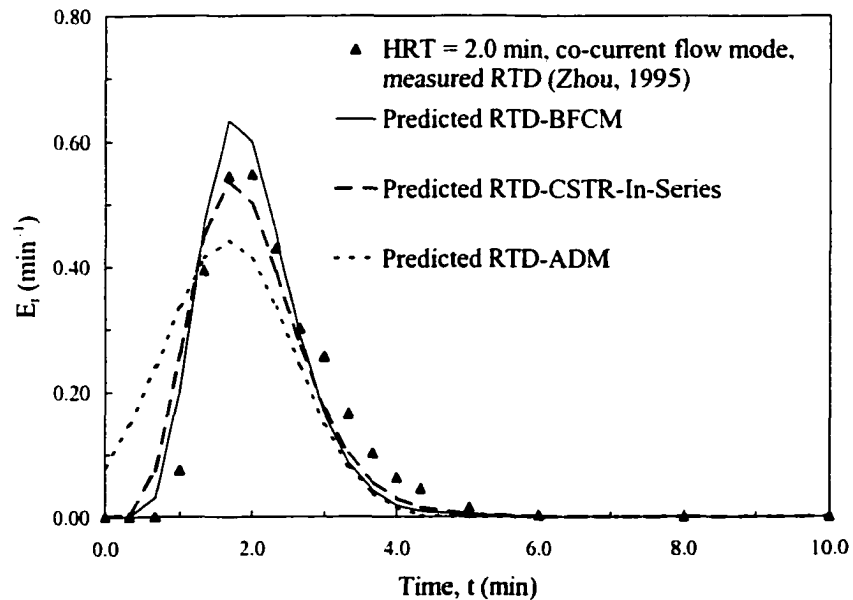


Figure 2.19 Comparison between the transient BFCM, ADM, and CFSTR's model in predicting the RTD's in a co-current bubble column.

In order to compare the predictions of the transient BFCM with the predictions of the traditionally used transient ADM and transient CFSTR's model, the RTD's obtained

by the three models are shown in Figure 2.19. From the tracer data and by applying Equation 2.5, the  $Pe_L$  number and  $N_{CFSTR}$  were determined and used as initial guesses to determine the actual  $Pe_L$  and  $N_{CFSTR}$  using a similar minimization technique to the one previously used for the transient BFCM. The values of these parameters obtained using the experimental tracer data should only be used as initial guesses. This is due to the problems usually encountered while conducting tracer experiments. Those problems might be caused by some unrecorded data points as a result of using longer sampling intervals. It is shown that the transient BFCM was superior to the other models in describing the backmixing process in bubble columns. The transient ADM predicted similar RTD's using either the equation for small deviations from plug flow conditions or the equation for open-open boundary conditions presented in Levenspiel (1972). By applying the minimization technique, the two equations predicted a  $Pe_L$  of 19.2 while the tracer data yielded a  $Pe_L$  of 9.8. Both equations were not suitable for describing the hydrodynamics due to the inappropriate boundary conditions' assumptions associated with them. The inadequacy of the transient ADM in describing the hydrodynamics is also evident from Figure 2.19. The equation representing small deviations from plug flow conditions is not suitable due to the fact that actual conditions in the bubble column are closer to complete mixing conditions rather than plug flow conditions. On the other hand, the equation representing the open-open boundary conditions is not suitable for the actual boundary equations encountered in the bubble column due to the configuration at the column exit. The actual boundary conditions are usually closed-closed or closed-open conditions and unfortunately, no analytical solutions are available of the transient ADM for these conditions. The transient BFCM produced a  $Pe_L$  of 17.9 based on a number of cells equal to 10. The transient CFSTR's model produced an  $N_{CFSTR}$  of 5.5 and 7.0 using the experimental and the simulated RTD's, respectively. Applying a number of cells equal to 7 in the transient CFSTR's model produced a  $Pe_L$  of 12.9. As shown in Figure 2.19, the transient CFSTR's model predicted an RTD curve that was similar to the one predicted by the transient BFCM except for a lower peak. Using a number of cells equal to 7 in the transient CFSTR's model does not ensure plug flow conditions in the gas phase. Therefore, using the steady-state CFSTR's model to describe the overall ozonation process will not be appropriate.

## 2.6 CONCLUSIONS

As compared to the traditionally used transient ADM and transient CFSTR's in-series model, the transient BFCM can adequately describe the backmixing in the liquid phase in bubble columns over a wide range of operating conditions and under any given boundary conditions. Therefore, it has some advantages over the transient ADM and the transient CFSTR's in-series model. These advantages are as follows: (1) the transient BFCM can account for variable backmixing coefficient (i.e., variable  $Pe_L$ ) along the column height or along the length of a contacting chamber while predicting simultaneously the RTD curves at various sampling ports; (2) the transient BFCM has the capability to account for variable cross-sectional area along the column height or along the length of a contacting chamber; (3) the analytical solution of the transient ADM for a tracer pulse-input is only available for small deviations from plug flow conditions (Equation 2.11) under any given boundary conditions and for large deviations from plug flow conditions under only open-open boundary conditions. The closed-closed and closed-open boundary conditions are usually the cases in ozone contacting chambers. Therefore, in order to use the solution of transient ADM for a tracer pulse-input under small deviations from plug flow conditions (Equation 2.11) to describe the backmixing in the liquid phase in such ozone reactors will lead to inadequate modeling of the hydrodynamics; and (4) the transient BFCM is easy to formulate and solve using a spreadsheet program even for the cases where the mixing parameters are variable along the column height.

The number of cells in-series, as one of the mixing parameters to be considered for the transient BFCM simulations, has to be chosen carefully so that the transient BFCM predictions, of the hydrodynamic behavior in ozone contactors performance under different operating conditions, are closer to the actual backmixing conditions. The transient BFCM should be expanded to account for the backmixing in the gas phase to allow studying the effect of the gas-phase backmixing on the hydrodynamic performance of ozone bubble columns of small aspect ratios and full-scale ozone contactors where the gas phase can no longer be considered in the plug flow regime.

## 2.7 REFERENCES

1. Chianese, A., M.C. Annesini, R. De Santis, and L. Marrelli, "A Model of a Pilot Bubble Column Reactor for Benzene Alkylation by Ethylene", *Chem. Eng. J.* 22: 151-158 (1981).
2. Deckwer, W.-D., "Non-Isobaric Bubble Columns with Variable Gas Velocity", *Chem. Eng. Sci.* 31: 309-317 (1976).
3. Deckwer, W.-D., U. Graeser, H. Langemann, and Y. Serpemen, "Zones of Different Mixing in the Liquid Phase of Bubble Columns", *Chem. Eng. Sci.* 28: 1223-1225 (1973).
4. Hartland, S. and J.C. Mecklenburgh, "The Concept of Backmixing", *Chem. Eng. J.* 23: 186-187 (1968).
5. Hikita, H. and H. Kikukawa, "Liquid-Phase Mixing in Bubble Columns: Effect of Liquid Properties", *Chem. Eng. J.* 8: 191-197 (1974).
6. Houzelot, J.-L., M.-F. Thiebaut, J.-C. Charpentier, and J. Schiber, "Contribution to the Hydrodynamic Study of Bubble Columns", *Int. Chem. Eng.* 25: 645-650 (1985).
7. Jamialahmadi, M. and H. Müller-Steinhagen, "Effect of Electrolyte Concentration on Bubble Size and Gas Hold-Up in Bubble Columns", *Chem. Eng. Res. Des.* 68: 202-204 (1990).
8. Kawagoe, M., T. Otake, and C.W. Robinson, "Gas-Phase Mixing in Bubble Columns", *J. Chem. Eng. Japan* 22: 136-142 (1989).
9. Le Sauze, N., A. Laplanche, M.T. Orta De Velasquez, G. Martin, B. Langlais, and N. Martin, "The Residence Time Distribution of the Liquid Phase in a Bubble Column and its Effect on Ozone Transfer", *Ozone Sci. & Eng.* 14: 245-262 (1992).
10. Levenspiel, O., *Chemical Reaction Engineering, 2<sup>nd</sup> Edition* (New York, NY, USA: John Wiley and Sons, Inc., 1972), pp. 253-293.
11. Mecklenburgh, J.C. and S. Hartland, *The Theory of Backmixing*, (New York, NY, USA: John Wiley and Sons, Inc., 1975), pp. 1-32.
12. Mecklenburgh, J.C. and S. Hartland, "Design of Reactors with Backmixing-III. Numerical Difference Between Differential and Stagewise Models", *Chem. Eng. Sci.* 23: 81-85 (1968).

13. Ogawa, S., M. Kobayashi, S. Tone, and T. Otake, "Liquid Phase Mixing in the Gas-Liquid Jet Reactor with Liquid Jet Ejector", *J. Chem. Eng. Japan* 15: 469-474 (1982).
14. Ohki, Y. and H. Inoue, "Longitudinal Mixing of the Liquid Phase in Bubble Columns", *Chem. Eng. Sci.* 25: 1-16 (1970).
15. Reith, T., S. Renken, and B.A. Israel, "Gas Hold-Up and Axial Mixing in the Liquid Phase of Bubble Columns", *Chem. Eng. Sci.* 32: 619-629 (1968).
16. Shetty, S.A., M.V. Kantak, and B.G. Kelkar, "Gas-Phase Backmixing in Bubble-Column Reactors", *AIChE J.* 38: 1013-1026 (1992).
17. Van Vuuren, D. "The Transient Response of Bubble Columns", *Chem. Eng. Sci.* 43: 213-220 (1988).
18. Wachi, S. and Y. Nojima, "Gas-Phase Dispersion in Bubble Columns", *Chem. Eng. Sci.* 45: 901-905 (1990).
19. Zahradník, J. and M. Fialová, "The Effect of Bubbling Regime on Gas and Liquid Phase Mixing in Bubble Column Reactors", *Chem. Eng. Sci.* 51: 2491-2500 (1996).
20. Zhou, H., *Investigation of Ozone Disinfection Kinetics and Contactor Performance Modeling, Ph.D. Thesis* (Edmonton, AB, CANADA: University of Alberta, 1995), pp. 129-135.
21. Zhou, H., D.W. Smith, and S.J. Stanley "Modeling of Dissolved Ozone Concentration Profiles in Bubble Columns", *J. Environ. Eng., ASCE* 120: 821-840 (1994).

## **CHAPTER 3. OZONE MASS TRANSFER IN WATER TREATMENT: MASS TRANSFER MODELING OF OZONE BUBBLE COLUMNS\***

### **3.1 INTRODUCTION**

Ozonation of water is usually conducted in ozone bubble columns as the reacting chambers where ozone gas is bubbled through the liquid phase by utilizing conventional bubble diffusers, turbine mixers, negative pressure gas ejectors, positive pressure gas injectors, etc. During ozonation, a number of processes occur simultaneously. Those processes are convection and backmixing of the liquid flowing through the contacting chamber, convection of the gas flowing through the contacting chamber, ozone gas mass transfer from the gas phase to the liquid phase, ozone auto-decomposition, and competitive reactivity of constituents in water with dissolved ozone (Zhou *et al.*, 1994). The rates of individual phase transport and chemical transformation processes, contactor configuration, operating conditions, and water quality influence the overall performance of any ozonation system (Zhou, 1995). Ozonation process relies in its effectiveness on the concentration of dissolved ozone. Quantifying the dissolved ozone is crucial to obtain optimized designs and operations of ozone contactors.

Mathematical models that are often applied to predict the dissolved ozone profiles along bubble columns are based on one of the following liquid-phase flow regime assumptions: (1) complete mixing or (2) plug flow (Alvarez-Cuenca *et al.*, 1980; Alvarez-Cuenca *et al.*, 1981; Chang and Chian, 1981; Laplanche *et al.*, 1991; Hull *et al.*, 1992; Lev *et al.*, 1992). Applying such simplified models to describe the performance of ozone bubble columns will lead to unoptimized and unreliable designs and consequently poor performance of ozone contactors. The actual flow pattern in bubble columns is usually closer to being mixed flow rather than being plug flow, but still not completely mixed flow. Thus, it is essential to accurately characterize those fundamental processes and determine the variables that control and dictate the overall performance of any ozonation system.

---

A version of this chapter has been published. Gamal El-Din, M. and D.W. Smith, *Wat. Sci. & Technol.: Wat. Suppl.* 1: 123-130 (2001).

This chapter presents: (1) formulation of the steady-state BFCM for modeling the ozone mass transfer process in bubble columns; and (2) initial testing of the steady-state BFCM using the pilot-scale experimental data of Zhou (1995).

### 3.2 THEORETICAL BACKGROUND

In bubble columns, non-ideal flow conditions affect the rate of absorption and concentration profiles of dissolved ozone in tubular bubble columns. The backmixing process of the liquid phase involves the redistribution of liquid elements either by slippage due to shear forces or by turbulent eddies. Since, the redistribution process is repeated a considerable number of times during the flow of the fluid through the contacting chamber, it was assumed that these disturbances are statistical in nature as in molecular diffusion. Therefore, the empirical Fick's law is applied with replacing the molecular diffusion coefficient by a mixing parameter, the axial dispersion coefficient ( $D_L$ ), which combines the effects of a non-uniform velocity profile (shear dispersion), molecular and eddy diffusivities:

$$\text{Diffusive mass flux} = -D_L \frac{\partial C_L}{\partial \ell} \quad [3.1]$$

The mass transfer of ozone gas from the gas phase into the liquid phase can be described and quantified by the two-film model:

$$\psi = k_L a (C_L^* - C_L) \quad [3.2]$$

where:  $\psi$  = gas-absorption rate ( $\text{mgL}^{-1}\text{s}^{-1}$ ),  $k_L$  = local liquid mass transfer coefficient ( $\text{ms}^{-1}$ ),  $a$  = gas bubbles' specific interfacial area ( $\text{m}^{-1}$ ),  $C_L^*$  = concentration of the dissolved ozone in equilibrium with the bulk ozone gas ( $\text{mgL}^{-1}$ ), and  $C_L$  = concentration of the dissolved ozone in the bulk liquid ( $\text{mgL}^{-1}$ ). Since ozone gas diffuses much faster in the gas phase than in the liquid phase, the mass transfer in the liquid phase becomes a

rate-controlling step and the overall mass transfer coefficient is considered to consist entirely of the local mass transfer coefficient in the liquid phase (Zhou, 1995).

As ozone gas dissolves in water, it starts decaying through two pathways, auto-decomposition and oxidation of impurities in the liquid phase due to its extremely high oxidative properties (Hoigné, 1982). The overall ozone auto-decomposition rate is influenced by the concentration and the history of the ozonation process and this ozone auto-decomposition process could be represented by a modified pseudo-first-order rate expression (Yurteri and Gurol, 1988; Oke *et al.*, 1998). In the experimental study of Oke *et al.* (1998), it was shown that the commonly used first-order kinetics expression with a constant reaction rate constant was inadequate in describing the ozone auto-decomposition process especially in situations where the initial ozone demand was significant. It was demonstrated that the reaction rate constant was continuously decreasing along the course of ozonation as a result of the changes in the water characteristics. As a result, an exponentially decreasing function was proposed as a better alternative to describe the ozone auto-decomposition kinetics (Oke *et al.*, 1998). In that expression, the reaction rate constant was replaced by a variable referred to as the specific ozone utilization rate constant ( $k_w$ ) that is a function of the utilized ozone dose ( $\Delta O_3$ ):

$$\frac{dC_L}{dt} = -k_w C_L = -(k_1 + k_2 e^{-k_3 \Delta O_3}) C_L \quad [3.3]$$

where:  $C_L$  = instantaneous dissolved ozone concentration ( $\text{mgL}^{-1}$ ),  $k_w$  = specific ozone utilization rate constant ( $\text{s}^{-1}$ ),  $k_1$  = empirical non-linear regression constant ( $\text{s}^{-1}$ ),  $k_2$  = empirical non-linear regression constant ( $\text{s}^{-1}$ ),  $k_3$  = empirical non-linear regression constant ( $\text{Lmg}^{-1}$ ),  $t$  = reaction time (s), and  $\Delta O_3$  = amount of the utilized ozone ( $\text{mgL}^{-1}$ ).  $k_1$ ,  $k_2$ , and  $k_3$  are empirical constants that can be obtained by applying non-linear regression analysis to the kinetics data and they are also characteristics of the water to be treated. According to Equation 1.2, as the amount of the utilized ozone increases along the course of ozonation,  $k_w$  will decrease. At the beginning of the ozonation, i.e., when

the amount of the utilized ozone is zero,  $k_w$  is equal to  $k_1 + k_2$  as the ozone auto-decomposition process is only attributed to the initial ozone demand. In the study of Oke *et al.* (1998) and for clean deionized water, the initial ozone demand was practically equal to zero and therefore,  $k_w$  could be assumed constant during the course of the ozonation.

For an irreversible first-order reaction, Danckwerts (1970) proposed a criterion for neglecting the effect of chemical reactions on the local mass transfer coefficient and hence, the gas absorption can be dealt with as pure physical absorption in which the dissolved gas diffuses from the surface to the bulk liquid without reacting on the way:

$$H_a^2 = E^2 = M = \frac{D_{O_3} k_w}{k_L^2} \ll 1 \text{ (i.e., it reaches zero)} \quad [3.4]$$

where:  $H_a = E = \sqrt{M}$  = dimensionless Hatta number,  $k_L$  = local mass transfer coefficient ( $\text{ms}^{-1}$ ),  $D_{O_3}$  = molecular diffusivity of ozone gas in water ( $\text{m}^2\text{s}^{-1}$ ), and  $k_w$  = specific ozone utilization rate constant ( $\text{s}^{-1}$ ).  $k_w$  was reported to be  $4.7 \times 10^{-4} \text{ s}^{-1}$  for the deionized water tested by Zhou (1995). Yurteri and Gurol (1988) reported that  $k_w$  was in the order of  $2.8 \times 10^{-3} \text{ s}^{-1}$  for the tested raw surface water. The diffusivity of ozone in water was determined by the Wilke-Chang formula to be  $1.74 \times 10^{-9} \text{ m}^2\text{s}^{-1}$  (at 20 °C) which is comparable to the value of  $1.71 \times 10^{-9} \text{ m}^2\text{s}^{-1}$  obtained using the equation recommended by Johnson and Davis (1996).  $k_L$  was reported to be in the order of  $3.1 \times 10^{-4} \text{ ms}^{-1}$  for clean water and in the order of  $1.9 \times 10^{-4} \text{ ms}^{-1}$  for water containing organic substances (Beltrán *et al.*, 1997). Substituting for these typical values of  $D$ ,  $k_w$ , and  $k_L$  into Equation 3.4 yields squared-Hatta numbers of  $8.5 \times 10^{-6}$  and  $1.4 \times 10^{-4}$  for the deionized and the surface water, respectively. Based on these small Hatta numbers, it can be concluded that the chemical reactions that occur during the course of clean or surface water ozonation has negligible effect on the local mass transfer coefficient and hence, Equation 3.2 will be applied for ozone absorption without any modification.

### 3.3 DEVELOPMENT OF THE BACK FLOW CELL MODEL (BFCM)

#### 3.3.1 Transient BFCM

BFCM hypothesizes both back flow and exchange flow to characterize the axial dispersion in the liquid phase (Zhou, 1995). Figure 3.1 represents a BFCM schematic for co-current flow conditions in bubble columns, where the back flow ratio is equal to the exchange flow ratio, and both are constant along the column height. BFCM consists of two series of completely mixed cells, one series representing the liquid phase and the other representing the gas phase and each has a number of cells equals  $N_{\text{BFCM}}$ . The assumptions that govern the transient BFCM are: (1) back flow occurs only in the liquid phase; (2) back flow is negligible in the gas phase due to the large buoyancy of gas bubbles; (3) ozone bubble column is operated at constant liquid and gas flow rates; (4) gas hold-up and gas bubbles' interfacial surface area are constant along the column height; and (5) the inert tracer material does not exhibit any mass transfer or chemical decay.

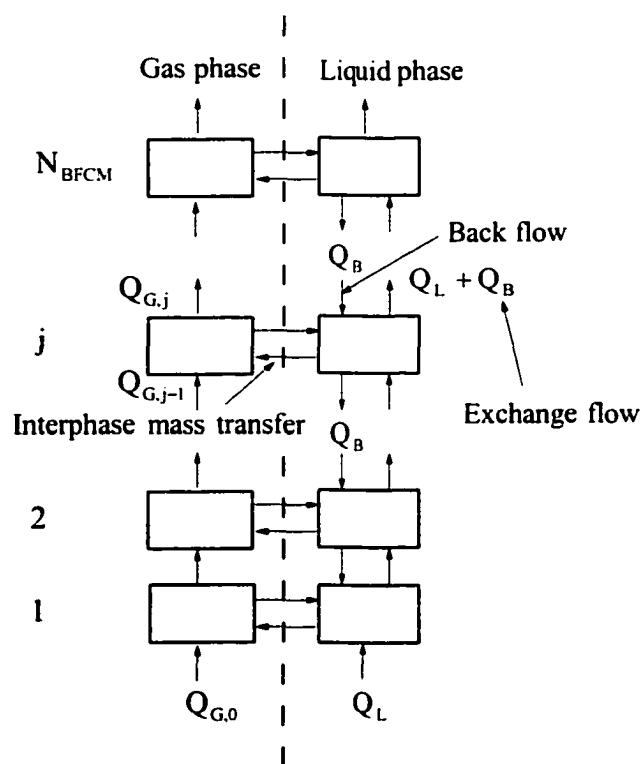


Figure 3.1 BFCM schematic for co-current flow conditions in bubble columns.

For the gas phase to flow in a regime close to the plug flow conditions, the number of the completely mixed cells ( $N_{BFCM}$ ) has to be equal to or greater than 10. By employing the mass balance with respect to the inert tracer around cell number 1, the mathematical relationship for the TBFCM is as follows:

$$Q_L C_0 + Q_B C_2 - (Q_L + Q_B) C_1 = \frac{dC_1}{dt} V_c \quad [3.5]$$

where:  $V_c$  is the cell volume and is equal to the total volume of the bubble column ( $V$ ) divided by the number of cells ( $N_{BFCM}$ ). Dividing Equation 3.5 by  $V_c C_0^*$  where:

$$C_0^* = \frac{M}{V_c} = \frac{M}{\frac{V}{N_{BFCM}}} \quad [3.6]$$

and  $M$  = volume of inert tracer, substituting in the resultant equation for:

$$r = \frac{Q_B}{Q_L} \quad [3.7]$$

where  $r$  is the back flow ratio, and rearranging, one can obtain:

$$\frac{dY_1}{dt} = -\frac{1+r}{\tau / N_{BFCM}} Y_1 + \frac{r}{\tau / N_{BFCM}} Y_2 \quad [3.8]$$

where:

$$Y_j = \frac{C_j}{C_0^*} = \frac{VC_j}{MN_{BFCM}} = \frac{E_{\theta,j}}{N_{BFCM}} \quad [3.9]$$

Following the same procedure used to derive Equation 3.8, one can obtain the transient BFCM equations for the cells from  $j = 2$  to  $j = N_{\text{BFCM}}$  as follows. For  $2 \leq j \leq N_{\text{BFCM}} - 1$ :

$$\frac{dY_j}{dt} = \frac{1+r}{\tau/N_{\text{BFCM}}} Y_{j-1} - \frac{1+2r}{\tau/N_{\text{BFCM}}} Y_j + \frac{r}{\tau/N_{\text{BFCM}}} Y_{j+1} \quad [3.10]$$

and for  $j = N_{\text{BFCM}}$ :

$$\frac{dY_{N_{\text{BFCM}}}}{dt} = \frac{1+r}{\tau/N_{\text{BFCM}}} Y_{N_{\text{BFCM}}-1} - \frac{1+r}{\tau/N_{\text{BFCM}}} Y_{N_{\text{BFCM}}} \quad [3.11]$$

BFCM and ADM describe the backmixing of the liquid phase using different mixing parameters ( $Pe_L$ ,  $N_{\text{BFCM}}$ , and  $r$ ). Those parameters are interrelated by the following relationship (Mecklenburgh and Hartland, 1975):

$$r = \frac{N_{\text{BFCM}}}{Pe_L} - 0.5 = \frac{D_L N_{\text{BFCM}}}{u_L L} - 0.5 \quad [3.12]$$

Equations 3.8, 3.10, and 3.11 are  $N_{\text{BFCM}}$  first-order ordinary differential equations in  $N_{\text{BFCM}}$  unknowns ( $Y_j$ 's). Those differential equations were solved numerically by applying an explicit technique for time discretisation to transform them into a system of linear algebraic equations which were then solved using a simple spreadsheet program. The initial conditions for that system of equations (for pulse-input tracer tests) are as follows:

at  $t = 0$ :

$$Y_1 = 1$$

$$Y_j = 0 \text{ for } 2 \leq j \leq N_{\text{BFCM}}$$

### 3.3.2 Steady-State BFCM

The assumptions that govern the application of the BFCM for modeling two-phase flows in ozone bubble columns are the same as the assumptions, 1 through 4, used to derive the TBFCM equations. In addition to those assumptions, further assumptions are needed. Those assumptions include: (1) ozone mass transfer process is limited by the mass rate in the liquid phase; (2) enhancement factor of the mass transfer due to the occurrence of chemical reactions was assumed to be 1.0 as the absorption of ozone in water could be considered to occur in the slow-reaction kinetics regime; (3) steady-state isothermal operation; (4) Henry's law applies; (5) gas-phase constituents, other than ozone, are assumed to be inert; (6) local mass transfer coefficient ( $k_L$ ) is constant along the column height; (7) owing to the hydrostatic head, total pressure varies linearly with the column depth; (8) superficial gas velocity is variable due to ozone absorption, ozone gas depletion, and hydrostatic pressure decrease along the column height; and (9) ozone auto-decomposition, in the liquid phase, is described by a pseudo-first-order rate expression and is negligible in the gas phase.

For a co-current flow mode and by referring to Figure 1, the basic mass balance with respect to the dissolved ozone within each cell leads to the following equations.

For  $j=1$ :

$$\begin{aligned} Q_L C_{L,0} + Q_B C_{L,2} + k_L a (C_{L,1}^* - C_{L,1}) \frac{V}{N_{BFCM}} \\ - k_w C_{L,1} \epsilon_L \frac{V}{N_{BFCM}} - (Q_L + Q_B) C_{L,1} = 0 \end{aligned} \quad [3.13]$$

For  $2 \leq j \leq N_{BFCM}-1$ :

$$\begin{aligned} (Q_L + Q_B) C_{L,j-1} + Q_B C_{L,j+1} + k_L a (C_{L,j}^* - C_{L,j}) \frac{V}{N_{BFCM}} \\ - k_w C_{L,j} \epsilon_L \frac{V}{N_{BFCM}} - (Q_L + 2Q_B) C_{L,j} = 0 \end{aligned} \quad [3.14]$$

For  $j = N_{\text{BFCM}}$ :

$$\begin{aligned} (Q_L + Q_B)C_{L,N_{\text{BFCM}}-1} + k_L a (C_{L,N_{\text{BFCM}}}^* - C_{L,N_{\text{BFCM}}}) \frac{V}{N_{\text{BFCM}}} \\ - k_w C_{L,N_{\text{BFCM}}} \varepsilon_L \frac{V}{N_{\text{BFCM}}} - (Q_L + Q_B)C_{L,N_{\text{BFCM}}} = 0 \end{aligned} \quad [3.15]$$

For cell number  $j$ , and for the gaseous ozone and total gas respectively, the basic mass balance leads to the following equations:

$$Q_{G,j-1}C_{G,j-1} - Q_{G,j}C_{G,j} - k_L a (C_{L,j}^* - C_{L,j}) \frac{V}{N_{\text{BFCM}}} = 0 \quad [3.16]$$

$$Q_{G,j-1}C_{T,j-1} - Q_{G,j}C_{T,j} - k_L a (C_{L,j}^* - C_{L,j}) \frac{V}{N_{\text{BFCM}}} = 0 \quad [3.17]$$

The hydrostatic head  $P_j$  in the column decreases linearly with the depth  $l$  assuming that the change in the liquid hold-up is negligible, therefore:

$$P_j = P_T + \rho g \varepsilon_L \left( 1 - \frac{j-0.5}{N_{\text{BFCM}}} \right) L = P_o [1 + \alpha(j-0.5)] \quad [3.18]$$

where  $\alpha$  is defined by Equation 3.22. The equilibrium concentration ( $C_{L,j}^*$ ) is given by:

$$C_{L,j}^* = \frac{P_j}{H} y_j \quad [3.19]$$

The gaseous ozone concentration ( $C_{G,j}$ ) and the total gas concentration ( $C_{T,j}$ ) respectively, are given by:

$$C_{G,j} = \frac{P_j y_j}{RT} \quad [3.20]$$

$$C_{T,j} = \frac{P_j}{RT} \quad [3.21]$$

Introducing the following dimensionless terms into Equations 3.13 to 3.17:

$$\alpha = \frac{-\rho g \epsilon_L L}{N_{BFCM} P_0} \quad [3.22]$$

$$r = \frac{Q_B}{Q_L} \quad [3.23]$$

$$St_L = \frac{k_L a L}{N_{BFCM} u_L} \quad [3.24]$$

$$St_G = \frac{k_L a L}{N_{BFCM} u_{G,0}} \frac{RT}{H} \quad [3.25]$$

$$D_a = \frac{k_w \epsilon_L L}{N_{BFCM} u_L} \quad [3.26]$$

$$X_j = \frac{C_{L,j}}{C_{L,0}^*} \quad [3.27]$$

$$Y_j = \frac{y_j}{y_0} \quad [3.28]$$

$$q_{G,j} = \frac{Q_{G,j}}{Q_{G,0}} \quad [3.29]$$

and rearranging the resultant equations, yields the steady-state BFCM equations. For dissolved ozone and  $j = 1$ :

$$X_0 - (1 + r + D_a + St_L)X_1 + rX_2 + St_L \left(1 + \frac{\alpha}{2}\right)Y_1 = 0 \quad [3.30]$$

For  $2 \leq j \leq N_{\text{BFCM}} - 1$ :

$$(1 + r)X_{j-1} - (1 + 2r + D_a + St_L)X_j + rX_{j+1} + St_L [1 + \alpha(j - 0.5)]Y_j = 0 \quad [3.31]$$

For  $j = N_{\text{BFCM}}$ :

$$(1 + r)X_{N_{\text{BFCM}}-1} - (1 + r + D_a + St_L)X_{N_{\text{BFCM}}} + St_L [1 + \alpha(N_{\text{BFCM}} - 0.5)]Y_{N_{\text{BFCM}}} = 0 \quad [3.32]$$

For gaseous ozone and cell number  $j$ :

$$(1 + \alpha(j - 1.5))q_{G,j-1} Y_{j-1} - (1 + \alpha(j - 0.5))q_{G,j} Y_j - St_G [(1 + \alpha(j - 0.5))Y_j - X_j] = 0 \quad [3.33]$$

For total gas and cell number  $j$ :

$$(1 + \alpha(j - 1.5))q_{G,j-1} - (1 + \alpha(j - 0.5))q_{G,j} - St_G y_0 [(1 + \alpha(j - 0.5))Y_j - X_j] = 0 \quad [3.34]$$

Based on the definitions of variables (Equations 27 to 29), the zero-index variables are:

$$X_0 = \frac{C_{L,0}}{C_{L,0}^*} \quad [3.35]$$

$$Y_0 = 1 \quad [3.36]$$

$$q_{G,0} = 1 \quad [3.37]$$

A similar approach could be used to derive the equations for the counter-current flow mode. Equations 3.30 to 3.34 represent the steady-state BFCM for two-phase ozone absorption in surface waters systems and can be used to predict the performance of bubble columns as long as the operating parameters ( $Pe_L$ ,  $St_L$ ,  $St_G$ ,  $D_a$ ,  $\alpha$ , and  $y_0$ ) are specified.

### 3.4 RESULTS AND DISCUSSION

#### 3.4.1 Transient BFCM

The system of Equations 3.8, 3.10, and 3.11 was solved, for  $N_{BFCM} = 10$  and  $Pe_L$  ranging from 1 to 20, to examine the effect of  $Pe_L$  or  $r$  on the theoretical RTD. As shown in Figure 3.2, as  $Pe_L$  increases, the RTD at the bottom port narrows as the liquid phase flow conditions are approaching plug flow. The effect of  $Pe_L$  on RTD at the top sampling port is shown in Figure 3.3. As  $Pe_L$  increases, the RTD narrows and becomes more symmetrical and the peak increases as well, suggesting that the liquid flow conditions are approaching plug flow.

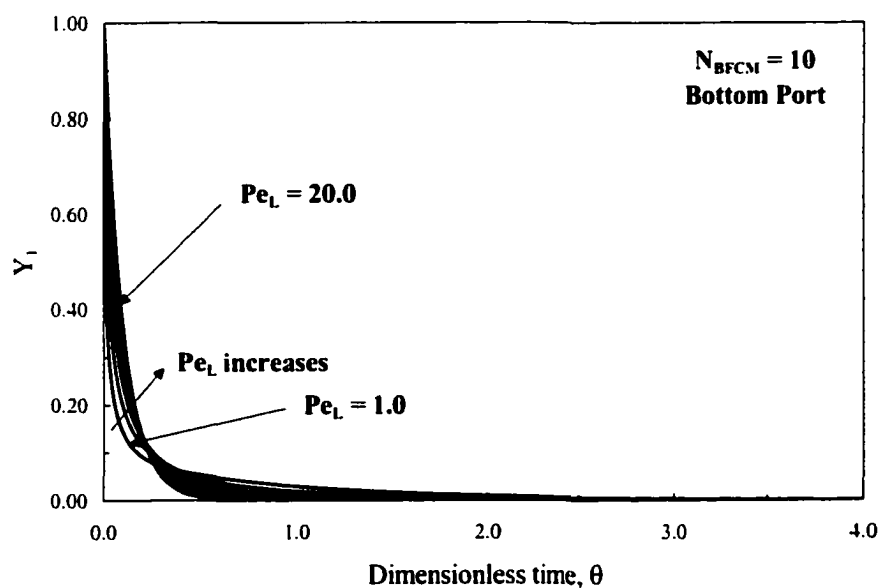


Figure 3.2 Theoretical RTD's for  $N_{BFCM} = 10$  at the bottom sampling port.

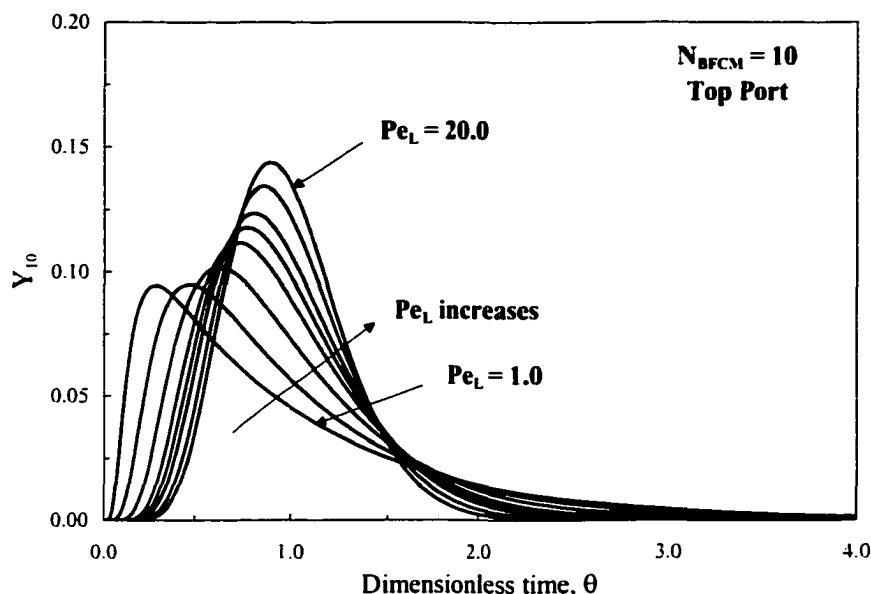


Figure 3.3 Theoretical RTD's for  $N_{BFCM} = 10$  at the top sampling port.

### 3.4.2 Steady-state BFCM

The predictions of the steady-state BFCM were tested using the pilot-scale experimental data of Zhou (1995). The bubble column used in the experiments was a cylindrical glass column with an inside diameter of 100 mm and a height of 2,000 mm. The water depth was kept constant at 1,750 mm. The gas sparger used was a 25 mm spherical fused crystalline aluminum stone. The water samples were withdrawn from six bell-shaped sampling taps that were installed at equal intervals along the column height. The operating conditions for the co-current and counter-current flow modes are shown in Tables 3.1 and 3.2 respectively.

Table 3.1 Operating conditions for the co-current flow mode.

Case #	$N_{BFCM}$	$Pe_L$	$r$	$\alpha$	$St_L$	$St_G$	$D_s$	$y_0$	$C_{L,0}$ (mgL <sup>-1</sup> )
DW4	10	34.48	-0.21	-0.014	0.024	0.125	0.006	0.013	7.20
DW5	10	17.86	0.06	-0.014	0.176	0.126	0.006	0.002	0.92
DW9	10	4.63	1.66	-0.014	0.024	0.008	0.014	0.002	0.88

Table 3.2 Operating conditions for the counter-current flow mode.

Case #	$N_{\text{BFCM}}$	$Pe_L$	$r$	$\alpha$	$St_L$	$St_G$	$D_a$	$y_0$	$C_{L,0}$ (mgL <sup>-1</sup> )
DW17	10	10.53	0.45	-0.014	0.056	0.112	0.014	0.010	5.56
DW18	10	5.35	1.37	-0.014	0.379	0.130	0.014	0.002	0.92

The number of completely mixed cells ( $N_{\text{BFCM}}$ ) was set equal to 10. A pseudo-first-order specific ozone utilization rate constant was assumed to equal  $4.7 \times 10^{-4} \text{ s}^{-1}$  for deionized water based on the measurements of Zhou (1995). Steady-state BFCM equations (Equations 3.30 to 3.34) were solved numerically using Newton Raphson technique by utilizing the TKSOLVER™ software. The program executed until a user-specified comparison tolerance of  $10^{-6}$  was satisfied. The program execution time was less than 1 s using a 366 MHz processor.

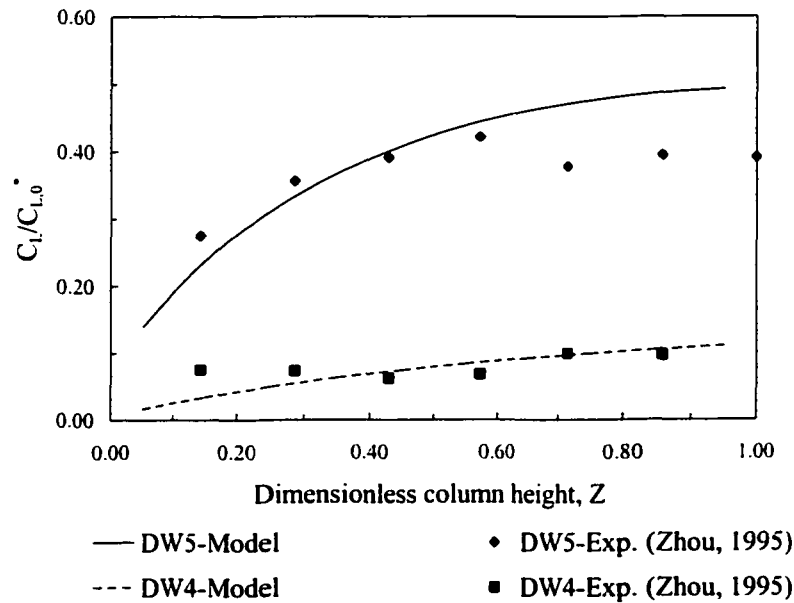


Figure 3.4 Steady-state BFCM testing for co-current flow mode.

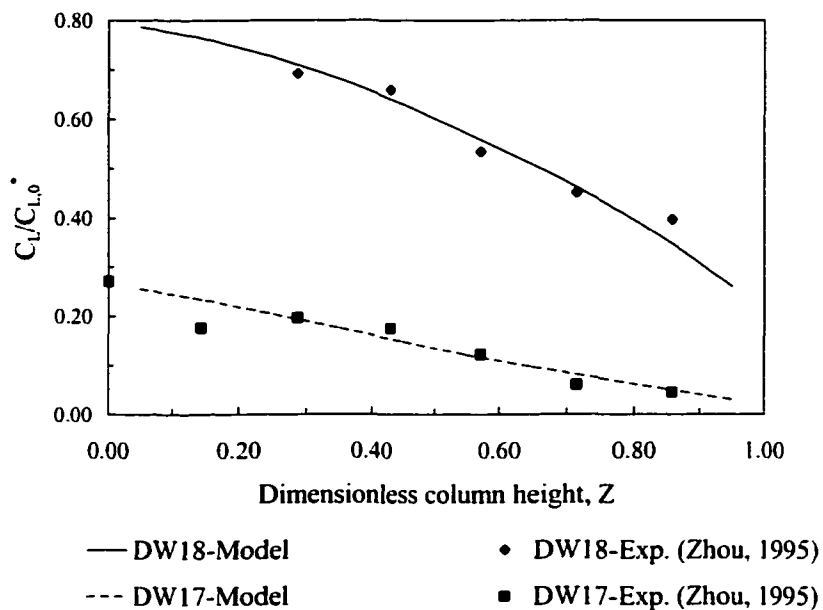


Figure 3.5 Steady-state BFCM testing for counter-current flow mode.

Figures 3.4 and 3.5 illustrate the applicability of the steady-state BFCM to describe the performance of an ozone bubble column that utilizes diffusers as the gas spargers in the co and counter-current flow modes, respectively. As shown, there was good agreement between the experimental dissolved ozone profiles and the predicted ozone profiles, except for few data points, where there was small deviation between the measured and the predicted dissolved ozone concentrations.

### 3.5 CONCLUSIONS

The steady-state BFCM has proven to provide good predictions of the performance of a pilot-scale fine-diffuser ozone bubble column. The model predictions should be further tested for different designs and scales of ozone bubble columns and under different operating conditions. Also, the model should be further expanded to account for variable mass transfer coefficient along the height bubble column for special bubble column designs where the mass transfer process is enhanced near the entrance of the contactor rather than along the entire column height.

### 3.6 REFERENCES

1. Alvarez-Cuenca, M. and M.A. Nerenberg, "Oxygen Mass Transfer in Bubble Columns Working at Large Gas and Liquid Flow Rates", *AIChE J.* 27(1): 66-73 (1981).
2. Alvarez-Cuenca, M., C.G.J. Baker, and M.A. Bergougnou, "Oxygen Mass Transfer in Bubble Columns", *Chem. Eng. Sci.* 35: 1121-1127 (1980).
3. Beltrán, F.J., J.F. García-Araya, and J.M. Encinar, "Henry and Mass Transfer Coefficients in the Ozonation of Wastewaters", *Ozone Sci. & Eng.* 19: 281-296 (1997).
4. Chang, B.-J. and E.S.K. Chian, "A Model Study of Ozone-Sparged Vessels for the Removal of Organics from Water", *Wat. Res.* 15: 929-936 (1981).
5. Danckwerts, P.V., *Gas-Liquid Reactions* (NY, USA: McGraw-Hill, Inc., 1970).
6. Hoigné, J., "Mechanisms, Rates and Selectivities of Oxidants of Organic Compounds Initiated by Ozonation in Water", *Handbook of Ozone Technology and Applications* (MI, USA: Ann Arbor Science Publishers, 1982).
7. Hull, C.S., P.C. Singer, K. Saravanan, and C.T. Miller, "Ozone Mass Transfer and Reaction: Completely Mixed Systems", *Proc. of the Annual AWWA Conf.: Water Quality*, Vancouver, BC, Canada, 1992.
8. Johnson, P.N. and R.A. Davis, "Diffusivity of Ozone in Water", *J. Chem. Eng. Data* 41: 1485-1487 (1996).
9. Laplanche, A., N. Le Sauze, G. Martin, and B. Langlais, "Simulation of Ozone Transfer in Water: Comparison with a Pilot Unit", *Ozone Sci. & Eng.* 13(5): 13, 535-558 (1991).
10. Levenspiel, O., *Chemical Reaction Engineering, 2<sup>nd</sup> ed.* (NY, USA: John Wiley and Sons, Inc., 1972).
11. Lev, O. and S. Regli, "Evaluation of Ozone Disinfection Systems: Characteristic Contact Time T", *J. Environ. Eng., ASCE* 118(2): 268-285 (1992).
12. Mecklenburgh, J.C. and S. Hartland, *The Theory of Backmixing*, (New York, NY, USA: John Wiley and Sons, Inc., 1975), pp. 1-32.

13. Oke, N.J., D.W. Smith, and H. Zhou, "An Empirical Analysis of Ozone Decay Kinetics in Natural Waters", *Ozone Sci. & Eng.* 20: 361-379 (1998).
14. TKSOLVER™, Release 3.32, Universal Technical Systems, Inc., IL, USA (1997).
15. Yurteri, C. and M.D. Gurol, "Ozone Consumption in Natural Waters: Effects of Background Organic Matter, pH and Carbonate Species", *Ozone Sci. & Eng.* 10: 277-290 (1988).
16. Zhou, H., *Investigation of Ozone Disinfection Kinetics and Contactor Performance Modeling: Ph.D. Thesis* (Edmonton, AB, Canada: University of Alberta, 1995).
17. Zhou, H., D.W. Smith, and S.J. Stanley, "Modeling of Dissolved Ozone Concentration Profiles in Bubble Columns", *J. Environ. Eng., ASCE* 120(4): 821-840 (1994).

## **CHAPTER 4. TWO-PHASE NON-ISOBARIC AXIAL DISPERSION MODELS FOR MODELING THE OZONATION PROCESS DYNAMICS–I. MODELS DEVELOPMENT**

### **4.1 INTRODUCTION**

#### **4.1.1 Ozonation Process Dynamics**

Ozonation of water and wastewater has been focused on, over the past two decades, as an advanced oxidation process (AOP) alternative for water and wastewater treatment. During ozonation of water and wastewater, it is important to quantify the dissolved and gaseous ozone concentrations in order to evaluate the effectiveness of the ozonation process. Regarding wastewater ozone treatment applications, the experimental data of Zhou and Smith (2000, 1997) showed that the ozonation of Kraft pulp mill effluents is a dynamic process. As a result, the enhanced overall mass transfer coefficient ( $Ek_{La}$ ), the induced enhancement factor ( $E$ ) of the fast or instantaneous chemical reactions, the reaction rate constant ( $k_w$ ) between ozone and the liquid-phase impurities, mainly organic compounds, were dependent on the amount of the utilized ozone. Also, the reduction efficiencies of color, AOX (absorbable organic halides), TOC (total organic carbon), and COD (chemical oxygen demand) varied over the course of ozonation. As the amount of the utilized ozone increases,  $Ek_{La}$  and  $k_w$  will decrease gradually after most of the highly reactive organic compounds are depleted. As the ozonation treatment proceeds, the color and AOX reduction efficiencies will decline gradually (Zhou and Smith, (2000, 1997).

#### **4.1.2 Bubble Column Parameters**

It is becoming more important to develop more efficient, accurate, and reliable models that can be used for describing the performance of ozone contactors to reduce the operating costs and to insure that the treatment objectives are met. By applying the appropriate design models, optimized designs and operating conditions of both the ozone contactors and the ozone off-gas destruction facilities can be achieved. The number of process variables, that affect the performance of ozone contactors, is large and obtaining

accurate estimates of those variables becomes a difficult task, especially, in situations where ozonation is carried out in complex chemical systems such as Kraft pulp mill effluents. Those process variables, that are dependent on the ozonation process operating conditions, can be estimated by applying simple mathematical models. Some of the process variables are influenced by the ozone contactor configuration, the type of the gas sparging technique, and the chemical composition of the treated liquid phase (Deckwer, 1976). Those variables include: the gas and liquid hold-ups; the enhanced overall mass transfer coefficient; the enhancement factor; the gas bubbles' specific interfacial area; and the backmixing coefficient.

#### 4.1.3 Dispersion Models for Two-Phase Flows

It is well known that in non-ideal flow conditions that exist in bubble columns, applying inappropriate design models can lead to significant lowering of the treatment efficiency of the bubble column. A large number of those models were based on one of the following two liquid-phase flow regimes' assumptions: (1) complete mixing flow regime; or (2) ideal plug flow regime. Although, the actual flow pattern in bubble columns is usually closer to the completely mixed flow regime rather than the plug flow regime (Zhou, 1995).

The objective of this chapter was to present more accurate two-phase axial dispersion models (2P-ADM's) for describing the performance of ozone bubble columns. Those dispersion models take into consideration the opposite effects of shrinkage of the gas phase caused by ozone gas absorption and ozone auto-decomposition. Those models also consider the gas-phase expansion caused by the reduced hydrostatic head. As a result, the superficial gas velocity will be considered to vary along the column height and ozone bubble columns will be dealt with as non-isobaric two-phase systems.

In bubble columns with small aspect ( $L/D$ ) ratios, the order of magnitude of the gas phase dispersion coefficient ( $D_G$ ) can be comparable to that of the liquid phase dispersion coefficient ( $D_L$ ) (Deckwer, 1976). Therefore, during the development of the two-phase

axial dispersion models (2P-ADM's), two conditions were considered:  $D_G = D_L/10$ , and  $D_G = D_L$ . The low-end of the gas-phase dispersion coefficient represents situations where gas bubbles are relatively large and due to their high buoyancy, they can rise inside the columns with high velocities but still those bubbles will be partially backmixed. Meanwhile, the high gas-phase dispersion coefficient represents situations where gas bubbles are relatively small and their buoyancy is relatively small. As a result, the gas phase can be assumed to be backmixed to a large extent and since the small bubbles are recirculated along with the liquid phase recirculation, it is assumed that their backmixing coefficient can be equal to that of the liquid phase (Shetty *et al.*, 1992). In the other type of the dispersion models, the gas phase is assumed to follow an ideal plug flow regime, and hence, the gas phase dispersion will be neglected in the development the model equations, i.e.,  $D_G = 0$ . This condition can be reasonably valid in bubble columns with large aspect ratios.

The most computationally efficient mechanistic models are those, for which, closed-form analytical solutions can be obtained. Unfortunately, for adequate and accurate description of the performance of bubble columns, dispersion models are needed and the analytical solutions of the equations representing those models are not available due to their complex construction. Those models are represented by non-linear differential equations that have to be solved simultaneously via numerical techniques.

## 4.2 PROCESSES FUNDAMENTALS

### 4.2.1 Slow-Chemical-Reaction-Kinetics-Regime Systems

During the ozonation of surface waters, the chemical reactions between the dissolved ozone and the organic and inorganic constituents in the liquid phase are considered to be in the slow-reaction-kinetics regime (Zhou *et al.*, 1994; Gamal El-Din and Smith, 2000). In order to describe the backmixing in the liquid phase, a diffusion-like process is assumed and superimposed on plug flow (Levenspiel, 1972). An empirical Fick's law is applied by replacing the molecular diffusion coefficient by the axial

dispersion coefficient ( $D_L$ ) as the mixing parameter in which the effects of the shear dispersion, molecular and eddy diffusivities are lumped together:

$$\text{Diffusive liquid-phase mass flux} = -D_L \frac{\partial C_L}{\partial \ell} \quad [4.1]$$

where:  $C_L$  = dissolved ozone concentration ( $\text{mgL}^{-1}$ ) and  $D_L$  = liquid-phase axial dispersion coefficient ( $\text{m}^2\text{s}^{-1}$ ). After a comprehensive review of the literature, it was found that the dispersion models that are applied to describe the performance of ozone bubble columns are based on the assumption that the gas phase follows an ideal plug flow regime and therefore, the gas phase backmixing was neglected. Development of new theoretically-based models such as the axial dispersion models that account for the backmixing in the liquid and gas phases simultaneously can lead to a great progress in the area of the design of ozone bubble columns. Deckwer (1976) suggested that the performance of bubble columns could be affected by the gas phase dispersion in columns with diameters greater than 500 mm. Although in columns with small diameters the assumption of the gas phase being in an ideal plug flow regime can be valid (Wachi and Morikawa, 1987), gas phase dispersion can be a significant factor in the ozonation process scale-up. In homogeneous bubble flow regimes, the bubble sizes are relatively small and their buoyancy is low and therefore, they are assumed to be backmixed (Shetty *et al.*, 1992). Gas phase backmixing can be measured experimentally using several techniques such as gas disengaging technique (GDT) or thermal conductivity detectors (TCD), etc. In those techniques, gases of low solubility such as helium are used as the tracer gases. There are several models, available in the literature, that can be used to estimate the gas phase backmixing (Towell and Ackermann 1972; Mangartz and Pilhofer, 1981; Wachi and Nojima, 1990). In most of those models, the gas phase backmixing is mainly dependent on the superficial gas velocity and the column diameter. In order to describe the backmixing in the gas phase, a diffusion-like process is assumed and superimposed on plug flow and Fick's law is applied by replacing the molecular diffusion coefficient by the axial dispersion coefficient ( $D_G$ ) as the mixing parameter:

$$\text{Diffusive gas-phase mass flux} = -D_G \frac{\partial C_G}{\partial \ell} \quad [4.2]$$

where:  $C_G$  = gaseous ozone concentration ( $\text{mgL}^{-1}$ ) and  $D_G$  = gas-phase axial dispersion coefficient ( $\text{m}^2\text{s}^{-1}$ ).

The overall ozone auto-decomposition process was represented by the modified pseudo-first-order rate expression as recommended by Oke. *et al.* (1998). The two-film model was applied to describe the ozone gas absorption in water. Assuming that no chemical reactions, between the dissolved gas and any constituents present in the liquid phase, occur during the mass transfer process, the gas-absorption rate ( $\psi$ ) is defined as:

$$\psi = k_L a (C_L^* - C_L) \quad [4.3]$$

where:  $\psi$  = gas-absorption rate ( $\text{mgL}^{-1}\text{s}^{-1}$ ),  $k_L$  = local liquid mass transfer coefficient ( $\text{ms}^{-1}$ ),  $a$  = gas bubbles' specific interfacial area ( $\text{m}^{-1}$ ),  $C_L^*$  = concentration of the dissolved ozone in equilibrium with the bulk ozone gas ( $\text{mgL}^{-1}$ ), and  $C_L$  = concentration of the dissolved ozone in the bulk liquid ( $\text{mgL}^{-1}$ ).

#### 4.2.2 Fast-Chemical-Reaction-Kinetics-Regime Systems

The backmixing in the liquid and gas phases are also represented by Equations 4.1 and 4.2, respectively. Chemical reactions occur during the ozonation of wastewater. In such applications, the dimensionless squared Hatta number ( $H_a^2 = M$ ) is often applied to compare between the amount of dissolved gas that reacts at the gas-liquid interface or in the liquid film near the interface and the amount of dissolved gas that reaches the bulk liquid in an unreacted state:

$$H_a^2 = E^2 = M = \frac{D_{O_3} k_w}{k_L^2} \quad [4.4]$$

where:  $H_a = E = \sqrt{M}$  = dimensionless Hatta number,  $k_L$  = local mass transfer coefficient ( $\text{ms}^{-1}$ ),  $D_{O_3}$  = molecular diffusivity of ozone gas in water ( $\text{m}^2\text{s}^{-1}$ ), and  $k_w$  = specific ozone utilization rate constant ( $\text{s}^{-1}$ ). For pseudo-first-order irreversible reactions, the location of those reactions that take place during the gas absorption process could be classified into two categories (Kramers and Westertrep, 1963; Kaštánek *et al.*, 1993). Reactions would take place in the bulk of the liquid or at the gas-liquid interface and/or in the liquid film near the interface at  $H_a < 0.03$  and  $H_a > 5.00$ , respectively (Kramers and Westertrep, 1963; Kaštánek *et al.*, 1993). Although, generally for bubble columns it can also be assumed that at that at  $H_a > 3.00$ , reactions would still be fast enough to occur predominantly at the gas-liquid interface and/or in the liquid film near the interface (Kaštánek *et al.*, 1993). Therefore, reactions would simultaneously take place in both regions at  $0.03 < H_a < 3.00$ . Equation 4.4 is only applicable in situations where two conditions have to be satisfied: (1)  $\sqrt{M} \gg 1$ ; and (2) fast or instantaneous irreversible first-order reactions with no bulk liquid concentration where the driving force for the mass transfer process will be maximized (Danckwerts, 1970). As a result, Equation 4.3 becomes:

$$\psi = Ek_L a C_L^* \quad [4.5]$$

where:  $Ek_L a$  = enhanced overall mass transfer coefficient ( $\text{s}^{-1}$ ). Zhou and Smith (1999) proposed that for wastewater ozonation, both the ozone auto-decomposition and its reactions with the organic and inorganic constituents in wastewater could be lumped together in a first-order rate constant ( $k_w$ ). Danckwerts (1970) proposed the following equation for the conditions when  $M > 0$  and  $C_L > 0$ :

$$\psi = k_L a \sqrt{1+M} \left( C_L^* - \frac{C_L}{1+M} \right) \quad [4.6]$$

When  $M \gg 1$  and  $C_L$  approaches zero (i.e.,  $C_L \cong 0$ ), Equation 4.6 reduces to Equation 4.5. The effects of chemical reactions on the local mass transfer coefficient for an

irreversible first-order reaction could be neglected and the gas absorption could be dealt with as pure physical absorption when  $M$  approaches zero (Danckwerts, 1970). Therefore, this assumption is valid when:

$$H_a^2 = E^2 = M = \frac{D_{O_3} k_w}{k_L^2} \ll 1 \quad [4.7]$$

$k_w$  was reported to be  $4.7 \times 10^{-4} \text{ s}^{-1}$  for the deionized water tested by Zhou (1995). Yurteri and Gurol (1988) reported that  $k_w$  was in the order of  $2.8 \times 10^{-3} \text{ s}^{-1}$  for the tested raw surface water. The diffusivity of ozone in water was determined by the Wilke-Chang formula to be  $1.74 \times 10^{-9} \text{ m}^2\text{s}^{-1}$  (at  $20 \text{ }^\circ\text{C}$ ) which is comparable to the value of  $1.71 \times 10^{-9} \text{ m}^2\text{s}^{-1}$  obtained using the equation recommended by Johnson and Davis (1996).  $k_L$  was reported to be in the order of  $3.1 \times 10^{-4} \text{ ms}^{-1}$  for clean water and in the order of  $1.9 \times 10^{-4} \text{ ms}^{-1}$  for water containing organic substances (Beltrán *et al.*, 1997). Substituting for these typical values of  $D$ ,  $k_w$ , and  $k_L$  into Equation 4.4 yields squared-Hatta numbers of  $8.5 \times 10^{-6}$  and  $1.4 \times 10^{-4}$  for the deionized and the surface water, respectively. Based on these small Hatta numbers, it can be concluded that the chemical reactions that occur during the course of clean or surface water ozonation has negligible effect on the local mass transfer coefficient and hence, Equation 4.3 will be applied for ozone absorption without any modification.

#### 4.3 DEVELOPMENT OF THE TWO-PHASE AXIAL DISPERSION MODEL (2P-ADM) EQUATIONS

When modeling a two-phase flow, the assumptions that govern the two-phase axial dispersion model (2P-ADM) are: (1) backmixing (i.e., dispersion) occurs in the liquid and gas phases; (2) ozone bubble column is operated at constant liquid and gas flowrates; (3) gas hold-up and gas bubbles' specific interfacial area are constant along the column height; (4) ozone mass transfer resistance for the ozone absorption is confined to the liquid side alone; (5) the enhancement factor ( $E$ ) of the mass transfer due to the occurrence of chemical reactions was assumed to be 1 (i.e.,  $M = 0$ ) as the absorption of

ozone in water treatment could be considered in the slow-reaction-kinetics regime and for wastewater the fast-reaction regime was assumed to prevail and the enhancement factor was assumed to be higher than 1 (i.e.,  $M > 0$ ); (6) steady-state isothermal operation for the liquid and gas phases; (7) Henry's law applies; (8) other air constituents are assumed to be inert gases; (9) local mass transfer coefficient ( $k_L$ ) is constant along the column height; (10) owing to the hydrostatic head, the total pressure ( $P$ ) varies linearly with the column height; (11) superficial gas velocity is variable due to ozone gas absorption and depletion, and hydrostatic pressure decrease along the column height; and (12) overall ozone auto-decomposition rate is assumed to follow a pseudo-first-order expression in the liquid phase, whereas negligible in the gas phase.

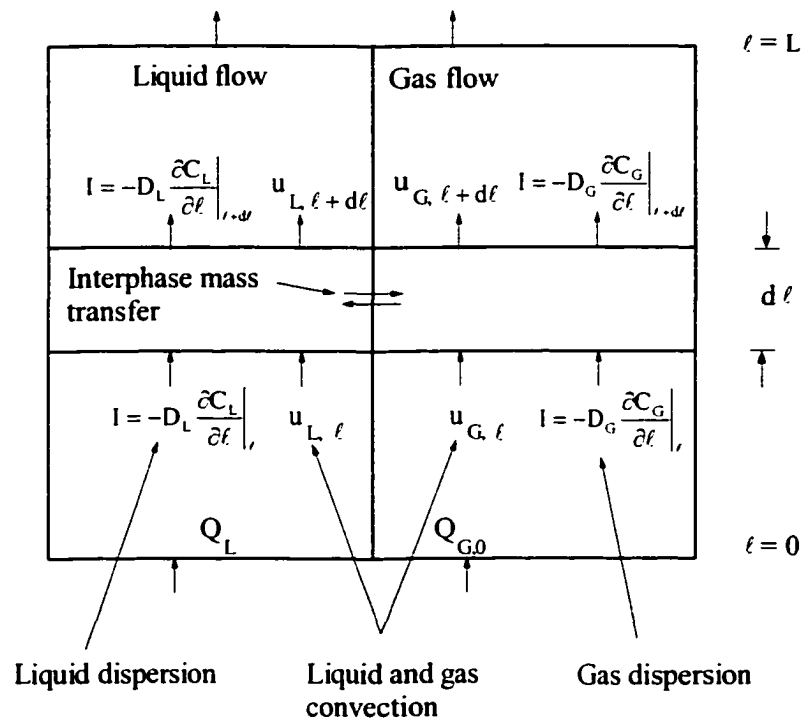


Figure 4.1 Schematic representation of the co-current axial dispersion model.

### 4.3.1 Considering the Gas-Phase Dispersion

#### 4.3.1.1 Wastewater Treatment Conditions

Considering the control volume shown in Figure 4.1 and conducting mass balance of the liquid and gas phases for wastewater treatment and steady-state conditions, yields:

$$\frac{d^2 C_{L,f}}{d\ell^2} D_L \varepsilon_L + a' u_L \frac{dC_{L,f}}{d\ell} + k_L a \sqrt{1+M} \left( C_{L,f}^* - \frac{C_{L,f}}{1+M} \right) - k_w C_{L,f} \varepsilon_L = 0 \quad [4.8]$$

$$\frac{d^2 C_{G,f}}{d\ell^2} D_G \varepsilon_G - \frac{d(u_{G,f} C_{G,f})}{d\ell} - k_L a \sqrt{1+M} \left( C_{L,f}^* - \frac{C_{L,f}}{1+M} \right) = 0 \quad [4.9]$$

where:  $a'$  is an identifier of the liquid phase flow direction.  $a' = +1$  for counter-current flow conditions and  $a' = -1$  for co-current flow conditions. Equations 4.8 and 4.9 are the steady-state mass balance equations for the liquid and gas phases, respectively. The relationships of  $P_r$ ,  $P_0$ ,  $C_{L,r}^*$ , and  $C_{L,0}^*$  are as follows:

$$P_r = P_T + \rho g \varepsilon_L (L - \ell) \quad [4.10]$$

$$P_0 = P_T + \rho g \varepsilon_L L \quad [4.11]$$

$$C_{L,r}^* = \frac{P_T + \rho g \varepsilon_L (L - \ell)}{H} y_r \quad [4.12]$$

$$C_{L,0}^* = \frac{P_T + \rho g \varepsilon_L L}{H} y_0 \quad [4.13]$$

From Equations 4.10 and 4.11, it can be seen that the hydrostatic head pressure ( $P$ ) is assumed to decrease linearly with the column depth ( $\ell$ ). In order to account for the dependency of the superficial gas velocity ( $u_{G,r}$ ) on the column depth, a mass balance of the inert gas phase constituents is considered. Since the concentration of ozone in the gas phase is usually small, the total amount of the gas will not be decreased significantly along the column height. Thus, the mass balance of the inert gas phase constituents yields:

$$\frac{d^2 C_{n,r}}{d\ell^2} D_G \varepsilon_G - \frac{d(u_{G,r} C_{n,r})}{d\ell} = 0 \quad [4.14]$$

where:  $C_{n,i}$  = concentration of the inert constituents in the gas phase and it can be described as follows by:

$$C_{n,i} = \frac{n_{n,i}}{V} = \frac{P_{n,i}}{RT} = \frac{P_i(1-y_i)}{RT} \quad [4.15]$$

Therefore, substituting for Equation 4.15 into Equation 4.14 yields:

$$\frac{d^2}{d\ell^2} \left[ \frac{P_i(1-y_i)}{RT} \right] D_G \epsilon_G - \frac{d}{d\ell} \left[ \frac{u_{G,i} P_i(1-y_i)}{RT} \right] = 0 \quad [4.16]$$

The ozone gas concentration ( $C_{G,i}$ ) is represented by:

$$C_{G,i} = \frac{n_{o_3,i}}{V} = \frac{P_T + \rho g \epsilon_L (L - \ell)}{RT} y_i \quad [4.17]$$

The partial pressure of the liquid vapour in the gas phase was assumed to be negligible with respect to the total pressure. Introducing the following dimensionless quantities:

$$Z = \frac{\ell}{L} \quad [4.18]$$

$$\alpha = \frac{\rho g \epsilon_L L}{P_T} \quad [4.19]$$

$$\beta = 1 + \alpha \quad [4.20]$$

$$Pe_L = \frac{u_L L}{D_L \epsilon_L} \quad [4.21]$$

$$Pe_G = \frac{u_{G,0} L}{D_G \epsilon_G} \quad [4.22]$$

$$St_L = \frac{k_L a L}{u_L} \quad [4.23]$$

$$St_G = \frac{k_L a L}{u_{G,0}} \frac{RT}{H} \quad [4.24]$$

$$D_s = \frac{k_w \epsilon_L L}{u_L} \quad [4.25]$$

$$X = \frac{C_{L,r}}{C_{L,0}} = \frac{C_{L,r}}{(P_T + \rho g \epsilon_L L) y_0} \frac{H}{P_T} = \frac{C_{L,r} H}{P_T (1 + \alpha) y_0} \quad [4.26]$$

$$Y = \frac{y_r}{y_0} \quad [4.27]$$

and

$$U = \frac{u_{G,r}}{u_{G,0}} \quad [4.28]$$

where:  $y_0$  = inlet ozone molar fraction in the gas phase and  $u_{G,0}$  = inlet superficial gas velocity at  $\ell = 0$ . Equations 4.18, 4.19, and 4.20 are substituted into Equations 4.10, 4.12, and 4.17. Then, the resultant equations and the dimensionless quantities are substituted into Equations 4.8, 4.9, and 4.16. Simplifying and rearranging the resultant equations gives:

$$\frac{1}{Pe_L} \frac{d^2 X}{dZ^2} + a' \frac{dX}{dZ} + \frac{St_L \sqrt{1+M}}{\beta} (\beta - \alpha Z) Y - \left( \frac{St_L}{\sqrt{1+M}} + D_s \right) X = 0 \quad [4.29]$$

$$\frac{1}{Pe_G} \frac{d^2 Y}{dZ^2} - \left( \frac{2\alpha}{(\beta - \alpha Z) Pe_G} + U \right) \frac{dY}{dZ} = \sqrt{1+M} St_G Y (1 - y_0 Y) - \frac{St_G \beta}{\sqrt{1+M}(\beta - \alpha Z)} X (1 - y_0 Y) \quad [4.30]$$

$$\frac{dU}{dZ} = \frac{\alpha}{(\beta - \alpha Z)} U - y_0 \sqrt{1+M} St_G Y + \frac{y_0 St_G \beta}{\sqrt{1+M}(\beta - \alpha Z)} X \quad [4.31]$$

Equations 4.29 and 4.30 represent the model equations of the ozone concentration in the liquid and gas phases, respectively. Equation 4.31 is a result of the mass balance of the gas-phase inert constituents and it represents the change in the superficial gas velocity with the column height. Equations 4.29, 4.30, and 4.31 are non-linear differential equations.

#### 4.3.1.2 Boundary Conditions

No special measurements are required for the boundary conditions except for the boundary condition at the column inlet where the inlet liquid and gas phases ozone concentrations ( $C_{L,inf}$  and  $y_0$ , respectively) have to be measured. The implementation of the boundary conditions follows logically from the physical basis of the model development approach. Assuming closed-closed boundary conditions and by referring to Figure 4.1, the mass balance of the ozone concentrations in the liquid and gas phases leads to the following boundary conditions. For the counter-current flow conditions ( $a' = +1$ ):

$$\left. \frac{dX}{dZ} \right|_{Z=0} = 0 \quad [4.32]$$

$$Y|_{Z=0} = Y_0 = 1 + \left. \frac{1}{Pe_G} \frac{dY}{dZ} \right|_{Z=0} \quad [4.33]$$

$$X|_{Z=1} = X_1 = X_{\text{inf}} - \frac{1}{\text{Pe}_L} \left. \frac{dX}{dZ} \right|_{Z=1} \quad [4.34]$$

$$\left. \frac{dY}{dZ} \right|_{Z=1} = 0 \quad [4.35]$$

For the co-current flow conditions ( $a' = -1$ ), the equations for the gas-phase boundary conditions are the same as those for the counter-current flow conditions. For the liquid phase, the equations, representing the boundary conditions, are:

$$X|_{Z=0} = X_0 = X_{\text{inf}} + \frac{1}{\text{Pe}_L} \left. \frac{dX}{dZ} \right|_{Z=0} \quad [4.36]$$

$$\left. \frac{dX}{dZ} \right|_{Z=1} = 0 \quad [4.37]$$

where:

$$X_{\text{inf}} = \frac{C_{L,\text{inf}}}{C_{L,0}} \quad [4.38]$$

The gas phase superficial velocity is assumed to increase continuously from the bottom to the top of the column with no occurrence of velocity jump at any point along the column height. Therefore the boundary condition with respect to the superficial gas velocity at the bottom of the column for the counter and co-current flow conditions is:

$$U|_{Z=0} = U_0 = 1 \quad [4.39]$$

### 4.3.2 Special Conditions of the Two-Phase Axial Dispersion Model (2P-ADM)

#### 4.3.2.1 Consideration of the Gas-Phase Dispersion (Water Treatment Conditions)

During the ozonation of surface water, the enhancement factor (E) is assumed to equal 1 (i.e.,  $M = 0$ ). As a result, the model equations (Equations 4.29, 4.30, and 4.31) reduce to:

$$\frac{1}{Pe_L} \frac{d^2X}{dZ^2} + a' \frac{dX}{dZ} + \frac{St_L}{\beta} (\beta - \alpha Z) Y - (St_L + D_s) X = 0 \quad [4.40]$$

$$\frac{1}{Pe_G} \frac{d^2Y}{dZ^2} - \left( \frac{2\alpha}{(\beta - \alpha Z) Pe_G} + U \right) \frac{dY}{dZ} = St_G Y (1 - y_0 Y) - \frac{St_G \beta}{(\beta - \alpha Z)} X (1 - y_0 Y) \quad [4.41]$$

$$\frac{dU}{dZ} = \frac{\alpha}{(\beta - \alpha Z)} U - y_0 St_G \left( Y - \frac{\beta}{(\beta - \alpha Z)} X \right) \quad [4.42]$$

Equations 4.40, 4.41, and 4.42 are non-linear differential equations and their boundary equations are also represented by Equations 4.32 to 4.39.

#### 4.3.2.2 Neglecting the Gas-Phase Dispersion

Neglecting the gas-phase backmixing, i.e., assuming that the gas phase follows in an ideal plug flow regime, the model equations reduce to a system of two non-linear differential equations. Those equations can be developed logically from the physical basis of the model development approach as done previously for the model that accounts for the gas phase backmixing. As a result, we can obtain the following model equations for wastewater treatment conditions:

$$\frac{1}{Pe_L} \frac{d^2 X}{dZ^2} + a' \frac{dX}{dZ} + \frac{St_L \sqrt{1+M}}{\beta} (\beta - \alpha Z) Y - \left( \frac{St_L}{\sqrt{1+M}} + D_3 \right) X = 0 \quad [4.43]$$

$$\frac{dY}{dZ} + \frac{St_G}{\beta(1-y_0)} (1-y_0 Y)^2 \left( \sqrt{1+M} (\beta - \alpha Z) Y - \frac{\beta}{\sqrt{1+M}} X \right) = 0 \quad [4.44]$$

The liquid-phase boundary equations for this system of equations are the same as for the model equations that consider the gas-phase backmixing. For the gas phase and since no backmixing is considered in the gas phase, the ozone concentration in the gas phase is assumed to decrease continuously from the bottom to the top of the column with no occurrence of concentration jump at any point along the column height. Therefore, the boundary condition with respect to the gas phase ozone concentration at the bottom of the column for the counter and co-current flow conditions is:

$$Y|_{Z=0} = Y_0 = 1 \quad [4.45]$$

In order to account for the dependency of the superficial gas velocity ( $u_{G,r}$ ) on the column depth ( $\ell$ ), a mass balance of the inert gas phase constituents is considered. Thus, the mass balance of the inert gas phase constituents yields:

$$\frac{d(u_{G,r} C_{n,r})}{d\ell} = 0 \quad [4.46]$$

Equation 4.46 is equivalent to:

$$u_{G,r} P_r (1 - y_r) = u_{G,0} P_0 (1 - y_0) \quad [4.47]$$

For the water treatment conditions, M is set equal to zero in Equations 4.43 and 4.44. With respect to the liquid and gas-phase boundary conditions, they are represented by the same equations used for the wastewater treatment conditions.

#### 4.4 NUMERICAL SOLUTION TECHNIQUE

The proposed models are 1-D-type models that are represented by systems of 2 or 3 non-linear differential equations. Those equations are interrelated and have to be solved simultaneously. Closed-form analytical solutions are not available for such systems of equations. Therefore, the finite difference technique was applied for the spatial discretization of the model differential equations. The backward (or upwind) difference scheme was applied to transform a system of non-linear differential equations into a system of non-linear algebraic equations that can be solved numerically using any of the available numerical solving algorithms such as Newton Raphson technique. The upwind difference scheme is shown in Figure 4.2.

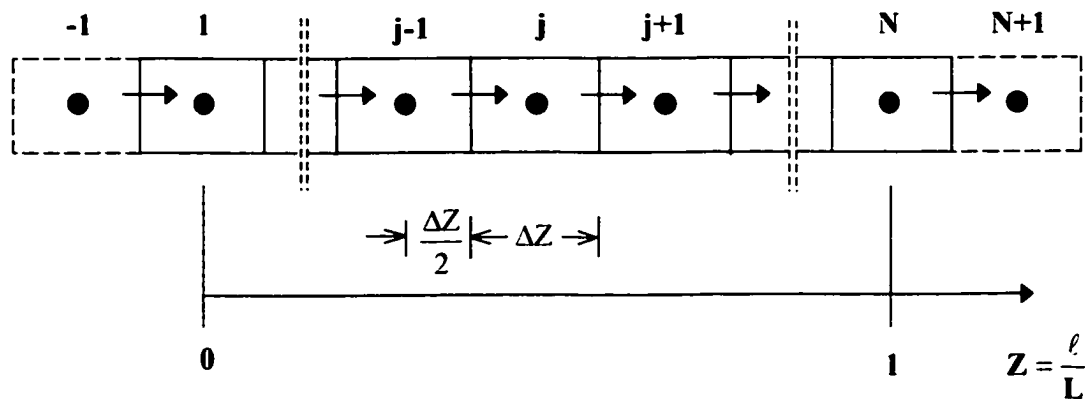


Figure 4.2 Computational upwind finite difference scheme.

In this scheme, the first and second-order derivatives, respectively, are defined as follows:

$$\left. \frac{dX}{dZ} \right|_j \cong \frac{X_j - X_{j-1}}{\Delta Z} \quad [4.48]$$

$$\left. \frac{d^2X}{dZ^2} \right|_j \cong \frac{X_{j+1} - 2X_j + X_{j-1}}{\Delta Z^2} \quad [4.49]$$

where:  $\Delta Z$  = the numerical dimensionless spatial step. It should be noted that the first-order derivatives representing the boundary conditions at  $Z = 0$  and  $1$  are defined using the centered-difference scheme since those boundary conditions are based on the dispersion term in the original mass balance equation. These first-order derivatives are defined as follows:

$$\left. \frac{dX}{dZ} \right|_{Z=0} \cong \frac{X_1 - X_{-1}}{2\Delta Z} \quad [4.50]$$

$$\left. \frac{dX}{dZ} \right|_{Z=1} \cong \frac{X_{N+1} - X_{N-1}}{2\Delta Z} \quad [4.51]$$

#### 4.4.1 2P-ADM With Gas-Phase Dispersion (Wastewater Treatment Conditions)

In the finite difference technique, a number of elements ( $N$ ) was assumed to represent the total column height ( $L$ ) and each element has a dimensionless length of ( $\Delta Z = 1/N$ ). As shown in Figure 4.2, two imaginary elements at  $j = -1$  and  $j = N+1$  were assumed for the numerical transformation of the differential boundary equations at the column boundaries. Referring to Figure 4.2 and applying the finite difference technique with the backward difference scheme, Equations 4.29, 4.30, and 4.31 were transformed into a system of three non-linear algebraic equations as follows:

$$X_{j+1} = A_j X_j - B_j X_{j-1} - C_j Y_j \quad [4.52]$$

$$Y_{j+1} = D_j Y_j - E_j Y_{j-1} - F_j Y_j^2 - G_j X_j + H_j X_j Y_j - I_j U_j Y_{j-1} + I_j U_j Y_j \quad [4.53]$$

$$U_j = J_j U_{j-1} - K_j Y_j + L_j X_j \quad [4.53]$$

where:

$$A_j = \left[ 2 - a' Pe_L \Delta Z + Pe_L \Delta Z^2 \left( \frac{St_L}{\sqrt{1+M}} + D_a \right) \right] \quad [4.54]$$

$$B_j = (1 - a' Pe_L \Delta Z) \quad [4.55]$$

$$C_j = \left[ \frac{\sqrt{1+M} St_L Pe_L \Delta Z^2}{\beta} (\beta - \alpha Z_j) \right] \quad [4.56]$$

$$D_j = \left[ 2 + \frac{2\alpha \Delta Z}{(\beta - \alpha Z_j)} + Pe_G \Delta Z^2 St_G \sqrt{1+M} \right] \quad [4.57]$$

$$E_j = \left[ 1 + \frac{2\alpha \Delta Z}{(\beta - \alpha Z_j)} \right] \quad [4.58]$$

$$F_j = (Pe_G \Delta Z^2 y_0 St_G \sqrt{1+M}) \quad [4.59]$$

$$G_j = \left[ \frac{Pe_G \Delta Z^2 \beta St_G}{(\beta - \alpha Z_j) \sqrt{1+M}} \right] \quad [4.60]$$

$$H_j = \left[ \frac{Pe_G \Delta Z^2 y_0 \beta St_G}{(\beta - \alpha Z_j) \sqrt{1+M}} \right] \quad [4.61]$$

$$I_j = Pe_G \Delta Z \quad [4.62]$$

$$J_j = \left[ \frac{(\beta - \alpha Z_j)}{(\beta - \alpha Z_j) - \alpha \Delta Z} \right] \quad [4.63]$$

$$K_j = \left[ \frac{\sqrt{1 + MSt_G y_0 (\beta - \alpha Z_j) \Delta Z}}{(\beta - \alpha Z_j) - \alpha \Delta Z} \right] \quad [4.64]$$

$$L_j = \left[ \frac{St_G y_0 \beta \Delta Z}{\sqrt{1 + M((\beta - \alpha Z_j) - \alpha \Delta Z)}} \right] \quad [4.65]$$

By applying the same numerical spatial discretization technique on the differential boundary equations obtained before, the following algebraic equations are obtained for the following boundary conditions:

$$X_{N-1} - X_{N+1} + M_j X_{inf} - M_j X_N = 0 \quad (\text{counter-current flow conditions}) \quad [4.66]$$

$$X_{-1} - X_1 + M_j X_0 + M_j X_{inf} = 0 \quad (\text{co-current flow conditions}) \quad [4.67]$$

$$X_{-1} - X_1 = 0 \quad (\text{counter-current flow conditions}) \quad [4.68]$$

$$X_{N+1} - X_{N-1} = 0 \quad (\text{co-current flow conditions}) \quad [4.69]$$

$$Y_{-1} - Y_1 + N_j Y_0 - N_j = 0 \quad (\text{counter and co-current flow conditions}) \quad [4.70]$$

$$Y_{N+1} - Y_{N-1} = 0 \quad (\text{counter and co-current flow conditions}) \quad [4.71]$$

$$U_0 = 1 \quad (\text{counter and co-current flow conditions}) \quad [4.72]$$

where:

$$M_j = 2Pe_L \Delta Z \quad [4.73]$$

$$N_j = 2Pe_G \Delta Z \quad [4.74]$$

#### 4.4.2 2P-ADM With Gas-Phase Dispersion (Water Treatment Conditions)

The non-linear differential equations are transformed into non-linear algebraic equations similar to those equations developed before for the wastewater treatment conditions with the exception of setting the factor (M) equal to zero.

#### 4.4.3 2P-ADM without gas phase dispersion

For the special case of 2P-ADM with no dispersion in the gas phase, the same procedure is used for the numerical transformation of the model non-linear differential equations into non-linear algebraic equations.

## 4.5 CONCLUSIONS

In this chapter, the two-phase axial dispersion model (2P-ADM) has been developed for describing the performance of ozone bubble columns. Two cases of the model have been developed: (1) the axial dispersion was considered for the liquid and gas phases; and (2) the axial dispersion was considered only in the liquid phase. The 2P-ADM non-linear differential equations were numerically transformed into non-linear algebraic equations that can be easily solved using any of the available numerical solving algorithms.

The main advantage of applying those comprehensive models is to be able to compare between their predictions when used to model the performance of ozone bubble columns. Those models' predictions may vary depending on the bubble column configuration and design as well as the operating conditions. As an example, regarding the effect of bubble column configuration, columns with small aspect ratios might exhibit large gas-phase backmixing that must be accounted for in the model equations. Therefore, most of the models that are currently applied to describe the performance of such ozone contactors are outdated because they are based on inaccurate assumptions with respect to the prevailing liquid and gas-phase flow regimes.

#### 4.6 REFERENCES

1. Beltrán, F.J., J.F. García-Araya, and J.M. Encinar, "Henry and Mass Transfer Coefficients in the Ozonation of Wastewaters", *Ozone Sci. & Eng.* 19: 281-296 (1997).
2. Danckwerts, P.V., *Gas-Liquid Reactions* (NY, USA: McGraw-Hill, Inc., 1970).
3. Deckwer, W.-D., "Non-Isobaric Bubble Columns With Variable Gas Velocity", *Chem. Eng. Sci.* 31: 309-317 (1976).
4. Gamal El-Din, M. and D.W. Smith, "Designing Ozone Bubble Columns: A Spreadsheet Approach to Axial Dispersion Model", *Proc. of IOA/PAG Conf.: Advances in Ozone Technology*, Orlando, FL, USA, 2000.
5. Hoigné, J., "Mechanisms, Rates and Selectivities of Oxidants of Organic Compounds Initiated by Ozonation in Water", *Handbook of Ozone Technology and Applications* (MI, USA: Ann Arbor Science Publishers, 1982).
6. Johnson, P.N. and R.A. Davis, "Diffusivity of Ozone in Water", *J. Chem. Eng. Data* 41: 1485-1487 (1996).
7. Kaštánek, J., J. Zahradník, J. Kratochvíl, and J. Čermák, *Chemical Reactors for Gas-Liquid Systems* (Chichester, England: Ellis Horwood, 1993).
8. Kramers, H. and K.R. Westerterp, *Elements of Chemical Reactor Design and Operation* (NY, USA: Academic Press, Inc., 1963).
9. Levenspiel, O., *Chemical Reaction Engineering, 2<sup>nd</sup> ed.* (NY, USA: John Wiley and Sons, Inc., 1972).
10. Mangartz, K.H. and Th. Pilhofer, "Interpretation of Mass Transfer Measurements in Bubble Columns Considering Dispersion of Both Phases", *Chem. Eng. Sci.* 31: 1069-1077 (1981).
11. Oke, N.J., D.W. Smith, and H. Zhou, "An Empirical Analysis of Ozone Decay Kinetics in Natural Waters", *Ozone Sci. & Eng.* 20: 361-379 (1998).
12. Shetty, S.A., M.V. Kantak, and B.G. Kelkar, "Gas-Phase Backmixing in Bubble Column Reactors", *AIChE J.* 38(7): 1013-1026(1992).

13. Towell, G.D. and G.H. Ackermann, "Axial Mixing of Liquid and Gas in Larger Bubble Reactors", *Proc. 5<sup>th</sup> European and 2<sup>nd</sup> Int. Sympos. Chem. Reaction Eng.* B3-1, Elsevier, Amsterdam, Netherlands (1972).
14. Wachi, S. and Y. Nojima., "Gas-Phase Dispersion in Bubble Columns", *Chem. Eng. Sci.* 45(4): 901-905 (1990).
15. Wachi, S. and H. Morikawa., "Chlorination of Ethylene in a Boiling Bubble Column Reactor", *J. Chem. Eng. Japan* 20: 238-245 (1987).
16. Yurteri, C. and M.D. Gurol, "Ozone Consumption in Natural Waters: Effects of Background Organic Matter, pH and Carbonate Species", *Ozone Sci. & Eng.* 10: 277-290 (1988).
17. Zhou, H. and D.W. Smith, "Ozonation Dynamics and its Implication for Off-Gas Ozone Control in Treating Pulp Mill Wastewaters", *Ozone Sci & Eng.* 22: 31-51 (2000).
18. Zhou, H. and D.W. Smith, "Applying Mass Transfer Theory to Study the Kinetics of Fast Ozone Reactions in Pulp Mill Effluents", *Proc. of the 14<sup>th</sup> Ozone World Congress*, Detroit, MI, USA, (1999).
19. Zhou, H. and D.W. Smith, "Process Parameter Development for Ozonation of Kraft Pulp Mill Effluents", *Wat. Sci. & Technol.* 35(2-3): 251-259 (1997).
20. Zhou, H., *Investigation of Ozone Disinfection Kinetics and Contactor Performance Modeling: Ph.D. Thesis* (Edmonton, AB, Canada: University of Alberta, 1995).

**CHAPTER 5. TWO-PHASE NON-ISOBARIC AXIAL DISPERSION MODELS  
FOR MODELING THE OZONATION PROCESS DYNAMICS–II.  
NUMERICAL ANALYSES AND EXPERIMENTAL VERIFICATION\***

### 5.1 INTRODUCTION

In chapter 4, a two-phase-non-isobaric axial dispersion model (2P-ADM) was developed for describing the dynamics of ozonation process in bubble columns for water and wastewater treatment applications. The 2P-ADM consists of a system of three non-linear differential equations representing the liquid-phase ozone concentration, the gas-phase ozone concentration, and the gas-phase inerts' concentrations. One of the special conditions of the 2P-ADM, that represents the situations where the gas phase is assumed to flow in an ideal plug flow regime, has been previously developed and applied for describing the performance of ozone contactors (Zhou *et al.*, 1994). Therefore, the backmixing in the gas phase can be neglected and the 2P-ADM reduces to a system of two non-linear differential equations. By applying the 2P-ADM, to describe the dynamics of the ozonation process in bubble columns, instead of the traditionally applied models such as plug flow model (PFM) or continuous flow stirred tank reactors (CFSTR's) in-series model, accurate and reliable designs of ozone contactors can be achieved. Consequently, the operating and capital costs can be minimized and the desired treatment objectives can be met. Accurate and reliable predictions of the ozone concentration in the exhaust gas leaving the ozone contactors will allow for more accurate and optimized designs of the ozone off-gas destruction facilities.

The objectives of this chapter are (1) to demonstrate the two-phase axial dispersion model capability to predict the performance of ozone bubble columns under different operating conditions for water and wastewater treatment applications; and (2) to test the model predictions against some existing experimental data from the literature.

---

A version of this chapter has been submitted for publication. Gamal El-Din, M. and D.W. Smith, *J. Environ. Eng. & Sci.* (July 2001).

First, the two-phase axial dispersion model was simulated under two different conditions of the gas-phase backmixing: (1) high gas-phase dispersion; and (2) low gas-phase dispersion. In situations where the gas-phase backmixing can be ignored and the gas-phase flow is considered to be in the ideal plug flow regime, were also considered in the model simulations. Under those conditions, the model was simulated for a wide range of typical operating conditions that are usually encountered in water and wastewater treatment applications. Sensitivity analyses of the model predictions were also performed to obtain the model sensitivities and responses towards changes in the model input parameters.

Second, the model predictions were tested against the experimental data of Zhou (1995) to demonstrate the model capability to describe the performance of a fine-bubble diffuser ozone contactor in the counter and co-current flow modes.

## 5.2 NUMERICAL SIMULATIONS AND SENSITIVITY ANALYSES

### 5.2.1 Numerical Solution Techniques of the 2P-ADM Equations

The system of three non-linear differential equations representing the general 2P-ADM was transformed numerically into a system of non-linear algebraic equations by applying the finite-difference technique, in which, a backward difference scheme was applied for spatial discretization. In the finite difference technique, the number of elements (N) was set equal to 50. As a result, 51 nodes were used and that led to 153 non-linear algebraic equations in addition to the boundary equations. When the gas-phase was assumed to flow in an ideal plug flow regime, the number of algebraic equations was reduced from 153 to 102. Those non-linear algebraic equations were solved using the Newton Raphson technique by utilizing the TKSOLVER<sup>TM</sup> software. The program executed until a user-specified comparison tolerance of  $10^{-6}$  was satisfied. The program execution time varied between runs depending on the values of the model input parameters.

## 5.2.2 Operating Conditions for Water Treatment Applications

The effects of the model input parameters ( $Pe_L$ ,  $Pe_G$ ,  $k_La$ ,  $D_a$ ,  $\alpha$ , and  $y_0$ ) on the dissolved ozone concentration, gaseous ozone concentration, and superficial gas velocity profiles were examined. The following typical conditions for the operation of ozone bubble columns were assigned as the base values for the model simulations: column height ( $L$ ) = 5,000 mm, ozone concentration in the feed gas ( $C_{G,0}$ ) = 1 % (w/w), applied ozone dose =  $1.35 \text{ mgL}^{-1}$ , mean theoretical hydraulic detention time =  $\tau = 180 \text{ s}$ ,  $Pe_L = 5.0$ ,  $k_w = 4.7 \times 10^{-4} \text{ s}^{-1}$ ,  $k_La = 5.0 \times 10^{-3} \text{ s}^{-1}$ , bubble column aspect ratio =  $L/D = 12.5$ , G/L ratio = 0.1, and gas hold-up ( $\epsilon_G$ ) = 0.008. The ozone decay process was assumed to follow pseudo-first-order reaction kinetics with the specific ozone utilization rate constant ( $k_w$ ) being constant throughout the course of ozonation. This is typical for situations where the concentrations of impurities in the liquid phase are too small, as in clean deionized water, to cause  $k_w$  to decrease during the course of ozonation as a result of the increasing amount of the utilized ozone as the ozonation process proceeds. Henry's law constant ( $H$ ) of  $0.22 \text{ kPaLmg}^{-1}$  was obtained from Sotelo *et al.* (1989). Water temperature was assumed to be  $20^\circ\text{C}$  and the pressure at the top of the column ( $P_T$ ) was set equal to 101.3 kPa. Therefore,  $\alpha$  and  $\beta$  were calculated to be 0.48 and 1.48, respectively.

The basic model input parameters were then calculated and they were as follows:  $Pe_L = 5.0$  (corresponding to  $D_L = 0.028 \text{ m}^2\text{s}^{-1}$ ),  $Pe_G = 618.3$  ( $D_G = D_L/10$ ), 61.83 ( $D_G = D_L$ ), and 0.0 ( $D_G = 0$ ),  $St_L = 0.90$ ,  $St_G = 2.07$ ,  $D_a = 0.0831$ , and  $y_0 = 0.00675$ . The 2P-ADM predictions of the dissolved ozone concentration, gaseous ozone concentration, and superficial gas velocity profiles along the bubble column were obtained for wide ranges of the model input parameters. The effects of each of the parameters ( $Pe_L$ ,  $Pe_G$ ,  $k_La$ ,  $D_a$ ,  $\alpha$ , and  $y_0$ ) on the model predictions, were studied by varying the parameter of interest while maintaining the others constant except for  $Pe_L$  and  $Pe_G$ , as they were varied together as the gas-phase backmixing is somewhat dependent on the liquid-phase backmixing.

### 5.2.3 Operating Conditions for Wastewater Treatment Applications

It was reported by Zhou and Smith (1999) that during the ozonation of Kraft pulp mill wastewaters,  $k_w$  ranged from 1,000 to 5,000  $s^{-1}$  and the enhancement factor pretreatment level the pulp mill wastewater had received before it was ozonated.  $E$  was smaller for the final pulp mill effluent than for the untreated pulp mill wastewater as the untreated pulp mill wastewater contained more organic content causing its reactivity towards ozone to be higher (Zhou and Smith, 2000). In their calculations of the amount of the utilized ozone, the bulk liquid ozone concentration was assumed to equal zero since it was practically below the detection limit and it was less significant compared to the total amount of applied ozone. They suggested that a typical value of  $k_L$  ranged from  $6.6 \times 10^{-4}$  to  $9.3 \times 10^{-4} \text{ ms}^{-1}$  and  $k_L a$  ranged from  $8.3 \times 10^{-3}$  to  $2.5 \times 10^{-2} \text{ s}^{-1}$ . The effects of  $Pe_L$ ,  $Pe_G$ ,  $k_L a$ ,  $D_a$ ,  $M$ ,  $\alpha$ , and  $y_0$  on the dissolved ozone concentration, gaseous ozone concentration, and superficial gas velocity profiles in bubble columns were examined by assigning the same typical operating conditions, used for the water treatment applications. Except for the specific ozone utilization rate constant ( $k_w$ ), the enhancement factor ( $M$ ), and the local mass transfer coefficient ( $k_L$ ). Lower values of  $k_w$ ,  $M$ , and  $k_L$  were chosen to study the model predictions for wastewater treatment applications in lower reactive environments compared to the highly reactive environments such as pulp mill wastewaters.  $k_w$  and  $k_L$  were set equal to  $500 \text{ s}^{-1}$  and  $8.0 \times 10^{-4} \text{ ms}^{-1}$ , respectively. The effects of the type of wastewater on  $k_w$ , and consequently, on the ozone reactivity with the liquid-phase impurities were investigated by varying  $k_w$  over a wide range ( $5.0 \times 10^{-1}$  to  $5.0 \times 10^4 \text{ s}^{-1}$ ). The change in the amount of the utilized ozone dose along the column height in the main direction of the liquid flow passing through the reactor was assumed to be negligible as a result of the relatively short mean theoretical hydraulic detention time in the reactor.

The basic model input parameters were then calculated and they were as follows:  $Pe_L = 5.0$  (corresponding to  $D_L = 0.028 \text{ m}^2 \text{ s}^{-1}$ ),  $Pe_G = 618.3$  ( $D_G = D_L/10$ ),  $61.83$  ( $D_G = D_L$ ), and  $0.0$  ( $D_G = 0$ ),  $St_L = 0.90$ ,  $St_G = 2.07$ ,  $D_a = 89000$ ,  $M = 1.166$ , and  $y_0 = 0.00675$ . The lower value of  $M$  was chosen to investigate the effect of chemical reactions in the

intermediate reaction-kinetics regime where they occur simultaneously near and/or at the gas-liquid interface and in the bulk liquid as usually experienced in lower reactive environments. The effects of each of the parameters ( $Pe_L$ ,  $Pe_G$ ,  $k_L a$ ,  $D_a$ ,  $M$ ,  $\alpha$ , and  $y_0$ ) on the model predictions, were studied by varying the parameter of interest while maintaining the others constant except for: (1)  $Pe_L$  and  $Pe_G$ ; and (2)  $D_a$  and  $M$ .  $D_a$  and  $M$  are interrelated through the pseudo-first-order specific ozone utilization rate constant ( $k_w$ ).

#### 5.2.4 Operating Conditions for Model Testing (Water Treatment Applications)

The 2P-ADM was tested, for ozone application in water treatment, using the pilot-scale experimental data of Zhou (1995). The pilot-scale bubble column utilized in the experiments was a cylindrical glass column with an inside diameter of 100 mm and a height of 2,000 mm. The water depth was maintained constant at 1,750 mm by using an overflow weir. A 25 mm spherical fused crystalline aluminum stone was used as the gas sparger. For the deionized water used in the experiments, a pseudo-first-order specific ozone utilization rate constant ( $k_w$ ) was assumed to equal  $4.7 \times 10^{-4} \text{ s}^{-1}$  based on the measurements of Zhou (1995). The operating conditions for the counter-current and co-current flow modes are presented in Tables 5.1 and 5.2, respectively.

Table 5.1 Operating conditions for the counter-current flow mode (water treatment).

Case #	$Pe_L$	$P_T$ (atm)	$St_L$	$St_G$	$D_a$	$y_0$	$C_{L,0}$ (mgL <sup>-1</sup> )
DW17	10.53	1.0	0.560	1.119	0.139	0.010	5.56
DW18	5.35	1.0	3.788	1.299	0.139	0.002	0.92

Table 5.2 Operating conditions for the co-current flow mode (water treatment).

Case #	$Pe_L$	$P_T$ (atm)	$St_L$	$St_G$	$D_i$	$\gamma_0$	$C_{L,0}$ (mgL <sup>-1</sup> )
DW4	34.48	1.0	0.235	1.247	0.056	0.013	7.20
DW5	9.84	1.0	1.755	1.258	0.056	0.002	0.92
DW9	4.63	1.0	0.235	0.081	0.139	0.002	0.88

### 5.3 RESULTS AND DISCUSSION

#### 5.3.1 Counter-Current Flow Mode (Water Treatment Applications)

The main feature of the counter-current flow mode is that the liquid flow passes from the top to the bottom of the column in the opposite direction to that of the gas flow. Figures 5.1 to 5.10 represent the predicted dissolved ozone concentration, gaseous ozone concentration, and superficial gas velocity profiles, along the column height, as functions of the dimensionless axial co-ordinate ( $Z$ ). The profiles representing the conditions of  $D_G = D_L/10$  and  $D_G = 0$  were virtually identical. Therefore, only the profiles representing the condition of  $D_G = D_L/10$  were presented. The effects of the inflow superficial liquid and gas velocities on the process overall mass transfer coefficient ( $k_L a$ ) are represented by  $St_L$  and  $St_G$ , respectively. Since  $St_L$  and  $St_G$  are interrelated through  $k_L a$ , therefore, the effects of  $St_L$  and  $St_G$  were studied simultaneously by varying  $k_L a$ . In all the cases, the gaseous ozone concentration decreased monotonically along the column height. The maximum dissolved ozone concentration occurred at the bottom of the column where the liquid exits the column.

Figure 5.1 represents the effects of  $Pe_L$  and  $Pe_G$  on the dissolved ozone concentration profiles. The  $Pe_L$  and  $Pe_G$  effects decreased as  $Pe_L$  and  $Pe_G$  increased from 1.0 to infinity and 12.4 (for  $D_G = D_L$ ) or 124.0 (for  $D_G = D_L/10$ ) to infinity with the rate of increase of the effluent dissolved ozone concentration per increase of  $Pe_L$  being virtually identical for both  $D_G = D_L$  and  $D_G = D_L/10$ . Meanwhile, the rate of increase in the effluent dissolved ozone concentration per increase in  $Pe_G$  was higher by almost one fold for  $D_G = D_L/10$ . As  $Pe_L$  increased from 1.0 to 20.0, the rate of increase in the effluent

dissolved ozone concentration per increase in  $Pe_L$  decreased from almost  $1.5 \times 10^{-2}$  to  $7.0 \times 10^{-4}$  and was virtually identical for both  $D_G = D_L$  and  $D_G = D_L/10$ . As  $Pe_G$  increased from 12.4 to 247.3 (for  $D_G = D_L$ ) and 124.0 to 2473.0 (for  $D_G = D_L/10$ ), respectively, the rate of increase in the effluent dissolved ozone concentration per increase in  $Pe_G$  decreased from almost  $1.1 \times 10^{-2}$  to  $6.0 \times 10^{-5}$  for  $D_G = D_L$  and was almost lower by one fold for  $D_G = D_L/10$ .

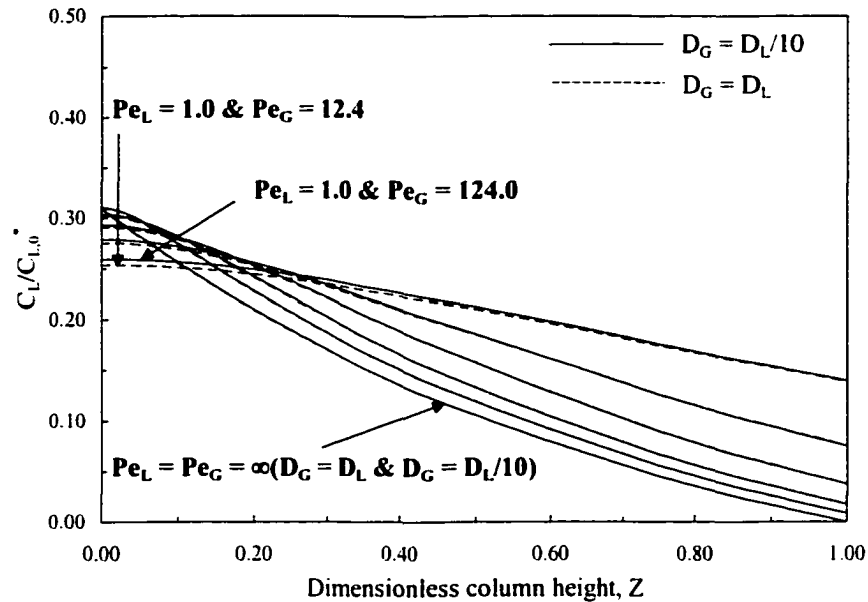


Figure 5.1  $Pe_L$  and  $Pe_G$  effects on the 2P-ADM predicted dissolved ozone concentration profiles in the counter-current flow mode and for water treatment applications ( $(Pe_L = 1.0, 2.5, 5.0, 10.0, 20.0, \text{ and } \infty)$  and  $(Pe_G = 12.4/124.0, 30.9/309.0, 61.8/618.0, 123.7/1237.0, 247.3/2473.0, \text{ and } \infty)$ ).

As shown in Figure 5.1, as  $Pe_L$  and  $Pe_G$  increased, the dissolved ozone concentration in the effluent increased and the profiles became steeper as the flow conditions in both phases approached the plug flow regime. The profiles exhibited an increasing axial gradient up to a turning point after which they started decreasing. As  $Pe_L$  and  $Pe_G$  increased from 1.0 to 20.0 and from 12.4 to 247.3 (for  $D_G = D_L$ ) or 124.0 to 2473.0 (for  $D_G = D_L/10$ ), respectively, the position of the turning point shifted from  $Z = 0.70$  and  $0.74$  to  $0.12$  and  $0.12$  at  $D_G = D_L/10$  and  $D_G = D_L$ , respectively. That could be

explained by the boundary conditions applied at the bottom (zero-axial gradient of the profile) and at the top of the column (a concentration jump). As the liquid and gas phases reached the plug flow regime at  $Pe_L$  and  $Pe_G = \infty$ , the backmixing and the concentration jump diminished and as a result the dissolved ozone concentration profiles exhibited a decreasing trend along the entire column height.

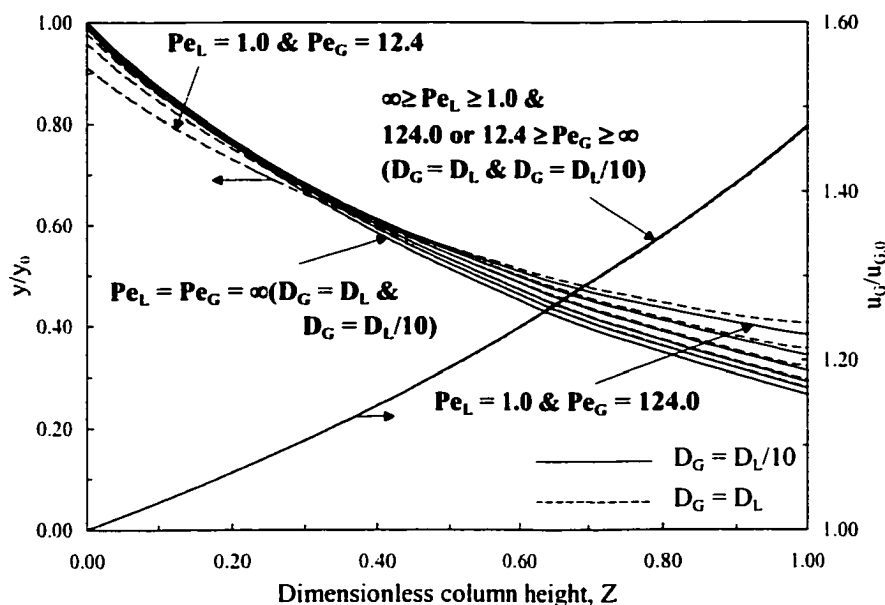


Figure 5.2  $Pe_L$  and  $Pe_G$  effects on the 2P-ADM predicted gaseous ozone concentration and superficial gas velocity profiles in the counter-current flow mode and for water treatment applications ( $(Pe_L = 1.0, 2.5, 5.0, 10.0, 20.0, \text{ and } \infty)$  and  $(Pe_G = 12.4/124.0, 30.9/309.0, 61.8/618.0, 123.7/1237.0, 247.3/2473.0, \text{ and } \infty)$ ).

As shown in Figure 5.2, the effects of  $Pe_L$  and  $Pe_G$  on the gaseous ozone concentration profiles decreased and the profiles became steeper as  $Pe_L$  and  $Pe_G$  increased. As  $Pe_L$  increased from 1.0 to 20.0, the rate of decrease in the ozone off-gas concentration per increase in  $Pe_L$  decreased from almost  $2.5 \times 10^{-2}$  to  $1.0 \times 10^{-3}$  and was virtually identical for both  $D_G = D_L$  and  $D_G = D_L/10$ . As  $Pe_G$  increased from 12.4 to 247.3 (for  $D_G = D_L$ ) and 124.0 to 2473.0 (for  $D_G = D_L/10$ ), respectively, the rate of decrease in ozone off-gas concentration per increase in  $Pe_G$  decreased from almost  $2.7 \times 10^{-3}$  to  $1.0 \times$

$10^{-4}$  for  $D_G = D_L$  and was almost lower by one fold for  $D_G = D_L/10$ . The highest effects of  $Pe_L$  and  $Pe_G$  on the gaseous ozone concentration profiles were in the upper one half of the column height where higher  $Pe_L$  and  $Pe_G$  improved the absorption efficiency due to the lower dissolved ozone concentrations in that region of the column resulting in higher mass transfer driving force (Zhou *et al.*, 1994). The superficial gas velocity profiles were virtually identical for the entire studied range of  $Pe_L$  and  $Pe_G$ .

The superficial gas velocity at the column exit was about 1.5 times higher than the inflow superficial gas velocity and the superficial gas velocity increase was almost a linear function of the axial co-ordinate ( $Z$ ) as a result of the gas expansion due to the linear decrease in the hydrostatic head along the column height. The slight deviation from the linearity is contributed to the effects of the ozone gas absorption and auto-decomposition processes.

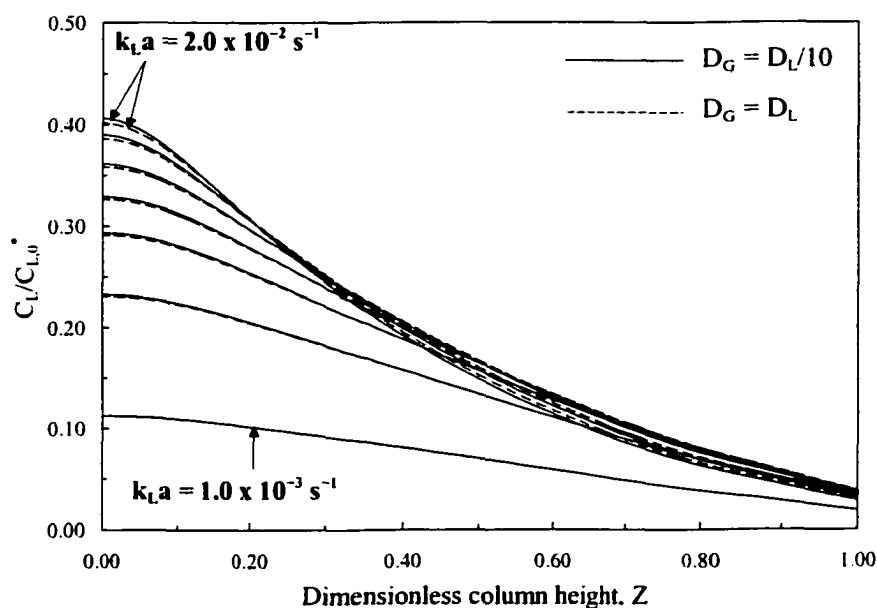


Figure 5.3  $k_{La}$  effects on the 2P-ADM predicted dissolved ozone concentration profiles in the counter-current flow mode and for water treatment applications ( $k_{La} = 1.0 \times 10^{-3}$ ,  $3.0 \times 10^{-3}$ ,  $5.0 \times 10^{-3}$ ,  $7.0 \times 10^{-3}$ ,  $1.0 \times 10^{-2}$ ,  $1.5 \times 10^{-2}$ , and  $2.0 \times 10^{-2} \text{ s}^{-1}$ ).

As shown in Figure 5.3, the effects of  $k_L a$  on the dissolved ozone concentration profiles decreased and the profiles became steeper as  $k_L a$  increased from  $1.0 \times 10^{-3}$  to  $2.0 \times 10^{-2} \text{ s}^{-1}$  and the rate of increase in the effluent dissolved ozone concentration per increase in  $k_L a$  decreased from 1.00 to 0.05 and was virtually identical for both  $D_G = D_L$  and  $D_G = D_L/10$ . The profiles exhibited an increasing axial gradient up to a turning point after which they started decreasing. As  $k_L a$  increased, the position of the turning point shifted from  $Z = 0.46$  to 0.18 for  $D_G = D_L/10$  and  $D_G = D_L$ . As shown in Figure 5.3, as  $k_L a$  increased from  $1.0 \times 10^{-2}$  to  $2.0 \times 10^{-2} \text{ s}^{-1}$  (i.e., the higher range of  $k_L a$ ), the dissolved ozone concentrations increased only up to a "Z" equal to about 0.20 and at "Z" higher than 0.20, the concentrations decreased. That could be explained by the fact that the mass transfer process was increased only near the bottom of the column. Therefore, the model predictions support the idea of the mass transfer enhancement near the bottom of the column being sufficient for better ozone bubble column performance (Zhou *et al.*, 1994; Gamal El-Din and Smith, 2000).

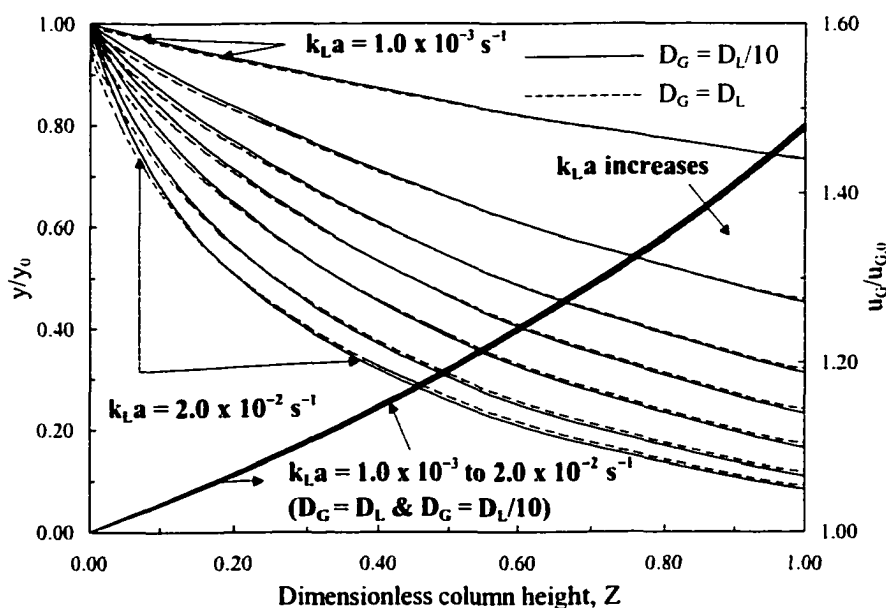


Figure 5.4  $k_L a$  effects on the 2P-ADM predicted gaseous ozone concentration and superficial gas velocity profiles in the counter-current flow mode and for water treatment applications ( $k_L a = 1.0 \times 10^{-3}$ ,  $3.0 \times 10^{-3}$ ,  $5.0 \times 10^{-3}$ ,  $7.0 \times 10^{-3}$ ,  $1.0 \times 10^{-2}$ ,  $1.5 \times 10^{-2}$ , and  $2.0 \times 10^{-2} \text{ s}^{-1}$ ).

As shown in Figure 5.4, the effects of  $k_{La}$  on the gaseous ozone concentration profiles decreased and the profiles became steeper as  $k_{La}$  increased and the rate of decrease in the ozone off-gas concentration per increase in  $k_{La}$  decreased from 2.3 to 0.1 and was virtually identical for both  $D_G = D_L$  and  $D_G = D_L/10$ . The superficial gas velocity profiles were almost identical for the entire studied range of  $k_{La}$  with the superficial gas velocity being higher at lower  $k_{La}$ . The superficial gas velocity at the column exit was about 1.5 times higher than the inflow superficial gas velocity and the superficial gas velocity increase was almost a linear function of the axial co-ordinate ( $Z$ ).

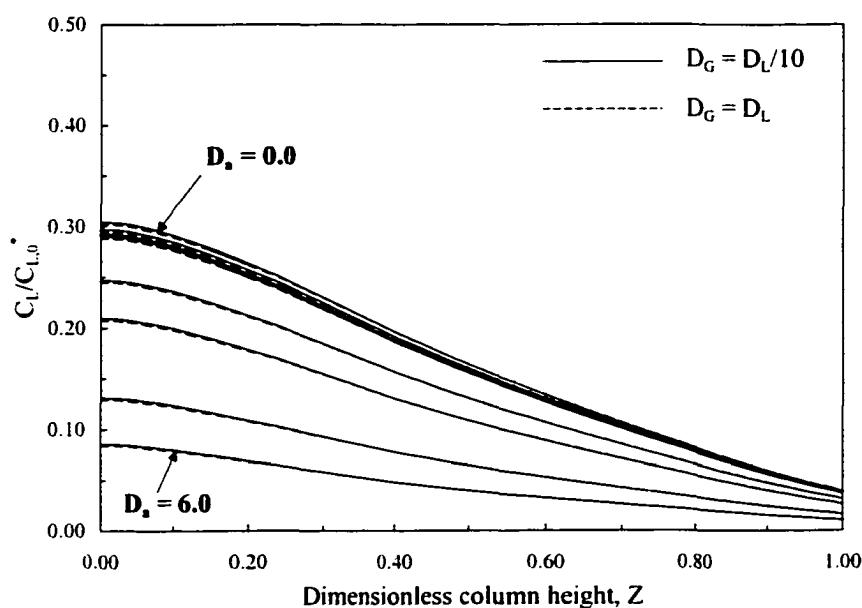


Figure 5.5  $D_a$  effects on the 2P-ADM predicted dissolved ozone concentration profiles in the counter-current flow mode and for water treatment applications ( $D_a = 0.0000, 0.0505, 0.0831, 0.1010, 0.5050, 1.0000, 3.0000,$  and  $6.0000$ ).

Figure 5.5 depicts the effects of the overall pseudo-first-order specific ozone utilization rate constant ( $k_w$ ) on the dissolved ozone concentration profiles.  $k_w$  is one of the parameters that describe the quality of the water being treated. A case where there is no decay of the dissolved gas, as in oxygen bubble columns, has been included in the analysis for the sack of comparison. As  $k_w$  increased from  $0.0$  to  $5.0 \times 10^{-2} \text{ s}^{-1}$  (i.e.,  $D_a$

increased from 0.0 to 6.0) the dissolved ozone concentration profiles became flatter and the effluent dissolved ozone concentration decreased as observed before by (Gamal El-Din and Smith, 2000). This is in agreement with the fact that the higher the pollution level in waters, i.e., the higher the pH, the higher the overall ozone decay rate resulting in higher ozone doses to be applied to meet the required residual ozone concentration in the effluents from ozone contactors (Zhou *et al.*, 1994). The effect of  $D_a$  on the dissolved ozone concentration profiles decreased as  $D_a$  increased from 0.0 to 6.0 and the rate of decrease in the effluent dissolved ozone concentration per increase in  $D_a$  decreased from 0.14 to 0.02 and was virtually identical for both  $D_G = D_L$  and  $D_G = D_L/10$ . The dissolved ozone concentration profiles exhibited an increasing axial gradient up to a turning point after which they started decreasing. As  $D_a$  increased from 0.0 to 6.0, respectively, the position of the turning point shifted from " $Z$ " = 0.32 to 0.20 for  $D_G = D_L/10$  and  $D_G = D_L$ .

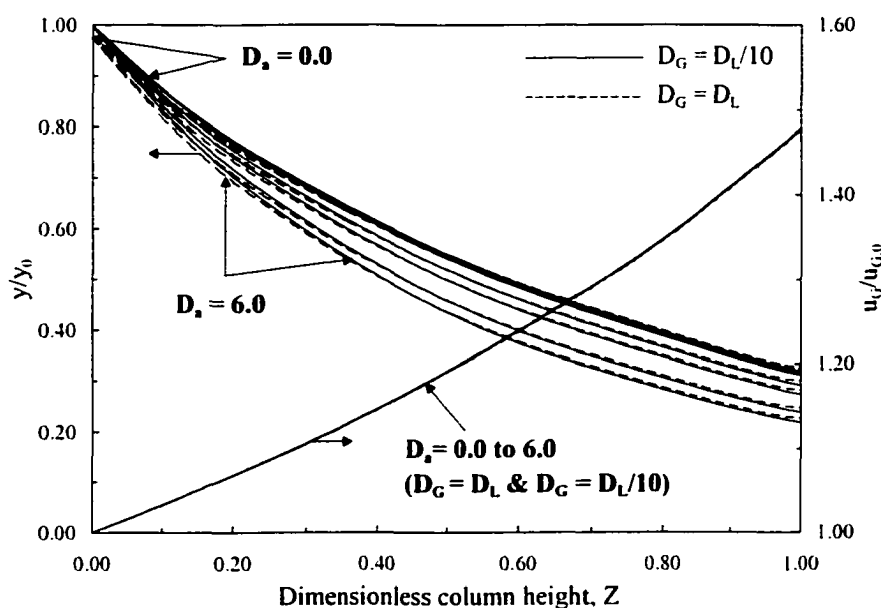


Figure 5.6  $D_a$  effects on the 2P-ADM predicted gaseous ozone concentration and superficial gas velocity profiles in the counter-current flow mode and for water treatment applications ( $D_a = 0.0000, 0.0505, 0.0831, 0.1010, 0.5050, 1.0000, 3.0000, \text{ and } 6.0000$ ).

As shown in Figure 5.6, the effects of  $D_a$  on the gaseous ozone concentration profiles decreased and the profiles became steeper as  $D_a$  increased and the rate of

decrease in the ozone off-gas concentration per increase in  $D_a$  decreased from 0.06 to 0.01 and was virtually identical for both  $D_G = D_L$  and  $D_G = D_L/10$ . The effects of  $D_a$  on the gaseous ozone concentration profiles were less significant than the effects of  $k_{La}$ . As noted before in chapter 4, the occurrence of chemical reactions during water treatment does not affect the pure physical mass transfer rate through the liquid film beneath the gas-liquid interface. As a result, any improvement in the absorption efficiency with increasing  $D_a$  is due to the auto-decomposition of the dissolved ozone concentration in the bulk liquid. The superficial gas velocity profiles were identical for the entire studied range of  $D_a$ . The superficial gas velocity at the column exit was about 1.5 times higher than the inflow superficial gas velocity and the superficial gas velocity increase was almost a linear function of the axial co-ordinate ( $Z$ ).

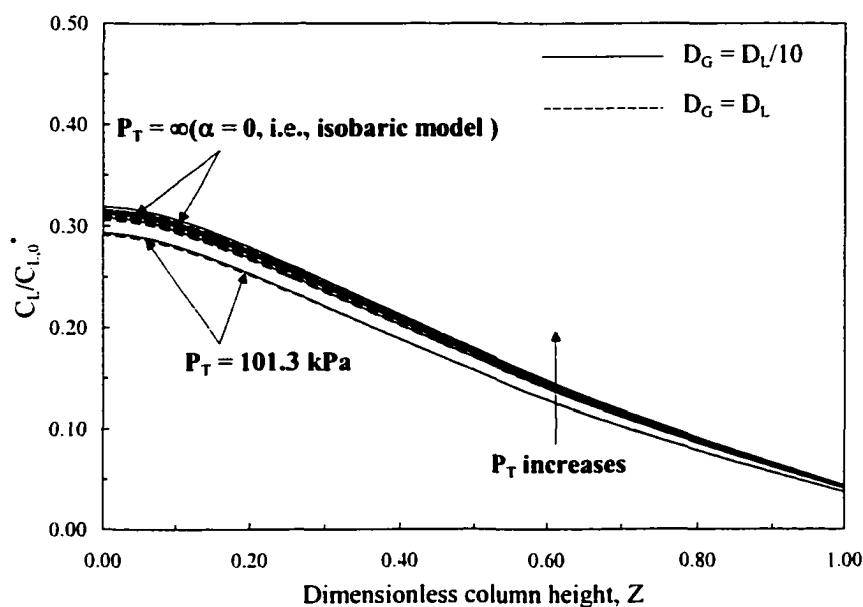


Figure 5.7  $P_T$  or  $\alpha$  effects on the 2P-ADM predicted dissolved ozone concentration profiles in the counter-current flow mode and for water treatment applications ( $P_T = 101.3, 303.9, 506.5, 709.1, 1013.0$ , and  $\infty$  kPa).

Figure 5.7 shows the effects of  $\alpha$  (i.e., the pressure at the top of the column ( $P_T$ )). For  $\alpha = 0$ , this means that the model is isobaric. As a result, the opposite effects of shrinkage and expansion of the gas phase caused by absorption, decay, and reduced

hydrostatic head, respectively are neglected. Increasing  $P_T$  from 101.3 kPa to infinity (i.e., decreasing  $\alpha$  from 0.48 to 0.00), caused the dissolved ozone concentration profiles to become steeper and the effluent dissolved ozone concentration increased. The increase in the total hydrostatic head due to the increase of  $P_T$  can cause the gas bubbles to become smaller and therefore the gas bubbles' specific interfacial area ( $a$ ) will increase causing the overall mass transfer coefficient ( $k_L a$ ) to increase. Compared to the  $k_L a$  effects on the dissolved ozone concentration profiles, the  $P_T$  effects were less significant. The rate of increase in the effluent dissolved ozone concentration per increase in  $P_T$  (i.e., decrease in  $\alpha$ ) increased from 0.04 to 0.07 and was virtually identical for both  $D_G = D_L$  and  $D_G = D_L/10$ . The effects of  $P_T$  on the dissolved ozone concentration profiles were more significant in the bottom half than in the upper half of the column. As shown in Figure 5.7, the dissolved ozone concentration profiles exhibited an increasing axial gradient up to a turning point after which they started decreasing. As  $\alpha$  decreased from 0.48 to 0.00, respectively, the effect of  $\alpha$  on the dissolved ozone concentration profiles increased and the position of the turning point shifted from " $Z$ " = 0.32 and 0.32 to 0.34 and 0.36 for  $D_G = D_L/10$  and  $D_G = D_L$ .

As shown in Figure 5.8, the effects of  $\alpha$  on the gaseous ozone concentration profiles decreased and the profiles became steeper as  $\alpha$  decreased and the rate of decrease in the ozone off-gas concentration per decrease in  $\alpha$  increased from 0.12 to 0.17 and was virtually identical for both  $D_G = D_L$  and  $D_G = D_L/10$ . The superficial gas velocity profiles became flatter as  $\alpha$  decreased. The superficial gas velocity at the column exit was about 1.5 times higher than the inflow superficial gas velocity and the superficial gas velocity increase was almost a linear function of the axial co-ordinate ( $Z$ ) at  $\alpha = 0.48$  (i.e.,  $P_T = 101.3$  kPa). The increase in the off-gas superficial velocity compared to the inflow superficial gas velocity decreased as  $\alpha$  decreased. Eventually, at  $\alpha = 0$  (isobaric conditions), the superficial gas velocity was constant along the entire column height. This phenomenon supports the importance of applying the appropriate model to describe the performance of ozone bubble columns. Applying non-isobaric models would result in

under-prediction of the total mass of the ozone off-gas and consequently the ozone destruction units will be under-designed and health hazardous conditions might occur.

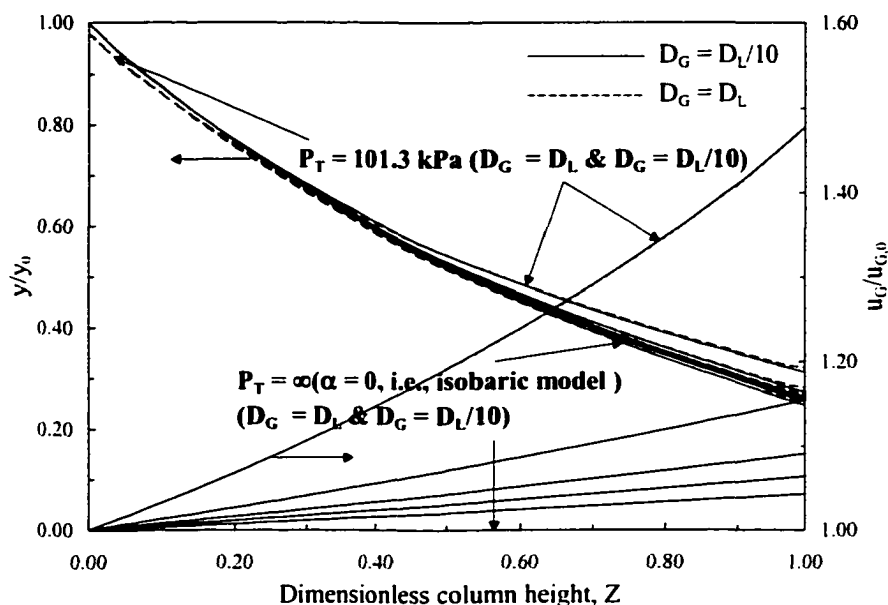


Figure 5.8  $P_T$  or  $\alpha$  effects on the 2P-ADM predicted gaseous ozone concentration and superficial gas velocity profiles in the counter-current flow mode and for water treatment applications ( $P_T = 101.3, 303.9, 506.5, 709.1, 1013.0,$  and  $\infty$  kPa).

The effects of the inflow ozone gas concentration ( $C_{G,0}$ ) on the dissolved ozone concentration, gaseous ozone concentration, and superficial gas velocity profiles in were also studied. The effluent dissolved ozone and ozone off-gas concentrations increased linearly with increasing  $C_{G,0}$  and their rates of increases per increase in  $C_{G,0}$  were virtually constant at 0.10 and 0.32, respectively. Those rates were identical for both  $D_G = D_L$  and  $D_G = D_L/10$ . The superficial gas velocity profiles became flatter as  $C_{G,0}$  increased. The maximum and minimum increases in the superficial gas velocity at the column exit, compared to the inflow superficial velocity, ranged from almost 1.5 to 1.4 times at  $C_{G,0}$  of 1 % w/w and 12 % w/w, respectively.

### 5.3.2 Co-Current Flow Mode (Water Treatment Applications)

In contrast to the counter-current flow mode, the liquid and gas phases flow through the bubble column from the bottom to the top. As the liquid and gas phases flow through the reactor, the ozone in the gas phase approaches equilibrium with the bulk liquid dissolved ozone concentration. Therefore, the mass transfer driving force ( $C_L^* - C_L$ ) becomes smaller and the bulk liquid concentration increases along the column height up to a certain point depending on the operating conditions. Thus, the model input parameters would exhibit effects on the dissolved ozone concentration, gaseous ozone concentration, and superficial gas velocity profiles. Those effects were different from those observed in the counter-current flow mode. Based on the flow arrangements in the co-current flow mode, the boundary conditions that are applied at the column entrance and exit are different from those applied in the counter-current flow mode. Therefore, the model predicted a concentration jump at the column inlet and the dissolved ozone concentration profiles reached their peaks at different locations along the column height. Those locations depended on the operating conditions. Also, the effluent from the column did not have the highest dissolved ozone concentration.

The predicted dissolved ozone concentration profiles were flatter than those predicted in the counter-current flow mode and under some operating conditions, the profiles were almost uniformly distributed along the column height. Generally the dissolved ozone concentration profiles exhibited a decreasing axial gradient along the entire column height except for the studied ranges of  $k_L a$  and  $D_a$  where the profiles exhibited a decreasing axial gradient up to a turning point after which it started increasing. The gaseous ozone concentration and superficial gas velocity profiles varied in a similar way as they did in the counter-current flow mode. As reported before by Gamal El-Din and Smith (2000), under the same operating conditions, the counter-current flow mode was superior compared to the co-current flow mode in terms of the predicted effluent dissolved ozone concentration. Since the maximum dissolved ozone concentration in the co-current flow conditions occurred somewhere along the column height rather than in the column effluent, therefore, it was relevant to compare the

effluent dissolved ozone concentration in the counter-current flow mode with the maximum dissolved ozone concentration in the co-current flow mode. This comparison revealed that the counter-current flow mode was superior compared to the co-current flow mode. The relative difference ranged from about 8 to 20 %, 5 to 29 %, 16 to 23 %, 18 to 16 %, and was constant at 17 % for the studied ranges of  $Pe_L$ ,  $Pe_G$ ,  $k_{La}$ ,  $D_a$ ,  $P_T$ , and  $y_0$ , going from the low to the high end of those ranges, respectively, for both  $D_G = D_L$  and  $D_G = D_L/10$ .

Regarding the ozone off-gas concentration, the co-current flow mode predicted higher concentrations compared to the counter-current flow mode as a result of the relatively higher ozone gas absorption efficiency in the counter-current flow mode. The relative difference ranged from about 10 to 34 %, 1 to 77 %, 24 to 1 %, 23 to 27 %, and was constant at 23 % for the studied ranges of  $Pe_L$ ,  $Pe_G$ ,  $k_{La}$ ,  $D_a$ ,  $P_T$ , and  $y_0$ , going from the low to the high end of those ranges, respectively, for both  $D_G = D_L$  and  $D_G = D_L/10$ .

For both the counter and co-current flow modes,  $k_{La}$  had the most significant effects on the dissolved and gaseous ozone concentration profiles. This phenomenon is in agreement with the fact that the gas-liquid mass transfer process is the main process that dictates the overall performance of ozone contactors operating in the slow-reaction kinetics regime. Compared to the rest of the parameters,  $\alpha$  (i.e.,  $P_T$ ) had the most significant effects on the superficial gas velocity profiles.

In both the counter and co-current flow conditions, the dissolved ozone concentration profiles representing the condition of  $D_G = D_L$  were lower, near the bottom of the column, than the ones representing the condition of  $D_G = D_L/10$ . As  $k_{La}$ ,  $P_T$ , and  $y_0$  increased and  $Pe_L$ ,  $Pe_G$ , and  $D_a$  decreased, respectively, the difference in the profiles between the two conditions of the gas-phase backmixing increased. The gaseous ozone concentration profiles were higher for the case of  $D_G = D_L/10$  near the bottom of the column and as  $Z$  increased, the gaseous ozone concentration profiles for the case of  $D_G = D_L$  became higher leading to higher ozone off-gas concentration. This phenomenon could

be explained by the gas-phase boundary conditions applied at the bottom of the column (a concentration jump) and at the top of the column (zero-axial gradient of the profile).

As shown in Figure 5.9, the effects of  $k_L a$  on the dissolved ozone concentration profiles decreased and the profiles became steeper as  $k_L a$  increased from  $1.0 \times 10^{-3}$  to  $2.0 \times 10^{-2} \text{ s}^{-1}$ . The rate of increase in the effluent dissolved ozone concentration per increase in  $k_L a$  decreased from about  $8.2 \times 10^{-1}$  to  $5.0 \times 10^{-3}$  and was virtually identical for both  $D_G = D_L$  and  $D_G = D_L/10$ . The profiles exhibited a decreasing axial gradient up to a turning point after which they started increasing up a second turning point after which they started decreasing again.

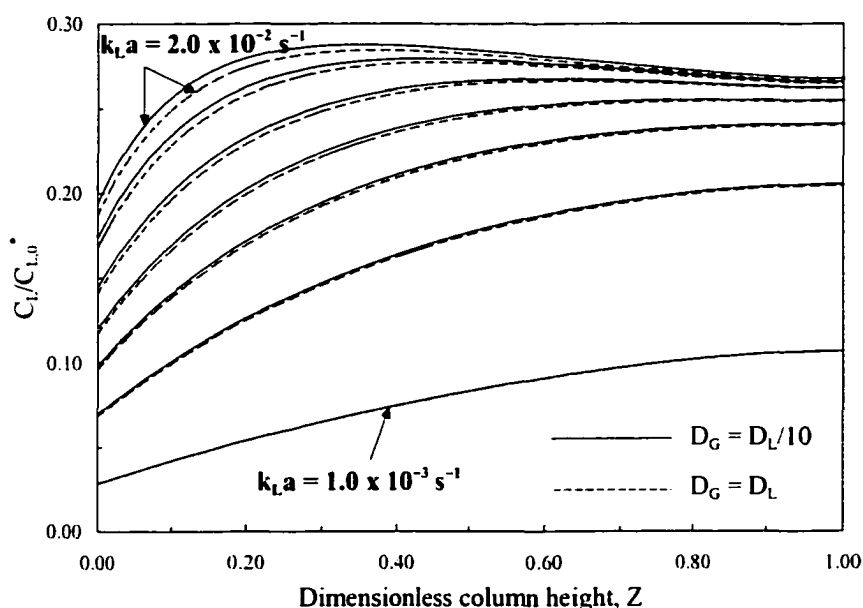


**Figure 5.9**  $k_L a$  effects on the 2P-ADM predicted dissolved ozone concentration profiles in the co-current flow mode and for water treatment applications ( $k_L a = 1.0 \times 10^{-3}$ ,  $3.0 \times 10^{-3}$ ,  $5.0 \times 10^{-3}$ ,  $7.0 \times 10^{-3}$ ,  $1.0 \times 10^{-2}$ ,  $1.5 \times 10^{-2}$ , and  $2.0 \times 10^{-2} \text{ s}^{-1}$ ).

As shown in Figure 5.9, when  $k_L a$  was increased from  $7.0 \times 10^{-3}$  to  $2.0 \times 10^{-2} \text{ s}^{-1}$ , the dissolved ozone concentrations increased only up to a point after which the concentrations started decreasing. The position of that point was at “Z” = 0.82, 0.60,

0.44, and 0.36 for  $k_L a = 7.0 \times 10^{-3}$ ,  $1.0 \times 10^{-2}$ ,  $1.5 \times 10^{-2}$ , and  $2.0 \times 10^{-2} \text{ s}^{-1}$ , respectively. Once again, that could be explained by the fact that the mass transfer process was increased only near the bottom of the column. Therefore, the model predictions support the idea of the mass transfer enhancement near the bottom of the column being sufficient for better ozone bubble column performance (Zhou *et al.*, 1994; Gamal El-Din and Smith, 2000).

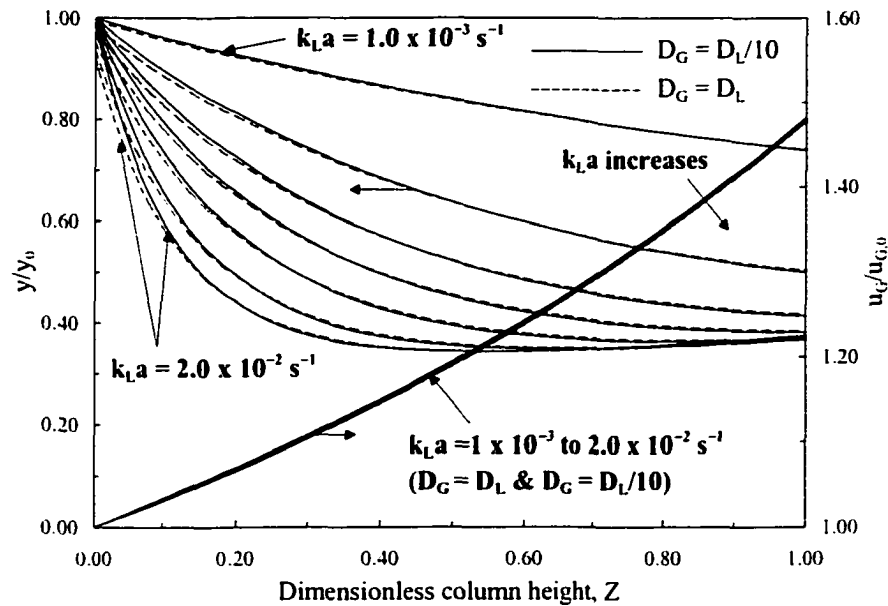


Figure 5.10  $k_L a$  effects on the 2P-ADM predicted gaseous ozone concentration and superficial gas velocity profiles in the co-current flow mode and for water treatment applications ( $k_L a = 1.0 \times 10^{-3}$ ,  $3.0 \times 10^{-3}$ ,  $5.0 \times 10^{-3}$ ,  $7.0 \times 10^{-3}$ ,  $1.0 \times 10^{-2}$ ,  $1.5 \times 10^{-2}$ , and  $2.0 \times 10^{-2} \text{ s}^{-1}$ ).

As shown in Figure 5.10, the effects of  $k_L a$  on the gaseous ozone concentration profiles decreased and the profiles became steeper as  $k_L a$  increased and the rate of decrease in the ozone off-gas concentration per increase in  $k_L a$  decreased from about 2.00 to 0.02 and was virtually identical for both  $D_G = D_L$  and  $D_G = D_L/10$ . As  $k_L a$  increased from  $1.0 \times 10^{-3}$  to  $7.0 \times 10^{-3} \text{ s}^{-1}$ , the gaseous ozone concentration profiles exhibited a decreasing axial gradient along the entire column height. In contrast, as  $k_L a$  increased from  $7.0 \times 10^{-3}$  to and  $2.0 \times 10^{-2} \text{ s}^{-1}$ , the gaseous ozone concentration profiles exhibited a

decreasing axial gradient up to a turning point after which it started increasing. The position of that turning point shifted from about  $Z = 0.82$  to  $0.53$  for both  $D_G = D_L$  and  $D_G = D_L/10$ . The superficial gas velocity profiles were almost identical for the entire studied range of  $k_{La}$  with the superficial gas velocity being higher at lower  $k_{La}$ . The superficial gas velocity at the column exit was about 1.5 times higher than the inflow superficial gas velocity and the superficial gas velocity increase was almost a linear function of the axial co-ordinate ( $Z$ ).

### 5.3.3 Counter-Current and Co-Current Flow Modes (Wastewater Treatment Applications)

Interestingly, for both flow modes, the dissolved ozone concentration, gaseous ozone concentration, and superficial gas velocity profiles were virtually identical. Although, in the lower range of  $D_a$  and  $M$  from  $D_a = 89$  and  $M = 0.037$  to  $D_a = 534$  and  $M = 0.090$ , the model predicted a concentration jump in the dissolved ozone concentration profile near the bottom of the column in the co-current flow mode. Generally, the dissolved ozone concentration profiles exhibited a decreasing axial gradient along the entire column height except for the lower range of  $D_a$  and  $M$ . The predicted dissolved ozone concentration, gaseous ozone concentration, and superficial gas velocity profiles were virtually identical for the counter and co-current flow conditions as  $Pe_L$ ,  $Pe_G$ ,  $\alpha$  or  $P_T$ , and  $y_0$  increased over their studied ranges.

The effects of  $k_{La}$  on the gaseous ozone concentration profiles were more significant than the effects of any other parameter since the  $D_a$ - $M$  range, used for the model simulations, represent situations where the intermediate-reaction kinetics regime prevails. As expected for the wastewater treatment conditions and in contrast to the water treatment conditions, the effects of  $D_a$  and  $M$  on the dissolved ozone concentration profiles were more significant than the effects of any other parameter. As observed before in the water treatment conditions, compared to the rest of the parameters,  $\alpha$  (i.e.,  $P_T$ ) had the most significant effects on the superficial gas velocity profiles.

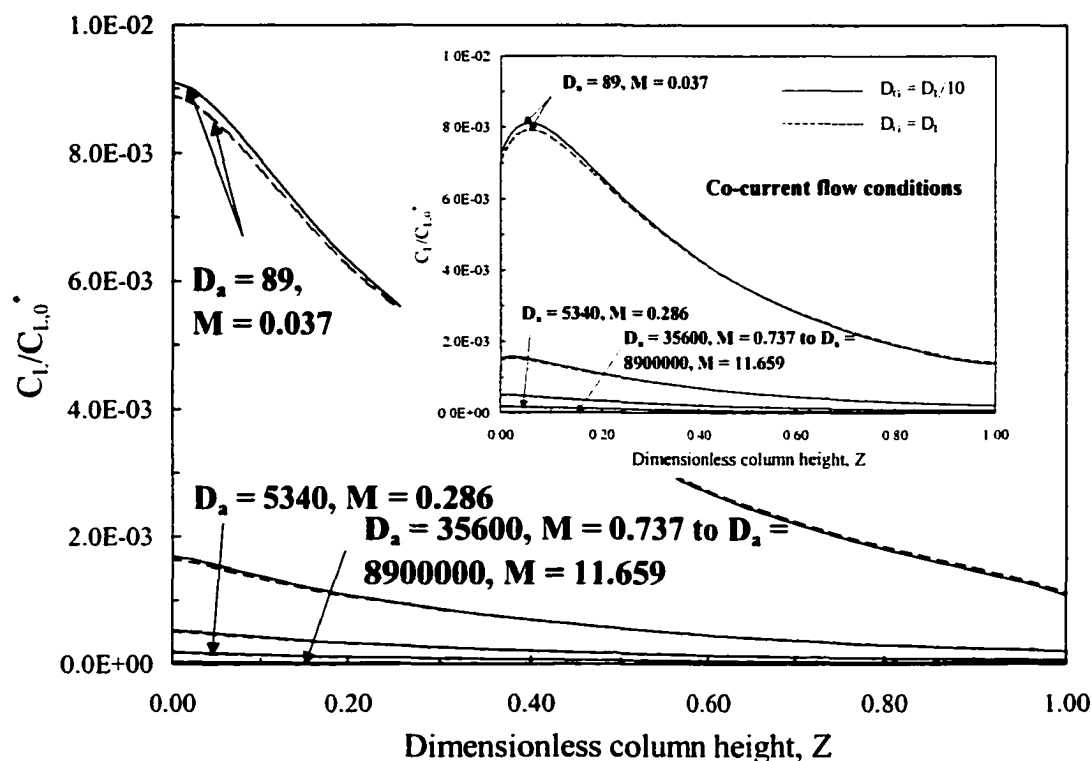


Figure 5.11  $D_a$  and  $M$  effects on the 2P-ADM predicted dissolved ozone concentration profiles in the counter and co-current flow mode and for wastewater treatment applications ( $D_a = 89$  and  $M = 0.037$  to  $D_a = 8900000$  and  $M = 11.659$ ).

Figure 5.11 depicts the effects of  $D_a$  and  $M$  on the dissolved ozone concentration profiles. The profiles, representing the co-current flow mode, are shown in a small-inserted picture. As  $D_a$  and  $M$  increased, the profiles became flatter till the concentrations virtually approached zero at  $35600 \leq D_a \leq 8900000$  and  $0.737 \leq M \leq 11.659$ . As shown in Figure 5.11, as  $D_a$  and  $M$  increased from 89 and 0.037 to 8900000 and 11.659, respectively, indicating the shift of the reaction kinetics from the slow to the fast regime. Also, the effluent dissolved ozone concentration decreased from about  $5.0 \times 10^{-3}$  to almost  $0.0 \text{ mgL}^{-1}$  and the rate of decrease in the effluent dissolved ozone concentration per increase in  $M$  decreased from  $1.4 \times 10^{-1}$  to  $6.6 \times 10^{-8}$ . The low values of the predicted dissolved ozone concentrations are in agreement with the observations of Zhou and Smith (1997). They reported that the dissolved ozone concentrations, in their continuous-flow

operations of the fine-diffuser ozone bubble column, were smaller than the detection limits and they were less insignificant compared to the amount of the applied ozone. Regarding the effect of  $D_G$ , the dissolved ozone concentrations for  $D_G = D_L$  were lower than those for  $D_G = D_L/10$ .

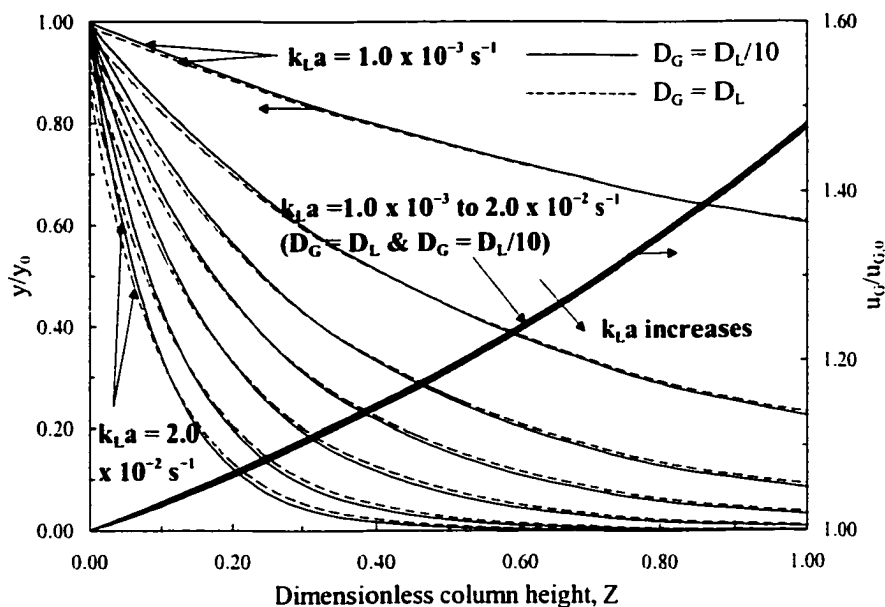


Figure 5.12  $k_{La}$  effects on the 2P-ADM predicted gaseous ozone concentration and superficial gas velocity profiles in the counter and co-current flow modes and for wastewater treatment applications ( $k_{La} = 1.0 \times 10^{-3}$ ,  $3.0 \times 10^{-3}$ ,  $5.0 \times 10^{-3}$ ,  $7.0 \times 10^{-3}$ ,  $1.0 \times 10^{-2}$ ,  $1.5 \times 10^{-2}$ , and  $2.0 \times 10^{-2} \text{ s}^{-1}$ ).

Figure 5.12 depicts the effects of  $k_{La}$  on the gaseous ozone concentration and superficial gas velocity profiles. As  $k_{La}$  increased from  $1.0 \times 10^{-3}$  to  $2.0 \times 10^{-2} \text{ s}^{-1}$ , the gaseous ozone concentration profiles became steeper and the effect of  $k_{La}$  on the profiles decreased. The rate of decrease in the ozone off-gas concentration per increase in  $k_{La}$  decreased from about  $3.2$  to  $3.0 \times 10^{-3}$  and was virtually identical for both  $D_G = D_L$  and  $D_G = D_L/10$ . As  $k_{La}$  increased, the ozone off-gas concentration decreased from about  $8.2$  to  $1.0 \times 10^{-3} \text{ mgL}^{-1}$ . The predicted ozone off-gas concentration, of  $1.0 \times 10^{-3} \text{ mgL}^{-1}$ , represents situations where the reactions between ozone and the liquid-phase impurities fall within the fast-reaction kinetics regime. This is in agreement with the observations of

Zhou and Smith (2000). They observed that the ozone off-gas concentrations were below the detection limit of the iodometric titration method (KI method) which is about  $7.0 \times 10^{-2} \text{ mgL}^{-1}$ . The same phenomena that was observed before in the water treatment conditions regarding the superficial gas velocity profiles were also observed in the model simulations for the wastewater treatment applications.

### 5.3.4 Model Testing for Water Treatment Applications

Figures 5.13 and 5.14 demonstrate the applicability of the 2P-ADM to predict the performance of the fine-diffuser ozone bubble column operating in a counter-current flow. There was excellent agreement between the predicted and the experimental dissolved ozone profiles. At 5 % significance level, t-tests have shown that there was no significant difference between the predictions of the different versions of the 2P-ADM.

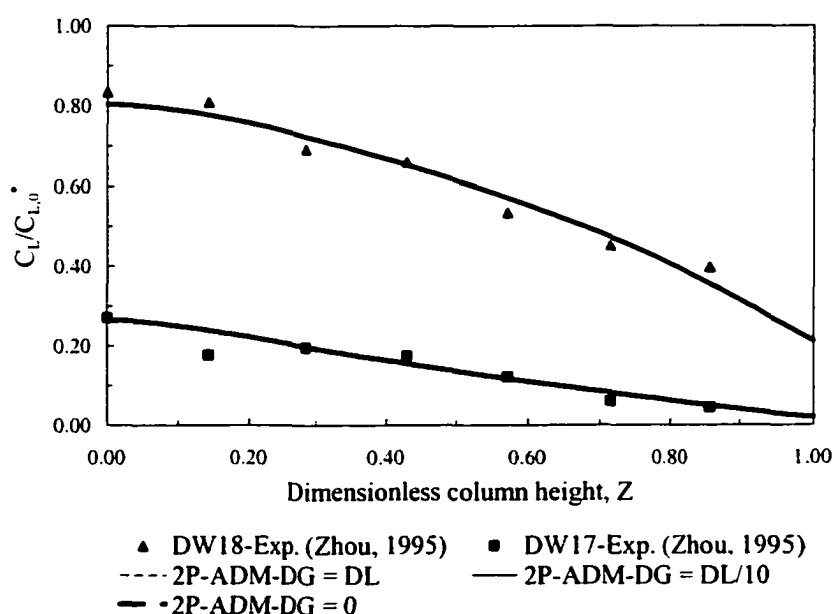


Figure 5.13 Comparison between the predicted and the measured dissolved ozone concentration profiles in a counter-current fine-bubble diffuser ozone bubble column for water treatment applications.

The same phenomenon was observed for the co-current flow mode. These observations are in agreement with the theoretical observations of Deckwer (1976) who suggested that the gas-phase dispersion could be ignored in bubble columns with diameters less than 500 mm. Although, it should be pointed out that in columns with small diameters, the assumption of the gas phase being in an ideal plug flow regime can be valid (Wachi and Morikawa, 1987), the gas-phase dispersion can be a significant factor in the ozonation process scale-up.

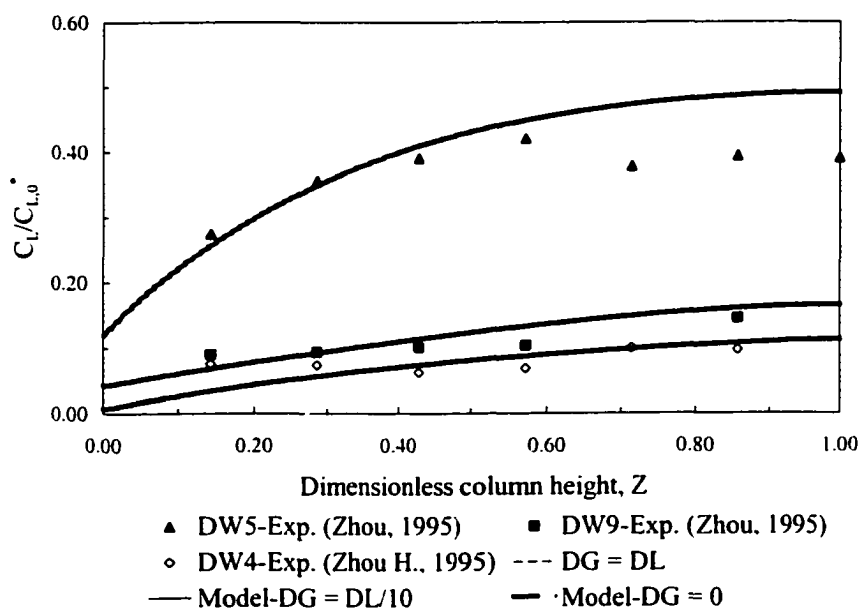


Figure 5.14 Comparison between the predicted and the measured dissolved ozone concentration profiles in a co-current fine-bubble diffuser ozone bubble column for water treatment applications.

## 5.4 CONCLUSIONS

The two-phase axial dispersion model (2P-ADM) has proven to be a powerful, accurate and reliable tool for predicting the performance of ozone contactors for both water and wastewater treatment applications. By applying the 2P-ADM instead of the traditionally applied models such as the plug flow model (PFM) or the continuous-flow stirred-tank-reactors (CFSTR's) in-series model, accurate and reliable designs of ozone contactors can be achieved. As a result, the operating and capital costs will be minimized and the desired treatment objectives can be met.

It should be noted that the current model testing is just an initial testing step. Therefore, further studies need to be conducted for both water and wastewater treatment applications and in different ozone contactors of different configurations, designs, and scales. This will help obtain a large and high-quality data set that can allow for further model testing in order to eliminate any uncertainties in the model predictions.

The simple version of the 2P-ADM that neglects the backmixing in the gas phase can be applied without affecting the accuracy of the model predictions in situations such as: (1) bubble columns that have large aspect ratios; and (2) when large bubbles are dominant in the gas-liquid flow as a result of using a gas sparging technique that creates large bubbles.

## 5.5 REFERENCES

1. Deckwer, W.-D., "Non-Isobaric Bubble Columns With Variable Gas Velocity", *Chem. Eng. Sci.* 31: 309-317 (1976).
2. Gamal El-Din, M. and D.W. Smith, "Designing Ozone Bubble Columns: A Spreadsheet Approach to Axial Dispersion Model", *Proc. of IOA/PAG Conf.: Advances in Ozone Technology*, Orlando, FL, USA, 2000.
3. Sotelo, J.L., F.J. Beltrán, F.J. Benitez, and J. Beltrán-Heredia, "Henry's Law Constant for the Ozone-Water System", *Wat. Res.* 23(10): 1239-1246 (1989).
4. TKSOLVER™, Release 3.32, Universal Technical Systems, Inc., IL, USA (1997).
5. Wachi, S. and H. Morikawa., "Chlorination of Ethylene in a Boiling Bubble Column Reactor", *J. Chem. Eng. Japan* 20: 238-245 (1987).
6. Zhou, H. and D.W. Smith, "Ozonation Dynamics and its Implication for Off-Gas Ozone Control in Treating Pulp Mill Wastewaters", *Ozone Sci & Eng.* 22: 31-51 (2000).
7. Zhou, H. and D.W. Smith, "Applying Mass Transfer Theory to Study the Kinetics of Fast Ozone Reactions in Pulp Mill Effluents", *Proc. of the 14<sup>th</sup> Ozone World Congress*, Detroit, MI, USA, 1999.
8. Zhou, H. and D.W. Smith, "Process Parameter Development for Ozonation of Kraft Pulp Mill Effluents", *Wat. Sci. & Technol.* 35(2-3): 251-259 (1997).
9. Zhou, H., *Investigation of Ozone Disinfection Kinetics and Contactor Performance Modeling: Ph.D. Thesis* (Edmonton, AB, Canada: University of Alberta, 1995).
10. Zhou, H., D.W. Smith, and S.J. Stanley, "Modeling of Dissolved Ozone Concentration Profiles in Bubble Columns", *J. Environ. Eng., ASCE* 120(4): 821-840 (1994).

## CHAPTER 6. THEORETICAL ANALYSIS AND EXPERIMENTAL VERIFICATION OF OZONE MASS TRANSFER IN BUBBLE COLUMNS\*

### 6.1 INTRODUCTION

During the course of ozonation, convection and backmixing processes of the liquid and gas phases flowing through the contacting chamber, ozone gas mass transfer process, ozone decay process, and competitive reactive processes of constituents in water and wastewater with dissolved ozone occur simultaneously (Zhou *et al.*, 1994). In addition to those processes, contactor configuration, operating conditions, and water or wastewater quality influence the overall performance of the ozonation treatment (Zhou, 1995). The ozonation process depends on the mass transfer of ozone gas into the liquid phase. Quantifying the dissolved ozone is essential for achieving reliable rational-design and optimum operation of ozone contactors while quantifying the off-gas ozone concentration leaving the contactor is important for achieving proper design of the ozone off-gas destruction facilities.

Several researchers have extensively studied the fundamentals of the processes dictating the performance of ozonation systems in water treatment over the last two decades (Langlais *et al.*, 1991). However, fewer studies have been conducted to examine the ozone mass transfer mechanisms and the effect of chemical oxidation on the rate of ozone absorption when treating industrial wastewater. Zhou and Smith (1997) showed that during the ozonation of Kraft pulp mill effluents, the chemical reactions were fast enough for the dissolved ozone to be completely depleted at the gas-liquid interface and/or within the liquid film. As a result, the dissolved ozone gradient became steeper than the one of the maximum physical absorption process. As shown in Figure 6.1, two distinct reaction kinetics regimes for the ozone gas absorption process were proposed by Zhou and Smith (1997): the fast or instantaneous-reaction kinetics regime and the slow-reaction kinetics regime. The relative rate of the gas absorption process with the occurrence of chemical reactions compared to the maximum physical gas absorption rate will determine the prevailing mass transfer regime (Zhou and Smith, 1997).

---

A version of this chapter has been accepted for publication. Smith, D.W. and M. Gamal El-Din, *Environ. Technol.* (May 2001).

Due to the low dissolved ozone concentrations during the mass transfer process occurring in the fast-reaction kinetics regime, the driving force of the mass transfer process is increased and also the local mass transfer coefficient will be enhanced by an enhancement factor ( $E$ ). During the ozonation of Kraft pulp mill effluents and regarding the gas absorption process, it was assumed that the fast or instantaneous-reaction kinetics regime prevailed at the beginning of the ozonation process as the amount of the utilized ozone was still relatively small (Zhou and Smith, 1997). That assumption was based on the experimental observations of Zhou and Smith (1997) that no dissolved ozone concentrations were detected during the course of ozonation. As the ozonation treatment proceeded, the gas absorption process shifted from the fast or instantaneous-reaction kinetics regime to the slow-reaction kinetics regime and the enhancement factor decreased (Zhou and Smith, 1997).

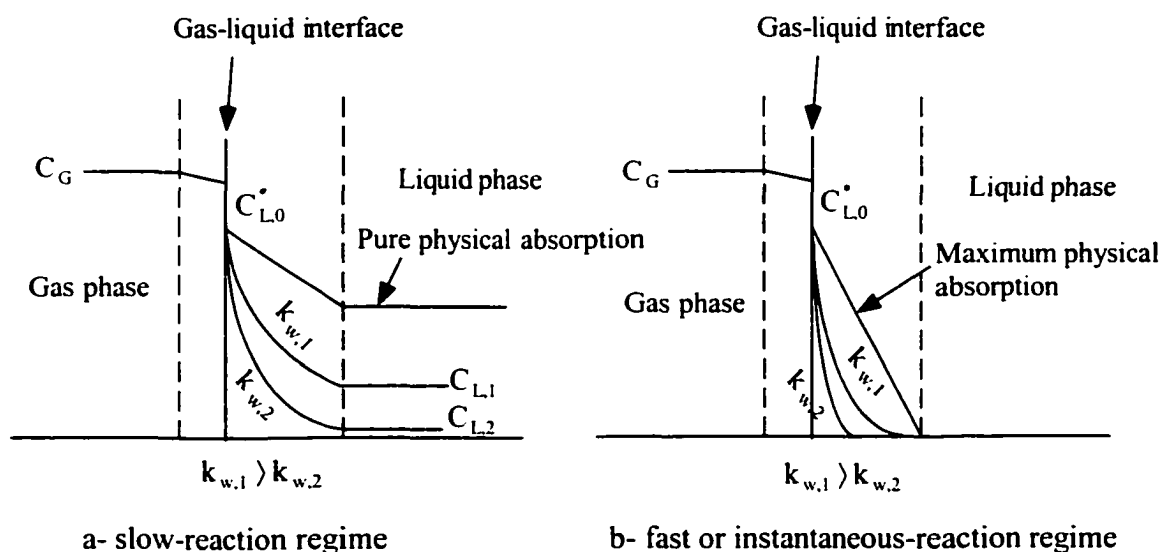


Figure 6.1 Reaction kinetics regimes for ozone absorption process (adapted from Zhou and Smith, 1997).

The mathematical models that were usually applied to predict the dissolved ozone and gaseous ozone profiles along ozone bubble columns were based on one of the following liquid-phase flow regimes: (1) complete mixing or; (2) plug flow (Alvarez-Cuenca *et al.*, 1980; Alvarez-Cuenca *et al.*, 1981; Chang and Chian, 1981; Laplanche *et al.*, 1991; Hull *et al.*, 1992, Lev and Regli, 1992). Neither one of those two liquid-phase

flow regimes can adequately describe the actual liquid-phase flow conditions in bubble columns as a result of the actual liquid-flow pattern in bubble columns usually being closer to mixed flow rather than plug flow, but still not completely mixed flow. Because of the low solubility and high reactivity of ozone gas, effective improvement and accurate quantification of the ozone absorption process is essential for achieving proper design and optimum operation of ozonation systems (Zhou, 1995). This goal can be met by applying more reliable and accurate models that can adequately describe the ozone gas absorption process in water and wastewater treatment applications.

This chapter presents: (1) the applicability of the back flow cell model (BFCM) and the axial dispersion model (ADM) for describing the ozonation process in bubble columns, and (2) initial testing of the models' predictions of the dissolved ozone concentration profiles, for water treatment applications, using the pilot-scale experimental data of Zhou (1995).

## 6.2 THEORETICAL BACKGROUND

In order to model the performance of ozone bubble columns, it is crucial to describe and quantify the rates of various physical and chemical processes that occur during the ozonation treatment. In tubular bubble columns, the non-ideal flow conditions affect the rate of absorption and the concentration profiles of dissolved and gaseous ozone. Although, a number of researchers proposed the BFCM for describing the performance of ozone bubble columns (Zhou *et al.*, 1994; Gamal El-Din and Smith, 2000b), the axial dispersion model has received the largest attention among researchers. In the ADM, it is assumed that the liquid phase is in axial dispersion regime, i.e., a diffusion-like process is assumed and superimposed on a plug flow regime (Levenspiel, 1972). During surface water ozonation, it was observed that the overall ozone auto-decomposition rate was influenced by the instantaneous dissolved ozone concentration and the changes in the properties of the water during the course of ozonation (Watt *et al.*, 1989; Zhou, 1995). Accordingly, a modified pseudo-first-order rate expression was proposed. In that

expression, the reaction rate constant was replaced by a variable referred to as the specific ozone utilization rate constant ( $k_w$ ):

$$\frac{dC_L}{dt} = -k_w C_L \quad [6.1]$$

where:  $C_L$  = instantaneous concentration of the dissolved ozone in the bulk liquid ( $\text{mgL}^{-1}$ ) and  $k_w$  = specific ozone utilization rate constant ( $\text{s}^{-1}$ ).

The mass transfer of ozone gas from the gas phase into the liquid phase can be described and quantified by the two-film model in which the rate of gas absorption ( $\psi$ ) is defined as:

$$\psi = k_L a (C_L^* - C_L) \quad [6.2]$$

where:  $\psi$  = gas absorption rate ( $\text{mgL}^{-1}\text{s}^{-1}$ ),  $k_L$  = local mass transfer coefficient ( $\text{ms}^{-1}$ ),  $a$  = gas bubbles' specific interfacial area ( $\text{m}^{-1}$ ),  $C_L^*$  = concentration of dissolved ozone in equilibrium with the ozone in the gas-phase ( $\text{mgL}^{-1}$ ), and  $C_L$  = concentration of the dissolved ozone in the bulk liquid ( $\text{mgL}^{-1}$ ). Ozone gas diffuses much faster in the gas phase than in the liquid phase, therefore, the mass transfer in the liquid phase becomes a rate-controlling step and the overall mass transfer coefficient is considered to entirely consist of the local mass transfer coefficient in the liquid phase. Ozonation of wastewater involves chemical reactions and the dimensionless squared Hatta number (referred to as  $H_a^2$  or  $E^2$  or  $M$ ) is used as a measure of the amount of dissolved ozone that reacts at the gas-liquid interface or in the liquid film near the interface compared to the amount of dissolved ozone that reaches the bulk liquid in an unreacted state. The dimensionless-squared Hatta number is defined as:

$$H_a^2 = E^2 = M = \frac{D_{O_3} k_w}{k_L^2} \quad [6.3]$$

where:  $D_{O_3}$  = molecular diffusivity of ozone in water ( $m^2s^{-1}$ ),  $k_L$  = local mass transfer coefficient ( $ms^{-1}$ ), and  $k_w$  = specific ozone utilization rate constant ( $s^{-1}$ ). Two distinctive regions of the location of reactions that occur during the ozone mass transfer process could be defined (Danckwerts; 1970; Kaštánek *et al.*, 1993). For  $H_a < 0.03$ , reactions would occur in the bulk of the liquid, while for  $H_a > 3.00$ , reactions would occur at the gas-liquid interface or in the liquid film near the interface. Therefore, for  $0.03 < H_a < 3.00$ , reactions would occur simultaneously in both regions. For a first-order irreversible reaction, Equation 6.3 is only applicable when  $M \gg 1$  (Danckwerts, 1970). This is usually the case for fast or instantaneous irreversible first-order reactions with no bulk liquid concentration where the driving force for the mass transfer will be maximized. For such a case, Equation 6.2 would become:

$$\psi = Ek_L a C_L^* \quad [6.4]$$

where:  $Ek_L a$  = enhanced overall mass transfer coefficient ( $s^{-1}$ ). For wastewater ozonation, we could assume that both ozone auto-decomposition and its reactions with the organic and inorganic constituents in wastewater could be lumped together in one rate constant ( $k_w$ ) (Zhou and Smith, 1999). During the ozonation of surface water, little enhancement of the mass transfer rate will occur leading to a lower value of  $M$  compared to those values encountered in wastewater ozonation. As a result, Equation 6.2 becomes:

$$\psi = k_L a \sqrt{1+M} \left( C_L^* - \frac{C_L}{1+M} \right) \quad [6.5]$$

For surface water ozonation and assuming that ozone reactions with the various impurities that are present in water follow an irreversible first-order kinetics, the effect of chemical reactions on the mass transfer coefficient can be neglected when  $M \ll 1$  (Danckwerts, 1970; Gamal El-Din and Smith, 2000b). As a result, the ozone gas absorption process can be dealt with as a pure physical absorption process as described by Equation 6.2.

### 6.3 OUTLINE OF THE MATHEMATICAL MODELS AND THE NUMERICAL SOLUTIONS TECHNIQUES

#### 6.3.1 Axial Dispersion Model (ADM)

The ADM visualizes the flow of fluids in tubular bubble columns as a plug flow on top of which a diffusion-like process is superimposed (Levenspiel, 1972). When modeling two-phase flows in bubble columns, several assumptions should be considered for the development and the formulation of the ADM. Detailed presentation of those assumptions can be found elsewhere (Zhou *et al.*, 1994; Gamal El-Din and Smith, 2000a). Considering the control volume shown in Figure 6.2, and conducting mass balance analyses in the liquid and the gas phases and applying mathematical manipulations, one can obtain the non-linear differential equations representing the ADM as reported before by Zhou *et al.* (1994) and Gamal El-Din and Smith (2000a). The ADM equations are presented in Table 6.1 and the dimensionless parameters pertaining to those equations are presented in Table 6.3.

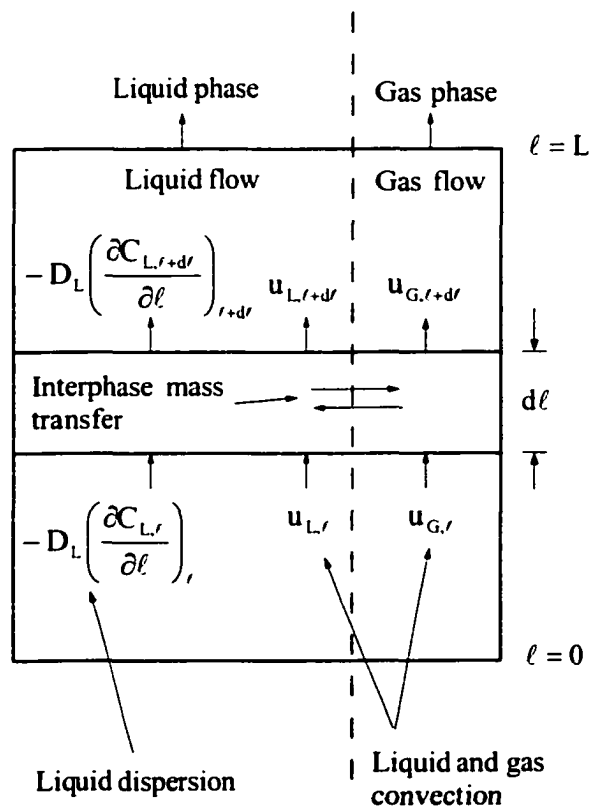


Figure 6.2 Schematic representation of the co-current ADM.

Table 6.1 Mathematical representation of the ADM (Zhou *et al.*, 1994; Gamal El-Din and Smith, 2000a).

Fluid phase		Equations
Aqueous ozone		$\frac{1}{Pe_L} \frac{\partial^2 X}{\partial Z^2} + a' \frac{\partial X}{\partial Z} + \frac{\sqrt{1+M} St_L}{\beta} (\beta - \alpha Z) Y - \left( \frac{St_L}{\sqrt{1+M}} + D_s \right) X = 0$
Gaseous ozone		$\frac{\partial Y}{\partial Z} + \frac{St_G}{\beta(1-y_0)} (1-y_0 Y)^2 \left[ \sqrt{1+M} (\beta - \alpha Z) Y - \frac{\beta}{\sqrt{1+M}} X \right] = 0$
Closed-closed boundary conditions	Co-current flow mode	at $Z = 0$ : $X_{inf} = X _{Z=0} - \frac{1}{Pe_L} \frac{\partial X}{\partial Z} \Big _{Z=0}$ $Y = 1$ at $Z = 1$ : $\frac{\partial X}{\partial Z} \Big _{Z=1} = 0$
	Counter-current flow mode	at $Z = 0$ : $\frac{\partial X}{\partial Z} \Big _{Z=0} = 0$ $Y = 1$ at $Z = 1$ : $X _{Z=1} = X_{inf} - \frac{1}{Pe_L} \frac{\partial X}{\partial Z} \Big _{Z=1}$

Note:

$a' = -1$  for co-current flow mode

$a' = +1$  for counter-current flow mode

$M = 0$  for surface water treatment

$M > 0$  for wastewater treatment

As shown in Table 6.1, the ADM is described mathematically by a set of two non-linear partial differential equations that were solved numerically by applying a backward (upwind) finite difference scheme to transform those equations into non-linear algebraic equations. In the finite difference scheme, the total height of the column along the direction of the main liquid flow was divided into 50 elements. As a result, 51 nodes were

used and that led to 102 equations in addition to the boundary conditions' equations. Those equations were solved numerically using the Newton Raphson technique by utilizing the TKSOLVER™ software. The program executed until a user-specified comparison tolerance of  $10^{-6}$  was satisfied. The program execution time was under a minute using a 366 MHz processor.

### 6.3.2 Back Flow Cell Model (BFCM)

The BFCM is another mathematical model that is used to describe the performance of ozone bubble columns. The BFCM hypothesizes a back flow ( $Q_B$ ) in the opposite direction to the main liquid flow ( $Q_L$ ) and an exchange flow ( $Q_B$ ) in the main direction of the liquid flow (Zhou and Smith, 1994; Gamal El-Din and Smith, 2000b). Those two flows are used to characterize the axial dispersion in the liquid phase.

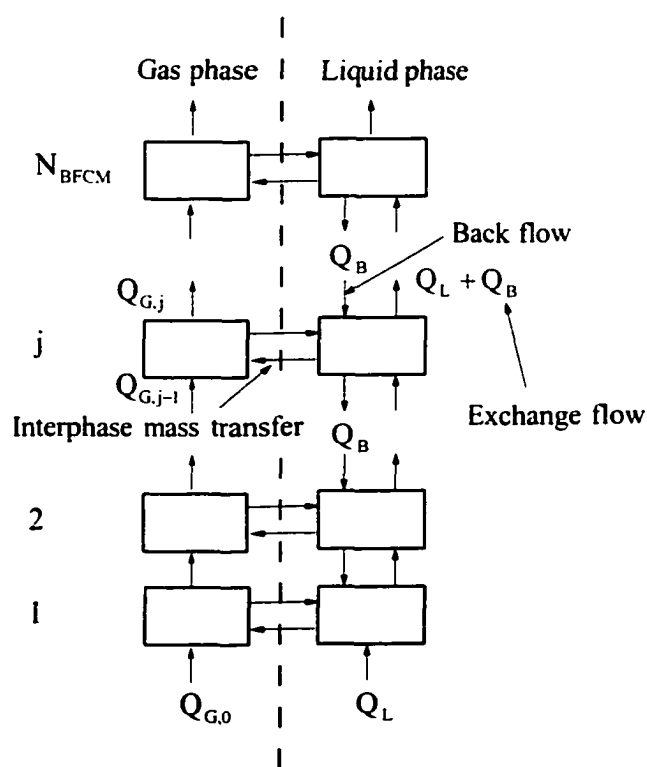


Figure 6.3 Schematic representation of the co-current BFCM.

Table 6.2 Mathematical representation of the BFCM (Gamal El-Din and Smith, 2000b).

Fluid phase	Equations
Aqueous ozone	<p><b>j = 1:</b></p> $a_2 X_0 - \left(1 + r + D_a + \frac{St_L}{1+M}\right) X_1 + (a_1 + r) X_2 + \sqrt{1+M} St_L \left(1 + \frac{\alpha}{2}\right) Y_1 = 0$ <p><b>2 ≤ j ≤ N<sub>BFCM</sub>-1:</b></p> $(a_2 + r) X_{j-1} - \left(1 + 2r + D_a + \frac{St_L}{1+M}\right) X_j + (a_1 + r) X_{j+1} + \sqrt{1+M} St_L [1 + \alpha(j-0.5)] Y_j = 0$ <p><b>j = N<sub>BFCM</sub>:</b></p> $a_1 X_0 + (a_2 + r) X_{N_{BFCM}-1} - \left(1 + r + D_a + \frac{St_L}{1+M}\right) X_{N_{BFCM}} + \sqrt{1+M} St_L [1 + \alpha(N_{BFCM} - 0.5)] Y_{N_{BFCM}} = 0$
Gaseous ozone	<p><b>j = j:</b></p> $(1 + \alpha(j-1.5)) q_{G,j-1} Y_{j-1} - (1 + \alpha(j-0.5)) q_{G,j} Y_j - \sqrt{1+M} St_G \left[ (1 + \alpha(j-0.5)) Y_j - \frac{X_j}{1+M} \right] = 0$
Total gas	<p><b>j = j:</b></p> $(1 + \alpha(j-1.5)) q_{G,j-1} - (1 + \alpha(j-0.5)) q_{G,j} - \sqrt{1+M} St_G y_0 \left[ (1 + \alpha(j-0.5)) Y_j - \frac{X_j}{1+M} \right] = 0$
Closed-closed boundary conditions	$X_0 = \frac{C_{L,inf}}{C_{L,0}}, Y_0 = 1, q_{G,0} = 1$

Note:

$a_1 = 0$  and  $a_2 = +1$  for co-current flow mode

$a_1 = +1$  and  $a_2 = 0$  for counter-current flow mode

$M = 0$  for surface water treatment

$M > 0$  for wastewater treatment

Figure 6.3 represents a BFCM schematic for co-current flow conditions in bubble columns where the back flow ratio ( $Q_B/Q_L$ ) is equal to the exchange flow ratio and both are assumed to remain constant along the column height. The BFCM consists of two series of completely mixed cells in which one series represents the liquid phase and the other represents the gas phase and each has a number of cells equal to  $N_{BFCM}$  (Mecklenburgh and Hartland, 1975; Deckwer and Hallensleben, 1980). The same assumptions that were used to develop the ADM equations were used to develop the BFCM equations. Considering the BFCM schematic shown in Figure 6.3 and conducting mass balance analyses for the liquid and gas phases and applying mathematical manipulations, one can obtain the non-linear algebraic equations representing the BFCM as reported before by Gamal El-Din and Smith (2000b). The BFCM equations are presented in Table 6.2 and the dimensionless parameters pertaining to those equations are presented in Table 6.3. As shown in Table 6.2, the BFCM is described mathematically by a set of  $3 \times N_{BFCM}$  non-linear algebraic equations. Those equations were numerically solved using the Newton Raphson technique by utilizing the TKSOLVER™ software. Compared to the ADM, the BFCM was easier to formulate and solve as a result of the BFCM equations being in a non-linear algebraic form while the ADM non-linear differential equations had to be transformed first into non-linear algebraic form before applying the Newton Raphson technique to obtain their solutions.

It should be noted that the BFCM and the ADM describe the backmixing of the liquid phase using different mixing parameters ( $Pe_L$ , and  $r$ ). Those parameters are interrelated by the following relationship (Mecklenburgh and Hartland, 1975):

$$r = \frac{N_{BFCM}}{Pe_L} - 0.5 = \frac{D_L \epsilon_L N_{BFCM}}{u_L L} - 0.5 \quad [6.6]$$

where:  $N_{BFCM}$  = number of cells in series,  $r = \frac{Q_B}{Q_L}$  = back flow ratio = exchange flow ratio (dimensionless),  $Pe_L$  = Peclet number (dimensionless),  $D_L$  = liquid-phase axial dispersion

coefficient ( $\text{m}^2\text{s}^{-1}$ ),  $\varepsilon_L$  = liquid-phase hold-up (dimensionless), and  $u_L$  = superficial liquid-phase velocity ( $\text{ms}^{-1}$ ).

Table 6.3 Dimensionless parameters pertaining to the ADM and the BFCM.

Dimensionless parameter	ADM	BFCM
Z	$\ell/L$	$(j-0.5)/N_{\text{BFCM}}$
$\alpha$	$\rho g \varepsilon_L L / P_T$	$-\rho g \varepsilon_L L / N_{\text{BFCM}} P_0$
$\beta$	$1 + \alpha$	
r		$Q_B / Q_L$
$Pe_L$	$u_L L / D_L \varepsilon_L$	
$St_L$	$k_L a L / u_L$	$k_L a L / N_{\text{BFCM}} u_L$
$St_G$	$(k_L a L / u_{G,0})(RT/H)$	$(k_L a L / N_{\text{BFCM}} u_{G,0})(RT/H)$
$D_a$	$k_w \varepsilon_L L / u_L$	$k_w \varepsilon_L L / N_{\text{BFCM}} u_L$
M	$Dk_w / k_L^2$	$Dk_w / k_L^2$
X, $X_j$	$C_{L,r} / C_{L,0}^*$	$C_{L,j} / C_{L,0}^*$
Y, $Y_j$	$y_r / y_0$	$y_j / y_0$
$q_{G,j}$		$Q_{G,j} / Q_{G,0}$

## 6.4 OPERATING CONDITIONS FOR MODELS TESTING AND NUMERICAL ANALYSES

### 6.4.1 Water Treatment

The ADM and the BFCM were tested, for the ozone applications in water treatment, using the pilot-scale experimental data of Zhou (1995). The pilot-scale bubble column used in those experiments was a cylindrical glass column with an inside diameter of 100 mm and a height of 2000 mm. The water depth was kept constant at 1750 mm using an overflow weir. A 25 mm spherical fused crystalline aluminum stone was utilized as the gas sparger. Detailed information on those experiments and their operating conditions can be found in Zhou (1995). The operating conditions for the co-current and the counter-current flow modes are shown in Table 6.4. Based on the kinetics experiments conducted

by Zhou (1995) to characterize the ozone decay process in deionized water, the pseudo-first-order specific ozone utilization rate constant ( $k_w$ ) was found to be equal to  $4.7 \times 10^{-4} \text{ s}^{-1}$ .

Table 6.4 Operating conditions for the co-current and counter-current flow modes (water treatment).

Run #	Flow mode	$Q_L (\text{m}^3 \text{s}^{-1})$	$Q_G (\text{m}^3 \text{s}^{-1})$	Inlet $\text{O}_3$ gas conc. (% w/w)	Water temperature ( $^\circ\text{C}$ )	$N_{\text{BFCM}}$	$Pe_L$	$r$	$C_{L,0}^* (\text{mgL}^{-1})$
DW4	↑↑	1.1E-04	5.0E-06	1.98	21	10	34.5	-0.21	7.2
DW5		1.1E-04	3.7E-05	0.26	21	10	17.9	0.06	0.9
DW9		4.6E-05	3.1E-05	0.25	21	10	4.6	1.66	0.9
DW17	↑↓	4.6E-05	5.3E-06	1.54	21	10	10.5	0.45	5.6
DW18		4.6E-05	3.1E-05	0.25	21	10	5.4	1.37	0.9

#### 6.4.2 Wastewater Treatment

During the ozonation of Kraft pulp mill effluents, the overall pseudo-first-order ozone specific utilization rate constant ( $k_w$ ) ranged from 1,000 to 5,000  $\text{s}^{-1}$  and the enhancement factor ( $E$ ) ranged from 2 to 10 (Zhou and Smith, 1999). Also, the local mass transfer coefficient ( $k_L$ ) ranged from 0.066 to 0.093  $\text{ms}^{-1}$  and the overall mass transfer coefficient ( $k_{L,a}$ ) ranged from  $8.3 \times 10^{-3}$  to  $2.5 \times 10^{-2} \text{ s}^{-1}$ .

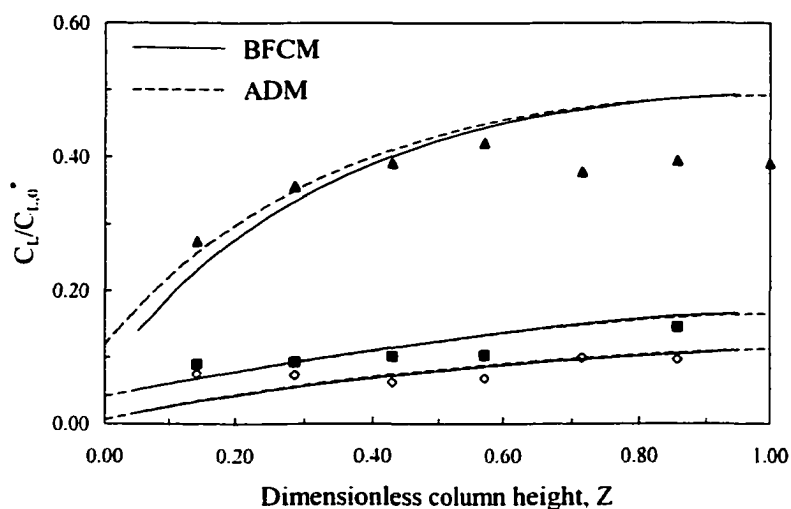
In order to examine the effects of  $Pe_L$  and  $k_{L,a}$  on the dissolved ozone, gaseous ozone, and superficial gas velocity profiles in bubble columns for wastewater treatment

applications, the following typical conditions for the operation of ozonation systems were assigned as the base values for the numerical analyses: column height ( $L$ ) = 5,000 mm, ozone concentration in the feed gas ( $C_0$ ) = 1 % (w/w %), applied ozone dosage = 1.35 mg/L, mean hydraulic detention time =  $\tau$  = 180 s,  $Pe_L$  = 5.0,  $k_w$  =  $0.5 \text{ s}^{-1}$ ,  $k_{La}$  =  $5 \times 10^{-3} \text{ s}^{-1}$ ,  $k_L$  =  $8 \times 10^{-4} \text{ ms}^{-1}$ , bubble column aspect ratio =  $L/D$  = 12.5, and gas-to-liquid flow ratio ( $G/L$ ) = 0.1. The Henry's law constant ( $H$ ) was set equal to  $0.22 \text{ kPaLmg}^{-1}$  (Sotelo *et al.*, 1989). The liquid-phase temperature was assumed to be  $20 \text{ }^\circ\text{C}$ . The basic model input parameters were then calculated and for the ADM as an example they were as follows: Peclet number ( $Pe_L$ ) = 5.0, liquid-phase Stanton number ( $St_L$ ) = 0.9, gas-phase Stanton number ( $St_G$ ) = 2.07, Damköhler number ( $D_3$ ) = 89,  $M$  = 0.037,  $\alpha$  (see Table 6.3) = 0.48, and the dimensionless mole fraction of ozone in the feed gas ( $y_0$ ) = 0.00675. The relatively low values of  $k_w$  and  $M$  were chosen for the models' simulations to investigate the effect of chemical reactions when they occur simultaneously near and/or at the gas-liquid interface and in the bulk liquid as it is usually the case when treating wastewaters that have relatively low reactivity towards ozone. The basic value assigned for  $Pe_L$  represents the typical mixing conditions that are normally encountered in ozone contactors of similar aspect ratios to the one assumed for the models' simulations. With respect to  $k_{La}$ , the chosen value of  $5.0 \times 10^{-3} \text{ s}^{-1}$  represents the ozone mass transfer conditions that are usually encountered in wastewaters of relatively low reactivity towards ozone. The sensitivity analyses of the models' predictions to changes in  $Pe_L$  and  $k_{La}$ , respectively, were performed by varying each one of the two parameters while maintaining the other one constant.

## 6.5 RESULTS AND DISCUSSION

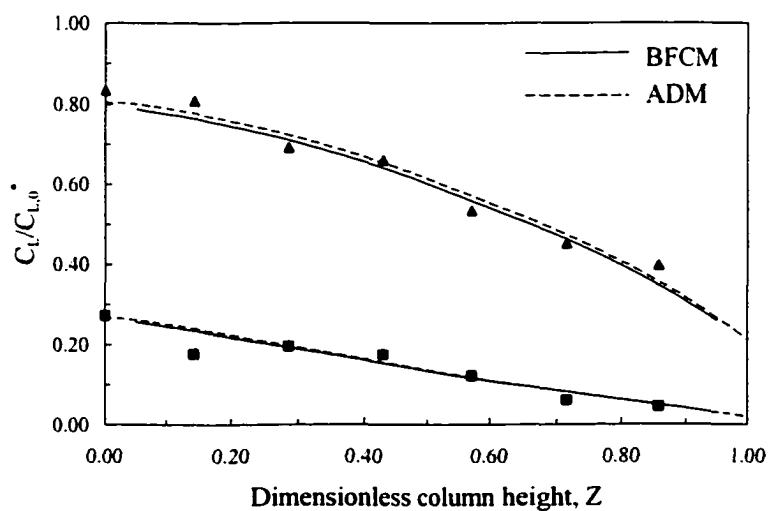
### 6.5.1 Water Treatment: Initial Testing of the Models

Figures 6.4 and 6.5 for the co-current and the counter-current flow modes, respectively, illustrate the applicability of the steady-state ADM and BFCM to describe the performance of ozone bubble columns in which conventional fine bubble diffusers were used as the gas spargers.



▲ DW5-Exp. (Zhou, 1995) ■ DW9-Exp. (Zhou, 1995) ◊ DW4-Exp. (Zhou, 1995)

Figure 6.4 Comparison between the predicted and the measured dissolved ozone concentrations in a co-current bubble column for water treatment applications.



▲ DW18-Exp. (Zhou, 1995) ■ DW17-Exp. (Zhou, 1995)

Figure 6.5 Comparison between the predicted and the measured dissolved ozone concentrations in a counter-current bubble column for water treatment applications.

The two models predicted virtually identical dissolved ozone concentration profiles except for run DW5 (co-current flow mode), where the two models were slightly different in their predictions in the vicinity of the column entrance (first quarter of the total column height). That could be explained by the concentration jump (due to the backmixing) predicted by the ADM at the column entrance being somewhat higher than it should be as a result of assigning a lower value to the  $Pe_L$  as one of the operating parameters in the ADM simulations. Generally, the two models were capable of providing good predictions of the dissolved ozone concentration profiles with the exception of few data points where the predicted concentrations were slightly deviated from the measured concentrations.

### 6.5.2 Wastewater Treatment

The dissolved ozone, gaseous ozone, and superficial gas velocity profiles were virtually identical for the co-current and the counter-current flow modes with the exception that the dissolved ozone concentration profiles did not exhibit a concentration jump near the bottom of the column for the case of ADM predictions in the counter-current flow mode. As shown in Figures 6.6 to 6.9, the profiles of the dissolved ozone, the gaseous ozone, and the superficial gas velocity are presented as functions of the dimensionless axial co-ordinate ( $Z$ ) in the co-current flow mode. The effects of the superficial liquid velocity ( $u_L$ ) and the superficial gas velocity ( $u_G$ ) were investigated together by studying the effects of the overall mass transfer coefficient ( $k_L a$ ). This is because the liquid-phase dimensionless Stanton number ( $St_L$ ) and the gas-phase dimensionless Stanton number ( $St_G$ ) take into account the effects of  $u_L$  and  $u_G$ , respectively, and both  $St_L$  and  $St_G$  are directly proportional to  $k_L a$ .

As shown in Figure 6.6 and Figure 6.8, the ADM predicted a peak of the dissolved ozone profiles near the bottom of the column ( $Z < 0.1$ ). This concentration jump is due to the boundary condition applied at the column inlet under the co-current flow conditions. The same phenomenon was reported before by several researchers (Levenspiel, 1972; Zhou *et al.*, 1994; Zhou and Smith, 1994; Zhou, 1995; Gamal El-Din and Smith, 2000a).

The BFCM did not predict the same concentration jump due to the fact that only 10 cells were used for the model simulations and complete mixing was assumed to take place in each cell. The dissolved ozone concentration profiles started from their highest points near the bottom of the column then monotonically decreased along the column height. In both models' predictions, the gradient of the dissolved ozone profiles exhibited a decreasing trend near the bottom of the column, followed by an increasing trend. The two models were more sensitive to changes in  $k_L a$  than changes in  $Pe_L$  in their predictions of the dissolved ozone profiles.

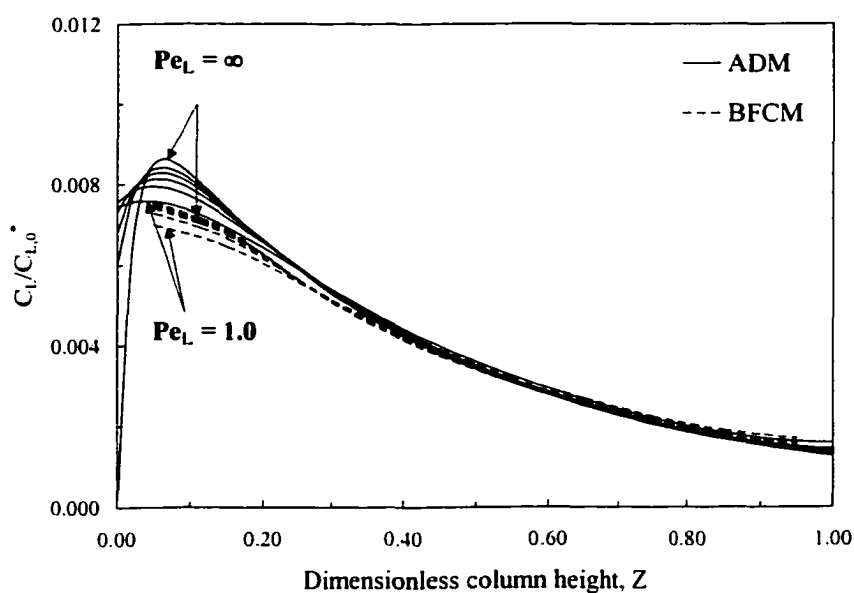


Figure 6.6 Effect of  $Pe_L$  on the dissolved ozone profiles in the co-current flow mode for wastewater treatment applications ( $Pe_L = 1.0, 2.5, 5.0, 10.0, 20.0,$  and  $\infty$ ),  $D_a = 89$ ,  $k_L a = 5.0 \times 10^{-3} \text{ s}^{-1}$ ,  $M = 0.037$ ,  $\alpha = 0.48$ , and  $y_0 = 0.00675$ ).

The effect of backmixing, characterized by  $Pe_L$ , on the dissolved ozone profiles are shown in Figure 6.6. As  $Pe_L$  increased, the extent of backmixing decreased as the liquid flow was approaching plug flow conditions. Therefore, the dissolved ozone profile became steeper and the peak of the profile increased. Also as  $Pe_L$  increased and at a dimensionless co-ordinate beyond  $Z \cong 0.25$ , the dissolved ozone concentration profiles became steeper leading to lower effluent-residual ozone concentrations.

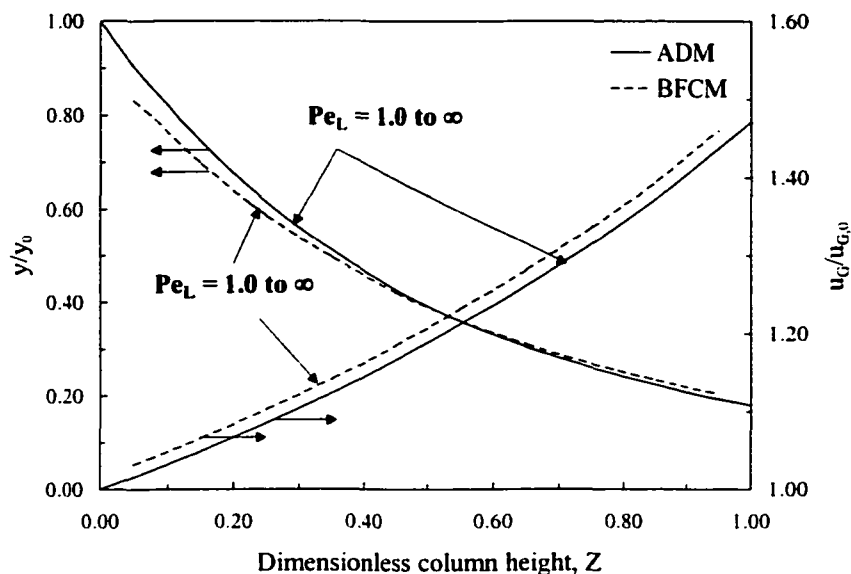


Figure 6.7 Effects of  $Pe_L$  on the gaseous ozone and the superficial gas velocity profiles in the co-current flow mode for wastewater treatment applications ( $Pe_L = 1.0, 2.5, 5.0, 10.0, 20.0,$  and  $\infty$ ),  $D_a = 89$ ,  $k_{La} = 5.0 \times 10^{-3} \text{ s}^{-1}$ ,  $M = 0.037$ ,  $\alpha = 0.48$ , and  $y_0 = 0.00675$ ).

This phenomenon could be explained by the fact that most of the gaseous ozone would be consumed before reaching the end of the column height, and thus, resulting in a lower driving force for the mass transfer process and causing lower ozone residuals in the effluent. Regarding the predictions of the ADM and the BFCM, the effect of  $Pe_L$  was higher in the range of  $Pe_L$  from 1.0 to 2.5 than in the range of  $Pe_L$  from 2.5 to infinity. With respect to the effect of  $Pe_L$  and compared to the BFCM, the ADM predicted higher dissolved ozone concentrations with the exception in the top quarter of the column where it predicted lower concentrations.

As shown in Figure 6.8 and as  $k_{La}$  increased from  $1 \times 10^{-3}$  to  $5 \times 10^{-3} \text{ s}^{-1}$ , an increase in the dissolved ozone concentrations occurred along the entire height of the column. Then as  $k_{La}$  increased from  $5 \times 10^{-3}$  to  $1 \times 10^{-2} \text{ s}^{-1}$ , an increase in the dissolved ozone concentrations occurred in the bottom half of the column. Finally, as  $k_{La}$  increased from  $1 \times 10^{-2}$  to  $2 \times 10^{-2} \text{ s}^{-1}$ , an increase in the dissolved ozone concentrations occurred

in the bottom quarter of the column. Based on these observations, more efforts should be directed towards enhancing the mass transfer process in the vicinity of the column entrance that could lead to higher treatment levels in ozone bubble columns. Therefore, the use of new gas sparging techniques such as venturi injectors could improve the mass transfer process, and consequently, lead to higher ozonation treatment levels. The venturi injectors can be used to create two-phase impinging turbulent jets in the ambient fluid that can lead to an increase in the mass transfer rates by maximizing the turbulence produced in the liquid phase.

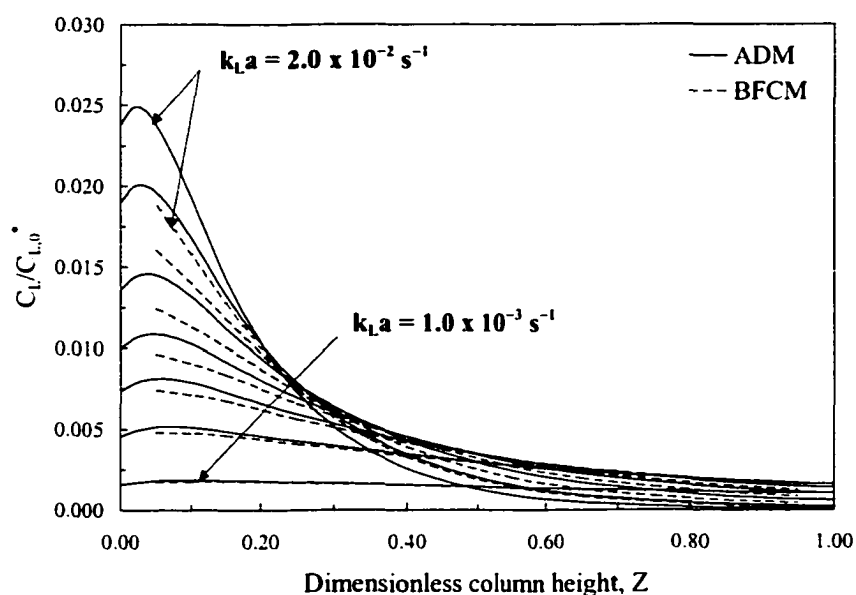


Figure 6.8 Effect of  $k_L a$  on the dissolved ozone profiles in the co-current flow mode for wastewater treatment applications ( $(k_L a = 1.0 \times 10^{-3}, 3.0 \times 10^{-3}, 5.0 \times 10^{-3}, 7.0 \times 10^{-3}, 1.0 \times 10^{-2}, 1.5 \times 10^{-2}, \text{ and } 2.0 \times 10^{-2} \text{ s}^{-1})$ ,  $Pe_L = 5.0$ ,  $Da = 89$ ,  $M = 0.037$ ,  $\alpha = 0.48$ , and  $y_0 = 0.00675$ ).

As shown in Figure 6.8 and regarding the effect of  $k_L a$ , the ADM predicted higher dissolved ozone concentrations than those predicted by the BFCM with the exception in the top half of the column where it predicted lower concentrations.

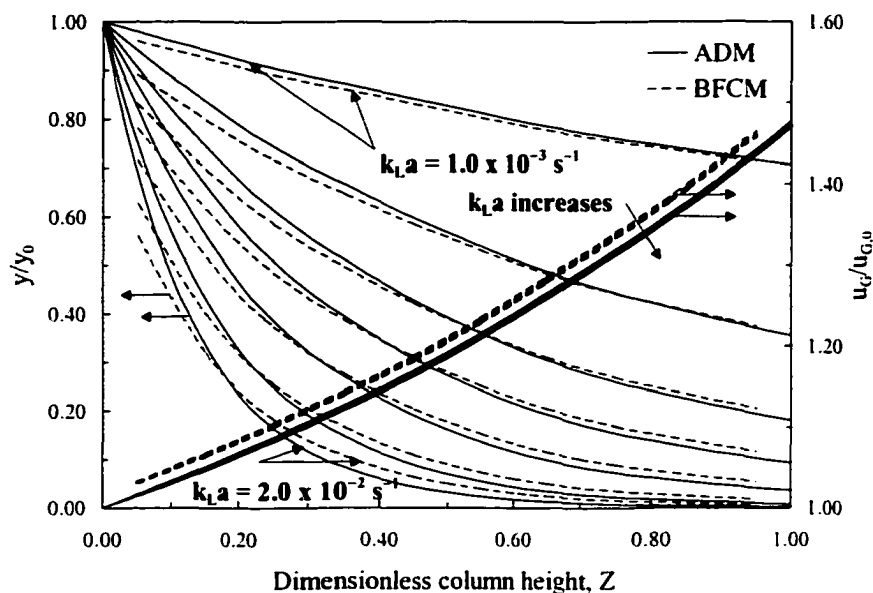


Figure 6.9 Effects of  $k_L a$  on the gaseous ozone and the superficial gas velocity profiles in the co-current flow mode for wastewater treatment applications ( $(k_L a = 1.0 \times 10^{-3}, 3.0 \times 10^{-3}, 5.0 \times 10^{-3}, 7.0 \times 10^{-3}, 1.0 \times 10^{-2}, 1.5 \times 10^{-2},$  and  $2.0 \times 10^{-2} \text{ s}^{-1})$ ,  $Pe_L = 5.0$ ,  $D_a = 89$ ,  $M = 0.037$ ,  $\alpha = 0.48$ , and  $y_0 = 0.00675$ ).

As shown in Figure 6.7 and Figure 6.9, the two models predicted that the gaseous ozone concentration profiles would decrease monotonically along the column height as the ozone in the gas phase would be continuously depleted along the column height during the gas absorption process. The axial gradient of the gaseous ozone profiles exhibited an increasing trend along the column height. As shown in Figure 6.9 and at higher  $k_L a$  values, the decreasing trend of the gaseous ozone profile was faster. This could be explained by the mass transfer rates being high enough to cause faster depletion of the gaseous ozone.

As shown in Figure 6.7 and Figure 6.9, both models were sensitive in their predictions of the gaseous ozone profiles to changes in  $k_L a$  while the predicted gaseous ozone profiles were virtually insensitive to changes in  $Pe_L$ . As shown in Figure 6.7 and Figure 6.9, the two models predicted that the superficial gas velocity would increase

monotonically along the column height with both models being slightly sensitive to changes in  $k_{La}$  and virtually insensitive to changes in  $Pe_L$ . The BFCM predicted slightly higher superficial gas velocities than those predicted by the ADM. As  $Z$  increases, the mass transfer rate would decrease and further ozone gas depletion would occur leading to gas-phase shrinkage. Also, a gas-phase expansion would occur due to the decreasing hydrostatic pressure along the column height. The effect of the gas-phase expansion would be higher than that of the gas-phase shrinkage, and as a result, the superficial gas velocity would increase along the column height. Generally, the gradient of the superficial gas velocity profiles exhibited an increasing trend along the column height.

In the co-current and the counter-current flow modes, the maximum predicted dissolved ozone concentration was observed at the highest  $k_{La}$ . Under the same operating conditions and in the counter-current and the co-current flow modes, the two models predicted virtually identical dissolved ozone concentrations (0.13 and 0.11  $\text{mgL}^{-1}$ , respectively) at the highest  $k_{La}$  ( $2 \times 10^{-2} \text{ s}^{-1}$ ). These predicted low dissolved ozone concentrations are in agreement with the experimental observations of Zhou and Smith (1997 and 2000).

The predicted off-gas ozone concentration ranged from 9.50 to 0.02  $\text{mgL}^{-1}$  at  $k_{La}$  ranging from  $1 \times 10^{-3}$  to  $2 \times 10^{-2} \text{ s}^{-1}$  which suggests that most of the amount of the applied ozone would be absorbed near the bottom of the ozone contactor. During the ozonation experiments conducted by Zhou and Smith (2000) on Kraft pulp mill effluents, the enhancement factor ( $E$ ) was  $> 2$  (i.e.,  $M > 4$ ) and the typical  $k_{La}$  value was  $1.7 \times 10^{-2} \text{ s}^{-1}$ . Under such high  $M$  and  $k_{La}$  conditions, they reported that the off-gas ozone concentration was always below the detection limit ( $0.03 \text{ mgL}^{-1}$ ) of the modified KI method. Those observations by Zhou and Smith (2000) are in agreement with the current models' predictions of the off-gas ozone concentrations under high  $k_{La}$  conditions.

## 6.6 CONCLUSIONS

The axial dispersion model (ADM) and the back flow cell model (BFCM) have proven to be sufficient and reliable in their predictions of the performance of ozone bubble columns, however, the BFCM was easier to formulate and solve.

For wastewater treatment applications and with all the operating conditions being the same, the ADM and the BFCM predicted that the counter-current and the co-current flow modes would exhibit similar characteristics with respect to the dissolved ozone, gaseous ozone, and superficial gas velocity profiles. Changes in the backmixing coefficient, represented by changes in  $Pe_L$ , had relatively small effect on the dissolved ozone concentration profiles and virtually no effect on the gaseous ozone concentration and superficial gas velocity profiles. On the other hand, changes in the overall mass transfer coefficient ( $k_La$ ) had large effects on the dissolved ozone and gaseous ozone profiles and a very small effect on the superficial gas velocity profiles.

Reliable and accurate quantification of the dissolved ozone concentrations is essential for achieving optimized designs and operations of ozone contactors. Additional information on the performance of the models can be developed through the examination of their sensitivity to changes in the other operating parameters including  $k_w$ , and  $M$ . The sensitivity analyses should be conducted using typical operating conditions that are often used in the operations of ozone bubble columns.

## 6.7 REFERENCES

1. Alvarez-Cuenca, M. and M.A. Nerenberg, "Oxygen Mass Transfer in Bubble Columns Working at Large Gas and Liquid Flow Rates", *AIChE J.* 27(1): 66-73 (1981).
2. Alvarez-Cuenca, M., C.G.J. Baker, and M.A. Bergougnou, "Oxygen Mass Transfer in Bubble Columns", *Chem. Eng. Sci.* 35: 1121-1127 (1980).
3. Chang, B.-J. and E.S.K. Chian, "A Model Study of Ozone-Sparged Vessels for the Removal of Organics from Water", *Wat. Res.* 15: 929-936 (1981).
4. Danckwerts, P.V., *Gas-Liquid Reactions* (NY, USA: McGraw-Hill, Inc., 1970).
5. Deckwer, W.-D. and J. Hallensleben, "Exclusion of Gas Sparger Influence on Mass Transfer in Bubble Columns", *Canadian J. Chem. Eng.* 58: 190-196 (1980).
6. Gamal El-Din, M. and D.W. Smith, "Designing Ozone Bubble Columns: A Spreadsheet Approach to Axial Dispersion Model", *Proc. of IOA/PAG Conf.: Advances in Ozone Technology*, Orlando, FL, USA, 2000a.
7. Gamal El-Din, M. and D.W. Smith, "Ozone Mass Transfer in Water Treatment: Hydrodynamics and Mass Transfer Modeling of Ozone Bubble Columns", *Proc. of the Water Supply and Water Quality Conf.*, Kraków, Poland, 2000b.
8. Hull, C.S., P.C. Singer, K. Saravanan, and C.T. Miller, "Ozone Mass Transfer and Reaction: Completely Mixed Systems", *Proc. of the Annual AWWA Conf.: Water Quality*, Vancouver, BC, Canada, 1992.
9. Kaštanek, J., J. Zahradník, J. Kratochvíl, and J. Čermák, *Chemical Reactors for Gas-Liquid Systems* (Chichester, England: Ellis Horwood, 1993).
10. Langlais, B., D.A. Reckhow, and D.R. Brink, *Ozone in Water Treatment: Application and Engineering* (MI, USA: Lewis Publishers, Inc., 1991).
11. Laplanche, A., N. Le Sauze, G. Martin, and B. Langlais, "Simulation of Ozone Transfer in Water: Comparison with a Pilot Unit", *Ozone Sci. & Eng.* 13(5): 13, 535-558 (1991).
12. Levenspiel, O., *Chemical Reaction Engineering*, 2<sup>nd</sup> ed. (NY, USA: John Wiley and Sons, Inc., 1972).

13. Lev, O. and S. Regli, "Evaluation of Ozone Disinfection Systems: Characteristic Contact Time T", *J. Environ. Eng., ASCE* 118(2): 268-285 (1992).
14. Mecklenburgh, J.C. and S. Hartland, *The Theory of Backmixing*, (New York, NY, USA: John Wiley and Sons, Inc., 1975), pp. 1-32.
15. Sotelo, J.L., F.J. Beltrán, F.J. Benitez, and J. Beltrán-Heredia, "Henry's Law Constant for the Ozone-Water System", *Wat. Res.* 23: 1239-1246 (1989).
16. TKSOLVER™, Release 3.32, Universal Technical Systems, Inc., IL, USA (1997).
17. Watt, R.D., E.J. Kirsch, and C.P.Jr. Leslie Grady, "Ozone Consumption Kinetics in Filtered Activated Sludge Effluents: A Modified Approach", *Wat. Res.* 23: 471-480 (1989).
18. Zhou, H. and D.W. Smith, "Applying Mass Transfer Theory to Study the Kinetics of Fast Ozone Reactions in Pulp Mill Effluents", *Proc. of the 14<sup>th</sup> Ozone World Congress*, Detroit, MI, USA, 1999.
19. Zhou H. and D.W. Smith, "Ozonation Dynamics and its Implications for Off-Gas Ozone Control in Treating Pulp Mill Wastewaters", *Ozone Sci. Eng.* 22: 31-51 (2000).
20. Zhou, H. and D.W. Smith, "Process Parameter Development for Ozonation of Kraft Pulp Mill Effluents", *Wat. Sci. & Technol.* 35(2-3): 251-259 (1997).
21. Zhou H. and D.W. Smith, "Theoretical Analysis of Ozone Disinfection Performance in a Bubble Column", *Ozone Sci. Eng.* 16: 429-441 (1994).
22. Zhou, H., *Investigation of Ozone Disinfection Kinetics and Contactor Performance Modeling: Ph.D. Thesis* (Edmonton, AB, Canada: University of Alberta, 1995).
23. Zhou, H., D.W. Smith, and S.J. Stanley, "Modeling of Dissolved Ozone Concentration Profiles in Bubble Columns", *J. Environ. Eng., ASCE* 120(4): 821-840 (1994).

## CHAPTER 7. DESIGNING OZONE BUBBLE COLUMNS: A SPREADSHEET APPROACH TO AXIAL DISPERSION MODEL \*

### 7.1 INTRODUCTION

Based on a literature review, it was found that most of the models that dealt with ozone contactors were directed to the water treatment applications with very little done to model the ozonation process for wastewater treatment. Most of the models are two-phase flow (i.e., gas-liquid) models that are applied to predict the dissolved and the gaseous ozone profiles along bubble columns. In order to simplify the design process of ozone bubble columns, a large number of the models were based on one of the following two liquid-phase flow regimes: (1) complete mixing or; (2) plug flow (Alvarez-Cuenca *et al.*, 1980; Alvarez-Cuenca *et al.*, 1981; Chang and Chian, 1981; Laplanche *et al.*, 1991; Hull *et al.*, 1992; Lev and Regli, 1992). Although, the actual flow pattern in bubble columns is usually closer to being mixed flow rather than plug flow, but still not completely mixed flow. Zhou *et al.* (1994) modeled the performance of ozone bubble columns by using the 2P-ADM and an elaborate numerical technique was needed to solve the model equations. The 2P-ADM demonstrated excellent capability of predicting the dissolved ozone profiles in bubble columns.

The design of ozone bubble columns usually encounter two major sources of uncertainties: (1) the complications and unreliable methods utilized for measuring and estimating operating parameters of bubble columns; and (2) the application of the pertinent design model, particularly, when designing an ozonation treatment facility for a complicated chemical system such as the effluents from the pulping and bleaching processes. Although constructing ozone contactors is an easy task, optimizing their operations is not as simple. The operating parameters of ozone contactors are interrelated and thus, they cause difficulty in the design, operation, and scale-up. Therefore, reliable and accurate methods of measuring and estimating such parameters should be applied.

---

A version of this chapter has been accepted for publication. Gamal El-Din, M. and D.W. Smith, *Ozone Sci. & Eng.* (June 2001).

A number of processes occur simultaneously during the ozonation process. Those processes are: the convection and the backmixing processes of the liquid and gas phases flowing through the contacting chamber; the ozone gas mass transfer process; the ozone auto-decomposition process, and the competitive reactive processes of the constituents in water and wastewater with dissolved ozone (Zhou *et al.*, 1994). Besides those processes, the contactor configuration, the operating conditions, and the water or wastewater quality influence the overall performance of the ozonation process (Zhou, 1995). For any ozonation system, it is crucial to quantify the dissolved ozone to achieve reliable rational design and optimum operation of ozone contactors. Meanwhile, quantifying the gaseous ozone, i.e., the ozone off-gas leaving the contactor, is essential for achieving optimum and reliable design of the off-gas destruction facilities.

Several studies have been conducted to study the fundamentals of the processes that control the performance of ozone contactors in water treatment over the past decades with a fewer number of studies aimed at investigating the ozone mass transfer mechanisms and the effect of chemical reactions on the rate of ozone absorption when treating industrial wastewater. Heinzl *et al.* (1992) could not detect any dissolved nor gaseous ozone when they studied the ozonation of the wastewater generated from the chlorine bleaching and the proceeding alkaline extraction processes after being passed through a biological treatment. As the ozone dose increased to 250 mgL<sup>-1</sup> or higher, ozone off-gas began to exit the system and it was detected at levels that increased gradually as the ozone dose increased. Meanwhile, as the ozone dose reached 500 mgL<sup>-1</sup> or higher, they started detecting dissolved ozone. Similar observations were reported by Beltrán *et al.* (1995) as they investigated the ozonation of distillery and tomato industrial wastewater in a laboratory-scale bubble column. During the ozonation of pulp mill effluents, Zhou and Smith (2000) simulated the pilot-scale bubble column operations in the counter-current and the co-current flow conditions using a number of CFSTR's in series ranging from 8 to 39. The ozone off-gas concentrations were predicted to be lower than 0.01 mgL<sup>-1</sup> while the measured concentrations were lower than 0.03 mgL<sup>-1</sup>. The low off-gas concentrations could be a result of the initial chemical reactions being fast enough for the dissolved ozone to be completely depleted at the gas-liquid interface and/or within

the liquid film during the course of ozonation of Kraft pulp mill effluents as reported before by Zhou and Smith (1997). Consequently, the dissolved ozone gradient became steeper than the gradient of the maximum physical ozone absorption process. Based on that, they assumed that the fast or instantaneous-reaction regime prevailed for the gas absorption process when ozonating pulp mill effluents. Two distinct reaction kinetics regimes were defined as shown in Figure 7.1: (1) the slow-reaction kinetics regime; and (2) the fast or instantaneous-reaction kinetics regime. In the fast-reaction kinetics regime and because of the low dissolved ozone concentrations, the driving force of the mass transfer process is increased and also the local mass transfer coefficient is enhanced by an enhancement factor (E). This factor is defined as the actual rate of mass transfer with the occurrence of chemical reactions divided by the maximum rate of physical absorption with no occurrence of chemical reactions.

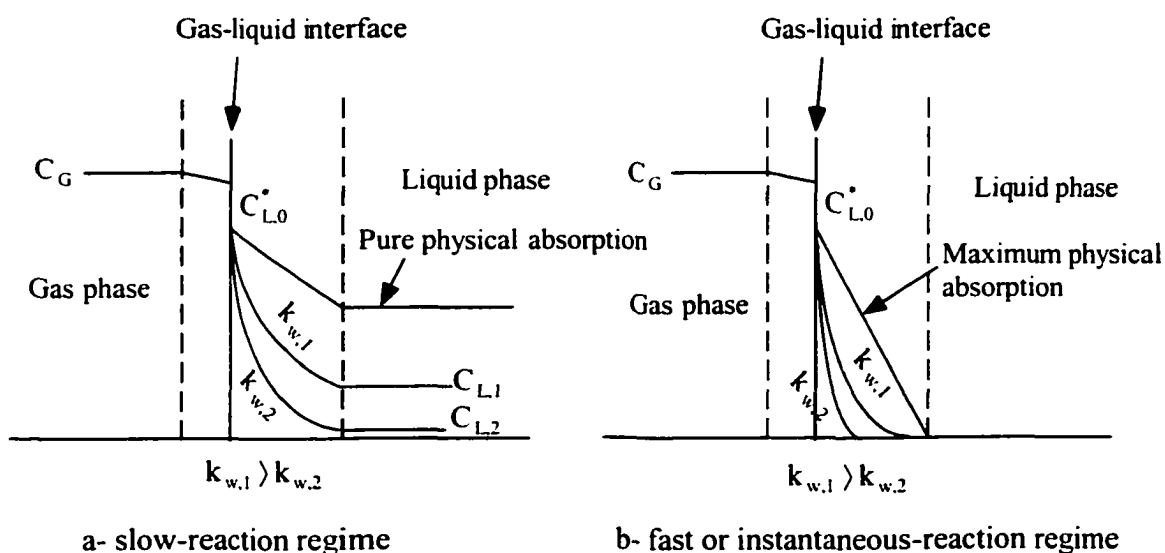


Figure 7.1 Reaction kinetics regimes for ozone absorption process (adapted from Zhou and Smith, 1997).

This chapter presents: (1) a detailed formulation of the one-phase axial dispersion model (1P-ADM) to provide a simple and accurate method to predict the performance of the counter-current and the co-current ozone contactors for ozone applications in water and wastewater treatment; and (2) initial model testing for ozone applications in water treatment using the pilot-scale experimental data of Zhou (1995).

## 7.2 DISPERSION MODELS FOR TWO-PHASE FLOWS

### 7.2.1 Process Fundamentals

There are several models that account for backmixing in the liquid phase. Among those models that are available for predicting the performance of bubble columns, is the axial dispersion model (ADM). In the ADM, a diffusion-like process is assumed and superimposed on a plug flow (Levenspiel, 1972). An empirical Fick's law is applied by replacing the molecular diffusion coefficient by the axial dispersion coefficient ( $D_L$ ) as the mixing parameter:

$$\text{Diffusive mass flux} = -D_L \frac{\partial C_L}{\partial \ell} \quad [7.1]$$

where:  $C_L$  = dissolved ozone concentration ( $\text{mgL}^{-1}$ ) and  $D_L$  = axial dispersion coefficient ( $\text{m}^2\text{s}^{-1}$ ). In the  $D_L$ , the effects of the non-uniform velocity profile (shear dispersion), the molecular, and eddy diffusivities are lumped together.

The overall ozone auto-decomposition rate is influenced by the concentration and the history of the ozonation process and this ozone auto-decomposition process could be represented by a modified pseudo-first-order rate expression (Yurteri and Gurol, 1988; Oke *et al.*, 1998). In the experimental study of Oke *et al.* (1998), it was shown that the commonly used first-order kinetics expression with a constant reaction rate constant was inadequate in describing the ozone auto-decomposition process especially in situations where the initial ozone demand was significant. It was demonstrated that the reaction rate constant was continuously decreasing along the course of ozonation as a result of the changes in the water characteristics. As a result, an exponentially decreasing function was proposed as a better alternative to describe the ozone auto-decomposition kinetics (Oke *et al.*, 1998). In that expression, the reaction rate constant was replaced by a variable referred to as the specific ozone utilization rate constant ( $k_w$ ) that is a function of the utilized ozone dose ( $\Delta\text{O}_3$ ):

$$\frac{dC_L}{dt} = -k_w C_L = -(k_1 + k_2 e^{-k_3 \Delta O_3}) C_L \quad [7.2]$$

where:  $C_L$  = instantaneous dissolved ozone concentration ( $\text{mgL}^{-1}$ ),  $k_w$  = specific ozone utilization rate constant ( $\text{s}^{-1}$ ),  $k_1$  = empirical non-linear regression constant ( $\text{s}^{-1}$ ),  $k_2$  = empirical non-linear regression constant ( $\text{s}^{-1}$ ),  $k_3$  = empirical non-linear regression constant ( $\text{Lmg}^{-1}$ ),  $t$  = reaction time (s), and  $\Delta O_3$  = amount of the utilized ozone ( $\text{mgL}^{-1}$ ).  $k_1$ ,  $k_2$ , and  $k_3$  are empirical constants that can be obtained by applying non-linear regression analysis to the kinetics data and they are also characteristics of the water to be treated. As shown in Equation 7.2, as the utilized ozone dose increases along the course of ozonation  $k_w$  will decrease. At the beginning of the ozonation, i.e., when the amount of the utilized ozone is zero,  $k_w$  is equal to  $k_1 + k_2$  as the ozone decay process is only attributed to the initial ozone demand. In the Oke *et al.* (1998) study and for clean deionized water, the initial ozone demand was practically equal to zero and therefore,  $k_w$  could be assumed constant during the course of the ozonation.

The two-film model is usually used to describe the absorption of ozone gas from the gas phase into the liquid phase. In this model, the gas-absorption rate ( $\psi$ ) is defined as:

$$\psi = k_L a (C_L^* - C_L) \quad [7.3]$$

where:  $\psi$  = gas-absorption rate ( $\text{mgL}^{-1}\text{s}^{-1}$ ),  $k_L$  = local liquid mass transfer coefficient ( $\text{ms}^{-1}$ ),  $a$  = specific gas bubbles' interfacial area ( $\text{m}^{-1}$ ),  $C_L^*$  = concentration of the dissolved ozone in equilibrium with the bulk ozone gas ( $\text{mgL}^{-1}$ ), and  $C_L$  = concentration of the dissolved ozone in the bulk liquid ( $\text{mgL}^{-1}$ ). Due to the fact that ozone gas diffuses much faster in the gas phase than in the liquid phase, the mass transfer in the liquid phase is assumed to be the rate-controlling step. Consequently, the overall mass transfer coefficient ( $k_L a$ ) is considered to entirely consist of the local mass transfer coefficient in the liquid phase.

## 7.2.2 Mass Transfer Process with Chemical Reactions

Chemical reactions occur during the ozonation of wastewater. In such applications, the dimensionless squared Hatta number ( $H_a^2 = M$ ) is often applied to compare between the amount of dissolved gas that reacts at the gas-liquid interface or in the liquid film near the interface and the amount of dissolved gas that reaches the bulk liquid in an unreacted state:

$$H_a^2 = E^2 = M = \frac{Dk_w}{k_L^2} \quad [7.4]$$

where:  $H_a = E = \sqrt{M}$  = dimensionless Hatta number,  $k_L$  = local mass transfer coefficient ( $\text{ms}^{-1}$ ),  $D_{O_3}$  = molecular diffusivity of ozone gas in water ( $\text{m}^2\text{s}^{-1}$ ), and  $k_w$  = specific ozone utilization rate constant ( $\text{s}^{-1}$ ). For pseudo-first-order irreversible reactions, the location of those reactions that take place during the gas absorption process could be classified into two categories (Kramers and Westertrep, 1963; Kaštánek *et al.*, 1993). Reactions would take place in the bulk of the liquid or at the gas-liquid interface and/or in the liquid film near the interface at  $H_a < 0.03$  and  $H_a > 5.00$ , respectively (Kramers and Westertrep, 1963; Kaštánek *et al.*, 1993). Although, generally for bubble columns it can also be assumed that at that at  $H_a > 3.00$ , reactions would still be fast enough to occur predominantly at the gas-liquid interface and/or in the liquid film near the interface (Kaštánek *et al.*, 1993). Therefore, reactions would simultaneously take place in both regions at  $0.03 < H_a < 3.00$ . Equation 7.4 is only applicable in situations where two conditions have to be satisfied: (1)  $\sqrt{M} \gg 1$ ; and (2) fast or instantaneous irreversible first-order reactions with no bulk liquid concentration where the driving force for the mass transfer process will be maximized (Danckwerts, 1970). As a result, Equation 7.3 becomes:

$$\psi = Ek_L aC_L^* \quad [7.5]$$

where:  $Ek_L a$  = enhanced overall mass transfer coefficient ( $s^{-1}$ ). Zhou and Smith (1999) proposed that for wastewater ozonation, both the ozone auto-decomposition and its reactions with the organic and inorganic constituents in wastewater could be lumped together in a first-order rate constant ( $k_w$ ). Danckwerts (1970) proposed the following equation for the conditions when  $M > 0$  and  $C_L > 0$ :

$$\psi = k_L a \sqrt{1+M} \left( C_L^* - \frac{C_L}{1+M} \right) \quad [7.6]$$

When  $M \gg 1$  and  $C_L$  approaches zero (i.e.,  $C_L \cong 0$ ), Equation 7.6 reduces to Equation 7.5. The effects of chemical reactions on the local mass transfer coefficient for an irreversible first-order reaction could be neglected and the gas absorption could be dealt with as pure physical absorption when  $M$  approaches zero (Danckwerts, 1970). Therefore, this assumption is valid when:

$$H_3^2 = M = \frac{Dk_w}{k_L^2} \ll 1 \quad [7.7]$$

$k_w$  was reported to be equal to  $4.7 \times 10^{-4} s^{-1}$  for the deionized water tested by Zhou (1995). Yurteri and Gurol (1988) reported that  $k_w$  was in the order of  $2.8 \times 10^{-3} s^{-1}$  for the tested raw surface water. The diffusivity of ozone in water was determined by the Wilke-Chang formula to be  $1.74 \times 10^{-9} m^2s^{-1}$  (at 20 °C) which is comparable to the value of  $1.71 \times 10^{-9} m^2s^{-1}$  obtained using the equation recommended by Johnson and Davis (1996).  $k_L$  was reported to be in the order of  $3.1 \times 10^{-4} ms^{-1}$  for clean water and in the order of  $1.9 \times 10^{-4} ms^{-1}$  for water containing organic substances (Beltrán *et al.*, 1997). Substituting for these typical values of  $D$ ,  $k_w$ , and  $k_L$  into Equation 7.4 yields squared-Hatta numbers of  $8.5 \times 10^{-6}$  and  $1.4 \times 10^{-4}$  for the deionized and the surface water, respectively. Based on these small Hatta numbers, it can be concluded that the chemical reactions that occur during the course of clean or surface water ozonation has negligible

effect on the local mass transfer coefficient and hence, Equation 7.3 will be applied for ozone absorption without any modification.

### 7.2.3 Two-Phase Axial Dispersion Model (2P-ADM)

Zhou *et al.* (1994) applied the complete two-phase axial dispersion model (2P-ADM) to study the performance of ozone bubble columns under various operating conditions for water treatment applications. When modeling gas-liquid flows, several assumptions govern the development of the 2P-ADM as reported by Zhou *et al.* (1994). The enhancement factor of the mass transfer process due to the occurrence of chemical reactions was assumed to be negligible (i.e.,  $M = 0$ ) as the absorption of ozone gas in water could be considered to take place in the slow-reaction kinetics regime. For wastewater, the fast-reaction kinetics regime was assumed to prevail and the enhancement factor ( $M$ ) was assumed to be higher than 0.

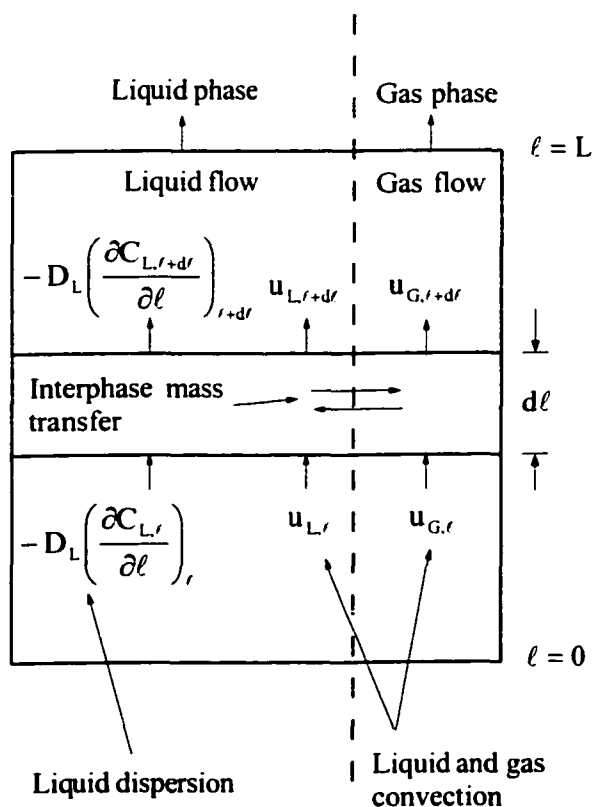


Figure 7.2 Schematic representation of the co-current ADM.

Considering the control volume shown in Figure 7.2, and conducting mass balance for the liquid and gas phases with respect to the dissolved and the gaseous ozone concentrations and applying mathematical manipulations, one can obtain the generalized model equations for water and wastewater treatment applications as presented in Table 7.2.

Table 7.1 Dimensionless parameters that are used to describe the 1P-ADM and the 2P-ADM.

Dimensionless parameter	1P-ADM/2P-ADM
Z	$l/L$
$\alpha^\diamond$	$\rho g \varepsilon_L L / P_T$
$\beta^\diamond$	$1 + \alpha$
$Pe_L$	$u_L L / D_L \varepsilon_L$
$St_L$	$k_L a L / u_L$
$St_G$	$(k_L a L / u_{G,0}) (RT/H)$
$D_a$	$k_w \varepsilon_L L / u_L$
M	$D k_w / k_L^2$
X	$C_{L,r} / C_{L,0}^\diamond$
Y	$y_r / y_0$

Note:  $\diamond$  denotes the parameters that are only used in the 2P-ADM.

The boundary conditions pertaining to those equations are the same as those described by Zhou *et al.* (1994). The dimensionless parameters pertaining to those equations are presented in Table 7.1. As shown in Table 7.2, the 2P-ADM is described mathematically by a system of two non-linear partial differential equations that need to be solved simultaneously. A numerical technique must be used to solve those equations by transforming them into non-linear algebraic equations. Therefore, for the design and the process control purposes, solving that system of non-linear algebraic equations becomes complicated and time-consuming. A simple and accurate model needed to be

developed to simplify the design process of ozone contactors and for the operators of such contactors to use when modifications to the operating conditions need to be done in order to optimize the performance of ozone contactors.

Table 7.2 Mathematical representation of the 2P-ADM for water and wastewater treatment applications.

<b>Model equations</b>	Aqueous ozone	$\frac{1}{Pe_L} \frac{\partial^2 X}{\partial Z^2} + I \frac{\partial X}{\partial Z} + \frac{\sqrt{1+M} St_L}{\beta} (\beta - \alpha Z) Y - \left( \frac{St_L}{\sqrt{1+M}} + D_a \right) X = 0$
	Gaseous ozone	$\frac{\partial Y}{\partial Z} + \frac{St_G}{\beta(1-y_0)} (1-y_0 Y)^2 \left[ \sqrt{1+M} (\beta - \alpha Z) Y - \frac{\beta}{\sqrt{1+M}} X \right] = 0$

Note:

$I = -1$  for co-current flow mode and  $I = +1$  for counter-current flow mode.

$M = 0$  for water treatment applications.

#### 7.2.4 Development of the One-Phase Axial Dispersion Model (1P-ADM)

The assumptions pertaining to the modified non-isobaric steady-state one-phase axial dispersion model (1P-ADM) are the same as those used to develop the steady-state 2P-ADM with the exception that the 1P-ADM describes only the liquid phase. In order to account for changes in the superficial gas velocity due to the effects of gas shrinkage and expansion caused by the gas absorption and depletion and the reduced hydrostatic head, respectively, an exponential function was assumed to describe the variation of the gaseous mole fraction along the column height:

$$y_z = y_r = y_0 \exp(-a_1 Z) \quad [7.8]$$

where:  $y_0$  = gaseous ozone mole fraction in the gas phase at the column entrance,  $Z$  = dimensionless axial coordinate of the column, and  $a_1$  = dimensionless coefficient of gaseous ozone mole fraction decrease along the column height. It was assumed that  $a_1$  is

a function of  $Pe_L$ ,  $St_L$ ,  $St_G$ , and  $D_a$  for water treatment conditions and a function of  $Pe_L$ ,  $St_L$ ,  $St_G$ ,  $D_a$ , and  $M$  for wastewater treatment conditions. The proposed exponential model represented by Equation 7.8 was obtained by fitting an exponential function to the theoretical gaseous ozone profiles predicted by the complete axial dispersion model (2P-ADM) in the study conducted by Zhou *et al.* (1994) for water treatment applications under a wide range of operating conditions. For wastewater treatment applications, the 2P-ADM was executed under a wide range of operating conditions. Then, the model predictions of the gaseous ozone profiles were fitted to an exponential function. The correlation coefficient ( $r$ ) ranged from 0.90 to 0.99. The proposed exponential model can be considered semi-empirical in its nature since it is based on fitting the exponential function to the ozone gas-phase concentration profiles predicted by the 2P-ADM. There was an attempt to verify the applicability of the exponential model to predict the ozone gas-phase concentration profiles. Figure 7.3 depicts examples of the gaseous ozone profiles for the counter-current and the co-current flow modes for water and wastewater treatment applications.

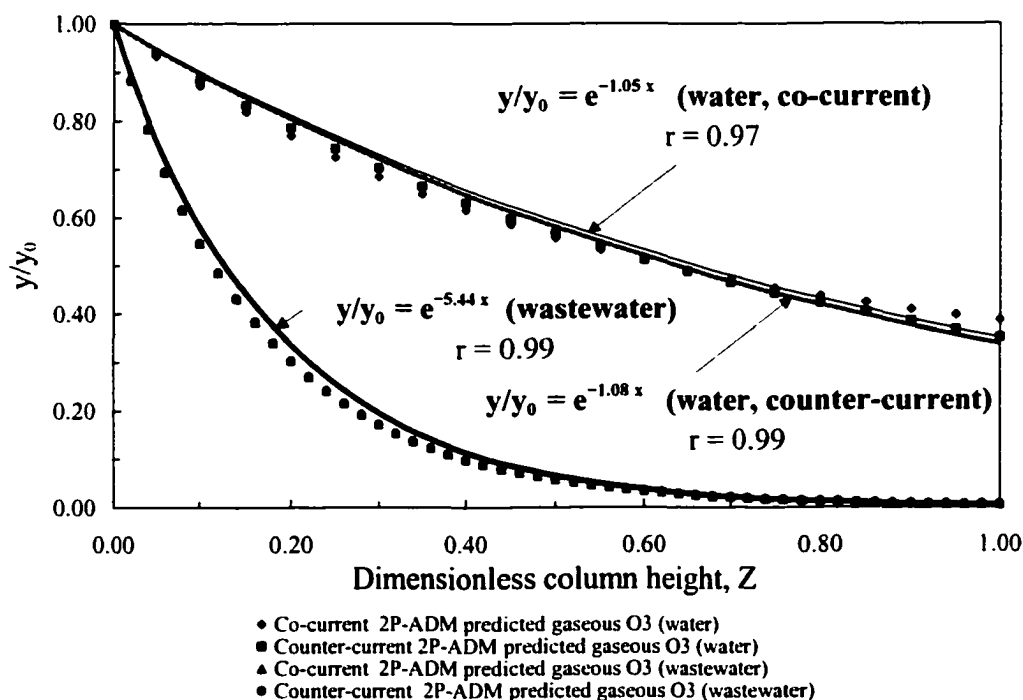


Figure 7.3 Typical gaseous ozone profiles in bubble columns for water and wastewater treatment conditions.

For wastewater treatment applications, the 2P-ADM predicted identical gaseous ozone profiles for the two flow modes, while the profiles were almost identical for water treatment applications. Linear regression technique was applied to correlate between the independent parameter ( $a_1$ ) and the dependent parameters ( $Pe_L$ ,  $St_L$ ,  $St_G$ ,  $D_a$ , and  $M$ ). The models obtained for water and wastewater treatment applications in the counter-current and the co-current flow modes are presented in Table 7.3. For water treatment applications, the models have some similarities in terms of the number and types of the dependent parameters that were included and they are different in terms of the values of the regression coefficients. The dependent parameter ( $St_L$ ) was excluded by the linear regression process from the predicted models for the water treatment applications. Interestingly, as shown in Table 7.3, the models for the counter-current and the co-current flow modes are almost identical for wastewater treatment conditions. For water treatment conditions, the correlation coefficient ( $r$ ) for the linear regression models was 0.99 and 0.97 for the counter-current and the co-current flow modes, respectively. For wastewater treatment conditions,  $r$  was equal to 0.99 for both the counter-current and the co-current flow modes.

Table 7.3 Coefficients of the exponential model used for the prediction of the gaseous ozone profiles.

Treatment type	Flow mode	Equations
Water	Co-current	$a_1 = 0.413 + 0.35 St_G + 1.646 \times 10^{-3} Pe_L + 0.121 D_a$
	Counter-current	$a_1 = 0.221 + 0.515 St_G - 8.93 \times 10^{-3} Pe_L + 0.1 D_a$
Wastewater	Co-current	$a_1 = 0.13 + 0.816 St_G - 2.71 \times 10^{-2} St_L - 1.04 \times 10^{-3} Pe_L - 3.3 \times 10^{-7} D_a + 0.613 M$
	Counter-current	$a_1 = 0.129 + 0.817 St_G - 2.69 \times 10^{-2} St_L - 1.05 \times 10^{-3} Pe_L - 3.29 \times 10^{-7} D_a + 0.612 M$

Conducting mass balance for the liquid phase in the co-current flow mode and for water treatment conditions yields:

$$\frac{d^2 C_{L,r}}{d\ell^2} D_L \varepsilon_L - u_L \frac{dC_{L,r}}{d\ell} + k_L a (C_{L,r}^* - C_{L,r}) - k_w C_{L,r} \varepsilon_L = 0 \quad [7.9]$$

Using the relationships of  $P_r$ ,  $P_0$ , and  $C_{L,r}^*$ :

$$P_r = P_T + \rho g \varepsilon_L (L - \ell) \quad [7.10]$$

$$P_0 = P_T + \rho g \varepsilon_L L \quad [7.11]$$

$$C_{L,r}^* = \frac{P_T + \rho g \varepsilon_L (L - \ell)}{H} y_r \quad [7.12]$$

Since:

$$y_Z = y_r = y_0 \exp(-a_1 Z) \quad [7.13]$$

and

$$Z = \frac{\ell}{L} \quad [7.14]$$

Therefore, substituting for Equations 7.13 and 7.14 into Equation 7.12 yields:

$$C_{L,r}^* = \frac{[P_T + \rho g \varepsilon_L L(1 - Z)]}{H} y_0 \exp(-a_1 Z) = (P_T + \rho g \varepsilon_L L) \frac{y_0}{H} \exp(-a_1 Z) - \frac{\rho g \varepsilon_L L}{H} y_0 Z \exp(-a_1 Z) \quad [7.15]$$

Equation 7.15 can be re-written as:

$$C_{L,r}^* = a' y_0 \exp(-a_1 Z) + b' y_0 Z \exp(-a_1 Z) \quad [7.16]$$

where:

$$a' = \frac{(P_T + \rho g \epsilon_L L)}{H} \quad [7.17]$$

and

$$b' = \frac{-\rho g \epsilon_L L}{H} \quad [7.18]$$

Re-writing Equation 7.16 as:

$$C_{L,r}^* = \alpha_1 \exp(-a_1 Z) + \beta_1 Z \exp(-a_1 Z) \quad [7.19]$$

where:

$$\alpha_1 = a' y_0 \quad [7.20]$$

and

$$\beta_1 = b' y_0 \quad [7.21]$$

As a result:

$$C_{L,0}^* = \alpha_1 \quad [7.22]$$

Multiplying Equation 7.9 by  $\frac{L}{u_L C_{L, \infty}}$ , substituting for the dimensionless parameters defined in Table 7.1 and Equation 7.22 into the resulting equation, and rearranging, one can obtain:

$$\frac{1}{Pe_L} \frac{dX^2}{dZ^2} - \frac{dX}{dZ} - (St_L + D_s)X + St_L \left[ \exp(-a_1 Z) + \frac{\beta_1}{\alpha_1} Z \exp(-a_1 Z) \right] = 0 \quad [7.23]$$

The general 1P-ADM for the co-current and counter-current flow modes is as follows:

$$\frac{1}{Pe_L} \frac{dX^2}{dZ^2} + I \frac{dX}{dZ} - (St_L + D_s)X + St_L \left[ \exp(-a_1 Z) + \frac{\beta_1}{\alpha_1} Z \exp(-a_1 Z) \right] = 0 \quad [7.24]$$

where:  $I = -1$  for the co-current flow mode and  $I = +1$  for the counter-current flow mode. The boundary conditions pertaining to Equation 7.24 are the same as those for the 2P-ADM. Equation 7.24 is a non-homogeneous linear second-order ordinary differential equation that represents the 1P-ADM. This equation was solved analytically by applying the method of variation of parameters (Kreyszig, 1988). The analytical solution of Equation 7.24 for the co-current flow conditions is as follows:

$$X = \frac{\left[ D_1 \lambda_2 e^{\lambda_2} + E_1 \left( 1 - \frac{\lambda_2}{Pe_L} \right) \right]}{N} \exp(\lambda_1 Z) - \frac{\left[ D_1 \lambda_1 e^{\lambda_1} + E_1 \left( 1 - \frac{\lambda_1}{Pe_L} \right) \right]}{N} \exp(\lambda_2 Z) + K_0 \exp(-a_1 Z) + K_1 Z \exp(-a_1 Z) \quad [7.25]$$

where:

$$\lambda_{1,2} = Pe_L \pm \sqrt{Pe_L^2 + 4Pe_L (St_L + D_s)} \quad [7.26]$$

$$K_0 = \frac{Pe_L St_L}{(\lambda_2 - \lambda_1)} \left[ \frac{1}{(a_1 + \lambda_2)} + \frac{\beta_1}{\alpha_1 (a_1 + \lambda_2)^2} - \frac{1}{(a_1 + \lambda_1)} - \frac{\beta_1}{\alpha_1 (a_1 + \lambda_1)^2} \right] \quad [7.27]$$

$$K_1 = \frac{-\beta_1 Pe_L St_L}{\alpha_1 (a_1 + \lambda_1)(a_1 + \lambda_2)} \quad [7.28]$$

$$D_1 = X_{inf} - K_0 \left( \frac{a_1}{Pe_L} + 1 \right) + \frac{K_1}{Pe_L} \quad [7.29]$$

$$E_1 = [-(K_0 + K_1)a_1 + K_1] \exp(-a_1) \quad [7.30]$$

and

$$N = \left( 1 - \frac{\lambda_1}{Pe_L} \right) \lambda_2 \exp(\lambda_2) - \left( 1 - \frac{\lambda_2}{Pe_L} \right) \lambda_1 \exp(\lambda_1) \quad [7.31]$$

The same procedure can be followed to obtain the 1P-ADM for the counter-current flow conditions. The general 1P-ADM for the counter-current and the co-current flow modes and for wastewater treatment applications is as follows:

$$\frac{1}{Pe_L} \frac{dX^2}{dZ^2} + I \frac{dX}{dZ} - \left( \frac{St_L}{\sqrt{1+M}} + D_3 \right) X + St_L \sqrt{1+M} \left[ \exp(-a_1 Z) + \frac{\beta_1}{\alpha_1} Z \exp(-a_1 Z) \right] = 0 \quad [7.32]$$

The analytical solution of Equation 7.32 for the co-current flow conditions is as follows:

$$X = \frac{\left[ D_1 \lambda_2 e^{\lambda_2} + E_1 \left( 1 - \frac{\lambda_2}{Pe_L} \right) \right]}{N} \exp(\lambda_1 Z) - \frac{\left[ D_1 \lambda_1 e^{\lambda_1} + E_1 \left( 1 - \frac{\lambda_1}{Pe_L} \right) \right]}{N} \exp(\lambda_2 Z) + K_0 \sqrt{1+M} \exp(-a_1 Z) + K_1 \sqrt{1+M} Z \exp(-a_1 Z) \quad [7.33]$$

where:  $D_1$ ,  $E_1$ , and  $N$  are defined by Equations 7.29 to 7.31 and:

$$\lambda_{1,2} = Pe_L \pm \sqrt{Pe_L^2 + 4Pe_L \left( \frac{St_L}{\sqrt{1+M}} + D_a \right)} \quad [7.34]$$

### 7.3 OPERATING CONDITIONS FOR THE MODEL SIMULATIONS AND TESTING

#### 7.3.1 Water Treatment Conditions

Similar operating conditions to those used in the study of Zhou *et al.* (1994) were considered for examining the applicability of the 1P-ADM compared to the 2P-ADM to describe the performance of ozone bubble columns. In order to examine the effects of  $Pe_L$ ,  $k_La$ , and  $D_a$  on the dissolved and the gaseous ozone profiles for ozone applications in water treatment, the following typical conditions for the operation of ozone bubble columns were assigned as the base values for the 1P-ADM simulations: column height ( $L$ ) = 5000 mm; ozone concentration in the feed gas ( $C_0$ ) = 1 % (w/w %); applied ozone dose = 1.35 mgL<sup>-1</sup>; mean theoretical hydraulic retention time ( $\tau$ ) = 180 s;  $Pe_L$  = 5;  $k_w$  = 4.7 x 10<sup>-4</sup> s<sup>-1</sup>;  $k_La$  = 5.0 x 10<sup>-3</sup> s<sup>-1</sup>; bubble column aspect ratio =  $L/D$  = 12.5; gas-to-liquid flowrate ( $G/L$ ) ratio = 0.1; and gas hold-up ( $\epsilon_G$ ) = 0.008. Henry's law constant ( $H$ ) of 0.22 kPaLmg<sup>-1</sup> was obtained from Sotelo *et al.* (1989). Water temperature was assumed to be 20 °C and the pressure at the top of the column was assumed to equal 1.0 atm. The basic model input parameters were then calculated and they were as follows:  $Pe_L$  = 5.0;  $St_L$  = 0.9;  $St_G$  = 2.07;  $D_a$  = 0.0831; and  $y_0$  = 0.00675. The sensitivity analyses of the 1P-ADM to changes in each one of the parameters ( $Pe_L$ ,  $k_La$ , and  $D_a$ ) were performed by varying each one of the parameters while maintaining the others constant.

#### 7.3.2 Wastewater Treatment Conditions

It was reported by Zhou and Smith (1999) that for pulp mill effluents,  $k_w$  ranged from 1,000 to 5,000 s<sup>-1</sup> and the enhancement factor ( $E$ ) ranged from 2 to 10. For the sake of practicality, the bulk liquid ozone concentration was assumed to equal zero since it

was below the detection limit. They suggested that a typical value of  $k_L$  in the range from  $6.6 \times 10^{-4}$  to  $9.3 \times 10^{-4} \text{ ms}^{-1}$  and  $k_L a$  in the range from  $8.3 \times 10^{-3}$  to  $2.5 \times 10^{-2} \text{ s}^{-1}$ . The effects of  $Pe_L$ ,  $k_L a$ ,  $D_a$ , and  $M$  on the dissolved and the gaseous ozone profiles for wastewater treatment conditions were examined by assigning the same typical operating conditions used for the water treatment conditions except for:  $k_w = 500 \text{ s}^{-1}$ ; and  $k_L = 8.0 \times 10^{-4} \text{ ms}^{-1}$ . The basic model input parameters were then calculated and they were as follows:  $Pe_L = 5.0$ ;  $St_L = 0.9$ ;  $St_G = 2.07$ ;  $D_a = 89,000$ ;  $M = 1.166$  (to investigate the effect of the chemical reactions when they occur simultaneously near and/or at the gas-liquid interface and in the bulk liquid); and  $y_0 = 0.00675$ . The sensitivity analyses of the 1P-ADM were performed by varying each one of the parameters ( $Pe_L$ ,  $k_L a$ ,  $D_a$ , and  $M$ ) while maintaining the others constant except for  $M$  and  $D_a$  as they were varied together since they are interrelated through the pseudo-first-order specific ozone utilization rate constant ( $k_w$ ) and the local mass transfer coefficient ( $k_L$ ) as shown in Table 7.1.

### 7.3.3 Experimental Conditions for the Initial Testing of the 1P-ADM

The 1P-ADM was tested for the ozone application in water treatment using the pilot-scale experimental data of Zhou (1995). The pilot-scale bubble column used in the experiments was a cylindrical glass column with an inside diameter of 100 mm and a total height of 2,000 mm. The water depth was maintained constant at 1,750 mm by using an overflow weir. A 25 mm-spherical fused crystalline aluminum stone was used as the gas sparger. For the tested deionized water,  $k_w$  was determined experimentally by Zhou (1995) to be equal to  $4.7 \times 10^{-4} \text{ s}^{-1}$ . The operating conditions for the counter-current and the co-current flow modes are presented in Tables 7.4 and 7.5, respectively.

Table 7.4 Operating conditions for the counter-current flow mode (water treatment).

Case #	$Pe_L$	$P_T$ (atm)	$St_L$	$St_G$	$D_a$	$y_0$	$C_{L,0}^*$ ( $\text{mgL}^{-1}$ )
<b>DW17</b>	10.53	1.0	0.560	1.119	0.139	0.010	5.56
<b>DW23</b>	9.71	1.0	1.365	1.098	0.139	0.007	3.63

Table 7.5 Operating conditions for the co-current flow mode (water treatment).

Case #	$Pe_L$	$P_T$ (atm)	$St_L$	$St_G$	$D_a$	$y_0$	$C_{L,0}^*$ ( $mgL^{-1}$ )
DW4	34.48	1.0	0.235	1.247	0.056	0.013	7.20
DW5	9.84	1.0	1.755	1.258	0.056	0.002	0.92
DW9	4.63	1.0	0.235	0.081	0.139	0.002	0.88

## 7.4 RESULTS AND DISCUSSION

### 7.4.1 Theoretical Analyses of the IP-ADM Predictions

#### 7.4.1.1 Water Treatment Applications: Counter-Current Flow Mode

Figures 7.4 to 7.6 depict the dissolved and the gaseous ozone profiles as functions of the dimensionless axial coordinate ( $Z$ ). The superficial liquid and gas velocities effects that are represented by  $St_L$  and  $St_G$ , respectively, were investigated together by studying the effects of the overall mass transfer coefficient ( $k_L a$ ) as both  $St_L$  and  $St_G$  are directly proportional to  $k_L a$ . The predicted dissolved ozone concentrations increased monotonically along the column height as the contact time between the gas phase and the liquid phase increases as the liquid flow passes through from the top to the bottom of the column. As shown in Figure 7.4 and as  $Pe_L$  increased, i.e., the magnitude of the backmixing decreased, the dissolved ozone profiles became steeper. The highest dissolved ozone concentrations occurred at the bottom of the column and as  $Pe_L$  increased from 1.0 to 20.0, the highest bottom concentration (i.e., the predicted dissolved ozone concentration in the effluent leaving the column) increased from 1.14 to 1.50  $mgL^{-1}$ , respectively. As  $Pe_L$  increased, the effects of  $Pe_L$  on the dissolved ozone profiles and the rate of increase of  $(C_L/C_{L,0}^*)$  per increase of  $Pe_L$ , at  $Z = 0.00$ , decreased. The dissolved ozone profiles exhibited an increasing axial gradient (slope) up to a turning point after which the slope of the profiles started to decrease. This could be explained by the boundary conditions applied at the bottom (zero-axial gradient of the profile) and at the top of the column (a concentration jump). As the liquid phase reaches plug flow conditions, the backmixing and the concentration jump will diminish (Lev and Regli, 1992; Zhou *et al.*, 1994). As  $Pe_L$  increased, the gaseous ozone concentrations increased and their profiles became flatter which was the only contradiction between the

predictions of the 1P-ADM and the 2P-ADM, but interestingly, both models were insensitive to changes in  $Pe_L$  in terms of their predicted gaseous ozone profiles. The rate of increase of  $(y/y_0)$  per increase of  $Pe_L$ , at  $Z = 1.00$ , increased and the predicted ozone off-gas concentration increased from 3.72 to 4.41  $\text{mgL}^{-1}$  as  $Pe_L$  increased from 1.0 to 20.0, respectively.

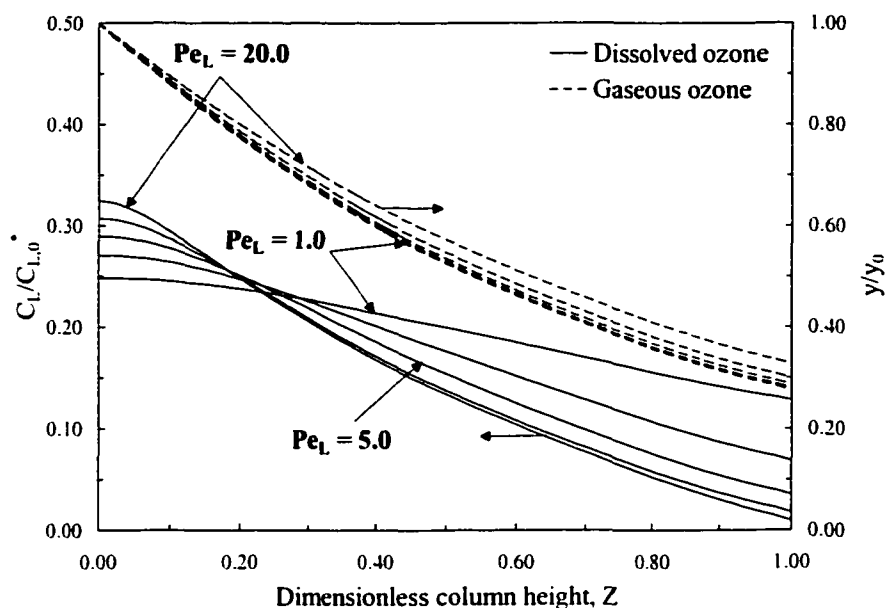


Figure 7.4  $Pe_L$  effects on the concentration profiles in the counter-current flow mode and water treatment applications.

As shown in Figure 7.5, the  $k_{La}$  effects on the concentration profiles decreased as  $k_{La}$  increased and those effects were more significant in the range of  $k_{La}$  from  $1.0 \times 10^{-3}$  to  $7.0 \times 10^{-3} \text{ s}^{-1}$ . In that range, the mass transfer increased along the entire column height and the profiles became steeper, while the mass transfer increased only near the bottom of the column (up to  $Z = 0.10$ ) and beyond that point the dissolved ozone concentrations decreased and the profiles became much more steeper as  $k_{La}$  increased from  $7.0 \times 10^{-3}$  to  $1.5 \times 10^{-2} \text{ s}^{-1}$ . As  $k_{La}$  increased, the rate of increase of  $(C_L/C_{L,0})$  per increase of  $k_{La}$ , at  $Z = 0.00$ , decreased. Zhou *et al.* (1994) observed the same phenomenon when they applied the 2P-ADM to predict the performance of ozone bubble columns under water treatment conditions.

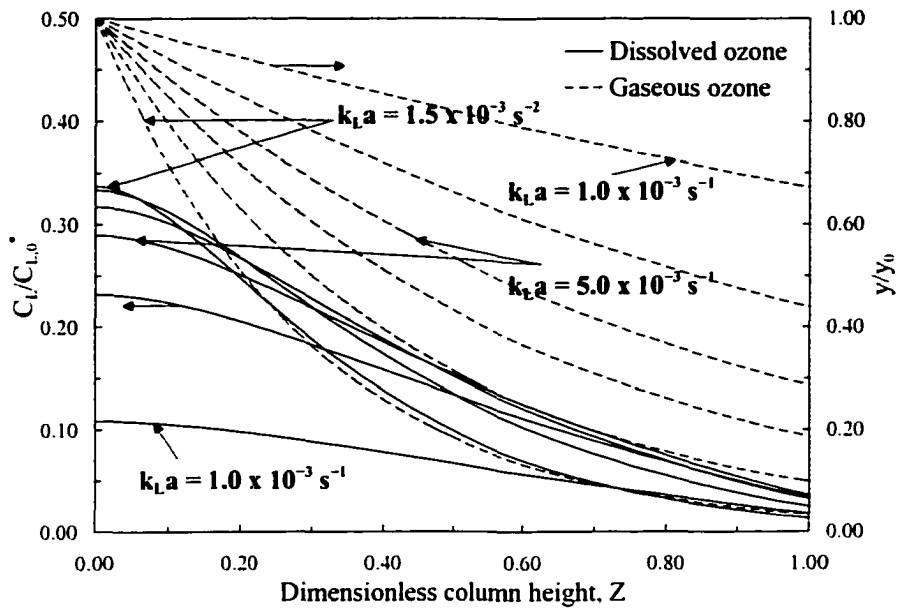


Figure 7.5  $k_L a$  effects on the concentration profiles in the counter-current flow mode and water treatment applications.

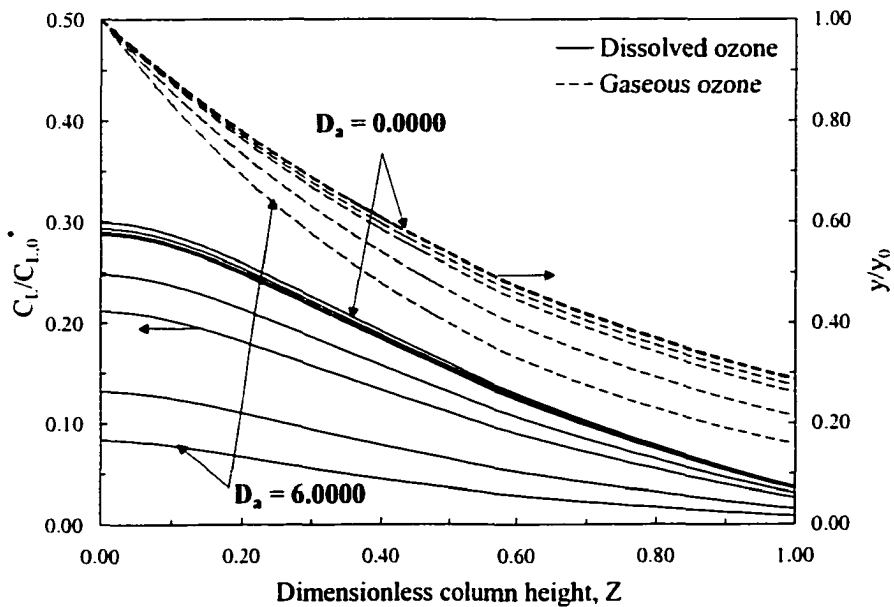


Figure 7.6  $D_2$  effects on the concentration profiles in the counter-current flow mode and water treatment applications.

As a result, improving the design of bubble columns to enhance the mass transfer process is essential and is only crucial near the column entrance. The same phenomenon

was observed before by Zhou *et al.* (1994). As  $k_L a$  increased, the dissolved ozone profiles became steeper and the predicted residual ozone concentration, in the effluent, increased from 0.50 to 1.55  $\text{mgL}^{-1}$ . The slope of the dissolved ozone profiles exhibited a similar trend to that observed over the studied range of  $Pe_L$ . As  $k_L a$  increased, the gaseous ozone profiles became steeper and the gaseous ozone concentrations decreased considerably along the entire column height. The rate of decrease of  $(y/y_0)$  per increase of  $k_L a$ , at  $Z = 1.00$ , decreased and the predicted ozone off-gas concentration decreased from 9.05 to 0.46  $\text{mgL}^{-1}$  as  $k_L a$  increased from  $1.0 \times 10^{-3}$  to  $1.5 \times 10^{-2} \text{ s}^{-1}$ , respectively.

Figure 7.6 depicts the effects of the overall pseudo-first order specific ozone utilization rate constant ( $k_w$ ) as one of the parameters that describe the quality of the water.  $k_w$  is represented by the dimensionless parameter ( $D_a$ ). A zero specific ozone utilization rate constant was included in the analysis as a base line and for the sake of comparison. As  $k_w$  increased from 0.00 to 0.05  $\text{s}^{-1}$  (i.e.,  $D_a$  increased from 0.0000 to 6.0000), the dissolved ozone profiles became flatter, the predicted effluent dissolved ozone concentration decreased, the gaseous ozone profiles became steeper, the predicted ozone off-gas concentration decreased, and the mass transfer process was suppressed over the entire column height. The effects of the  $D_a$  on the dissolved ozone profiles were more significant in the range of  $D_a$  from 0.0000 to 0.5050. The effluent dissolved ozone concentration decreased from 1.38 to 1.14  $\text{mgL}^{-1}$  and from 1.14 to 0.38  $\text{mgL}^{-1}$  as  $D_a$  increased from 0.0000 to 0.5050 and from 0.5050 to 6.0000, respectively. The rate of decrease of  $(C_L/C_{L,0}^*)$  per increase of  $D_a$ , at  $Z = 0.00$ , decreased as  $D_a$  increased. This is in agreement with the concept of slow and fast-reaction-kinetics regimes, and the slow-reaction kinetics regime exists when  $k_w$  is equal to or less than  $2.8 \times 10^{-3} \text{ s}^{-1}$ . The slope of the dissolved ozone profiles exhibited a similar trend to that observed over the studied range of  $Pe_L$ . The rate of decrease of  $(y/y_0)$  per increase of  $D_a$ , at  $Z = 1.00$ , decreased and the predicted ozone off-gas concentration decreased from 3.89 to 2.13  $\text{mgL}^{-1}$  as  $D_a$  increased from 0.0000 to 6.0000, respectively.

The effects of  $k_L a$  on the gaseous ozone profiles were more significant than the effects of  $Pe_L$  and  $D_a$ . This is in agreement with the gas-liquid mass transfer process

being the main process that dictates the overall performance of ozone bubble columns operating in the slow-reaction kinetics regime. Regarding the dissolved ozone profiles,  $k_L a$  and  $D_a$  were superior to  $Pe_L$  in their effects on the effluent residual dissolved ozone concentration.

#### 7.4.1.1 Water Treatment Applications: Co-Current Flow Mode

Figures 7.7 to 7.9 show the effects of  $Pe_L$ ,  $k_L a$ , and  $D_a$ , respectively, on the dissolved and the gaseous ozone profiles in the co-current flow mode in which the liquid and gas phases flow together in the same direction from the bottom to the top of the column.

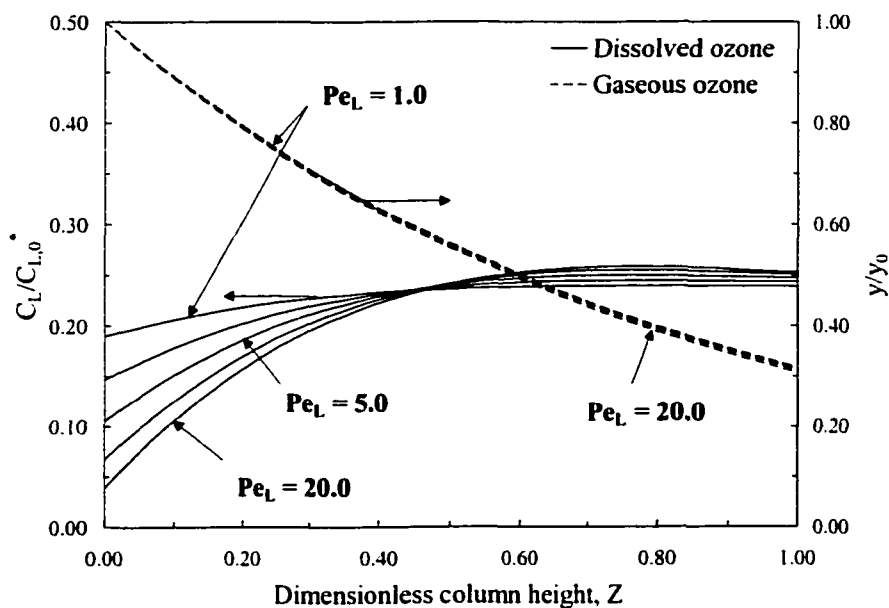


Figure 7.7  $Pe_L$  effects on the concentration profiles in the co-current flow mode and water treatment applications.

Based on that, the boundary conditions that are applied for the liquid phase are different from those applied in the counter-current flow mode and the dissolved ozone profiles exhibited a different trend from the one observed in the counter-current flow mode. The 1P-ADM predicted a concentration jump at the column inlet and the profiles reached

their peaks at different locations along the column height depending on the operating conditions that were considered for the model simulations. This phenomenon was observed before in the study of Zhou *et al.* (1994). Therefore, the effluent did not have the highest dissolved ozone concentration and the dissolved ozone profiles were flatter than those in the counter-current flow mode. Under some of the operating conditions assumed for the model simulations, the dissolved ozone profiles were closer to being uniformly distributed along the column height. The slope of the dissolved ozone profiles exhibited a decreasing trend up to a turning point after which it started to increase. The only exception for that observed trend was in the lower range of  $k_{La}$  from  $1.0 \times 10^{-3}$  to  $3.0 \times 10^{-3} \text{ s}^{-1}$  where the axial gradient of the dissolved ozone profiles exhibited a decreasing trend along the entire column height. As  $Pe_L$  and  $k_{La}$  increased and  $D_a$  decreased, the dissolved ozone profiles became steeper and they were generally more sensitive to changes in  $k_{La}$  and  $D_a$ . As  $Pe_L$  increased, the maximum predicted dissolved ozone concentration and the effluent dissolved ozone concentration increased from 1.10 to 1.20  $\text{mgL}^{-1}$  and from 1.10 to 1.16  $\text{mgL}^{-1}$ , respectively. Interestingly, the location at which the maximum dissolved ozone concentration occurred ( $Z = 0.76$ ) remained the same for the entire  $Pe_L$  range. The effects of  $Pe_L$  on the dissolved ozone profiles are similar to those observed in the counter-current flow mode. As  $Pe_L$  increased, the changes in the gaseous ozone profiles were insignificant and the predicted ozone off-gas concentration remained practically constant at 4.22  $\text{mgL}^{-1}$ .

The  $k_{La}$  effects on the dissolved ozone profiles were similar to those observed in the counter-current flow mode. As  $k_{La}$  increased from  $1.0 \times 10^{-3}$  to  $7.0 \times 10^{-3} \text{ s}^{-1}$ , the effluent and the maximum dissolved ozone concentrations increased from 0.45 to 1.17  $\text{mgL}^{-1}$  and from 0.45 to 1.25  $\text{mgL}^{-1}$ , respectively, and the location of the maximum concentration shifted from  $Z = 1.00$  to  $Z = 0.56$ , respectively. Meanwhile, as  $k_{La}$  increased from  $7.0 \times 10^{-3}$  to  $1.5 \times 10^{-2} \text{ s}^{-1}$ , the maximum dissolved ozone concentration increased from 1.25 to 1.40  $\text{mgL}^{-1}$ , the effluent dissolved ozone concentration decreased from 1.17 to 0.81  $\text{mgL}^{-1}$ , and the location of the maximum concentration shifted from  $Z = 0.56$  to  $Z = 0.22$ , respectively.

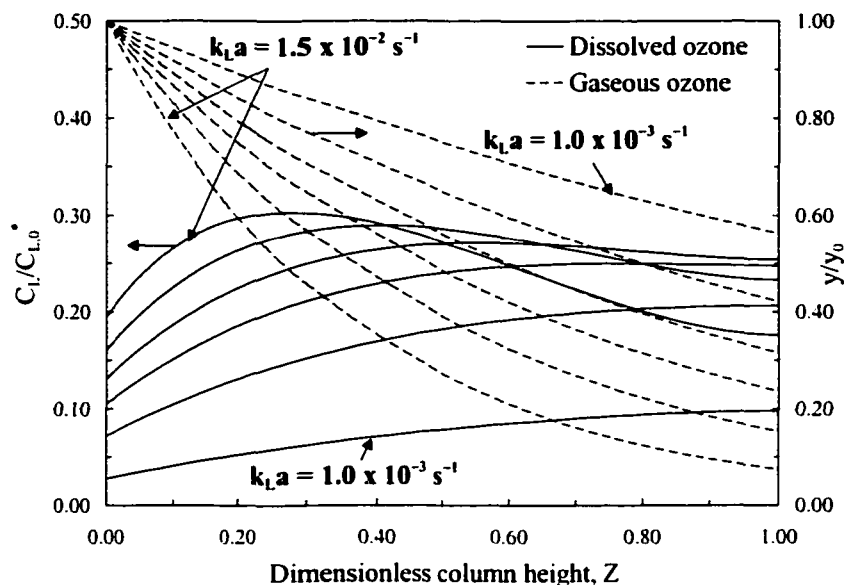


Figure 7.8  $k_{L,a}$  effects on the concentration profiles in the co-current flow mode and water treatment applications.

Therefore, we can define two distinctive regions of the mass transfer process as the behavior of the co-current ozone bubble column changed in terms of the predicted dissolved ozone concentration in the effluent leaving the column. As  $k_{L,a}$  increased above  $7.0 \times 10^{-3} \text{ s}^{-1}$ , most of the gaseous ozone would have been absorbed near the bottom of the column, thus, causing the peak of the dissolved ozone profiles to increase and consequently, the concentrations at  $Z > 0.40$  and  $Z > 0.63$ , at  $k_{L,a} = 1.0 \times 10^{-2}$  and  $1.5 \times 10^{-2} \text{ s}^{-1}$ , respectively, to decrease. The  $k_{L,a}$  effects on the gaseous ozone profiles were similar to those observed in the counter-current flow mode. The predicted ozone off-gas concentration decreased from  $7.57$  to  $1.00 \text{ mgL}^{-1}$  as  $k_{L,a}$  increased from  $1.0 \times 10^{-3}$  to  $1.5 \times 10^{-2} \text{ s}^{-1}$ , respectively.

As  $k_w$  increased from  $0.00$  to  $0.05 \text{ s}^{-1}$  (i.e.,  $D_a$  increased from  $0.0000$  to  $6.0000$ ), the effects on the dissolved and the gaseous ozone profiles were similar to those observed in the counter-current flow mode. As shown in Figure 7.9 and as  $D_a$  increased from  $0.0000$  to  $0.5050$ , respectively, the effluent and the maximum dissolved ozone concentrations decreased from  $1.19$  to  $0.90 \text{ mgL}^{-1}$  and from  $1.20$  to  $0.94 \text{ mgL}^{-1}$ , respectively, and the

location of the maximum concentration shifted from  $Z = 0.80$  to  $Z = 0.60$ , respectively. Then, as  $D_a$  increased from 0.5050 to 6.0000, respectively, the effluent and the maximum dissolved ozone concentrations decreased from  $0.90$  to  $0.12 \text{ mgL}^{-1}$  and from  $0.94$  to  $0.30 \text{ mgL}^{-1}$ , respectively, and the location of the maximum concentration shifted from  $Z = 0.60$  to  $Z = 0.22$ , respectively. As  $D_a$  increased, the ozone off-gas concentration decreased from  $4.28$  to  $2.07 \text{ mgL}^{-1}$ .

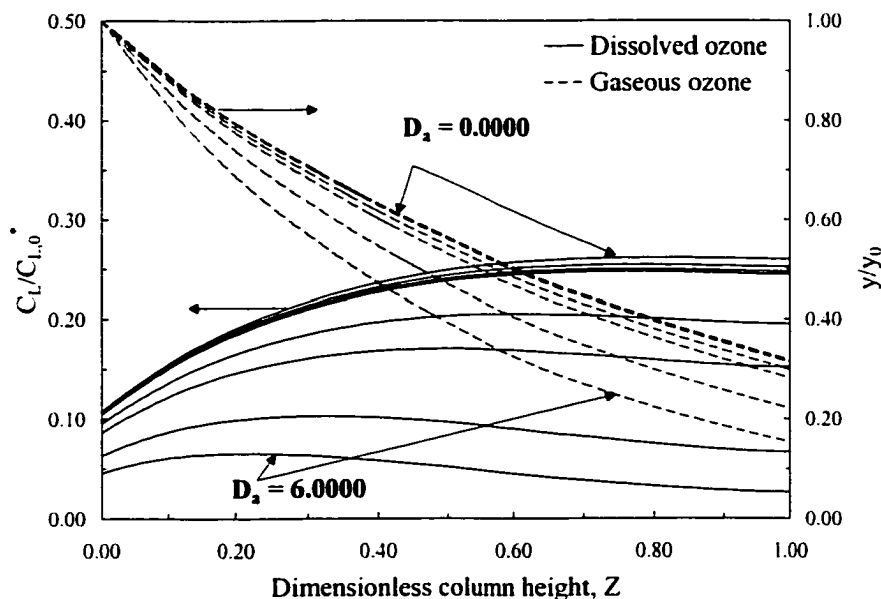


Figure 7.9  $D_a$  effects on the concentration profiles in the co-current flow mode and water treatment applications.

Under the same operating conditions, the counter-current flow mode was superior compared to the co-current flow mode in terms of the predicted dissolved ozone concentrations in the effluent leaving the column. In the counter-current and the co-current flow modes, the effects of  $k_{La}$  on the gaseous ozone profiles were more significant than the effects of  $Pe_L$  and  $D_a$  as the gas-liquid mass transfer process being the main process that dictates the overall performance of ozone bubble columns operating in the slow-reaction kinetics regime. Regarding the predicted ozone off-gas concentrations, both models predicted comparable concentrations with a relative difference that ranged from 13 to 6%, 16 to 54%, and 9 to 3% over the studied ranges of  $Pe_L$ ,  $k_{La}$ , and  $D_a$ ,

respectively, going from the low end to the high end of those ranges. Interestingly, the high relative difference (54%) at the high end of the  $k_L a$  range should not mislead us as the predicted ozone off-gas concentration ranged from 0.16 to 0.50  $\text{mgL}^{-1}$ .

#### 7.4.1.2 Wastewater Treatment Applications: Counter-Current and Co-Current Flow Modes

Figures 7.10 to 7.12 depict the effects of  $Pe_L$ ,  $k_L a$ , and  $D_a$  and  $M$ , respectively, on the dissolved and the gaseous ozone profiles in the counter-current flow mode. Interestingly, both flow modes produced similar dissolved and gaseous ozone profiles except for the lower range of  $D_a$  and  $M$  ( $D_a = 89$ ,  $M = 0.037$ ; and  $D_a = 534$ ,  $M = 0.090$ ) as shown in Figure 7.12. Under these operating conditions, the co-current 1P-ADM predicted dissolved ozone profiles with concentration jumps near the bottom of the column.

Generally, the dissolved ozone profiles exhibited a decreasing slope along the entire column height except at the high end of the  $D_a$  and  $M$  range as shown in Figure 7.12. The effects of  $k_L a$  on the gaseous ozone profiles were more significant than the effects of  $Pe_L$ , and  $D_a$  and  $M$ . Since the  $D_a$ - $M$  range used in the model simulations represents an intermediate range between the slow and the fast-reaction kinetics regimes, their effects on the gaseous ozone profiles are still inferior to the effects of  $k_L a$ . It should be noted that at  $Pe_L$  higher than 5.0, the 1P-ADM predicted very small dissolved ozone concentrations that were virtually equal to zero. As  $Pe_L$  increased from 1.0 to 5.0 and from 1.0 to 20.0, respectively, the dissolved and the gaseous ozone profiles were virtually identical. As shown in Figure 7.11 and as  $k_L a$  increased, the dissolved and the gaseous ozone profiles became steeper. The rate of increase of  $(C_L/C_{L,0}^*)$  per increase of  $k_L a$ , at  $Z = 0.00$ , was relatively high and it decreased as  $k_L a$  increased. Interestingly, the effluent dissolved ozone concentration exhibited a very small rate of change of  $(C_L/C_{L,0}^*)$  per increase of  $k_L a$  at  $Z = 1.00$ . As  $k_L a$  increased, this rate decreased. The dissolved ozone concentration, at  $Z = 1.00$ , started to increase as  $k_L a$  increased from  $1.0 \times 10^{-3}$  to  $3.0 \times 10^{-3} \text{ s}^{-1}$ , then as  $k_L a$  increased above  $3.0 \times 10^{-3} \text{ s}^{-1}$ , it started to decrease. As  $k_L a$  increased, its effect on

the gaseous ozone profiles decreased and the rate of decrease of  $(y/y_0)$  per increase of  $k_L a$ , at  $Z = 1.00$ , was relatively high and it decreased as  $k_L a$  increased.

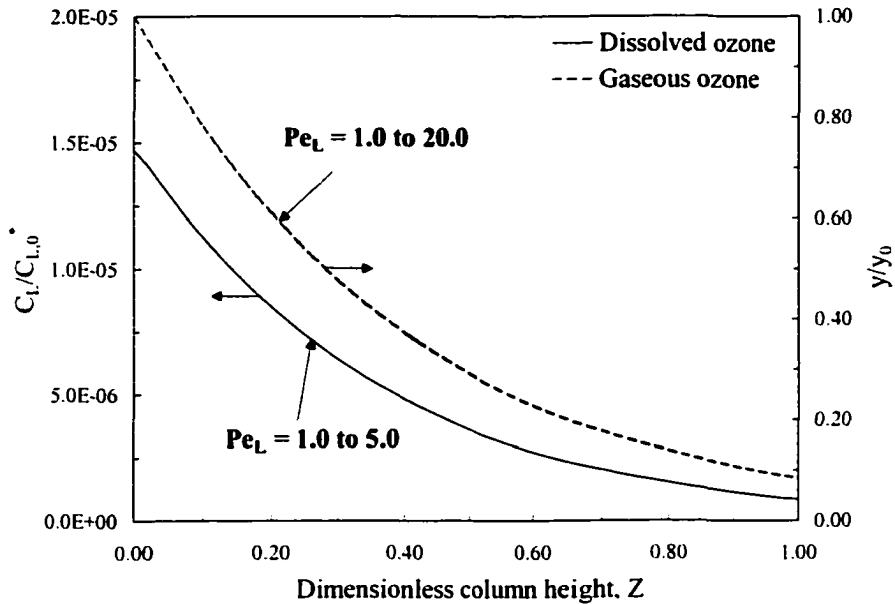


Figure 7.10  $Pe_L$  effects on the concentration profiles in the wastewater treatment applications.

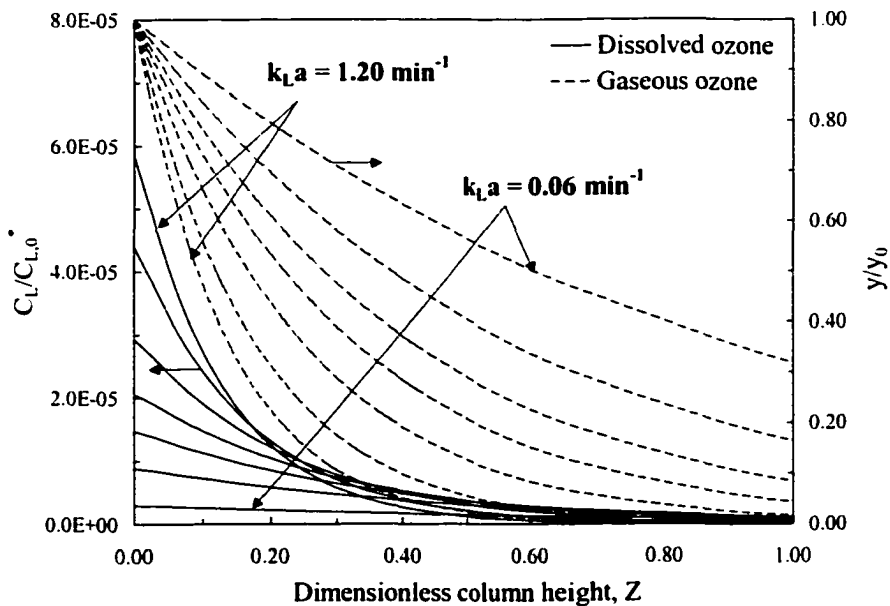


Figure 7.11  $k_L a$  effects on the concentration profiles in the wastewater treatment applications.

As shown in figure 7.12 and as  $D_a$  and  $M$  increased, the dissolved ozone profiles became flatter and the gaseous ozone profiles became steeper. The effects of  $D_a$  and  $M$  on the dissolved and the gaseous ozone profiles were more significant at the lower end of the  $D_a$  and  $M$  range. As  $D_a$  and  $M$  reached 35600 and 0.737, respectively, the dissolved ozone concentrations were practically equal to zero. The rates of decrease of  $(C_L/C_{L,0}^*)$  and  $(y/y_0)$  per increase of  $D_a$  and  $M$ , at  $Z = 0.00$  and  $Z = 1.00$ , respectively, increased as  $D_a$  and  $M$  increased. Those rates were virtually identical in the counter-current and the co-current flow modes.

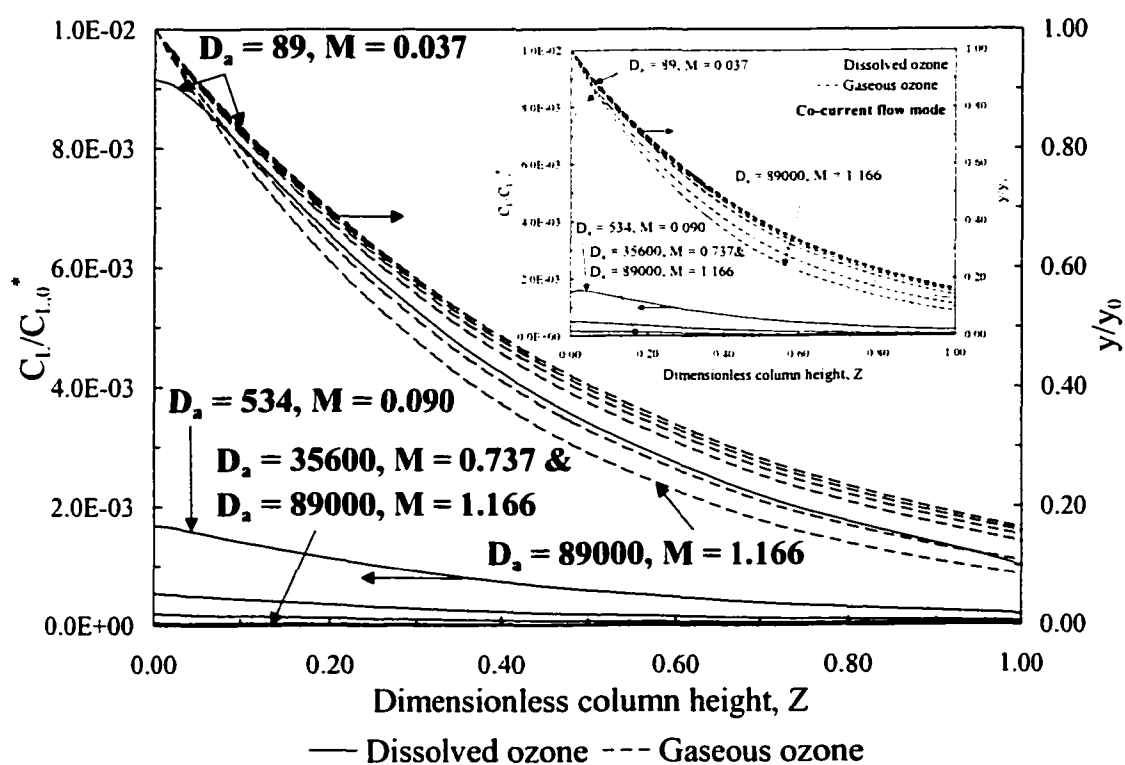


Figure 7.12  $D_a$  and  $M$  effects on the concentration profiles in the wastewater treatment applications.

The predicted ozone off-gas concentration ranged from 1.13 to 1.15  $\text{mgL}^{-1}$ , from 4.30 to 0.01  $\text{mgL}^{-1}$ , and from 2.20 to 1.13  $\text{mgL}^{-1}$  over the tested ranges of  $Pe_L$ ,  $k_{La}$ , and  $D_a$  and  $M$ , respectively (going from the low end to the high end of those ranges). Under the typical operating conditions ( $Pe_L = 5.0$ ;  $St_L = 0.9$ ;  $St_G = 2.07$ ;  $D_a = 89000$  (i.e.,  $k_w =$

500 s<sup>-1</sup>); and M = 1.166), the predicted ozone off-gas concentration was 1.13 mgL<sup>-1</sup>. With all the operating parameters being the same except for k<sub>L</sub>a which was set equal to 1.5 x 10<sup>-2</sup> s<sup>-1</sup>, the ozone off-gas concentration was predicted to be 0.04 mgL<sup>-1</sup> which is less than the detection limit of the iodometric titration (KI) method. Therefore, the model predictions of the ozone off-gas are in agreement with the previous experimental observations reported by Zhou and Smith (1997) and Zhou and Smith (2000).

Regarding the dissolved ozone profiles, k<sub>L</sub>a, and D<sub>a</sub> and M were superior to Pe<sub>L</sub> in their effects on those profiles and D<sub>a</sub> and M had the highest effects on the dissolved ozone concentrations. The predicted dissolved and gaseous ozone profiles were virtually identical in both the counter-current and the co-current flow modes. As a result, both flow modes are identical in terms of their efficiency towards the ozone absorption in bubble columns operating under wastewater treatment conditions. The maximum predicted dissolved ozone concentration of 4.2 x 10<sup>-2</sup> mgL<sup>-1</sup> (at the lower end of D<sub>a</sub> and M range) is less than the detection limit of the Indigo method which is in agreement with the experimental observations of undetectable dissolved ozone concentrations in the studies conducted by Zhou and Smith (1997) and Zhou and Smith (2000).

#### 7.4.2 Initial Model Testing for Water Treatment Conditions

Figures 7.13 and 7.14, respectively, demonstrate the applicability of the IP-ADM to predict the performance of counter-current and co-current bubble columns that use conventional fine-bubble diffusers as the gas spargers. Generally, there was an excellent agreement between the predicted and the experimental dissolved ozone profiles except for few data points where the model slightly predicted higher concentrations.

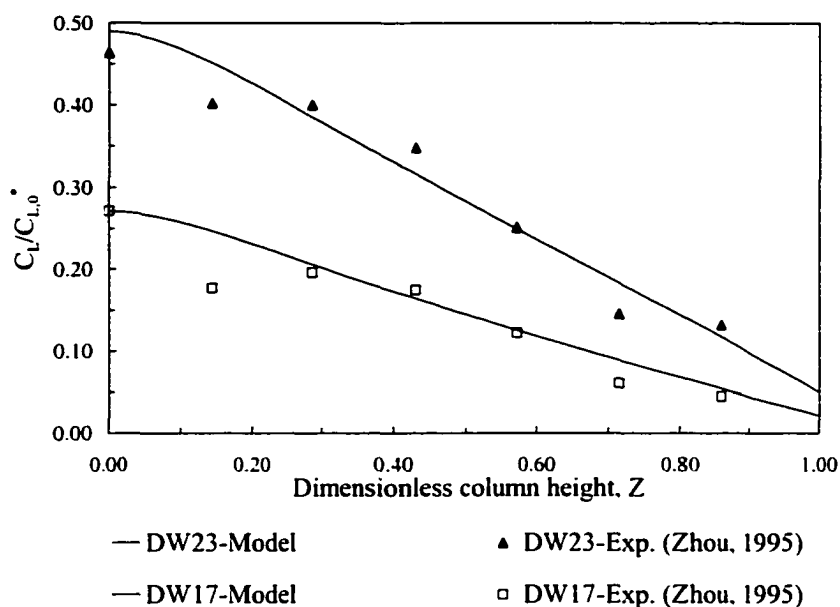


Figure 7.13 Comparison between the predicted and the experimental dissolved ozone concentrations in an ozone bubble column under water treatment conditions for the counter-current flow mode.

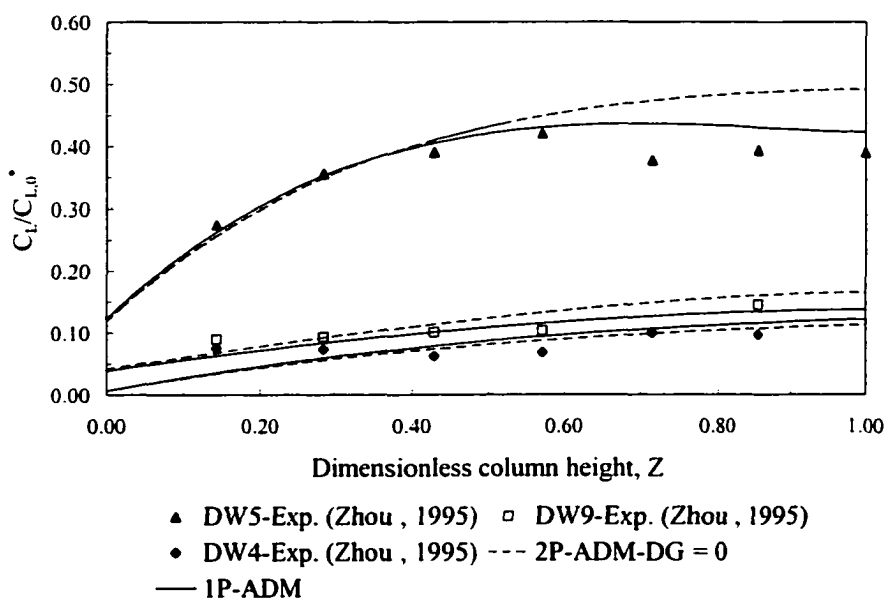


Figure 7.14 Comparison between the predicted and the experimental dissolved ozone concentrations in an ozone bubble column under water treatment conditions for the co-current flow mode.

Figure 7.14 depicts a comparison between the predictions of the 2P-ADM and the 1P-ADM in a co-current flow mode. There was a good agreement between the predicted and the experimental dissolved ozone profiles except for few data points where there was slight deviation between the predicted and the measured dissolved ozone concentrations. At 5 % significance level, t-tests have shown that there was no significant difference between the predictions of the 2P-ADM ( $D_G = 0$ ) and the 1P-ADM with the exception of run # 9, where there was no significant difference at a 1 % significance level. Therefore, when compared to the complete versions of the ADM, the 1P-ADM has proven to be an easy, reliable, and accurate tool for describing the performance of fine-diffuser ozone bubble columns.

## 7.5 CONCLUSIONS

The 1P-ADM can be solved analytically while the complete axial dispersion model (2P-ADM) requires an elaborate numerical technique to solve the model's equations. Therefore, describing the analytical solution of the 1P-ADM in terms of a simple spreadsheet program facilitates obtaining the model predictions for any operating conditions represented by the model input parameters entered into the spreadsheet program. Compared to the 2P-ADM predictions of the ozone bubble column performance that was presented in the study of Zhou *et al.* (1994), the 1P-ADM has proven to provide excellent predictions of the performance of ozone bubble columns operating under either water treatment conditions and in both the counter-current and the co-current flow modes. The 1P-ADM also provided good predictions of the performance of ozone bubble columns for the wastewater treatment applications. The 1P-ADM is easy and reliable tool to be used for the design and the process-control of bubble columns' operations.

## 7.6 REFERENCES

1. Alvarez-Cuenca, M. and M.A. Nerenberg, "Oxygen Mass Transfer in Bubble Columns Working at Large Gas and Liquid Flow Rates", *AIChE J.* 27(1): 66-73 (1981).
2. Alvarez-Cuenca, M., C.G.J. Baker, and M.A. Bergougnou, "Oxygen Mass Transfer in Bubble Columns", *Chem. Eng. Sci.* 35: 1121-1127 (1980).
3. Beltrán, F.J., J.F. García-Araya, and J.M. Encinar, "Henry and Mass Transfer Coefficients in the Ozonation of Wastewaters", *Ozone Sci. & Eng.* 19: 281-296 (1997).
4. Beltrán, F.J., J.M. Encinar, J.F. García-Araya, and M.G. Muñoz, "Modelling Industrial Wastewater Ozonation in Bubble Contactors-Part I: Rate Coefficient Determination", *Ozone Sci. & Eng.* 17: 355-378 (1995).
5. Chang, B.-J. and E.S.K. Chian, "A model Study of Ozone-Sparged Vessels for the Removal of Organics from Water", *Wat. Res.* 15(7): 929-936 (1981).
6. Danckwerts, P.V., *Gas-Liquid Reactions* (NY, USA: McGraw-Hill, Inc., 1970), pp. 105-114.
7. Deckwer, W.-D., K. Nguyen-Tien, B.G. Kelkar, and Y.T. Shah, "Applicability of Axial Dispersion Model to Analyze Mass Transfer Measurements in Bubble Columns", *AIChE J.* 29(6): 915-922 (1983).
8. Deckwer, W.-D. and J. Hallensleben, "Exclusion of Gas Sparger Influence on Mass Transfer in Bubble Columns", *Canadian J. Chem. Eng.* 58: 190-196 (1980).
9. Heinzle, E., F. Geiger, M. Fahmy, and O.M. Kut, "Integrated Ozonation-Biotreatment of Pulp Bleaching Wastewaters Containing Chlorinated Phenolic Compounds", *Biotechnol. Prog.* 8(1): 67-77 (1992).
10. Hoigné, J., "Mechanisms, Rates and Selectivities of Oxidants of Organic Compounds Initiated by Ozonation in Water", *Handbook of Ozone Technology and Applications* (MI, USA: Ann Arbor Science Publishers, 1982).
11. Hull, C.S., P.C. Singer, K. Saravanan, and C.T. Miller, "Ozone Mass Transfer and Reaction: Completely Mixed Systems", *Proc. of the Annual AWWA Conf.: Water Quality*, Vancouver, BC, Canada, 1992.

12. Jokela, J.K., M. Lalne, M. Ek, and M. Salkinoja-Salnoen, "Effect of Biological Treatment on Halogenated Organics in Bleached Kraft Pulp Mill Wastewaters Studied by Molecular Weight Distribution Analysis", *Environ. Sci. & Technol.* 27(3): 547-557 (1993).
13. Johnson, P.N. and R.A. Davis, "Diffusivity of Ozone in Water", *J. Chem. Eng. Data* 41: 1485-1487 (1996).
14. Kaštánek, J., J. Zahradník, J. Kratochvíl, and J. Čermák, *Chemical Reactors for Gas-Liquid Systems* (Chichester, England: Ellis Horwood, 1993), pp. 22-23.
15. Kramers, H. and K.R. Westerterp, *Elements of Chemical Reactor Design and Operation* (NY, USA: Academic Press, Inc., 1963), pp. 146-150.
16. Kreyszig, E., *Advanced Engineering Mathematics, 6<sup>th</sup> ed.* (NY, USA: John Wiley and Sons, Inc., 1988), pp. 145-146.
17. Kuo, C.H., "Mass Transfer in Ozone Absorption", *Environ. Prog.* 1(3): 189-195 (1982).
18. Langlais, B., D.A. Reckhow, and D.R. Brink, *Ozone in Water Treatment: Application and Engineering* (MI, USA: Lewis Publishers, Inc., 1991).
19. Laplanche, A., N. Le Sauze, G. Martin, and B. Langlais, "Simulation of Ozone Transfer in Water: Comparison with a Pilot Unit", *Ozone Sci. & Eng.* 13(5): 13, 535-558 (1991).
20. Lev, O. and S. Regli, "Evaluation of Ozone Disinfection Systems: Characteristic Contact Time T", *J. Environ. Eng., ASCE* 118(2): 268-285 (1992).
21. Levenspiel, O., *Chemical Reaction Engineering, 2<sup>nd</sup> ed.* (NY, USA: John Wiley and Sons, Inc., 1972).
22. Mecklenburgh, J.C. and S. Hartland, *The Theory of Backmixing* (NY, USA: John Wiley and Sons, Inc., 1975), pp. 15-23.
23. Oke, N.J., D.W. Smith, and H. Zhou, "An Empirical Analysis of Ozone Decay Kinetics in Natural Waters", *Ozone Sci. & Eng.* 20: 361-379 (1998).
24. Sotelo, J.L., F.J. Beltrán, F.J. Benitez, and J. Beltrán-Heredia, "Henry's Law Constant for the Ozone-Water System", *Wat. Res.* 23(10): 1239-1246 (1989).

25. Yurteri, C. and M.D. Gurol, "Ozone Consumption in Natural Waters: Effects of Background Organic Matter, pH and Carbonate Species", *Ozone Sci. & Eng.* 10: 277-290 (1988).
26. Zhou, H. and D.W. Smith, "Ozone Mass Transfer in Water and Wastewater Treatment: Experimental Observations Using a 2D-Laser Particle Dynamics Analyzer", *Wat. Res.* 34: 909-921 (2000).
27. Zhou, H. and D.W. Smith, "Applying Mass Transfer Theory to Study the Kinetics of Fast Ozone Reactions in Pulp Mill Effluents", *Proc. of the 14<sup>th</sup> Ozone World Congress*, Detroit, MI, USA, 1999.
28. Zhou, H. and D.W. Smith, "Process Parameter Development for Ozonation of Kraft Pulp Mill Effluents", *Wat. Sci. & Technol.* 35(2-3): 251-259 (1997).
29. Zhou, H., *Investigation of Ozone Disinfection Kinetics and Contactor Performance Modeling: Ph.D. Thesis* (Edmonton, AB, Canada: University of Alberta, 1995), pp. 307-312.
30. Zhou, H., D.W. Smith, and S.J. Stanley, "Modeling of Dissolved Ozone Concentration Profiles in Bubble Columns", *J. Environ. Eng., ASCE* 120(4): 821-840 (1994).

## CHAPTER 8. DEVELOPMENT OF DESIGN PARAMETERS OF AN IMPINGING-JET BUBBLE COLUMN\*

### 8.1 INTRODUCTION

Ozonation is one of the treatment processes used in treating water and wastewater and it is one of many chemical processes that take place in gas-liquid reactors. In water treatment applications, ozonation is limited by the mass transfer process as it is considered the controlling process that dictates the overall performance of ozone contactors (Gamal El-Din and Smith, 2000; Zhou *et al.*, 1994). Bubble-diffuser contactors are the most common method used for treating water using the on-site generated ozone gas. In order to maximize the treatment level achieved in ozone contactors, the contactor and the gas absorber geometry need to be modified to achieve higher turbulence and mixing in the liquid phase. According to Danckwerts' theory of surface renewal, as the mixing increases, the liquid film at the gas-liquid interface will be renewed at a higher rate causing the local mass transfer coefficient ( $k_L$ ) to increase (Danckwerts, 1970). Increasing the turbulence in the liquid phase will lead to higher turbulent shear stresses. As a result, the gas bubbles will become smaller. Consequently, the gas bubbles' specific interfacial area will increase leading to higher overall mass transfer coefficient ( $k_{La}$ ). The ozone gas-absorption in water treatment is assumed to follow the slow-reaction kinetics regime (Zhou *et al.*, 1994; Gamal El-Din and Smith, 2000). Since the ozone gas diffusivity in the liquid phase is much smaller than that in the gas phase, the gas diffusion through the liquid film becomes the rate-limiting step of the mass transfer process (Valentin, 1967). The higher turbulent shear stresses will also cause the liquid film to become thinner, and as a result, the ozone gas will diffuse through the liquid film at a higher rate causing  $k_L$  to increase.

In the study of Witze (1974), when two axisymmetrical circular turbulent air jets (i.e., having the same nozzle diameter and momentum) intersected at an angle of  $180^\circ$ , the resultant jet behaved like a radial jet that grew at about three times the rate of a single radial jet.

---

A version of this chapter has been submitted for publication. Gamal El-Din, M. and D.W. Smith, Wat. Res. (March 2001).

As a result of the impingement, higher turbulent shear stresses were developed in the ambient fluid and a region of backflow was observed. The same phenomenon was observed in the study of Khan (1989) who studied the impingement of circular turbulent water and air jets. Guo and Sharp (1996) studied the characteristics of radial jets and mixing under buoyant conditions. They observed that the turbulence intensity increased with the width of the orifice. Unger and Muzzio (1999) investigated the effect of a jet impingement at an intersecting angle of  $90^\circ$  on the mixing characteristics. It was observed that efficient and homogeneous mixing occurred at jets' Reynolds numbers ( $Re_j$ 's) greater than 300. Fitzgerald and Holley (1979) used two turbulent jets intersecting at an angle of  $90^\circ$  to investigate the resultant effects on the mixing behaviour. They observed more uniform and improved mixing across the annular tube.

Many researchers have attempted to improve the performance of bubble columns by maximizing the rate of physical gas absorption process. These attempts included: adding internal baffles (Catros, 1986), utilizing perforated plates (Chen *et al.*, 1986), inducing internal liquid circulation in air-lift reactors (Lewis and Davidson, 1985), and utilizing motionless mixers (Wang and Fan, 1978).

Gas injectors were utilized by many researchers in order to improve the mass transfer process. Wachsmann *et al.* (1984) studied the mass transfer process using an injection-type nozzle. Gas was introduced under positive and negative pressures. They observed remarkable increase in the overall mass transfer coefficient ( $k_L a$ ) due to the generation of bubbles that had a large specific interfacial area. They also observed that the values of  $k_L a$  in the gas-injection mode varied from those in the gas-ejection mode. Thalasso *et al.* (1995) used a venturi-type injector to increase the gas transfer rates, and that led to an improvement in the performance of a bioreactor. Under gas injection mode, they observed an increase in  $k_L a$  as the liquid superficial velocity ( $u_L$ ) and the gas superficial velocity ( $u_G$ ) increased. In a gas-liquid spouted vessel, gas was absorbed under positive pressure into the liquid-phase flow (Nishikawa *et al.*, 1977). It was observed that as  $u_G$  and  $u_L$  increased,  $k_L a$  increased and  $k_L a$  was more dependent on  $u_G$  than on  $u_L$ . Wang and Fan (1978) studied the mass transfer process in bubble columns packed with

motionless mixers. They observed that  $k_L a$  was dependent on  $u_G$  and  $u_L$  and as  $u_G$  and  $u_L$  increased,  $k_L a$  increased. Huynh *et al.* (1991) studied the mass transfer process in an upward venturi-bubble column combination. They correlated  $k_L a$  with  $u_G$  and  $u_L$  for the bubble/venturi combination. As  $u_G$  and  $u_L$  increased,  $k_L a$  increased. The increase in  $u_G$  could have caused an increase in the gas bubbles' specific interfacial area while the increase in  $u_L$  could have resulted in an increase in the liquid-phase shear stresses (Huynh *et al.*, 1991). Higher turbulent shear stresses would cause the formation of smaller bubbles resulting in higher specific interfacial area. Also, higher shear stresses would cause the mixing to increase and the liquid film at the gas-liquid interface to be renewed at a higher rate leading to an increase in  $k_L$ . Zhou and Smith (2000) investigated the effects of gas flowrates on the gas bubbles' specific interfacial area using a 2D-Laser particle dynamics analyzer. They observed a proportional increase in the bubbles' specific interfacial area with the increase in  $u_G$  as a result of the linear increase in the gas hold-up. The same phenomenon was also reported by Roustan *et al.* (1996).

In the current study, two venturi injectors (Mazzei<sup>®</sup> injectors) were utilized to create turbulent gas-liquid jets in the ambient fluid. The intersecting of the gas-liquid jets caused an increase in the turbulence intensity produced in the ambient fluid and therefore, increased the rate of the gas mass transfer. The ozone auto-decomposition process in the deionized water was investigated in a headspace-free reactor under a wide range of initial ozone concentrations and liquid-phase temperatures. The ozonation experiments were conducted in a pilot-scale impinging-jet bubble column that was operated in a co-current flow mode under a wide range of operating conditions. The mass transfer and the backmixing processes were characterized by fitting the measured dissolved and gaseous ozone concentration profiles with the concentration profiles obtained using the modified non-isobaric one-phase axial dispersion model (1P-ADM) through a three-parameter optimization technique.

## 8.2 OUTLINE OF THE MODIFIED NON-ISOBARIC ONE-PHASE AXIAL DISPERSION MODEL (1P-ADM)

A number of processes occur simultaneously during the ozonation treatment. These processes are: convection and backmixing processes of the liquid and gas phases flowing through the contacting chamber, ozone gas mass transfer process, ozone auto-decomposition process, and competitive reactive processes of dissolved ozone with the constituents that are present in the water. In addition to these processes, the contactor configuration, the operating conditions, and the water quality will influence the overall performance of the ozonation treatment (Zhou, 1995). The overall ozone auto-decomposition rate is influenced by the concentration and the history of the ozonation process. Ozone auto-decomposition process could be represented by a modified pseudo-first-order rate expression when ozonation is used to treat waters that do not exhibit significant initial ozone demand (Yurteri and Gurol, 1988; Oke et al., 1998):

$$\frac{dC_L}{dt} = -k_w C_L \quad [8.1]$$

where:  $C_L$  = instantaneous dissolved ozone concentration ( $\text{mgL}^{-1}$ ),  $k_w$  = specific ozone utilization rate constant ( $\text{s}^{-1}$ ), and  $t$  = reaction time (s).

Axial dispersion model visualizes the flow of fluids in tubular bubble columns as plug flow on top of which a diffusion-like process is superimposed. When applying this model, it should be noted that the dispersion process is a macroscopic phenomenon. Thus, dispersed flow might not be fully developed close to the boundaries of the reactor (Deckwer *et al.*, 1983). The assumptions pertaining to the development of the modified non-isobaric steady-state one-phase axial dispersion model (1P-ADM) along with the detailed model development can be found in Gamal El-Din and Smith (2000). Schematic representation of a gas-liquid flow in a co-current bubble column is shown in Figure 8.1. The 1P-ADM is different from the complete axial dispersion model, or referred to as the two-phase axial dispersion model (2P-ADM), in its simple use for practical design and

process control of ozone contacting chambers. The 2P-ADM is represented by a system of two non-linear partial differential equations (Zhou *et al.*, 1994; Gamal El-Din and Smith, 2000). In order to solve that system of equations, an elaborate numerical solving technique is needed. On the other hand, the 1P-ADM is composed of a single non-homogeneous second-order linear ordinary differential equation representing the liquid phase. Yet, this liquid-phase differential equation accounts for the countering effects of the gas shrinkage and expansion caused by gas depletion and absorption and reduced liquid hydrostatic head.

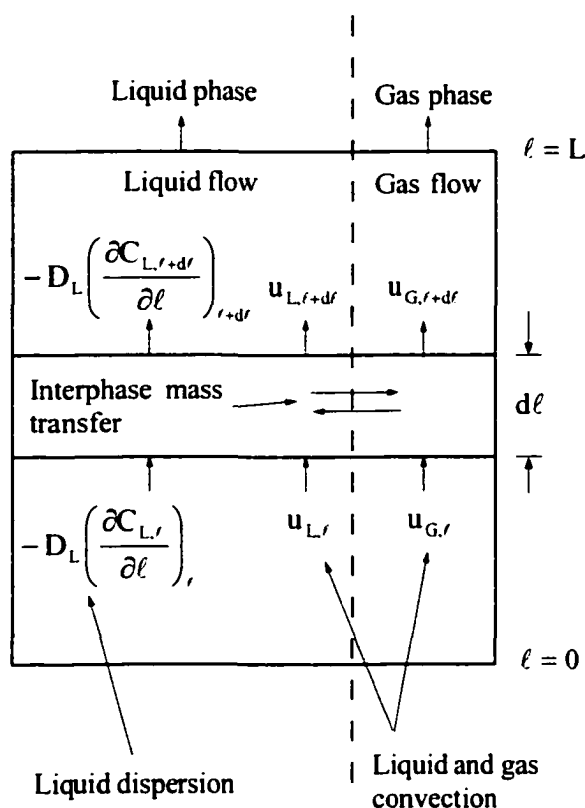


Figure 8.1 Schematic representation of the 1P-ADM.

The differential equation was solved analytically by the method of variation of parameters. The 1P-ADM was expressed in terms of dimensionless operating parameters and the available analytical solution of the differential equation representing the model was applied to determine the column-average overall mass transfer coefficient ( $k_{La}$ ), the liquid-phase axial dispersion coefficient ( $D_L$ ), and the coefficient of the gas-phase ozone molar fraction decrease along the column height ( $a_1$ ). This was achieved through a three-

parameter optimization technique by fitting the measured dissolved and gaseous ozone concentration profiles to the concentration profiles obtained using the 1P-ADM. In order to account for variable superficial gas velocity along the height of the bubble column, an exponential function was assumed to describe the variation of the gaseous ozone molar fraction along the column height (Gamal El-Din and Smith, 2000):

$$y_z = y_r = y_0 e^{-a_1 Z} \quad [8.2]$$

where:  $Z = \frac{\ell}{L}$  = dimensionless axial co-ordinate of the column,  $L$  = total height of the bubble column,  $y_0$  = gas-phase ozone molar fraction at the column entrance (i.e., at  $Z = 0$ ),  $y_z$  = gas-phase ozone mole fraction at the dimensionless axial co-ordinate ( $Z$ ), and  $a_1$  = coefficient of the gas-phase ozone molar fraction decrease along the column height. It is practically impossible to measure experimentally the rate of any ozone auto-decomposition that would take place inside the gas bubbles flowing through the bubble column. In the development of the 1P-ADM, the ozone auto-decomposition was assumed to be negligible in the gas phase as done by several researchers when they modeled the ozonation treatment process in ozone bubble columns (Roustan, 1987; Zhou *et al.*, 1994). The gas phase was assumed to flow in a plug flow regime as a result of the relatively high buoyancy of the gas bubbles. Based on the above,  $a_1$  represents the overall decrease in the gas-phase ozone mole fraction due to the effects of the gas-liquid mass transfer and the gas-phase convection processes. Based on the theoretical data of Zhou *et al.* (1994) and Gamal El-Din and Smith (2000) regarding the gaseous ozone concentration profiles, it was assumed that  $a_1$  is a function of the ozonation process operating parameters. Those parameters include: Peclet number ( $Pe_L$ ), liquid-phase and gas-phase Stanton numbers ( $St_L$  and  $St_G$ , respectively), and Damköhler number ( $D_a$ ). The exponent ( $a_1$ ) can be determined experimentally by continuously monitoring the ozone concentrations in the feed and off-gas lines. The mathematical representations of the 1P-ADM input parameters are shown in Table 8.1. The non-homogeneous second-order linear ordinary differential equation representing the 1P-ADM and the pertaining boundary conditions are presented in Table 8.2.

Table 8.1 Dimensionless parameters pertaining to the 1P-ADM.

Dimensionless parameters	1P-ADM
Z	$z/L$
$Pe_L$	$u_L L / D_L \epsilon_L$
$St_L$	$k_L a L / u_L$
$St_G$	$(k_L a L / u_{G,0})(RT/H)$
$Da$	$k_w \epsilon_L L / u_L$
X	$C_{L,r} / C_{L,0}^*$
Y	$y_r / y_0$

Table 8.2 Mathematical representation of the 1P-ADM differential equation and boundary conditions.

Equations	
<b>Model differential equation</b>	$\frac{1}{Pe_L} \frac{d^2 X}{dZ^2} - \frac{dX}{dZ} - (St_L + Da)X + St_L (e^{-\alpha_1 Z} + \frac{\beta_1}{\alpha_1} Z e^{-\alpha_1 Z}) = 0$
<b>Closed-closed boundary conditions</b>	<p>at <math>Z = 0</math>:</p> $X_{inf} = X _{Z=0} - \frac{1}{Pe_L} \frac{\partial X}{\partial Z} _{Z=0}$ <p><math>Y = 1</math></p> <p>at <math>Z = 1</math>:</p> $\frac{\partial X}{\partial Z} _{Z=1} = 0$

Gamal El-Din and Smith (2000) developed the closed-form solution of the differential equation that describes the 1P-ADM to be as follows:

$$X = \frac{\left[ D_1 \lambda_2 e^{\lambda_2} + E_1 \left( 1 - \frac{\lambda_2}{Pe_L} \right) \right]}{N} e^{\lambda_2 z} - \frac{\left[ D_1 \lambda_1 e^{\lambda_1} + E_1 \left( 1 - \frac{\lambda_1}{Pe_L} \right) \right]}{N} e^{\lambda_1 z} + K_0 e^{-a_1 z} + K_1 Z e^{-a_1 z} \quad [8.3]$$

where:

$$\lambda_1 = Pe_L + \sqrt{Pe_L^2 + 4Pe_L(St_L + D_s)} \quad [8.4]$$

$$\lambda_2 = Pe_L - \sqrt{Pe_L^2 + 4Pe_L(St_L + D_s)} \quad [8.5]$$

$$K_0 = \frac{Pe_L St_L}{(\lambda_2 - \lambda_1)} \left[ \frac{1}{(a_1 + \lambda_2)} + \frac{\beta_1}{\alpha_1 (a_1 + \lambda_2)^2} - \frac{1}{(a_1 + \lambda_1)} - \frac{\beta_1}{\alpha_1 (a_1 + \lambda_1)^2} \right] \quad [8.6]$$

$$K_1 = \frac{-\beta_1 Pe_L St_L}{\alpha_1 (a_1 + \lambda_1)(a_1 + \lambda_2)} \quad [8.7]$$

$$D_1 = X_{inf} - K_0 \left( \frac{a_1}{Pe_L} + 1 \right) + \frac{K_1}{Pe_L} \quad [8.8]$$

$$E_1 = e^{-a_1} [-(K_0 + K_1)a_1 + K_1] \quad [8.9]$$

$$N = \left( 1 - \frac{\lambda_1}{Pe_L} \right) \lambda_2 e^{\lambda_2} - \left( 1 - \frac{\lambda_2}{Pe_L} \right) \lambda_1 e^{\lambda_1} \quad [8.10]$$

$$\alpha_i = a'y_0 = \frac{(P_T + \rho g \epsilon_L L)}{H} y_0 \quad [8.11]$$

and

$$\beta_i = b'y_0 = \frac{-\rho g \epsilon_L L}{H} y_0 \quad [8.12]$$

### 8.3 EXPERIMENTAL AND DATA ANALYSES METHODS

#### 8.3.1 Bench Tests: Ozone Auto-Decomposition kinetics Study

The ozone auto-decomposition kinetics batch experiments were conducted in a 1200 mL floating-lid headspace-free reactor made from glass (see Figure 8.2). Clean deionized water was used in these experiments as the test water. The main average characteristics of the test water are summarized in Table 8.3. As shown in Table 8.3, the quality of the deionized water was not high as indicated by its relatively high TOC (total organic carbon) concentration that was about  $0.51 \text{ mgL}^{-1}$ .

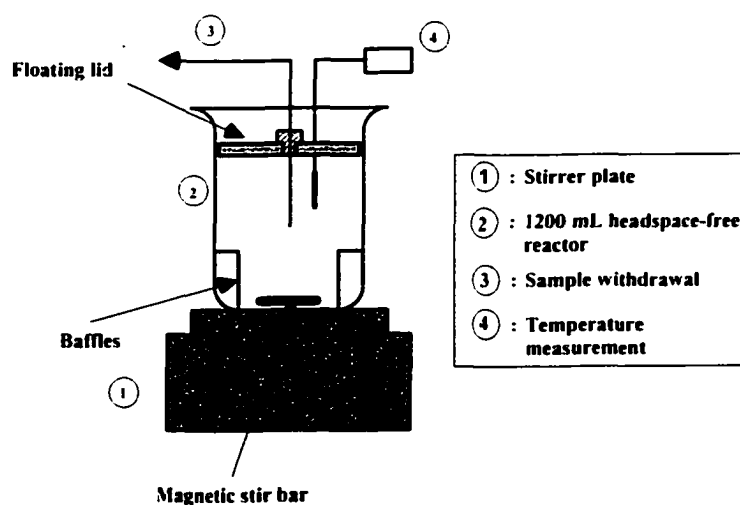


Figure 8.2 Schematic of the headspace-free reactor.

Table 8.3 Main Average characteristics of the deionized water.

<b>Parameters</b>	<b>TOC (mgL<sup>-1</sup>)</b>	<b>pH</b>	<b>A<sub>245 nm</sub><sup>10 mm</sup> (mm<sup>-1</sup>)</b>
Mean	0.51	5.99	0.004
Standard deviation	0.29	0.26	0.000

A volume of 800 mL of the deionized water was added to a 400 mL of an ozone stock solution to obtain a total of 1200 mL of an ozonated solution. The ozone gas was generated from an extra-dry oxygen gas using a corona-discharge ozone generator (model C2P-9C-4 PCI<sup>®</sup>). The ozone stock solution was prepared by continuously bubbling the generated ozone gas into 400 mL of clean deionized water in a 500 mL gas wash bottle for about 1,800 s to ensure that enough dissolved ozone concentration was present in the solution. In every test and after the ozone stock solution was transferred into the reactor, mixing started immediately. In all the tests, care was taken to ensure minimum ozone loss during the transfer of the ozone stock solution into the reactor.

Quality control tests were conducted in each test to assess the ozone loss during the transfer of the ozone stock solution, two samples were withdrawn from the ozone stock solution before transfer and after it was transferred and initially mixed with the deionized water. The two samples were analyzed to correct for the ozone loss during the transfer of the ozone stock solution into the reactor. The 1200 mL volume of the headspace-free reactor was chosen to allow for an adequate number of the samples to be withdrawn during the experiments while leaving enough water volume in the reactor to keep the floating-lid above the baffles and therefore, to prevent any headspace to develop. Immediately after the ozone stock solution was added to the test water inside the reactor, mixing was started and timing was initiated using a stopwatch. The contents of the reactor were mixed continuously using a slow magnetic stirrer bar. At pre-set sampling times, 15 mL samples of the reactor test water were withdrawn from the reactor and transferred immediately into 100 mL volumetric flasks to minimize any ozone loss during the sampling process. Each 100 mL volumetric flask contained 10 mL of indigo reagent and 75 mL of ozone demand-free (ODF) water. In all the tests, all the glassware that

came in contact with ozone was made ozone demand-free. An ozone-saturated solution was prepared by bubbling ozone gas into clean deionized water (ELGA<sup>®</sup> water) for at least 2,700 s. The ozonated water was then poured into the glassware that was sealed with aluminum foil and left overnight to satisfy any ozone demand. After that, the glassware was emptied and oven-dried before being used. All the experimental set-up components that came in contact with ozone during the experiments were made of glass, teflon, stainless steel, or PVC to reduce any possible interference that would result from the reactions between ozone and the experimental set-up components.

In order to measure the initial ozone demand of the test water, the first sample was withdrawn immediately, at  $t = 0$  s, as the ozone stock solution was initially mixed with the test water inside the reactor and after 30 s, the second sample was withdrawn. The difference in the dissolved ozone concentrations between the two samples represented the initial ozone demand of the test water. The samples absorbances were measured using a spectrophotometer (model ULTROSPEC 3000<sup>®</sup>) at a wave length of 600 nm and a path length of 10 mm. Each sample absorbance was then compared to the absorbance of a blank solution that was prepared by adding 10 mL of indigo reagent and 75 mL of ODF water into 15 mL of the test water. The dissolved ozone concentration was then calculated based on an absorbance coefficient of  $0.042 \text{ mm}^{-1}\text{Lmg}^{-1}$  according to the indigo method developed by Bader and Hoigné (1982). The tests were conducted over a wide range of initial dissolved ozone concentrations and water temperatures to investigate their effects on the ozone auto-decomposition kinetics. The initial dissolved ozone concentration and temperature of the test water ranged from 2.0 to 3.1  $\text{mgL}^{-1}$  and from 2.6 to 38.5 °C, respectively.

### 8.3.2 Pilot-Scale Tests: Ozone Mass Transfer Study

The ozone mass transfer experiments were conducted in a pilot-scale impinging-jet bubble column (see Figure 8.3). The bubble column was made from PVC and had an inside diameter of 100 mm and a total height of 1,520 mm.

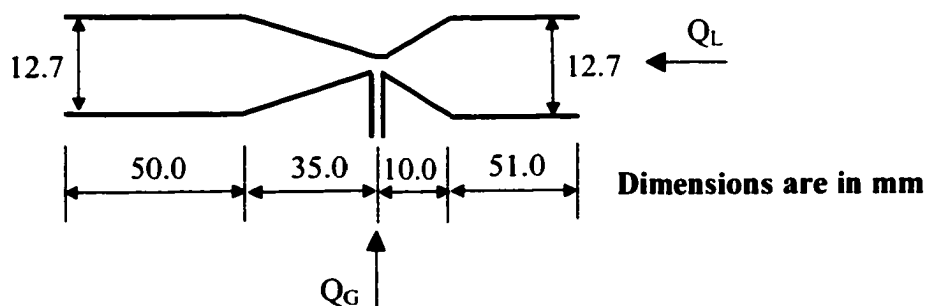
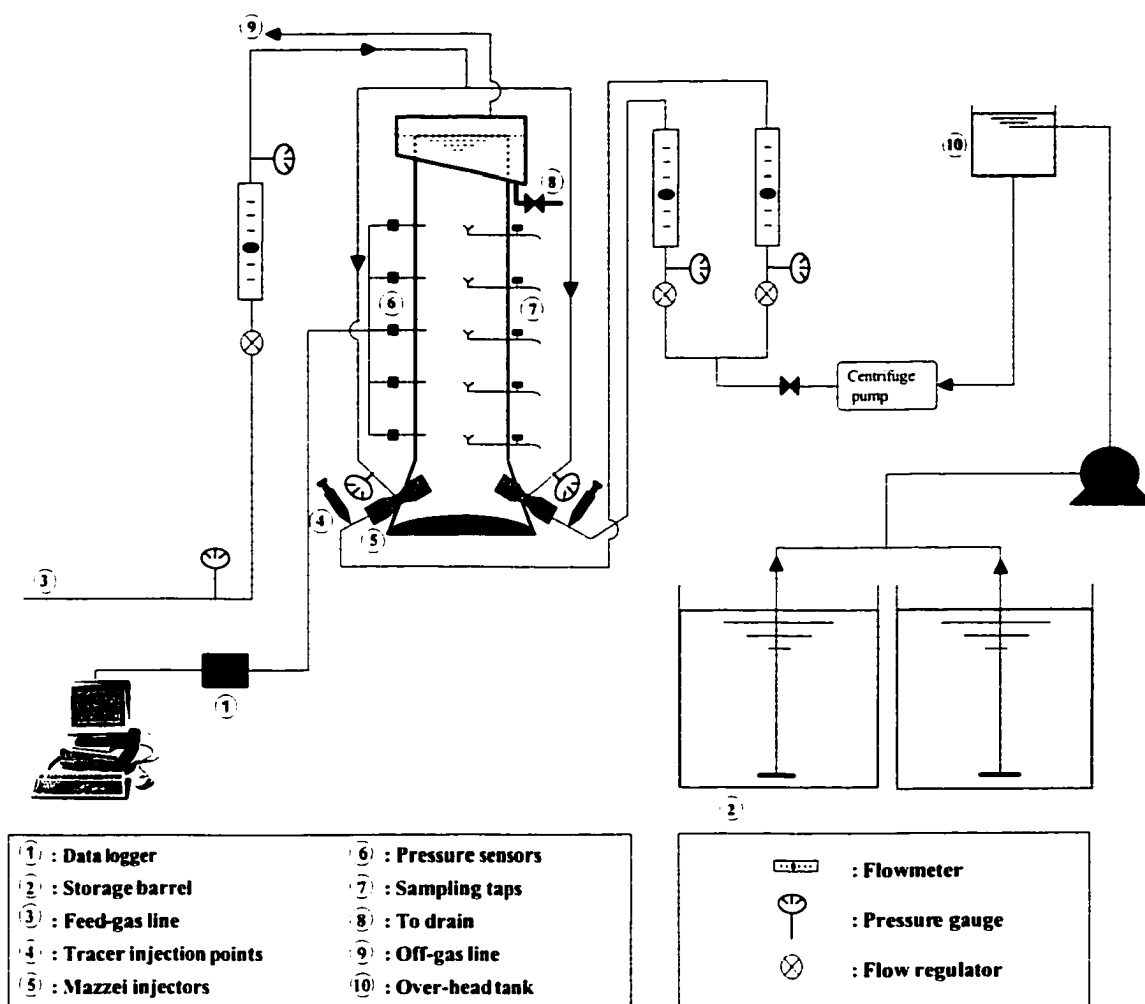


Figure 8.3 Schematics of the pilot-scale impinging-jet bubble column and the configuration of the Mazzei<sup>®</sup> injector (model 384).

The water depth was kept constant at 1,315 mm using an overflow weir that was placed at the top of the column. A ring tube was also installed at the top of the column with a 20 mm-diameter hole facing downward. A schematic of the configuration of the

kynar Mazzei<sup>®</sup> venturi injectors (model 384) is shown in Figure 8.3. The injectors were placed 25 mm above the bottom of the column at an intersecting angle of 125° and the distance between the centers of the nozzles was set equal to 60 mm. The bottom part of the bubble column consisted of an elliptical base to reduce the effect of the backward jet that was created in the ambient fluid as a result of the jet impingement and the sidewalls of that part of the column had a conical shape. With this geometry at the bottom of the column, the effects of short-circuiting were minimized. Based on the above reactor configuration, it was reasonable to assume that the backmixing along the column height was uniform. This assumption was also validated by the results of tracer experiments that were conducted in the bubble column.

During ozonation tests, water samples were withdrawn from the column from five bell-shaped sampling taps that were inserted inside the reactor at a distance equal to 1/3 of the column diameter and at equal intervals along the column height. The bell shape of the sampling taps helped minimizing the entrainment of gas bubbles into the withdrawn water samples for measuring the dissolved ozone concentrations. During each ozonation test, five water samples were withdrawn directly from the sampling taps into volumetric flasks at an adequate flowrate to minimize any ozone loss during the sampling procedure. The dissolved ozone concentrations were measured and calculated following the same procedure described in the kinetics study section. Five pressure sensors (Model 26PC Honeywell<sup>®</sup>) were inserted inside the reactor, at a distance equal to 1/3 of the column diameter and at intervals equal to those of the bell-shaped sampling taps, to monitor the pressure along the column height. The test water used in the experiments was clean deionized water of similar characteristics to those of the water used in the kinetics study. The ozone gas was generated from extra-dry pure oxygen using a corona discharge ozone generator (model GLS-7, PCI-WEDECO<sup>®</sup>). The ozone generator was allowed to stabilize for at least 1,800 s in order to obtain a stable ozone concentration in the feed gas. During the ozonation tests, the ozone concentrations in the feed and off-gas lines were continuously monitored using PCI-WEDECO<sup>®</sup> ozone monitors (models HC400 and LC, respectively). The ozone monitors were allowed at least 900 s to stabilize before recording their readings. Periodic calibration of the ozone monitors was conducted using

the KI method as described by the standard methods for examination of water and wastewater (APHA-AWWA-WEF, 1995). All the materials that came in contact with ozone during the experiments were made of glass, teflon, stainless steel, or PVC to reduce the possible interference that would result from the reactions between the dissolved and/or gaseous ozone and the experimental set-up components.

The ozone contactor was operated in a co-current flow mode and the gas was sparged into the liquid flow under two modes of pressure: positive pressure (i.e., injection) mode and negative or suction pressure (i.e., ejection) mode. In order to minimize the fluctuations in the liquid flowrates during experiments, the test water was pumped from two storage barrels into an overhead tank using peristaltic pumps then the water was pumped from the overhead tank into two lines leading into the injectors using a centrifugal pump. As the liquid motive flow passed through the injectors, the gas flow was introduced into the flow through the injectors' throats. The liquid flow, after being divided into two lines, was passed through two flowmeters to measure the liquid flowrates. The gas flow was passed through a gas rotameter to measure the gas flowrate. Pressure gauges were installed on the liquid-flow lines to measure the liquid pressure in the lines. Pressure gauges were also installed at the gas rotameter exit and at the injectors' throats to measure the gas pressures in the gas lines. All the pressure gauges were calibrated prior to their use. The bubble column was operated for a period of time that was at least eight theoretical reactor retention times to allow for the ozonation process to reach isothermal steady-state conditions and that was verified by reaching a constant off-gas ozone concentration in the exhaust-gas line. The gas hold-up data along the column height was obtained by continuous monitoring of the pressure readings along the column height. The pressure data were collected instantaneously and downloaded to a PC using a Lakewood<sup>®</sup> data logger. A wide range of superficial liquid velocities, and feed-gas velocities, and feed-gas ozone concentrations was investigated in order to study their effects on the performance of the impinging-jet ozone bubble column. The operating conditions of the pilot-scale ozonation experiments are presented in Table 8.4.

Table 8.1 Operating conditions of the pilot-scale ozone mass transfer experiments.

TR#	Flow pattern	Gas sparging mode	$u_G$ (ms <sup>-1</sup> )	$u_L$ (ms <sup>-1</sup> )	$T_L$ °C	$T_G$ °C	$C_{G0}$ (mgL <sup>-1</sup> )	$C_{G\text{eff}}$ (mgL <sup>-1</sup> )	$D_p$ (m <sup>2</sup> s <sup>-1</sup> )	1P-ADM fitted $k_L a$ (s <sup>-1</sup> )	1P-ADM fitted $a_p$	SSR	St <sub>L</sub>	St <sub>G</sub>	Pe <sub>L</sub>	D <sub>p</sub>
1			2.5E-03	7.7E-03	23.4	22.3	75.0	35.1	8.3E-03	1.3E-02	0.76	1.0E-03	2.20	1.55	1.17	6.1E-02
2			2.5E-03	1.4E-02	22.0	23.0	74.3	27.0	1.0E-02	1.8E-02	1.01	2.0E-03	1.59	2.05	1.70	2.9E-02
3			3.8E-03	7.7E-03	23.0	22.0	73.7	40.9	4.1E-03	2.5E-02	0.50	8.3E-03	4.05	1.93	2.35	5.9E-02
4			2.4E-03	1.4E-02	21.1	21.8	37.8	14.3	1.1E-02	2.1E-02	0.97	1.8E-03	1.93	2.60	1.61	2.6E-02
5			3.8E-03	7.5E-03	24.5	22.0	37.2	21.5	3.0E-03	2.2E-02	0.55	5.8E-04	3.67	1.70	3.21	7.0E-02
6	↕		3.6E-03	1.4E-02	23.0	22.0	37.9	17.1	6.1E-03	2.4E-02	0.80	1.7E-04	2.13	1.93	2.91	3.2E-02
7			7.5E-03	7.7E-03	24.2	22.1	37.5	26.4	1.5E-03	3.9E-02	0.30	2.7E-03	6.51	1.56	6.58	6.8E-02
8			7.3E-03	1.4E-02	23.1	22.1	37.4	21.8	5.3E-03	5.2E-02	0.54	8.8E-04	4.75	2.15	3.44	3.3E-02
9			1.1E-02	2.4E-02	22.7	22.5	37.3	21.2	3.2E-03	8.0E-02	0.30	6.9E-03	4.40	2.17	9.51	1.9E-02
10			2.6E-03	7.7E-03	22.7	22.3	11.6	5.7	5.7E-03	1.7E-02	0.50	2.2E-03	2.86	2.00	1.71	5.7E-02
11			3.8E-03	7.9E-03	24.0	22.5	11.2	6.5	3.3E-03	2.1E-02	0.50	2.2E-05	3.32	1.61	2.99	6.4E-02
12			2.6E-03	7.9E-03	21.1	22.0	37.5	18.5	6.3E-03	1.6E-02	0.33	1.4E-03	2.56	1.83	1.57	4.7E-02
13			1.8E-03	2.4E-02	21.3	22.8	74.6	15.8	2.4E-02	1.2E-02	1.55	4.1E-04	0.67	2.06	1.24	1.6E-02
14			2.8E-03	2.4E-02	21.3	22.3	75.4	21.2	2.3E-02	1.8E-02	1.27	2.6E-04	0.94	1.84	1.29	1.6E-02
15			1.4E-02	2.8E-02	21.0	22.5	22.5	13.3	1.2E-02	1.2E-01	0.53	1.9E-03	5.56	2.66	3.08	1.3E-02
16			1.8E-03	2.3E-02	19.5	22.1	38.0	8.2	2.3E-02	1.3E-02	1.53	3.8E-04	0.72	2.18	1.28	1.3E-02
17			2.9E-03	2.3E-02	22.6	22.2	37.8	11.1	2.3E-02	1.8E-02	1.23	4.9E-04	0.95	1.81	1.27	1.9E-02
18	↕		6.4E-03	2.3E-02	22.2	21.7	37.9	17.2	2.2E-02	5.2E-02	0.79	8.6E-04	2.89	2.46	1.40	1.8E-02
19			1.0E-02	2.8E-02	22.4	22.4	38.8	20.2	1.2E-02	7.6E-02	0.40	1.1E-03	3.46	2.19	3.00	1.5E-02
20			1.8E-03	2.3E-02	22.0	21.8	14.5	3.9	2.6E-02	1.1E-02	1.30	3.5E-04	0.58	1.75	1.13	1.7E-02
21			2.9E-03	2.3E-02	22.4	21.9	11.8	3.9	2.3E-02	1.6E-02	1.11	1.1E-03	0.90	1.70	1.31	1.9E-02
22			8.8E-03	2.3E-02	19.9	22.0	22.1	12.0	2.1E-02	8.7E-02	0.53	1.3E-03	4.75	2.95	1.41	1.4E-02
23			8.0E-03	2.8E-02	19.9	22.7	22.3	10.7	1.3E-02	5.7E-02	0.58	7.2E-03	2.61	2.13	2.74	1.2E-02

### 8.3.3 Data Analysis Method for the Kinetics Study

The ozone auto-decomposition process was assumed to follow first-order kinetics as described by Equation 8.1 and this assumption was considered valid if the plotted data of  $\ln [O_3]_t$  versus  $t$  could be represented by a straight line. The slope of that line would represent specific ozone utilization rate constant ( $k_w$ ) while the intercept would represent  $\ln[O_3]_{t=0s}$ . In all the ozonation tests,  $\ln[O_3]_{t=30s}$  was compared to  $\ln[O_3]_{t=0s}$  to calculate the initial ozone demand of the test water. A linear regression technique was employed to obtain the slope and the intercept of the proposed straight line. The predicted values of  $k_w$  were pooled together to investigate the effect of the water temperature ( $T_L$ ) on the ozone auto-decomposition kinetics. It was assumed that this effect could be described by the well-known van't Hoff-Arrhenius relationship:

$$\ln(k_w|_{T_L^{\circ}C}) = \ln(k_w|_{20^{\circ}C}) + (T_L - 20)\ln\theta \quad [8.13]$$

where:  $\theta$  = dimensionless temperature correction factor,  $k_w$  = specific ozone utilization rate constant ( $s^{-1}$ ), and  $T_L$  = water temperature ( $^{\circ}C$ ).

### 8.3.4 Data Analysis Method for the Mass Transfer Study

The solution of the steady-state 1P-ADM represented by Equation 8.3 was used to create a simple spreadsheet program in which the product cells were assigned to the column-average overall mass transfer coefficient ( $k_{La}$ ), liquid-phase axial dispersion coefficient ( $D_L$ ), and coefficient of the gas-phase ozone molar fraction decrease along the column height ( $a_1$ ). The specific ozone utilization rate constant ( $k_w|_{T_L^{\circ}C}$ ) had to be provided through the dimensionless Damköhler number ( $D_a$ ). For each ozonation test, since the water temperature ( $T_L$ ) was measured, a temperature correction factor ( $\theta$ ) that was obtained from the kinetics study was used to calculate  $k_w|_{T_L^{\circ}C}$ . In the spreadsheet program, the target cell was assigned to the following error norm:

$$SSR(k_L a, D_L, a_1) = \sum_{i=1}^{i=6} (X_{\text{measured},i} - X_{\text{calculated},i})^2 \quad [8.14]$$

Equation 8.14 represents the summation of squared residuals (SSR) of the difference between the measured and predicted dimensionless dissolved ozone concentrations. The spreadsheet program executed and the values of  $k_L a$ ,  $D_L$ , and  $a_1$  were varied until the SSR was minimized.

## 8.4 EXPERIMENTAL RESULTS

### 8.4.1 Bench Tests: Ozone Auto-Decomposition Kinetics Study

Comparisons of the  $\ln[O_3]_{t=30\text{ s}}$  with the  $\ln[O_3]_{t=0\text{ s}}$  values produced a relative error of  $\leq 0.6\%$ . This result supported the assumption that the clean deionized water had negligible or essentially no initial ozone demand. The plots of  $\ln[O_3]_t$  versus the reaction time ( $t$ ) were described by straight lines through the linear regression analyses with the coefficients of correlation ( $r$ 's)  $\geq 0.87$ .

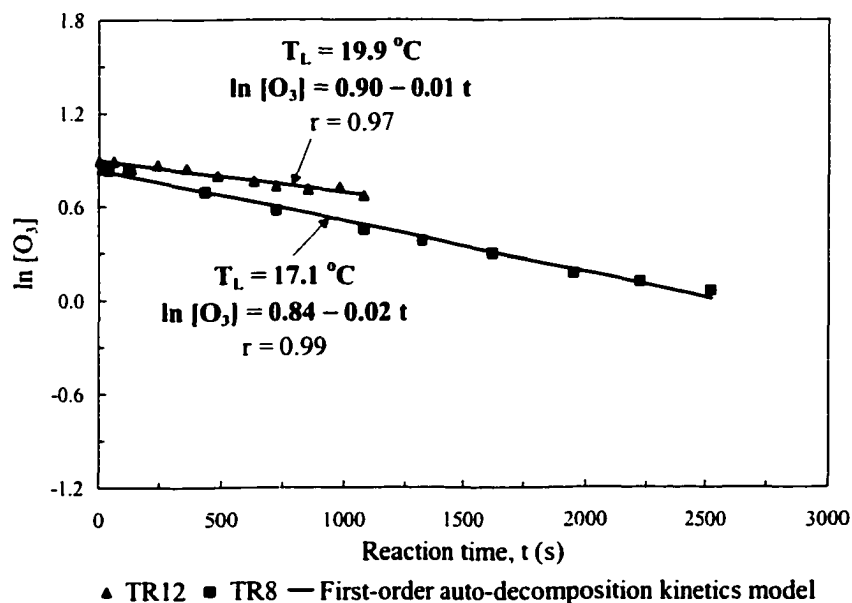


Figure 8.4 Typical ozone auto-decomposition kinetics in deionized water.

Figure 8.4 depicts typical plots of  $\ln[O_3]_t$  values versus as functions of the reaction time during two of the ozone auto-decomposition kinetics experiments under two different temperatures. As shown in Figure 8.4, the first-order kinetics can adequately describe the ozone auto-decomposition process in clean waters that have negligible initial ozone demand. The regression analysis produced similar specific ozone utilization rate constants ( $k_w$ 's) for the tests that were conducted at the same initial water temperature and different initial dissolved ozone concentrations. Therefore, it can be concluded that there was no effect of the initial ozone concentration on the specific ozone utilization rate constant.

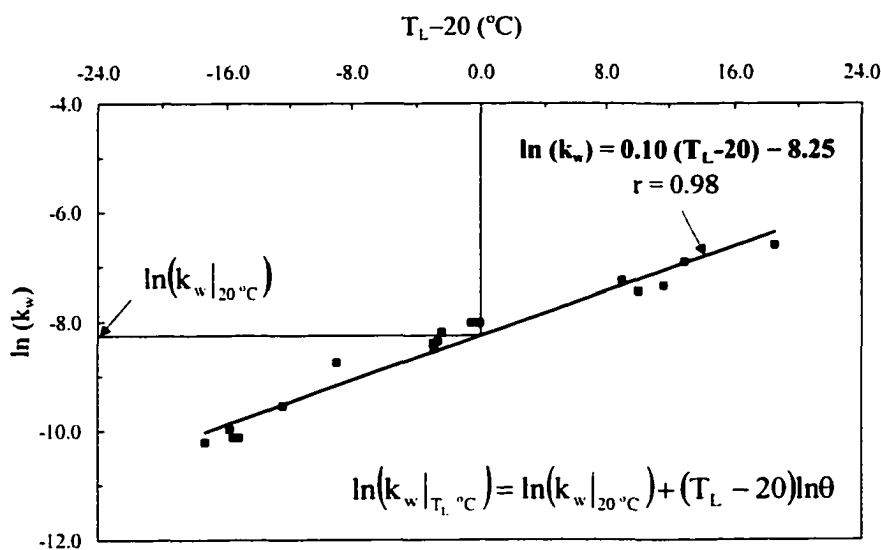


Figure 8.5 The effect of water temperature on the ozone auto-decomposition rate constant.

Figure 8.5 shows the effect of temperature on the ozone auto-decomposition rate constant. The temperature correction factor ( $\theta$ ) and  $k_w|_{20^\circ\text{C}}$  were found to be 1.11 and  $2.61 \times 10^{-4} \text{ s}^{-1}$ , respectively, and the coefficient of correlation ( $r$ ) was equal to 0.96. Yurteri and Gurol (1988) investigated the ozone auto-decomposition process in natural waters that are characterized by their high initial ozone demands.  $k_w|_{20^\circ\text{C}}$  was determined

to be  $2.78 \times 10^{-3} \text{ s}^{-1}$ . A comparison of the  $k_w|_{20^\circ\text{C}}$  value obtained in the current study with value obtained in the study of Yurteri and Gurol (1988) indicates that the ozone auto-decomposition process in clean waters, that exhibit negligible initial ozone demands, is a very slow process.

#### 8.4.2 Pilot-Scale Tests: Ozone Mass Transfer Study

In order to solve Equation 8.3 that represents the 1P-ADM, the spreadsheet program was allowed a maximum number of 200 iterations. Despite that, the convergence criterion was satisfied in less than 200 iterations and the SSR was minimized with a relative error in the  $\text{SSR} \leq 10^{-3}$ . Sensitivity analysis was conducted to test the sensitivity of the predicted dissolved ozone concentration profiles towards changes in  $k_{L,a}$ ,  $D_L$ , and  $a_1$ . The results indicated that these profiles were more sensitive to changes in  $k_{L,a}$  than changes in  $D_L$  and  $a_1$ . The same phenomenon was observed before by Deckwer *et al.* (1983) when they solved the axial dispersion model (ADM) in the liquid phase only to estimate  $k_{L,a}$  and  $D_L$  for a co-current 1mm-perforated-plate bubble column using a similar two-parameter minimization technique by varying  $k_{L,a}$  and  $D_L$ . At low liquid superficial velocity ( $u_L$ ) of  $5.4 \times 10^{-2}$ , there was reasonable agreement between the  $D_L$  values obtained using the minimization technique and the values using the correlation of Deckwer *et al.* (1974). The operating conditions and the results of the minimization solution technique for the pilot-scale ozone mass transfer experiments are shown in Table 8.4. Figures 8.6 and 8.7 depict typical dimensionless dissolved ozone concentration profiles in the injection and ejection modes, respectively. The dimensionless dissolved ozone concentrations are plotted as functions of the dimensionless axial co-ordinate of the column. Henry's law constant ( $H$ ) of  $0.22 \text{ kPaLmg}^{-1}$  was obtained from Sotelo *et al.* (1989).

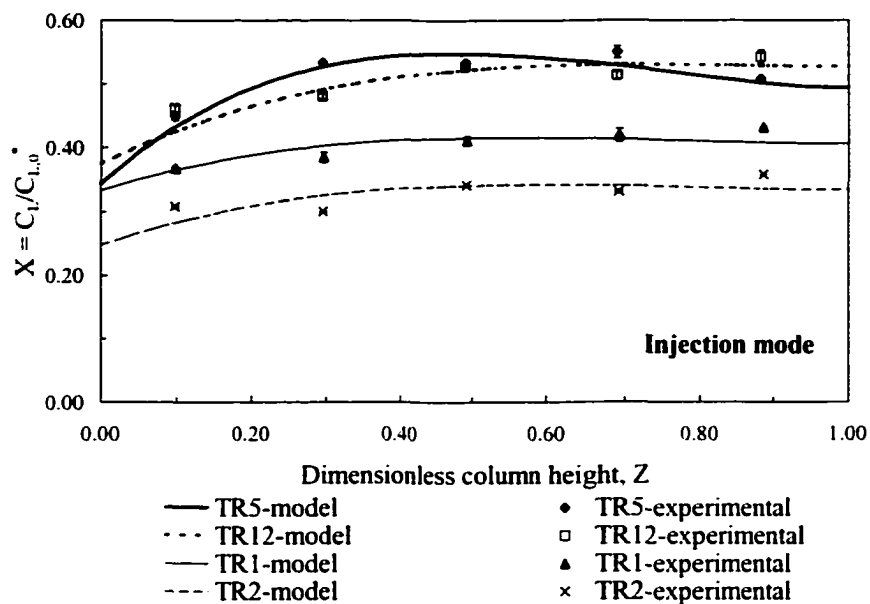


Figure 8.6 Typical dimensionless dissolved ozone concentration profiles in the impinging-jet bubble column operated in a gas-injection mode.

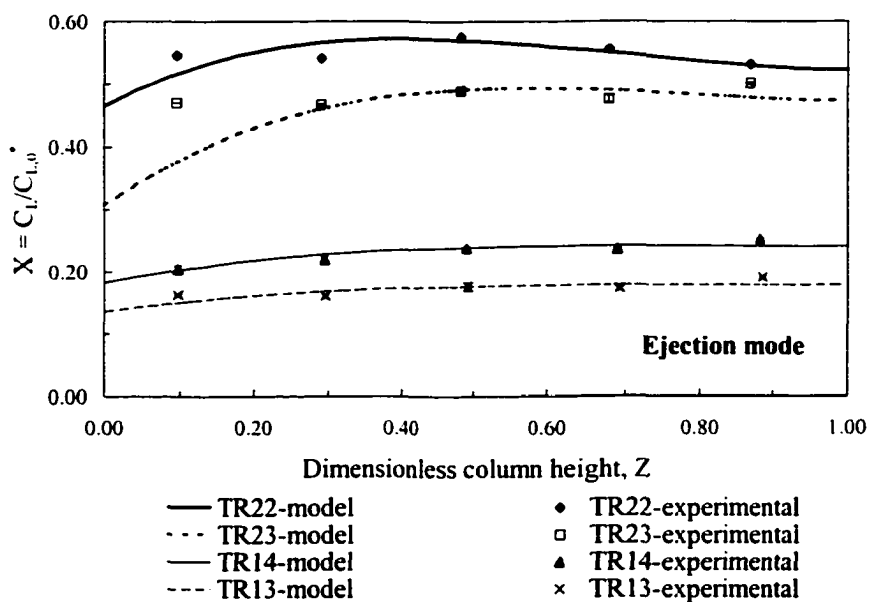


Figure 8.7 Typical dimensionless dissolved ozone concentration profiles in the impinging-jet bubble column operated in a gas-ejection mode.

Each ozone concentration was based on a number of two replicates. The absolute error between each pair of dissolved ozone concentrations was  $\leq 5.5\%$  with a mean value of  $1.3\%$ . The normalized standard deviation ( $SD/C_{L,0}^*$ ) of each pair of replicates was  $\leq 1.9 \times 10^{-2}$  with a mean value of  $3.7 \times 10^{-3}$ . As shown in Figures 8.6 and 8.7 and despite some deviations of the measured concentrations from the ones estimated by the 1P-ADM, the 1P-ADM has provided excellent predictions of the dissolved ozone concentration profiles. This is evident from the conformity between the measured and the predicted dissolved ozone concentrations. At the first sampling tap near the bottom of the column, the measured concentrations were sometimes higher than the estimated concentrations. This could be a result of the location of the first sampling tap being very close to the injectors' exit points and sometimes that led to entrainment of some gas bubbles into the liquid withdrawn from the sampling tap especially in the experiments that were conducted at high  $u_G$ 's. Due to the operating nature of the venturi injectors, the impinging-jet bubble column had to be operated in a co-current flow mode. Generally, the dissolved ozone concentrations, estimated by the 1P-ADM, increased along the column height up to a point where they started decreasing. The location of this point varied depending on the operating conditions.

Regarding the effect of  $u_G$  on the dissolved ozone concentration profiles, the profiles of TR's 5 and 12 were compared. Those tests were conducted in the injection mode at almost the same  $u_L$ . As  $u_G$  increased from  $2.6 \times 10^{-3} \text{ ms}^{-1}$  in TR 12 to  $3.8 \times 10^{-3} \text{ ms}^{-1}$  in TR 5, the maximum estimated dissolved ozone concentrations increased and their locations shifted from  $Z = 0.72$  to  $Z = 0.47$ . The same phenomenon was reported by Gamal El-Din and Smith (2000) when they investigated the effect of  $k_L a$  on the dissolved ozone concentration profiles in conventional diffuser bubble columns. The estimated  $k_L a$  increased from  $1.6 \times 10^{-2}$  in TR 12 to  $2.2 \times 10^{-2} \text{ s}^{-1}$  in TR 5 and the estimated  $D_L$  decreased by almost  $50\%$ . The estimated  $a_l$  increased from  $0.33$  in TR 12 to  $0.55$  in TR 5. A similar trend was observed in the ejection mode when comparing the profiles of TR's 13 and 22 except that the effect of increasing  $u_G$  on the estimated value of  $k_L a$  was

higher than that in the injection mode. Meanwhile, the effect of increasing  $u_G$  on the estimated value of  $D_L$  was lower than that in the injection mode.

Regarding the effect of  $u_L$  on the dissolved ozone concentration profiles, the profiles of TR's 1 and 2 were compared. Those tests were conducted in the injection mode at the same  $u_G$ . As  $u_L$  increased from  $7.7 \times 10^{-3} \text{ ms}^{-1}$  in TR 1 to  $1.4 \times 10^{-2} \text{ ms}^{-1}$  in TR 2, the maximum estimated dissolved ozone concentrations decreased. Also, the locations, of those maximum concentrations, were near the middle point of the column height (at  $Z = 0.54$  and  $Z = 0.58$  in TR 1 and 2, respectively). The same phenomenon was reported by Gamal El-Din and Smith (2000) when they investigated the effect of  $Pe_L$  on the dissolved ozone concentration profiles in conventional diffuser bubble columns. The estimated  $k_L a$  increased from  $1.3 \times 10^{-2}$  in TR 1 to  $1.8 \times 10^{-2} \text{ s}^{-1}$  in TR 2 and the estimated  $D_L$  increased by almost 20 %. The estimated  $a_1$  decreased from 1.55 in TR 13 to 0.53 in TR 22.

In the current bubble column design, the mass transfer process was maximized considerably and that led to higher mass transfer driving force ( $C_{L,i}^* - C_{L,i}$ ) throughout the entire column height. The ozone auto-decomposition process had minimal impact on the dissolved ozone profiles as a result of the low specific ozone utilization rate constant exhibited by the deionized water used in the current study. As a result, the mass transfer process was superior to the ozone auto-decomposition process in determining the shape of the dissolved ozone concentration profiles as well as the residual ozone concentration levels achieved in the column effluent.

The design of the impinging-jet bubble column is different from the conventional bubble column designs in terms of the interrelated effects of the superficial gas and liquid velocities ( $u_G$  and  $u_L$ ) on the performance of the gas-liquid injectors and ultimately, on the performance of the impinging-jet bubble column. Operating the venturi injectors in the injection or ejection mode and increasing  $u_L$ , an increase in  $u_G$  and a decrease in the injector throat pressure will occur, while operating at the same  $u_L$  and increasing  $u_G$  will cause the injector throat pressure to increase. The difference in pressure between the gas

introduction point and the exit point of the injector, inside the column, will affect the size of the gas bubbles leaving the injectors and consequently, the bubbles' specific interfacial area will change. At almost similar  $u_G$ , this differential pressure was generally higher and occurred at higher  $u_G$ 's in the ejection mode compared to those in the injection mode. As a result, the same combination of  $u_G$  and  $u_L$  cannot coexist in the injection and ejection modes. Therefore, the two modes of gas absorption had to be analyzed separately. Part of the overall system-mass-transfer efficiency is attributed to the contact time between the gas phase and the liquid phase inside the intense mixing zone inside the venturi injector, i.e., from the gas introduction point to the exit point of the injector inside the column (Mazzei and Bollyky, 1991). As a result, an increase in this contact time will lead to an increase in the efficiency of the overall mass transfer process.

## 8.5 DEVELOPMENT OF PROCESS-PARAMETER CORRELATIONS

In order to study the effects of the gas and liquid flowrates on the 1P-ADM estimations of the column-average  $k_{La}$  and  $D_L$ , relationships that correlate these two parameters with the superficial gas and liquid velocities ( $u_G$  and  $u_L$ ) were developed through non-linear regression analyses. Comparisons of the performance of the impinging-jet bubble column with the conventional bubble columns, in terms of  $k_{La}$ , were also conducted in order to assess the improvement in the mass transfer process by utilizing the impinging-jet technique for the ozone gas absorption process. The effects of the process variables on  $a_1$  were also studied by correlating  $a_1$  to the process variables  $Pe_L$ ,  $St_L$ ,  $St_G$ , and  $D_a$  by applying a linear regression technique.

As discussed earlier regarding the dynamic nature of the venturi injectors as gas absorbers, it was observed that they exhibited variable behaviour in the injection mode from that in the ejection mode. Therefore, the regression analyses were conducted for the gas-injection mode separately from the gas-ejection mode to obtain process parameter correlations that can be used for estimating the process variables ( $k_{La}$ ,  $D_L$ , and  $a_1$ ) using the operating conditions encountered during the ozonation process. The mass transfer process is a liquid-phase-temperature dependent while the backmixing process

dependency on the liquid-phase temperature is minimal (Deckwer, 1992). As a result, and due to the variable water temperature during the tests, the predicted  $k_L a$ 's were corrected for the temperature effect using a temperature correction factor ( $\theta$ ) equal to 1.024 as suggested by Roustan *et al.* (1996).

### 8.5.1 Correlations of the Mass Transfer Coefficient

In the impinging-jet bubble column,  $k_L a$  was affected by  $u_G$  and  $u_L$  in contrast to the case in most conventional bubble columns where it is usually affected only by  $u_G$  except for few studies involving other designs of bubble columns where  $k_L a$  was affected by  $u_G$  and  $u_L$ . Among these few studies, the combined venturi-bubble columns studied by Huynh *et al.* (1991) and Briens *et al.* (1992) emerged as promising new bubble column designs. For conventional diffuser bubble column, Deckwer *et al.* (1974) proposed an empirical correlation to be as follows:

$$k_L a = \alpha u_G^\beta \quad [8.15]$$

where:  $k_L a$  = overall mass transfer coefficient ( $s^{-1}$ ),  $u_G$  = superficial gas velocity ( $ms^{-1}$ ), and  $\alpha$  and  $\beta$  = empirical coefficients that are obtained through a non-linear regression analysis. In order to correct for the difference in diffusivity between oxygen and ozone, Danckwerts' surface renewal theory is applied as follows:

$$\frac{(k_L a)_{O_3}}{(k_L a)_{O_2}} = \sqrt{\frac{D_{O_3}}{D_{O_2}}} \quad [8.16]$$

The use of Equation 8.17, to correct  $k_L a$  from being an oxygen-based to ozone-based, has been previously validated (Sherwood *et al.*, 1975).  $D_{O_3}$  and  $D_{O_2}$  are the molecular diffusivities of ozone and oxygen gases, respectively, in water.  $D_{O_3}$  and  $D_{O_2}$  were taken as  $1.74 \times 10^{-9}$  and  $2.50 \times 10^{-9} m^2 s^{-1}$ , respectively. Based on "state of science" review of the literature, and after correcting for the temperature effect and converting  $k_L a$  to be

ozone-based instead of oxygen-based parameter, it was found that  $\alpha$  and  $\beta$  varied from 0.06 to 1.16 and from 0.54 to 0.88.  $\beta$  was found to be independent on the sparger type, however,  $\alpha$  was strongly affected by the sparger type and the liquid medium (Shah *et al.*, 1982). This variability in  $\alpha$  and  $\beta$  values could be attributed to the variable bubble column physical properties and scales, the type of gas sparging technique, neglecting the effect of test water properties on the ozone decay process, and more importantly the method of  $k_{La}$  determination. In most of these studies,  $k_{La}$  was calculated based on one of two assumptions regarding the backmixing in the liquid phase. The liquid phase was considered to flow in an ideal completely mixed or plug flow regimes. As a matter of fact, neither one of these flow regimes exists in bubble columns, since the liquid flow is usually closer to be in the completely mixed regime as a result of the backmixing process (Zhou *et al.*, 1994).

In the study conducted by Roustan *et al.* (1987), the conventional ozone contactor had a water height of 4,300 mm and two compartments in series, 117 m<sup>3</sup> and 128 m<sup>3</sup> in volume, respectively. In that study, two assumptions were made that seemed to have a significant impact on the determined values of  $k_{La}$ 's and that might have led to some discrepancy with the reported values of  $k_{La}$  in the literature. First, a complete mixing regime was assumed to dominate the liquid flow through the contactor and second, the ozone decay process was neglected in the potable test water since the water temperature was about 5 °C. Another source of discrepancy may have resulted from  $k_{La}$  being calculated based on conducting mass balance analyses of the ozone in the gas and liquid phases using only the influent and effluent dissolved and gaseous ozone concentrations. This method was not appropriate since the dissolved ozone concentration in the effluent might not have been sensitive to  $k_{La}$ , especially in situations where high-absorption efficiency existed. Also, any experimental errors that might be encountered in measuring the effluent concentration can lead to a large bias in estimating  $k_{La}$  (Zhou, 1995).

Laplanche *et al.* (1991) studied the ozone mass transfer process in a bubble column that had a height and a diameter equal to 4300 mm and 190 mm, respectively. They neglected the ozone decay process in the potable test water that was used in the

experiments and also the backmixing in the liquid phase was neglected leading to the assumption that the liquid flow through the reactor was in perfect plug flow regime.

Deckwer *et al.* (1974) studied the oxygen mass transfer process in two bubble columns that had diameters of 200 mm 150 mm, and heights of 7230 mm and 4400 mm. They used the axial dispersion model to describe the bubble column performance. A one-parameter minimization technique was applied to determine  $k_{L,a}$  by fitting the measured dissolved oxygen profiles to the predicted profiles. This approach seems to be the most appropriate method to characterize the mass transfer in bubble columns operated in a continuous-flow mode since it takes into account the backmixing effect on  $k_{L,a}$  and the resultant concentration jump occurring at the column inlet due to the column inlet boundary conditions. Also, it uses the concentration profiles along the entire column height to determine the column-average  $k_{L,a}$ .

Deckwer *et al.* (1983) examined the applicability of the 2P-ADM to analyze the mass transfer measurements in bubble columns. They used the same approach applied by Deckwer *et al.* (1974) except for using a two-parameter ( $k_{L,a}$  and  $D_L$ ) instead of a 1-parameter ( $k_{L,a}$ ) minimization technique. In order to examine the sensitivity of the predicted  $k_{L,a}$  to changes in the backmixing coefficient ( $D_L$ ), they calculated  $D_L$  using the relationship suggested by Deckwer *et al.* (1974) that correlated  $D_L$  with the superficial gas velocity and the bubble column diameter. Then, they used the one-parameter minimization technique to determine  $k_{L,a}$ . They observed that  $k_{L,a}$  varied only slightly (< 10 %) between the two minimization techniques.

In the studies conducted by Huynh *et al.* (1991) and Briens *et al.* (1992),  $k_{L,a}$  was correlated to  $u_G$  and  $u_L$  according to the following relationship:

$$k_{L,a} = \alpha u_G^\beta u_L^\gamma \quad [8.17]$$

where:  $k_{L,a}$  = overall mass transfer coefficient ( $s^{-1}$ ),  $u_G$  = superficial gas velocity ( $ms^{-1}$ ),  $u_L$  = superficial liquid velocity ( $ms^{-1}$ ), and  $\alpha$ ,  $\beta$ , and  $\gamma$  = empirical coefficients that are

obtained through a non-linear regression analysis. Huynh *et al.* (1991) correlated  $u_G$  and  $u_L$  to the venturi-bubble column average  $k_{L,a}$ . In that system, the liquid flowed upward and the injection mode was used for the gas absorption process. They assumed that ideal plug flow conditions existed in the venturi injector and the bubble column based on visual observations of the Methylene blue mixing patterns. The venturi injector had a 95.3 mm exit-diameter and a 380 mm height. The bubble column had a diameter and a height of 95 mm and 790 mm, respectively.  $\alpha$ ,  $\beta$ , and  $\gamma$  were estimated to be 2.56, 0.53, and 0.96, respectively.

Briens *et al.* (1992) correlated  $u_G$  and  $u_L$  to the venturi injector  $k_{L,a}$  separately from the bubble column  $k_{L,a}$ . In that system, the liquid flowed downward and the ejection mode was used for the gas absorption process.  $\alpha$ ,  $\beta$ , and  $\gamma$  were estimated to be 0.81, 1.91, and  $-1.91$ , respectively, for the venturi injector. For the bubble column,  $\alpha$ ,  $\beta$ , and  $\gamma$  were estimated to be 7.64, 0.99, and 0.00, respectively. Based on their tracer experiments, they assumed that ideal complete mixing conditions existed in the bubble column that had a height of 790 mm and a diameter of 95 mm. They observed that the superficial liquid velocity ( $u_L$ ) had no effect on  $k_{L,a}$ . As a result the relationship represented by Equation 8.16 was used to correlate  $k_{L,a}$  to  $u_G$  in the bubble column.

In the current study and under the injection mode for the gas absorption process,  $k_{L,a}$  was found to be dependent on  $u_G$  and  $u_L$ . The non-linear regression parameters ( $\alpha$ ,  $\beta$ , and  $\gamma$ ) were estimated to be 12.50, 0.83, and 0.37, respectively. The non-linear regression analysis produced a correlation coefficient ( $r$ ) of 0.99. As  $u_G$  increased,  $k_{L,a}$  increased considerably as observed before by several researchers (Deckwer *et al.*, 1974; Roustan *et al.*, 1987; Laplanche *et al.*, 1991; Huynh *et al.*, 1991; Zhou, 1995; Zhou and Smith, 2000). This could be explained by the following phenomenon: as  $u_G$  increases, the gas bubbles' mean specific interfacial area increases due to the increase in the volume-to-surface area mean bubble diameter (i.e., Sauter diameter,  $d_S$ ). Also as  $u_L$  increased,  $k_{L,a}$  increased. Similar observations were reported by Wang and Fan (1978) and Huynh *et al.* (1991).

In the impinging-jet bubble column, it is expected that as  $u_L$  increases, the intensity of turbulence will increase causing the turbulent shear stresses to increase considerably in the venturi injector as well as in the bubble column. Consequently, this will result in smaller bubbles and higher gas bubbles' mean specific interfacial area and as a result,  $k_{La}$  will increase. By contrast, and since a considerable amount of the overall mass transfer efficiency that can be obtained in the impinging-jet bubble will be attributed to the mass transfer process that takes place inside the venturi injector. Increasing  $u_L$  will cause the residence time inside the injectors to decrease, thus, leading to a decrease in the overall bubble column mass transfer efficiency, i.e., the column-average  $k_{La}$  will decrease. An experimental study was conducted in the impinging-jet bubble column to investigate the effects of the operating conditions on the characteristics of the gas bubbles. A 2-D laser particle dynamics analyzer that utilizes the laser Doppler anemometry (LDA) technique to measure the turbulence intensity and the phase Doppler anemometry (PDA) technique to measure the bubble size and concentration was used to perform such measurements in the impinging-jet bubble column. The same experimental procedure for the laser system set up as described by Zhou and Smith (2000) was used in the current study.

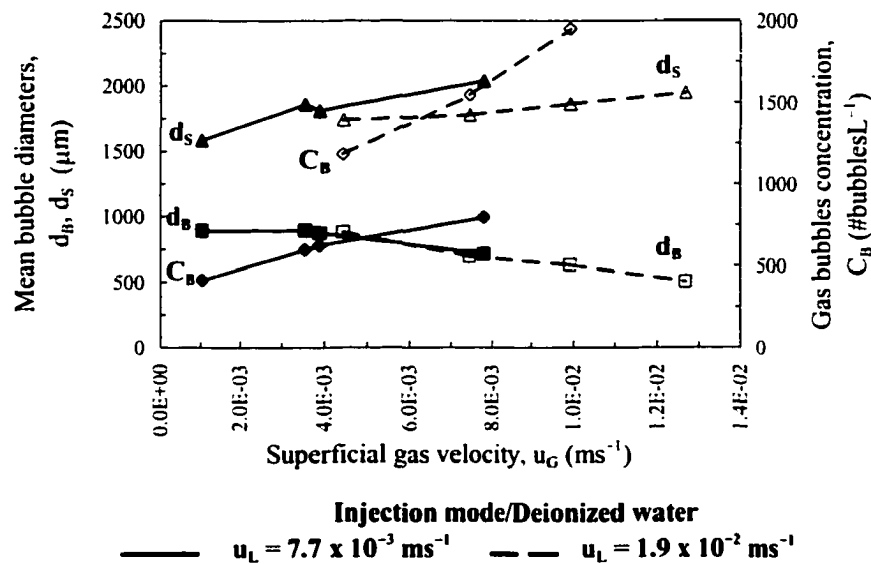


Figure 8.8 Effects of the  $u_G$  and  $u_L$  on the gas bubble diameters and concentrations in the injection mode.

Figure 8.8 depicts the effects of  $u_G$  and  $u_L$  on the Sauter mean bubble diameter ( $d_S$ ,  $\mu\text{m}$ ), the count mean bubble diameter ( $d_B$ ,  $\mu\text{m}$ ), and the concentration of gas bubbles ( $C_B$ ,  $\#\text{bubblesL}^{-1}$ ). As  $u_G$  increased,  $d_B$  decreased almost linearly while  $d_S$  and  $C_B$  increased almost linearly. As  $u_L$  increased, there was virtually no effect on  $d_B$  while it caused a significant decrease in  $d_S$  and also a significant increase in  $C_B$ . The Mixing intensities were found to be significantly high in the vertical and radial directions. Under the operating conditions represented in Figure 8.8, the turbulence % in the gas phase (= root mean square velocity/mean velocity) reached a maximum of 95 % and 5550 % in the vertical and radial directions, respectively. Although the turbulence intensity in the liquid phase was not measured, it was expected that since the turbulence levels in the gas phase were high, the liquid phase would as well exhibit high levels of turbulence.

During the gas-injection mode, the effect of the residence time inside the injectors on reducing  $k_{La}$  as  $u_L$  increases perhaps was smaller than that of increasing  $u_L$  leading to an increase in the shearing of the large gas bubbles into smaller bubbles and consequently, causing the mean gas bubbles' specific interfacial area to increase as well as  $k_{La}$ .

Figure 8.9 depicts a comparison between the  $k_{La}$  correlation developed in the current study, in the gas injection mode, with those developed in previous studies. As shown in Figure 8.9, the impinging-jet bubble column has proven to cause a significant increase in the overall ozone mass transfer coefficient ( $k_{La}$ ) compared to the conventional and upward-venturi-injector bubble columns. By operating the gas absorption process in the ejection mode,  $k_{La}$  was found to be dependent on  $u_G$  and  $u_L$ . The non-linear regression parameters ( $\alpha$ ,  $\beta$ , and  $\gamma$ ) were estimated to be 0.09, 1.43, and  $-1.78$ , respectively. These coefficients are comparable with those of Briens *et al.* (1992). The non-linear regression analysis produced a correlation coefficient of 1.00. The effect of  $u_G$  on  $k_{La}$  was higher than that in the injection mode. When operating in the ejection mode and contrary to its overall effect on  $k_{La}$  in the injection mode, as  $u_L$  increased,  $k_{La}$  decreased. As discussed earlier and since the injection mode was associated with higher  $u_L$ 's, the effect of the

residence time inside the injectors might have been higher than the effect of increasing the turbulent shear stresses on the shearing of the large gas bubbles into smaller bubbles.

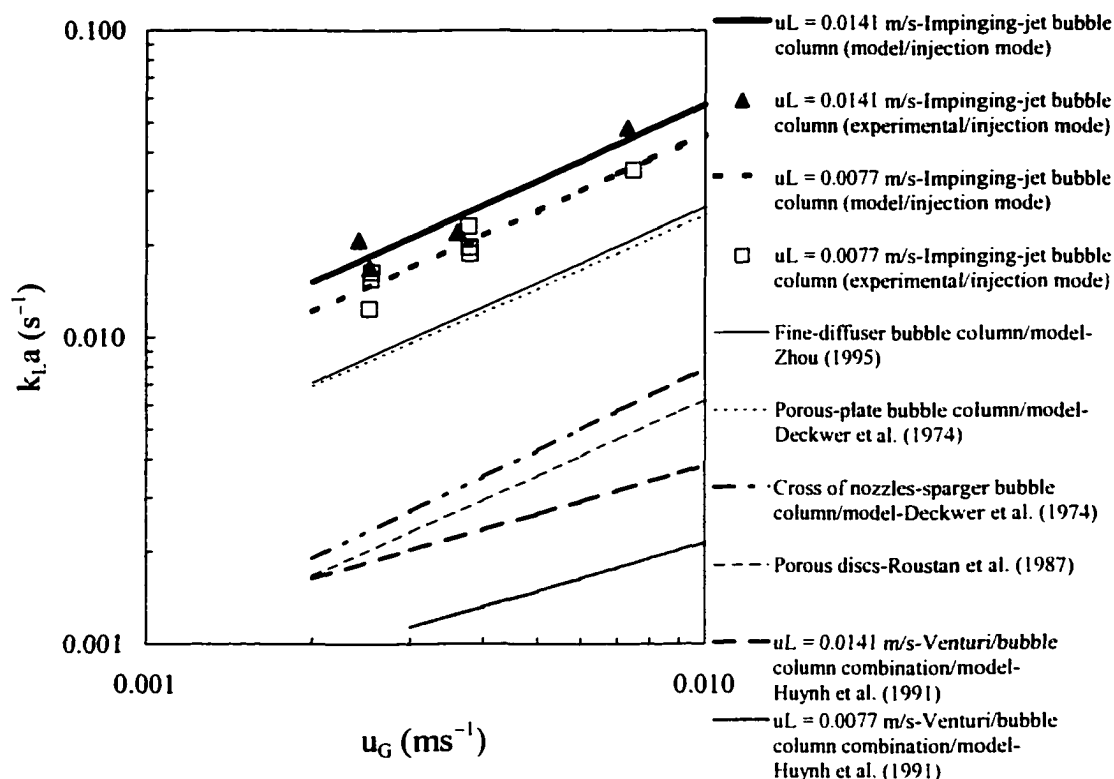


Figure 8.9 Comparison of the  $k_La$  correlations for gas sparging under positive pressure in various types of bubble columns.

Figure 8.10 depicts a comparison between the  $k_La$  predicted in the current study, in the gas ejection mode, with that predicted in the study conducted by Briens *et al.* (1992). Due to the downward-flow arrangement in the study of Briens *et al.* (1992), the gas-phase residence time inside the system increased leading to higher  $k_La$ . As shown in Figure 8.10, and despite the above operational advantage of the system investigated by Briens *et al.* (1992), the impinging-jet bubble column has proven to  $k_La$  that was comparable to that in the downward-venturi-injector bubble column. Comparisons between the impinging-jet-bubble-column average  $k_La$ 's that were obtained in the ejection mode with the  $k_La$ 's obtained in conventional bubble column designs have shown that the impinging-jet design was also superior in terms of its higher mass transfer efficiency.

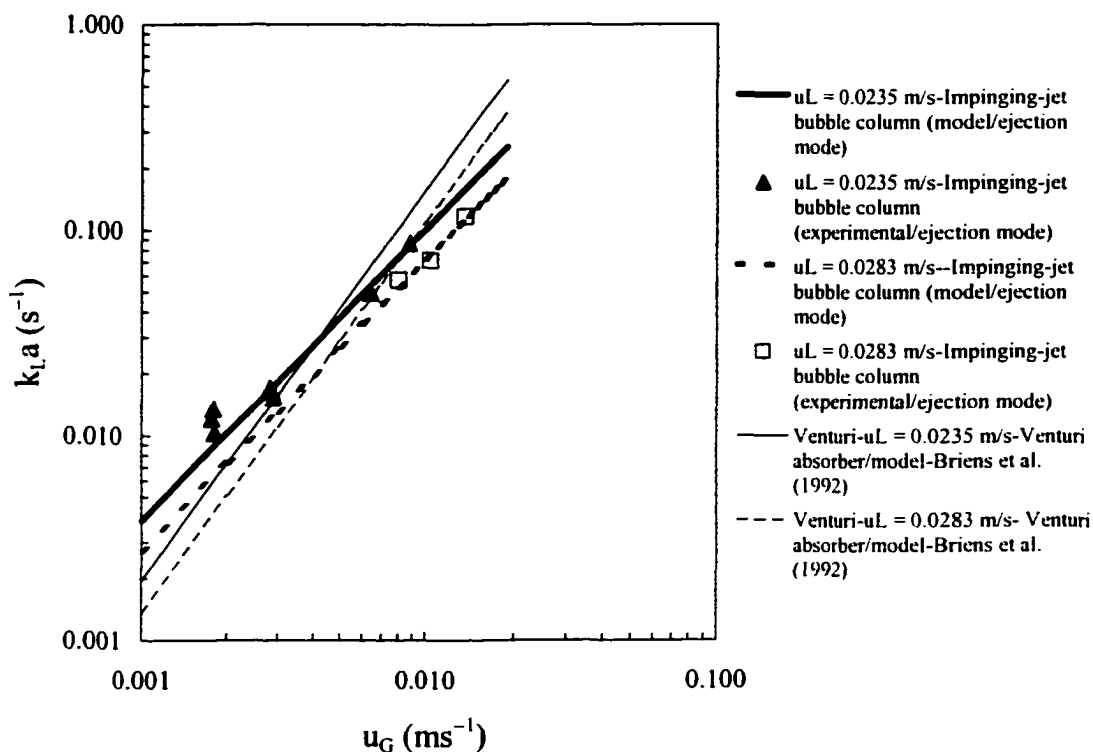


Figure 8.10 Comparison of the  $k_L a$  correlations for gas sparging under negative pressure in various types of bubble columns.

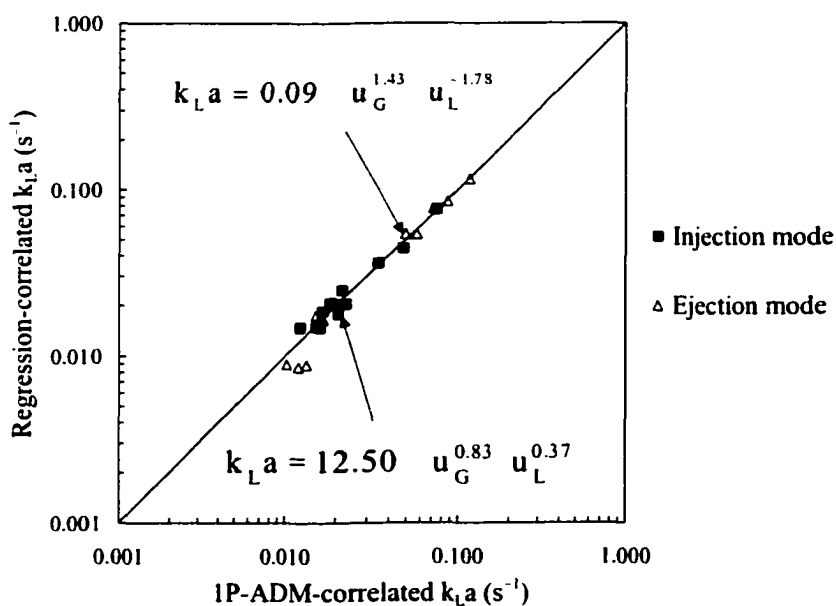


Figure 8.11 Comparison between the IP-ADM and the non-linear regression correlations of  $k_L a$ .

Figure 8.11 presents a comparison between the  $k_L a$  values that were estimated using the IP-ADM and the  $k_L a$  values estimated using the non-linear regression technique. The excellent conformity between the two methods strongly suggests the consistency of the IP-ADM in estimating  $k_L a$  under a wide range of gas and liquid flowrates.

### 8.5.2 Correlations of the Backmixing Coefficient

The liquid phase dispersion results from the entrainment of the surrounding liquid by the rising gas bubbles that carry the entrained liquid upwards (Deckwer, 1992). Using two-phase jets to create jet impingement in the ambient fluid will produce a jet that grows at a higher rate than a single jet. As the resultant jet travels forward and grows, it will entrain some of the surrounding ambient fluid, thus causing the mean jet flow to be higher than that at the jet nozzle as observed by several researchers (Rajaratnam, 1976). Based on the above, a circular flow will be developed above the convective flow and as a result, the liquid near the central axis of the flow will move upwards with most of the gas bubbles and the liquid near the walls will move downwards. Measurements of the radial velocity profiles can confirm the existence of the circular flow pattern (Deckwer, 1992).

In bubble columns characterized by their small bubble Sauter diameter range, all the liquid almost envelops the gas bubble and is entrained and dragged upwards. As a result, a sink will be developed near the gas distributor and pressure oscillations will occur. This will cause the gas-liquid dispersion to flow downwards again (Deckwer, 1992). The experimental data of König *et al.* (1978) have shown that, in an air-water bubble column equipped with perforated plates and as  $u_G$  increased up to  $2.0 \times 10^{-2} \text{ ms}^{-1}$ ,  $D_L$  decreased from about  $1.4 \times 10^{-2} \text{ m}^2\text{s}^{-1}$  to  $1.0 \times 10^{-2} \text{ m}^2\text{s}^{-1}$ . This could have been a result of the gas-liquid flow being in a homogeneous bubbly regime where it would be characterized by its high gas bubble concentration and, uniform gas bubble size, and gas bubble size distribution and therefore, constant rise velocity. This would have led to rising of the gas bubbles without mutual interference leading to uniform degrees of axial and radial distribution of gas hold-up and a low degree of macro-turbulence (Kaštánek *et al.*, 1993). Tracer tests were conducted and the estimated backmixing coefficients ( $D_L$ 's) were in

good agreement with the 1P-ADM estimated  $D_L$ 's under the tested conditions of  $u_G \leq 1.4 \times 10^{-2} \text{ ms}^{-1}$  and  $u_L \leq 2.8 \times 10^{-2} \text{ ms}^{-1}$ . The same phenomenon was observed in the study of Deckwer *et al.* (1983) when  $u_L$  was  $\leq 3.0 \times 10^{-2} \text{ ms}^{-1}$ . The estimated  $D_L$ 's, using the 1P-ADM, were converted to the dimensionless Peclet numbers ( $Pe_L$ 's).  $Pe_L$  ranged from 1.2 to 9.5 in the injection mode and from 1.1 to 3.1 in the ejection mode. The corresponding number of continuously flow stirred tank reactors (CFSTR's) in-series ranged from 1.4 to 5.3 in the injection mode and from 1.4 to 2.2 in the ejection mode. These results suggests that the backmixing in the impinging-jet bubble column can be described adequately using the axial dispersion model (ADM) rather than an ideal plug flow (PF) model or an ideal CFSTR model.

Non-linear regression analyses produced power-law relationships of the backmixing coefficient ( $D_L$ ) with respect to the gas and liquid superficial velocities ( $u_G$  and  $u_L$ ). For the injection mode, the relationship was as follows:

$$D_L = 5.4 \times 10^{-4} u_G^{-1.07} u_L^{0.81} \quad [8.18]$$

and for the ejection mode:

$$D_L = 3.9 \times 10^{-7} u_G^{-0.09} u_L^{-2.79} \quad [8.19]$$

where:  $D_L$  = liquid-phase dispersion coefficient ( $\text{m}^2\text{s}^{-1}$ ),  $u_G$  = superficial gas velocity ( $\text{ms}^{-1}$ ), and  $u_L$  = superficial liquid velocity ( $\text{ms}^{-1}$ ). The coefficient of correlation was equal to 0.94 and 0.99 for the injection and ejection modes, respectively. The injection mode was characterized by a higher Sauter mean bubble diameter ( $d_s$ ) and a gas bubble concentration ( $C_B$ ) than the ejection mode and as a result the gas-liquid flow was closer to the ideal homogeneous bubbly flow regime. Consequently,  $D_L$  was higher in the injection mode than in the ejection mode. In the injection mode and considering the above discussion, an increase in  $u_G$  will be expected to cause a decrease in  $D_L$  as a result of the increase in  $d_s$ . This phenomenon was verified by the results as shown in Equation

8.18. The same phenomenon occurred in the ejection mode (as shown by Equation 8.19) but to a lesser extent due to the fact that gas flowrates associated used in the ejection mode were slightly lower than those in the injection mode. Another reason is that during the ejection mode runs, the flow inside the column was closer to the ideal bubbly regime but still not in the homogeneous regime due to low gas bubble concentration ( $C_B$ ) as observed during the tests. The same phenomenon was reported before in the literature (Kaštánek *et al.*, 1993).

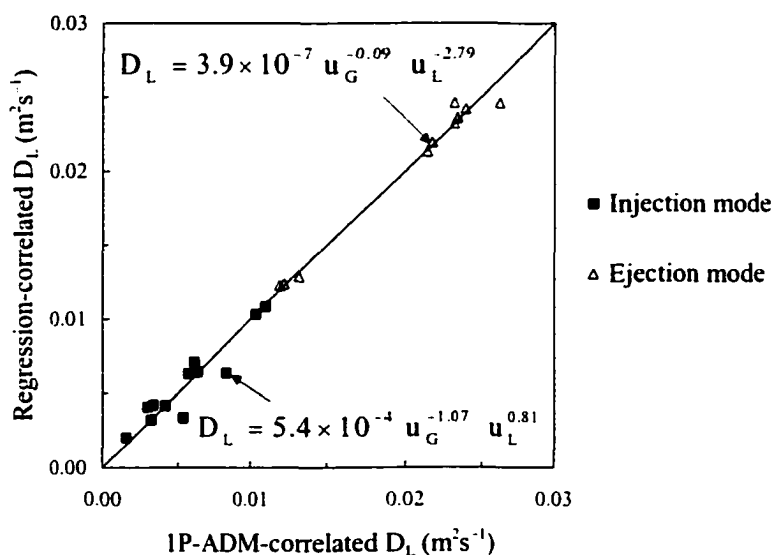


Figure 8.12 Comparison between the IP-ADM and the non-linear regression correlations of  $D_L$ .

In the injection mode and as  $u_L$  increases, the entrainment of the surrounding ambient fluid will increase as the resultant (due to jet impingement) jet grows upward and the entrainment of the liquid by the gas bubbles will increase as a result of the decrease in  $d_s$  and thus,  $D_L$  will increase. The same phenomenon was also observed in three other types of bubble columns, the first type was an upward-flow bubble column equipped with a gas-liquid ejector (Ogawa *et al.*, 1982), the second type was equipped with gauze cylinders suspended in the liquid phase (Deckwer, 1992), and the third type was equipped with porous plates (Kaštánek *et al.*, 1993). In the ejection mode and by contrast,  $u_L$

exhibited an opposite effect on  $D_L$ . In the ejection mode, the flow was closer to the ideal bubbly flow regime and as  $u_L$  increased,  $D_L$  decreased. The same phenomenon was observed before by Zhou (1995) who investigated the effect of  $u_L$  on  $D_L$  in a fine-bubble diffuser ozone bubble column in which the gas-liquid flow was in the bubbly flow regime. As shown in Figure 8.12, there was an excellent correlation between the estimated  $D_L$ 's using the 1P-ADM and the estimated  $D_L$ 's using the non-linear regression analyses.

### 8.5.3 Correlations of the Gas-phase-Concentration-Decrease Exponent

Linear regression analyses were performed in order to study the effects of the process variables on the exponent ( $a_1$ ) of the gas-phase ozone concentration decrease following the exponential decrease function represented by Equation 8.2. It was assumed that the ozone decay in the gas phase was negligible as well as the gas phase was flowing in a plug flow regime.

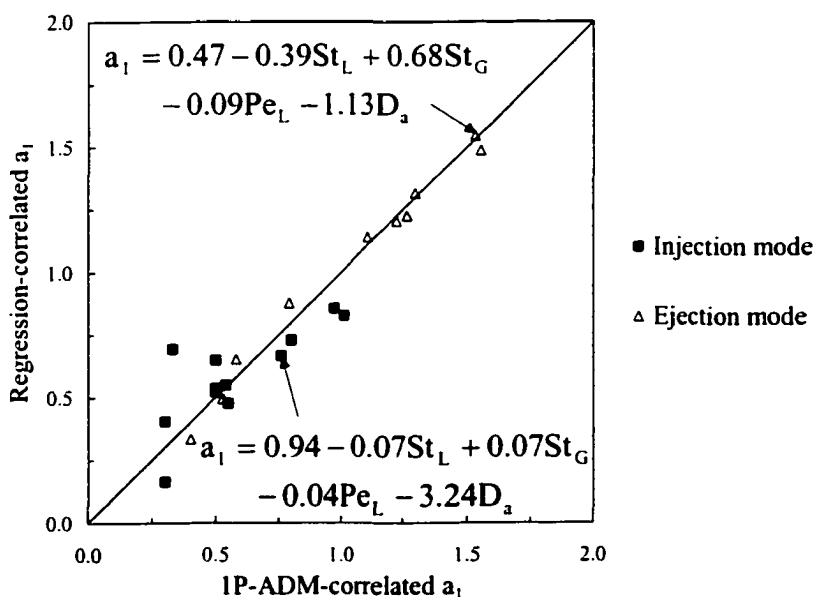


Figure 8.13 Comparison between the 1P-ADM and the linear regression correlations of  $a_1$ .

As a result,  $a_1$  represents the overall decrease in the gas-phase ozone molar fraction due to the effects of the gas-liquid mass transfer and the gas-phase convection processes (Gamal El-Din and Smith, 2000).  $a_1$  was correlated to the process dimensionless variables: Peclet number ( $Pe_L$ ), liquid-phase Stanton number ( $St_L$ ), gas-phase Stanton number ( $St_G$ ), and Damköhler number ( $D_a$ ) through a relationship similar to the one suggested by Gamal El-Din and Smith (2000):

$$a_1 = A' + B' \cdot St_L + C' \cdot St_G + D' \cdot Pe_L + E' \cdot D_a \quad [8.20]$$

where:  $A', B', C', D',$  and  $E' =$  empirical coefficients that were estimated through linear regression analyses. As a result of the linear regression analyses, and for the injection mode, the coefficients ( $A', B', C', D', E'$ ) were found to be 0.94,  $-0.07$ , 0.07,  $-0.04$ , and  $-3.24$ , respectively, and the coefficient of correlation was equal to 0.79. For the ejection mode,  $A', B', C', D', E'$  were 0.47,  $-0.39$ , 0.68,  $-0.09$ , and  $-1.13$ , respectively with the correlation coefficient equal to 0.99. Figure 8.13 shows an excellent conformity comparison between 1P-ADM and the linear regression estimations of  $a_1$ .

## 8.6 CONCLUSIONS

With respect to the measured dissolved and gaseous ozone concentration profiles in the impinging-jet bubble column, it can be concluded that:

- (1) the dissolved ozone concentration profiles along the bubble column height, can be well estimated using the one-phase axial dispersion model (1P-ADM) through the use of bubble column average parameters with respect to the overall mass transfer coefficient ( $k_L a$ ), liquid-phase backmixing coefficient ( $D_L$ ), and coefficient of the gas-phase ozone molar fraction decrease along the column height ( $a_1$ ).
- (2) for the tested deionized water, it was found that  $k_L a$  and  $D_L$  were dependent on the liquid and gas superficial velocities. The nature of this dependency varied from the gas injection mode to the gas ejection mode, and
- (3) the gas-phase dimensionless ozone concentration profiles can be well described using an exponential relationship representing the gas-phase ozone molar decrease along the column height. The exponent ( $a_1$ ) was found to be dependent on the process dimensionless variables ( $Pe_L$ ,  $St_L$ ,  $St_G$ , and  $D_a$ ) and the nature of this dependency was different in the injection mode from that in the ejection mode.

The use of the venturi injectors for the ozone gas absorption caused an increase in the mass transfer rates due to the contact between the gas and the liquid phases inside the injectors. Placing the injectors at an intersecting angle of  $125^\circ$  at the bottom of the bubble column caused an intersecting of the gas-liquid jets. This arrangement has led to a significant increase in the turbulence intensities in the ambient fluid and consequently, a significant increase in the mass transfer rates was achieved. The impinging-jet bubble column has proven to be a very promising gas-liquid contacting unit, when compared to the traditional bubble column designs due to its compact size that can handle higher liquid and gas flowrates without causing any decrease in the mass transfer efficiency of the bubble column.

## 8.7 REFERENCES

1. APHA-AWWA-WEF *Standard Methods for the Examination of Water and Wastewater*. 19<sup>th</sup> Ed. American Public Health Association, American Water Works Association, and Water Environment Federation, (Washington, DC, USA: American Public Health Association, 1995).
2. Bader, H., and Hoigné, J. "Determination of Ozone in Water by the Indigo Method: A Submitted Standard Method", *Ozone Sci & Eng.* 4: 169-176 (1982).
3. Briens, C.L., , L.X. Huynh, J.F. Large, A. Catros, J.R. Bernard, and M.A. Bergougnou, "Hydrodynamics and Gas-Liquid Mass Transfer in a Downward Venturi-Bubble Column Combination", *Chem. Eng. Sci.* 47: 3549-3556 (1992).
4. Catros, A. *Hydrodynamics and Mass Transfer in Three-Phase Fluidized Beds with Baffles*, *Ph.D. Thesis*, (London, Ontario, Canada: University of Western Ontario, 1986).
5. Chen, B.H., N.S. Yang, and A.F. McMillan, "Gas Holdup and Pressure Drop for Air-Water Flow through Plate Bubble Columns", *Can. J. Chem. Eng.* 64: 387-399 (1986).
6. Danckwerts, P.V., *Gas-Liquid Reactions* (NY, USA: McGraw-Hill, Inc., 1970).
7. Deckwer, W.-D., *Bubble Column Reactors*, Cottrell V. (Trans.), Field R.W. (Ed.), (Chichester, England: John Wiley & Sons Ltd., 1992).
8. Deckwer, W.-D., R.Burckhart, and G. Zoll, "Mixing and Mass Transfer in Tall Bubble Columns", *Chem. Eng. Sci.* 29: 2177-2188 (1974).
9. Deckwer, W.-D., K. Nguyen-Tien, , B.G. Kelkar, and Y.T. Shah, "Applicability of Axial Dispersion Model to Analyze Mass Transfer Measurements in Bubble Columns", *AIChE J.* 29: 915-922 (1983).
10. Fitzgerald, S.D. and E.R. Holley, *Research Report No. 144* (Urbana, IL, USA: Water Resources Centre, University of Illinois, 1979).
11. Gamal El-Din, M. and D.W. Smith, "Designing Ozone Bubble Columns: A Spreadsheet Approach to Axial Dispersion Model", *Proc. of IOA/PAG Conf.: Advances in Ozone Technology*, Orlando, FL, USA, 2000.

12. Guo, Z.-R. and J.J. Sharp, "Characteristics of Radial Jets and Mixing Under Buoyant Conditions", *J. Hydr. Eng.*, ASCE 122: 495-502 (1996).
13. Huynh, L.X., C.L. Briens, J.F. Large, A. Catros, J.R. Bernard, and M.A. Bergougnou, "Hydrodynamics and Mass Transfer in an Upward Venturi/Bubble Column Combination", *Can. J. Chem. Eng.* 69: 711-722 (1991).
14. Kaštánek, J., J. Zahradník, J. Kratochvíl, and J. Čermák, *Chemical Reactors for Gas-Liquid Systems* (Chichester, England: Ellis Horwood, 1993).
15. Khan, A.A. *A Study of Intersecting Circular Turbulent Jets, Ms.C. Thesis*, (Edmonton, AB, Canada: University of Alberta, 1989).
16. König, B., R. Buchholz, J. Lücke, and K. Schüger, "Longitudinal Mixing of the Liquid Phase in Bubble Columns", *Ger. Chem. Eng.* 1: 199-205 (1978).
17. Laplanche, A., N. Le Sauze, G. Martin, and B. Langlais, "Simulation of Ozone Transfer in Water: Comparison with a Pilot Unit", *Ozone Sci. & Eng.* 13(5): 13, 535-558 (1991).
18. Lewis, D.A. and J.F. Davidson, "Mass Transfer in a Recirculation Bubble Column", *Chem. Eng. Sci.* 40: 2013-2017 (1985).
19. Mazzei, A.L. and L.J. Bollyky, "Optimizing Mass Transfer Efficiency and Ozone Utilization with High Efficiency Venturi Injectors", *Proc. of the IOA/PAG Conf.*, Toronto, ON, Canada, 1991.
20. Nishikawa, M., K. Kosaka, and K. Hashimoto, "Gas Absorption in Gas-Liquid or Solid-Gas-Liquid Spouted Vessel", *Proc. 2<sup>nd</sup> Pacific Chem. Eng. Congress*, Denver, CO, USA, 1977.
21. Ogawa, S., M. Kobayashi, S. Tone, and T. Otake, "Liquid Phase Mixing in the Gas-Liquid Jet Reactor with Liquid Jet Ejector", *J. Chem. Eng. Japan* 15: 469-474 (1982).
22. Oke, N.J., D.W. Smith, and H. Zhou, "An Empirical Analysis of Ozone Decay Kinetics in Natural Waters", *Ozone Sci & Eng.* 20: 361-379 (1998).
23. Rajaratnam, N., *Developments in Water Science: Turbulent Jets* (New York, NY, USA: Elsevier, Inc., 1976).

24. Roustan, M., J.P. Duguet, B. Brette, E. Brodard, and J. Mallevalle, "Mass Balance Analysis of Ozone in Conventional Bubble Contactors", *Ozone Sci. & Eng.* 9: 289-297 (1987).
25. Roustan, M., R.Y. Wang, and D. Wolbert, "Modeling Hydrodynamics and Mass Transfer Parameters in a Continuous Ozone Bubble Column", *Ozone Sci. & Eng.* 18: 99-115 (1996).
26. Shah, Y.T., B.G. Kelkar, S.P. Godbole, and W.-D. Deckwer, "Design Parameters Estimations for Bubble Columns", *AIChE J.* 28: 353-379 (1982).
27. Sherwood, T.K., L.P. Robert, and R.W. Charles, *Mass Transfer* (New York, NY, USA: McGraw-Hill, Inc., 1975).
28. Sotelo, J.L., F.J. Beltrán, F.J. Benitez, and J. Beltrán-Heredia, "Henry's Law Constant for the Ozone-Water System", *Wat. Res.* 23: 1239-1246 (1989).
29. Thalasso, F., H. Naveau, and E.-J. Nyns, "Design and Performance of a Bioreactor Equipped with a Venturi Injector for High Gas Transfer Rates", *Chem. Eng. J.* 57: B1-B5 (1995).
30. Unger, D.R. and F. Muzzio, "Laser-Induced Fluorescence Technique for the Quantification of Mixing in Impinging Jets", *AIChE J.* 45: 2477-2486 (1999).
31. Valentin, F.H.H., *Absorption in Gas-Liquid Dispersions: Some Aspects of Bubble Technology*, Donald M.B. (Ed.). (London, England: E. & F.N. Spon Ltd., 1967).
32. Wachsmann, U., N. Rübiger, and A. Vogelpohl, "The Compact Reactor-A Newly Developed Loop Reactor with a High Mass Transfer Performance", *Ger. Chem. Eng.* 7: 39-44 (1984).
33. Wang, K.B. and L.T. Fan, "Mass Transfer in Bubble Columns Packed with Motionless Mixers", *Chem. Eng. Sci.* 33: 945-952 (1978).
34. Witze, P.O., *A Study of Impinging Axisymmetric Turbulent Flows: The Wall Jet, The Radial and Opposing Free Jets: Ph.D. Thesis* (Davis, CA, USA.: University of California, Davis, 1974).
35. Yurteri, C. and M.D. Gurol, "Ozone Consumption in Natural Waters: Effects of Background Organic Matter, pH and Carbonate Species", *Ozone Sci. & Eng.* 10: 277-290 (1988).

36. Zhou, H. and D.W. Smith, "Ozone Mass Transfer in Water and Wastewater Treatment: Experimental Observations Using a 2D-Laser Particle Dynamics Analyzer", *Wat. Res.* 34: 909-921 (2000).
37. Zhou, H., *Investigation of Ozone Disinfection Kinetics and Contactor Performance Modeling: Ph.D. Thesis* (Edmonton, AB, Canada: University of Alberta, 1995).
38. Zhou, H., D.W. Smith, and S.J. Stanley, "Modeling of Dissolved Ozone Concentration Profiles in Bubble Columns", *J. Environ. Eng., ASCE* 120(4): 821-840 (1994).

## **CHAPTER 9. MAXIMIZING THE ENHANCED OZONE OXIDATION OF KRAFT PULP MILL EFFLUENTS IN AN IMPINGING-JET BUBBLE COLUMN\***

### **9.1 INTRODUCTION**

Ozone contactors that utilize bubble diffusers are the most common practice used for treating water and wastewater. In order to achieve higher treatment levels in ozone contactors, the configuration and the design of the contacting unit and the type of the gas absorber need to be modified in an attempt to achieve higher turbulent mixing in the liquid phase. According to the theory of surface renewal proposed by Danckwerts (1970), an increase in the mixing intensity will cause the liquid film at the gas-liquid interface to be renewed at a higher rate leading to a higher local mass transfer coefficient ( $k_L$ ). Increasing the turbulence in the liquid phase will lead to higher turbulent shear stresses that will cause the thickness of the liquid film to decrease, and consequently, the ozone gas will diffuse through the liquid film at a higher rate causing  $k_L$  to increase. Higher turbulent shear stresses will also cause the gas bubbles to become smaller. As a result, the gas bubbles' specific interfacial area (bubbles' surface area/liquid volume) will increase leading to higher overall mass transfer coefficient ( $k_{La}$ ).

When two axisymmetrical circular turbulent air jets intersected at an angle of  $180^\circ$ , the resultant jet behaved like a radial jet that grew at about three times the rate of a single radial jet (Witze, 1974). The impingement produced higher turbulent shear stresses in the ambient fluid. The resultant radial jet consisted of two flow regions: a forward jet flow and a backward jet flow. The same phenomena were observed in the study of Khan (1989) who studied the impingement of circular turbulent water and air jets. Efficient and homogeneous mixing occurred at jets' Reynolds numbers ( $Re_j$ 's) greater than 300 when two liquid jets impinged at an intersecting angle of  $90^\circ$  (Unger and Muzzio, 1999). In an annular tube, when two turbulent liquid jets intersected at an angle of  $90^\circ$ , uniform and improved mixing across the tube was observed (Fitzgerald and Holley, 1979).

---

A version of this chapter has been accepted for publication. Gamal El-Din, M. and D.W. Smith, *Ozone Sci. & Eng.* (July, 2001)

There have been many attempts by several researchers to improve the performance of bubble columns. These attempts were aimed at maximizing the rate of the gas absorption process. These attempts included: (1) utilizing motionless mixers (Wang and Fan, 1978); (2) inducing internal liquid circulation in an air-lift reactor (Lewis and Davidson, 1985); (3) adding internal baffles (Catros, 1986); and (4) utilizing perforated plates (Chen *et al.*, 1986). Gas injectors were investigated by a number of researchers for dissolving gas into the liquid phase in order to improve the mass transfer rates. In the study of Wachsmann *et al.* (1984), the mass transfer process was examined using an injection-type nozzle. The gas was introduced into the liquid flow under positive and negative pressures. Significant increase in the overall mass transfer coefficient was observed. This was due to the generation of gas bubbles that had a large specific interfacial area. They also observed that the values of  $k_{L}a$ , in the gas-injection mode, varied from those in the gas-ejection mode. A venturi-type injector was used for achieving higher gas transfer rates in a bioreactor (Thalasso *et al.*, 1995). Under gas injection mode, it was observed that an increase in  $k_{L}a$  occurred as the liquid superficial velocity ( $u_L$ ) and the gas superficial velocity ( $u_G$ ) increased. Huynh *et al.* (1991) investigated the mass transfer process in an upward venturi-bubble column combination.  $k_{L}a$  was correlated with  $u_G$  and  $u_L$  for the bubble column as well as for the venturi-bubble column combination. In that contacting system, it was observed that there was essentially no backmixing and consequently,  $k_{L}a$  in the bubble column was only dependent on the  $u_G$  as observed before in most conventional bubble columns. In the venturi-bubble column combination,  $k_{L}a$  was dependent on  $u_G$  and  $u_L$  and as they increased,  $k_{L}a$  increased. In an attempt to study the effects of gas flowrates on the bubbles' specific interfacial area in a conventional diffuser bubble column, Zhou and Smith (2000) used a 2D-laser particle dynamics analyzer. They observed that as  $u_G$  increased, the bubbles' specific interfacial area increased almost proportionally. This phenomenon was attributed to the linear increase in the gas hold-up ( $\epsilon_G$ ) as a result of the increase in  $u_G$ .

Pulp mill effluents are characterized by their high concentrations of color, AOX, COD, and TOC-causing compounds. Recently, the color and AOX-causing contaminants have become the center of attention as a result of their high resistance towards

conventional biological treatment processes. In order to comply with the more stringent effluent discharge regulations, the focus of the pulp mill effluent treatment industry has shifted from the conventional biological treatment processes to other treatment alternatives (Haberl *et al.*, 1991; Zhou and Smith, 1997). Ozonation has emerged as a very promising technology for treating pulp mill effluents due to its high reduction efficiencies of color and AOX-causing compounds (Bauman and Lutz, 1974; Zhou and Smith, 1997). Ozone can selectively react with the chromophoric (color-causing) and halogenated (AOX-causing) functional groups through fast oxidation reactions as a result of these compounds' electrophilic nature (Bauman and Lutz, 1974). They observed that the color reduction efficiency was dependent mainly on the amount of the utilized ozone ( $\Delta O_3$ ), but to some extent it was also dependent on the wastewater initial characteristics in terms of color, COD, pH, and dissolved and suspended solids' concentrations.

For any ozonation system, it is important to quantify the dissolved ozone to achieve reliable designs and optimum operations of ozone contactors. Also, quantifying the ozone off-gas exiting the contactor is essential for optimum and reliable designs of the off-gas destruction facilities.

In the current study, two venturi injectors (Mazzei<sup>®</sup> injectors) were used to create turbulent gas-liquid jets in the ambient fluid. The intersecting of the gas-liquid jets caused an increase in the turbulence intensity produced in the liquid phase and therefore, increased the gas-liquid mass transfer. For modeling the ozonation process in deionized water, the ozone auto-decomposition kinetics had to be characterized. This was achieved through an ozone decay kinetics study that was conducted in a headspace-free reactor under a wide range of initial ozone concentrations and liquid-phase temperatures. Then, the mass transfer and the backmixing processes were characterized by fitting the measured dissolved and gaseous ozone concentration profiles with the modified non-isobaric one-phase axial dispersion model (1P-ADM) predictions through a three-parameter optimization technique. The ozone gas absorption process, in deionized water and pulp mill effluents, was investigated under two modes of gas sparging: the injection and ejection modes. The injection mode refers to the gas introduction, into the motive

liquid flow, under positive pressure and the ejection mode refers to the gas introduction under vacuum or negative pressure. The ozonation experiments, in deionized water and Kraft pulp mill effluent, were conducted in the pilot-scale impinging-jet bubble column that was operated in a co-current continuous-flow mode under a wide range of operating conditions. Meanwhile, in some of the pulp mill effluent ozonation experiments, the liquid phase was recirculated to simulate the conditions of the semibatch-flow mode.

This chapter presents: (1) a simple and reliable method for predicting the impinging-jet bubble-column average overall mass transfer coefficient ( $k_{La}$ ); and (2) an examination of the effects of various ozonation process variables on the treatment efficiencies and gas absorption dynamics during the ozonation of a Kraft pulp mill effluent.

## 9.2 FUNDAMENTALS OF THE OZONATION PROCESS

A number of processes occur simultaneously during the ozonation treatment. These processes are: convection and backmixing processes of the liquid and gas phases flowing through the contacting chamber; ozone gas mass transfer process; ozone auto-decomposition process; and competitive reactive processes of the dissolved ozone with the various constituents in the liquid phase (Zhou, 1995). A detailed discussion of the fundamentals of these processes can be found in Gamal El-Din and Smith (2000).

## 9.3 THE MODIFIED NON-ISOBARIC ONE-PHASE AXIAL DISPERSION MODEL (1P-ADM)

The assumptions pertaining to the development of the modified non-isobaric steady-state one-phase axial dispersion model (1P-ADM) and the detailed model development can be found in Gamal El-Din and Smith (2000). The 1P-ADM is composed of a single non-homogeneous second-order linear ordinary differential equation. Although this differential equation represents the liquid phase, it still accounts for the countering effects of the gas shrinkage and expansion caused by gas depletion and

absorption and reduced liquid hydrostatic head. The differential equation was solved analytically by the method of variation of parameters. The 1P-ADM was expressed in terms of a simple spreadsheet program. This program produced the model predictions of the dissolved and gaseous ozone concentration profiles along the bubble column under a wide range of the ozonation process operating conditions that were represented by the model-input parameters.

## 9.4 EXPERIMENTAL METHODS

### 9.4.1 Bench Tests: Ozone Auto-Decomposition Kinetics Study

The ozone auto-decomposition kinetics batch experiments were conducted in a 1200 mL floating-lid headspace-free reactor (see Figure 9.1).

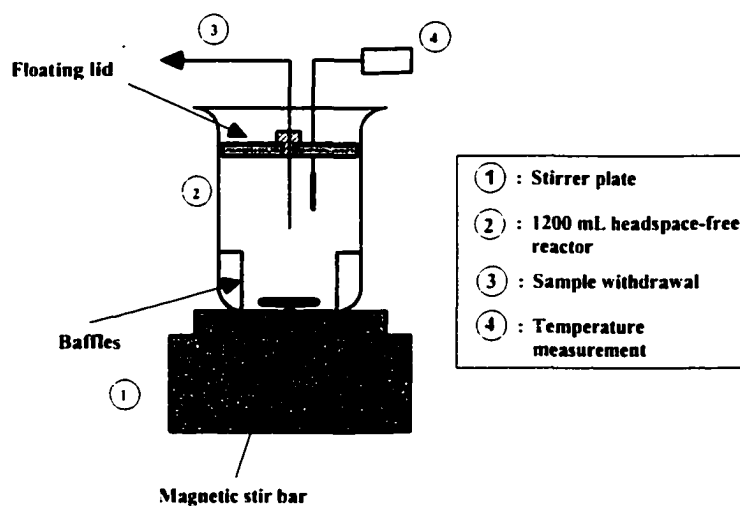


Figure 9.1 Schematic of the floating-lid headspace-free reactor.

The design of the experimental set-up and the experimental procedure were adapted from the study of Oke *et al.* (1998). Detailed description of the experimental methods can be found in Oke *et al.* (1998). In the current study, clean deionized water was used as the test water. The main average characteristics of the test water are summarized in Table 9.1. As shown in Table 9.1, the quality of the deionized water, that was used as the test water, was not high as indicated by its relatively high TOC (total organic carbon) concentration that was about  $0.51 \text{ mgL}^{-1}$ . The kinetics study was conducted over a range

of water temperatures and initial dissolved ozone concentrations in order to investigate their effects on the ozone auto-decomposition kinetics. The initial dissolved ozone concentration ranged from 2.0 to 3.1 mgL<sup>-1</sup> and the water temperature ranged from 2.6 to 38.5 °C.

Table 9.1 Average characteristics of the test water.

Parameters	TOC (mgL <sup>-1</sup> )	pH	A <sub>245 nm</sub> <sup>10 mm</sup> (mm <sup>-1</sup> )
Mean	0.51	5.99	0.004
Standard deviation	0.29	0.26	0.000

The ozone mass transfer experiments were conducted in a pilot-scale impinging-jet bubble column (see Figure 9.2). The bubble column was made from PVC and had an inside diameter of 100 mm and a total height of 1,520 mm. The water depth was kept constant at 1,315 mm by placing an overflow weir at the top of the column. A ring tube was also installed at the top of the column with a 20 mm-diameter hole facing downward. The Kynar Mazzei<sup>®</sup> venturi injectors had an inside diameter of 12.7 mm and were placed 25 mm above the bottom of the column. The injectors were placed at an intersecting angle of 125° and the distance between the centers of the nozzles was 60 mm. The bubble column had an elliptical base to reduce the effect of the backward jet that was created in the ambient fluid as a result of the jet impingement. The sidewalls of the bottom part of the column had a conical shape. With this configuration at the bottom of the column, dead pocketing effects were minimized. Based on the above reactor configuration, it was reasonably assumed that the backmixing along the column height was relatively uniform.

#### 9.4.2 Pilot-Scale Tests: Continuous-Flow Mode/Ozonation of Water and Pulp Mill Effluent

Five bell-shaped sampling taps were inserted inside the reactor at a distance equal to 1/3 of the column diameter and at equal intervals along the column height. The shape of the sampling taps minimized the possible gas bubbles' entrainment into the withdrawn

liquid samples. During each ozonation test, five liquid samples were withdrawn directly from the sampling taps into volumetric flasks and the dissolved ozone concentrations were measured and calculated following the procedure described by Bader and Hoigné (1982). Five pressure sensors (Model 26PC Honeywell<sup>®</sup>) were inserted inside the reactor, at a distance equal to 1/3 of the column diameter and at intervals equal to those of the bell-shaped sampling taps, to monitor the pressure along the column height. The liquid used in the water ozonation experiments was clean deionized water that had similar characteristics to those of the water used in the kinetics study. The ozone gas was generated from extra-dry pure oxygen using a corona discharge ozone generator (model GLS-7, PCI-WEDECO<sup>®</sup>). The ozone generator was allowed to stabilize for at least 1,800 s in order to obtain a stable ozone concentration in the feed gas. During the ozonation tests, the ozone concentrations in the feed and off-gas lines were continuously monitored using PCI-WEDECO<sup>®</sup> ozone monitors (models HC400 and LC, respectively). The ozone monitors were allowed at least 900 s to stabilize before recording their readings. Periodic calibration of the ozone monitors was conducted using the KI method as described by the Standard Methods for Examination of Water and Wastewater (APHA-AWWA-WEF, 1995). All the materials that came in contact with ozone during the experiments were made of glass, teflon, stainless steel, or PVC to reduce the possible interference that would result from the reactions between the dissolved and/or gaseous ozone and the experimental set-up components.

The ozone contactor was operated in a co-current flow mode. The test liquid was pumped from two storage barrels into an overhead tank using peristaltic pumps. Then, the test liquid was pumped from the overhead tank into the bottom of the bubble column using a centrifugal pump to reduce any fluctuations in the liquid flowrates during experiments. The liquid flow was divided equally into two lines leading into the injectors. As the liquid motive flow passed through the injectors, the gas flow was introduced into the liquid flow through the injectors' throats. The experiments were conducted under two modes of the gas sparging: positive pressure (i.e., injection) mode and vacuum or negative pressure (i.e., ejection) mode. The liquid flow, after being divided into two lines, was passed through two flowmeters to measure the liquid flowrates. The gas flow was

passed through a gas rotameter to measure the gas flowrate before the gas flow was divided into two lines leading to the injectors' throats. Pressure gauges were installed on the liquid-flow lines to measure the liquid pressure in the lines. Pressure gauges were also installed at the gas rotameter exit as well as at the injectors' throats to measure the gas pressures in the gas lines. All the pressure gauges were calibrated prior to their use.

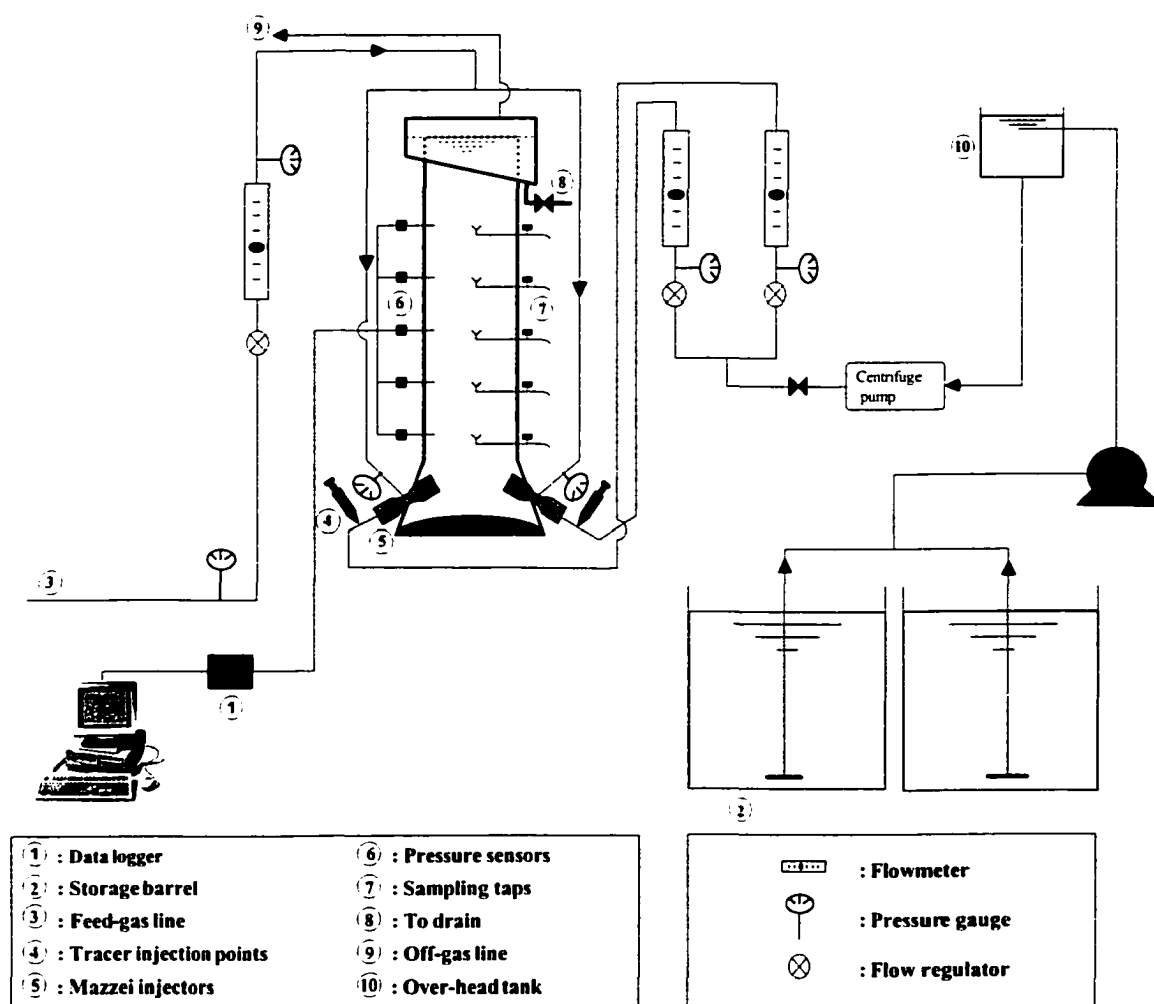


Figure 9.2 Schematic of the experimental set-up of the pilot-scale impinging-jet bubble column.

The bubble column was operated for a period of time that was at least eight turnovers of the reactor working volume to allow for the ozonation process to reach isothermal steady-state conditions in terms of the liquid flowrate, gas flowrate, dissolved ozone concentrations along the column height, and off-gas ozone concentration. During

the experiments, the point of time at which the steady-state conditions were reached was verified by reaching a constant off-gas ozone concentration in the exhaust-gas line. The gas hold-up data along the column height was obtained by continuous monitoring of the pressure readings. These readings were collected instantaneously and downloaded to a PC using a Lakewood<sup>®</sup> data logger. Wide ranges of the liquid flowrates, the feed-gas flowrates, and the feed-gas ozone concentrations were investigated. The liquid flowrate ranged from  $6.2 \times 10^{-5}$  to  $2.2 \times 10^{-4} \text{ m}^3\text{s}^{-1}$  leading to an average theoretical hydraulic retention time in the range of 48 to 174 s. During the water ozonation experiments, the feed-gas flowrate ranged from  $1.4 \times 10^{-5}$  to  $1.1 \times 10^{-4} \text{ m}^3\text{s}^{-1}$ , the feed-gas ozone concentration ranged from 0.9 to 6.0 % w/w, and the water temperature ranged from 19.5 to 24.5 °C. During the pulp mill effluent ozonation experiments, the feed-gas flowrate ranged from  $1.4 \times 10^{-5}$  to  $1.1 \times 10^{-4} \text{ m}^3\text{s}^{-1}$ , the feed-gas ozone concentration ranged from 9.0 to 11.0 % w/w, and the pulp mill effluent temperature ranged from 16.0 to 25.0 °C.

#### 9.4.3 Pilot-Scale Tests: Semibatch-Flow Mode/Ozonation of Pulp mill Effluent

Under similar operating conditions to those used in the pulp mill effluent ozonation tests that were operated in the continuous-flow mode, the liquid-phase was recirculated while the gas-phase was continuously introduced through the injectors' throats. This part of the experimental study was particularly designed for investigating the effects of the ozone contact time ( $t$ ) and the corresponding amount of the utilized ozone ( $\Delta\text{O}_3$ ) on the ozone gas absorption dynamics in terms of the enhanced overall mass transfer coefficient ( $Ek_{La}$ ), the enhancement factor ( $E$ ), and the ozone off-gas concentration. For that purpose, the ozone contact time was varied from 240 to 2,880 s. The measured feed-gas flowrates and ozone concentrations were corrected based on the actual air temperatures and barometric pressures during the experiments.

#### 9.4.4 Pulp Mill Effluent Characterization

During the continuous-flow mode ozonation tests, samples of the wastewater before and after ozonation were analyzed to determine the ozonation process treatment

efficiencies. These analyses were performed to determine the color, AOX, COD, TOC, and BOD<sub>5</sub>. The true color was analyzed according to the H5.P method suggested by the Canadian Pulp and Paper Association (1974). AOX was analyzed using Euroglas AOX analyzer according to the adsorption-pyrolysis- titrimetric method (APHA-AWWA-WEF, 1995). COD was analyzed according to the closed reflux-colorimetric method (APHA-AWWA-WEF, 1995) by employing silver-catalyzed oxidation with potassium dichromate in sulfuric acid. TOC was analyzed according to the combustion-infrared method (APHA-AWWA-WEF, 1995) using a Dohrmann carbon analyzer (model DC-80<sup>®</sup>). It should be noted that the raw pulp mill effluent characteristics varied over time and the average characteristics of the pulp mill effluent used in the current study are shown in Table 9.2.

Table 9.2 Average characteristics of the pulp mill effluent.

<b>Raw pulp mill effluent parameters</b>	<b>Continuous-flow mode</b>	<b>Semibatch-flow mode</b>
Color (TCU)	1199	1106
AOX (mgL <sup>-1</sup> )	10.1	11.2
COD (mgL <sup>-1</sup> )	750	681
TOC (mgL <sup>-1</sup> )	250	240
BOD <sub>5</sub> (mgL <sup>-1</sup> )	21.5	18.8
pH	7.7	7.6

## 9.5 RESULTS AND DISCUSSION

### 9.5.1 Bench Tests: Ozone Auto-Decomposition Kinetics

The ozone auto-decomposition process was assumed to follow first order decay kinetics as follows:

$$\frac{dC_L}{dt} = -k_w C_L \quad [9.1]$$

where:  $C_L$  = instantaneous dissolved ozone concentration (mgL<sup>-1</sup>),  $k_w$  = specific ozone utilization rate constant (s<sup>-1</sup>), and  $t$  = reaction time (s). Therefore, the kinetics data were

analyzed by plotting the  $\ln[\text{O}_3]_t$  versus the reaction time (t). The assumption was considered applicable if the plotted data could be represented by a straight line that would be predicted through a linear regression technique. For further investigation of the effect of water temperature ( $T_L$ ) on the ozone specific utilization rate constant ( $k_w$ ), the predicted  $k_w$ 's, for all the tests, were pooled together and analyzed using a linear regression technique. This kinetics' temperature-dependency was assumed to follow the well-known van't Hoff-Arrhenius relationship as follows:

$$\ln(k_w|_{T_L^\circ\text{C}}) = \ln(k_w|_{20^\circ\text{C}}) + (T_L - 20)\ln\theta \quad [9.2]$$

where:  $\theta$  = temperature correction factor, and  $T_L$  = water temperature ( $^\circ\text{C}$ ). The linear regression technique was applied to obtain  $\theta$  and  $k_w|_{20^\circ\text{C}}$ .

In all the tests, comparisons of the  $\ln[\text{O}_3]_{t=30\text{ sec}}$  with the  $\ln[\text{O}_3]_{t=0}$  yielded a very small relative error ( $\leq 0.6\%$ ). This was in agreement with the assumption that the clean deionized water had a negligible initial ozone demand. The plots of the  $\ln[\text{O}_3]_t$  versus the reaction time (t) were well described by straight lines and the linear regression analyses produced correlation coefficients ( $r$ 's)  $\geq 0.87$ . For the tests that had the same initial water temperature and different initial dissolved ozone concentrations, similar decay rate constants ( $k_w$ 's) were obtained suggesting that there was no effect of the initial ozone concentration on the decay rate constant of the ozone decay kinetics. The linear regression of the pooled  $k_w$ 's and  $T_L$ 's produced a correlation coefficient of 0.98. Figure 9.3 depicts the effect of water-temperature on the ozone specific utilization rate constant. The water-temperature correction factor ( $\theta$ ) and  $k_w|_{20^\circ\text{C}}$  were predicted to be 1.11, and  $2.61 \times 10^{-4} \text{ s}^{-1}$ , respectively. The  $k_w|_{20^\circ\text{C}}$  value implies that the ozone decay process in clean waters, with negligible initial ozone demands, is a very slow process compared to the fast ozone decay process that takes place in natural waters that are characterized by their high initial ozone demands.

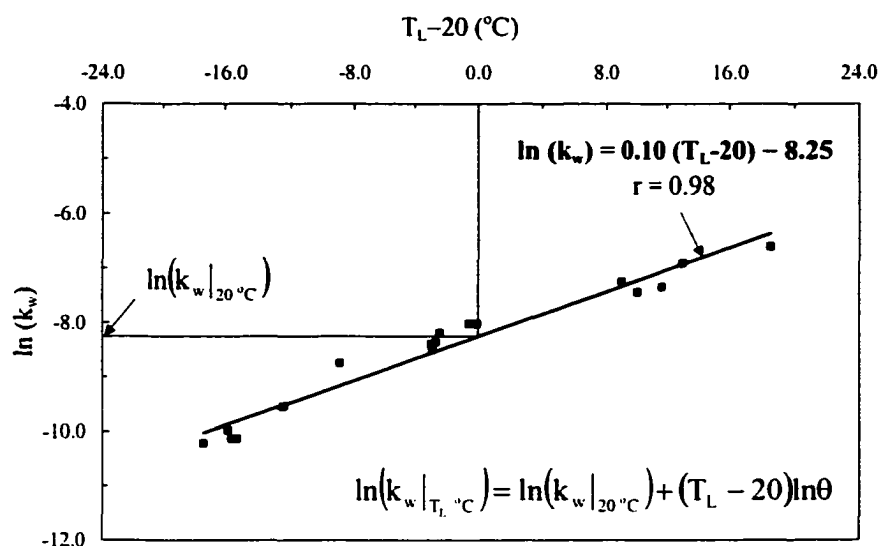


Figure 9.3 The effect of water temperature on the ozone auto-decomposition kinetics in deionized water.

### 9.5.2 Pilot-Scale Tests: Ozone Mass Transfer in Water

The design of the impinging-jet bubble column is different from the conventional bubble column designs in terms of the unique dynamic and interrelated effects of the liquid and gas flowrates on the performance of the venturi injectors. When the venturi injectors were operated in the injection or ejection mode and as the liquid flowrate was increased, an increase in the gas flowrate and a decrease in the injector throat pressure occurred. Operating at the same liquid flowrate and increasing the gas flowrate caused the injector throat pressure to increase. The differential pressure between the gas injection or ejection point and the backpressure inside the bubble column would affect the size of the gas bubbles leaving the injectors and as a result, the bubbles' specific interfacial area will change. At almost similar gas flowrates, this differential pressure was generally higher and coexisted with higher liquid flowrates in the ejection mode compared to those in the injection mode. Therefore, the same gas and liquid flowrates cannot coexist for the injection and ejection modes and as a result, the two modes of gas absorption had to be analyzed separately. Part of the overall system-mass-transfer efficiency is attributed to

the contact time between the gas phase and the liquid phase inside the intense mixing zone within the venturi injectors (Mazzei and Bollyky, 1991). As a result, an increase in this contact time will lead to an increase in the overall mass transfer efficiency in the impinging-jet bubble column.

Although the spreadsheet program that represented the 1P-ADM was allowed a maximum number of 200 iterations, the convergence criterion was met in less than 200 iterations and the minimum summation of the squared residuals ( $SSR = \sum (C_{O_2, \text{measured}} - C_{O_2, \text{calculated}})^2$ ) was reached.

In the impinging-jet bubble column,  $k_{L}a$  was affected by  $u_G$  and  $u_L$ . In an attempt to investigate the effects of the gas and liquid flowrates on the 1P-ADM predictions of the column-average  $k_{L}a$ , relationships that correlate  $k_{L}a$  with the superficial gas and liquid velocities ( $u_G$  and  $u_L$ , respectively) were developed, for the gas injection and ejection modes, through non-linear regression analyses.  $k_{L}a$  was correlated to  $u_G$  and  $u_L$  according to the following relationship:

$$k_{L}a = \alpha u_G^{\beta} u_L^{\gamma} \quad [9.3]$$

where:  $k_{L}a$  = overall mass transfer coefficient ( $s^{-1}$ ),  $u_G$  = superficial gas velocity ( $ms^{-1}$ ),  $u_L$  = superficial liquid velocity ( $ms^{-1}$ ), and  $\alpha$ ,  $\beta$ , and  $\gamma$  = empirical coefficients that were obtained through non-linear regression analyses. The mass transfer process is dependent on the liquid-phase temperature. Meanwhile, the backmixing process dependency on the liquid-phase temperature is minimal (Deckwer, 1992). Due to the variability of the water temperature from one experiment to another, the predicted  $k_{L}a$ 's were corrected for the temperature effect, to obtain the corresponding  $k_{L}a$ 's at 20 °C, using a temperature correction factor ( $\theta$ ) of 1.024. Operating in the gas injection mode, the non-linear regression analysis predicted the parameters ( $\alpha$ ,  $\beta$ , and  $\gamma$ ) to be 12.50, 0.83, and 0.37, respectively with a correlation coefficient ( $r$ ) of 0.99. When the gas absorption process was conducted in the ejection mode, the non-linear regression parameters ( $\alpha$ ,  $\beta$ , and  $\gamma$ )

were estimated to be 0.09, 1.43, and  $-1.78$ , respectively with a correlation coefficient of 1.00.

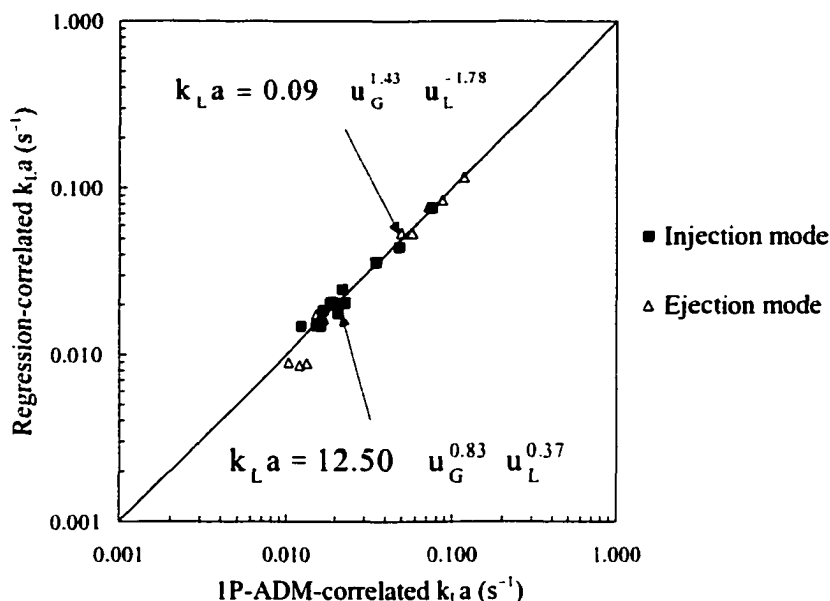


Figure 9.4 A comparison between the  $k_{L}a$ 's predicted using the 1P-ADM and the non-linear regression analyses.

A comparison between the predictions of  $k_{L}a$  using the 1P-ADM and the non-linear regression analyses is depicted in Figure 9.4. Excellent conformity between the two techniques of predictions has proven the consistency of the 1P-ADM in predicting  $k_{L}a$  under a wide range of gas and liquid flowrates in the gas-injection and ejection modes.

### 9.5.3 Ozone Mass Transfer in Pulp Mill Effluent: Gas Absorption Dynamics

In order to account for the different characteristics between the clean water and the pulp mill effluent and their effects on the overall mass transfer coefficient, a correction factor of 0.9 was used, as suggested by Metcalf and Eddy (1991), to correct  $k_{L}a$  that was obtained during the clean water ozonation tests. For ozone gas absorption in highly reactive environments, such as pulp mill effluents, the overall mass transfer coefficient ( $k_{L}a$ ) was enhanced by a factor (E). The enhanced overall mass transfer coefficient ( $Ek_{L}a$ )

was measured in order to determine the enhancement factor of the ozone gas absorption process ( $E = Ek_L a/k_L a$ ).

In the ozonation experiments, the residual ozone in the liquid phase was insignificant compared to the amount of the utilized ozone (< 1 %). As a result, at the beginning of the ozonation process, the ozone gas absorption in pulp mill effluent was assumed to occur in the fast or instantaneous-reaction-kinetics regime. In order to analyze the gas absorption data to determine  $Ek_L a$  as a function of the amount of the utilized ozone ( $\Delta O_3$ ) and the ozone contact time ( $t$ ), the bubble column was operated in a semibatch mode. This was achieved by continuously feeding the gas-phase into the bubble column through the injectors' throats while the liquid-phase was recirculated. In the semibatch mode, further assumptions needed to be considered. These assumptions included:

- (1) the gas phase flowed from the bottom to the top of the bubble column in a plug flow regime due to the relatively large buoyancy of the gas bubbles;
- (2) the ozone mass balance was conducted only for the gas phase as a result of the residual dissolved ozone concentrations being practically undetectable;
- (3) negligible accumulation of the ozone concentration in the gas phase, i.e., pseudo-steady state condition was assumed for the gas phase for the relatively small time intervals (30 s) over which the gas absorption data were collected;
- (4) due to the relatively small height of the bubble column, the off-gas flowrate decrease due to ozone gas auto-decomposition, ozone reactions with the contaminants in the liquid phase and the off-gas flowrate increase due to the hydrostatic head decrease along the reactor height were negligible, i.e.,  $Q_{G,out} = Q_{G,in} = Q_G$ ; and
- (5) Henry's law was applicable.

For the impinging-jet bubble column that was operated in the semibatch mode, conducting an ozone mass balance in the gas phase, and for pseudo-steady state

conditions at any given contact time, the bubble-column-average  $Ek_L a$  was determined as reported before by Zhou and Smith (1997) to be as follows:

$$Ek_L a = \left( \frac{Q_G H}{V_L} \right) \ln \left[ \frac{C_{G.in}}{C_{G.out}} \right] \quad [9.4]$$

where:  $Ek_L a$  = enhanced overall mass transfer coefficient ( $s^{-1}$ ),  $Q_G$  = gas flowrate ( $m^3 s^{-1}$ ),  $C_{G.in}$  = feed-gas ozone concentration ( $mgL^{-1}$ ),  $C_{G.out}$  = off-gas ozone concentration ( $mgL^{-1}$ ),  $V_L$  = effective reactor volume ( $m^3$ ), and  $H$  = Henry's constant. Henry's constant was calculated and found to be 4.0 mg gaseous ozone/mg dissolved ozone for the reactor used in the current study.  $Ek_L a$  was calculated for each ozonation test using Equation 9.4 and by using the previously determined  $k_L a$ ,  $E$  was then calculated.

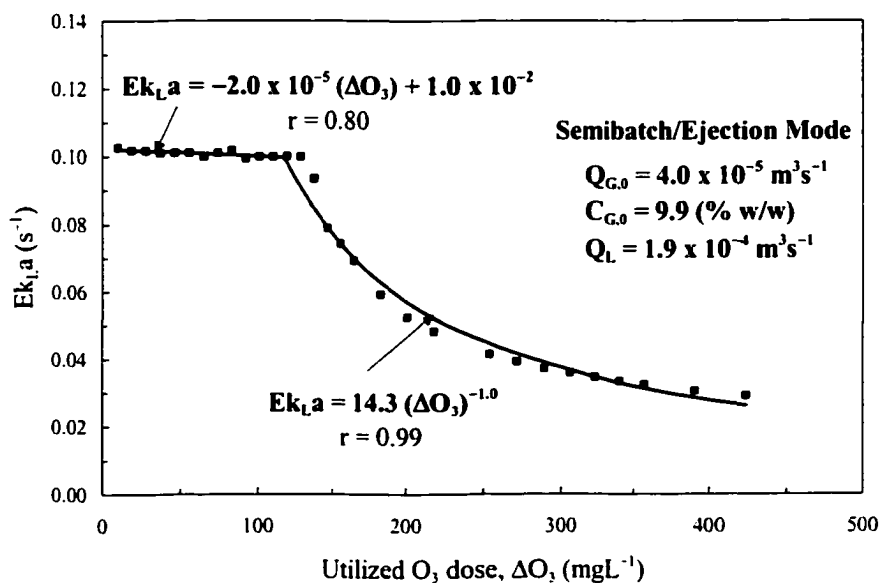


Figure 9.5 The effect of ozonation on  $Ek_L a$  values.

Figures 9.5 and 9.6 represent typical  $Ek_L a$  and  $E$  as functions of the amount of the utilized ozone in a semibatch-ejection mode. It is evident that the enhancement was higher at the beginning of the ozonation due to the very rapid ozone reactions with the contaminants in the liquid phase. As the ozonation proceeded, the enhancement factor

gradually decreased as observed before by Zhou and Smith (1997), except that in the impinging-jet bubble column, two distinctive regions of this gradual decrease in  $E$  and  $E_{k_L a}$  were observed as shown in Figures 9.5 and 9.6. This observation supports the phenomenon of the shift of the ozone gas absorption process from the fast or instantaneous to the intermediate-reaction kinetics regime as the ozonation proceeds. The rates of this gradual decrease in  $E_{k_L a}$  and  $E$  with the increase in the amount of the utilized ozone were much lower, especially at the beginning of ozonation process, than those observed in the conventional diffuser bubble column used in the study of Zhou and Smith (1997). This phenomenon could be attributed to the maximization of the enhanced ozone mass transfer process as a result of the use of the venturi injectors for the ozone gas absorption.

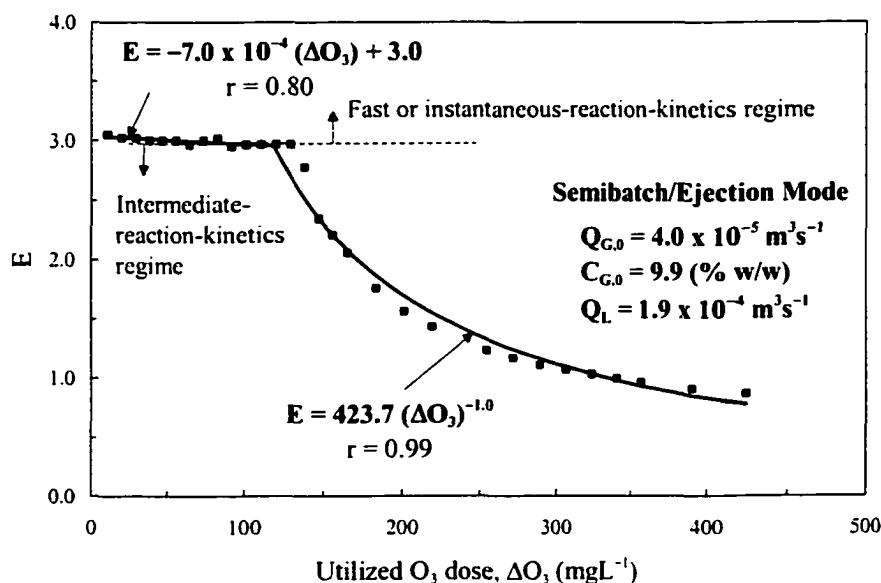


Figure 9.6 The effect of ozonation on  $E$  values.

Figure 9.7 depicts a comparison between the cumulative amounts of the applied, utilized, and exhausted ozone in a semibatch-ejection mode. The amount of the utilized ozone was practically equal to the amount of the applied ozone for most of the ozone contact time. As the ozonation proceeded, the amount of the exhausted ozone started to slightly increase due to the decrease in the available easily oxidizable sites for further

ozone oxidation. Consequently, the competing reactions between the remaining complex organic structures and ozone became more dominant and that led to a decrease in the amount of the utilized ozone.

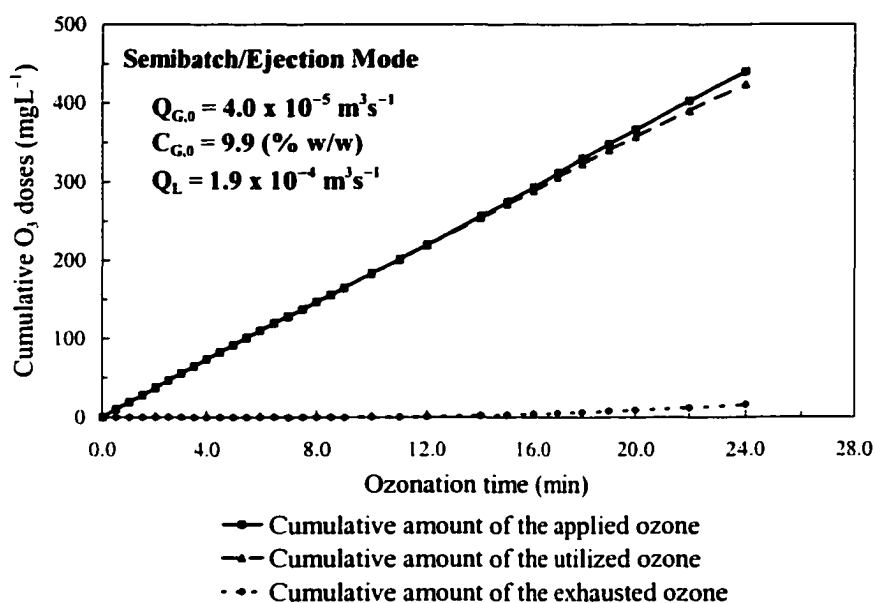


Figure 9.7 The effects of the ozone contact time on the amounts of the applied, utilized, and exhausted ozone.

Figure 9.8 shows a comparison between the measured and the predicted off-gas ozone concentrations in a semibatch-ejection mode. Equation 9.4 was used for predicting the off-gas ozone concentrations by applying the predicted  $Ek_{La}$ 's that were obtained using the best-fit linear and power expressions as shown in Figure 9.5. As shown in Figure 9.8, good correlation between the two sets of the off-gas ozone concentrations is evident.

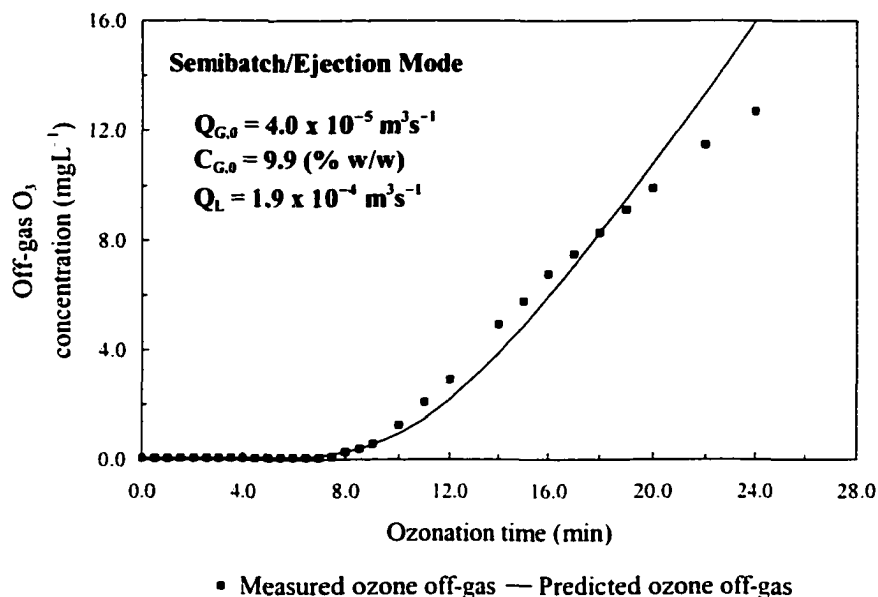


Figure 9.8 A comparison between the measured and the predicted off-gas ozone concentrations.

#### 9.5.4 Ozone Oxidation Efficiencies

The ozonation treatment efficiencies were defined as the reduction percentages of color, AOX, COD, and TOC and the increase percentage of the BOD<sub>5</sub> of the pulp mill effluent. The amount of the utilized ozone is defined as the amount of the applied ozone minus the amount of the unused ozone. The amount of the unused ozone is composed of the amount of the ozone off-gas that leaves the system in the exhaust-gas line and the amount of the residual ozone in the liquid phase. The average amount of the utilized ozone ( $\Delta O_3$ ) for an ozonation system operating in a continuous-flow mode is defined as:

$$\Delta O_3 = \left( \frac{Q_{G,in} C_{G,in}}{Q_L} \right) - \left( \frac{Q_{G,out} C_{G,out}}{Q_L} \right) - C_L \quad [9.5]$$

where:  $\Delta O_3$  = average amount of the utilized ozone ( $\text{mgL}^{-1}$ ),  $C_{G,in}$  = feed-gas ozone concentration ( $\text{mgL}^{-1}$ ),  $C_{G,out}$  = off-gas ozone concentration ( $\text{mgL}^{-1}$ ),  $Q_L$  = liquid flowrate ( $\text{m}^3\text{s}^{-1}$ ),  $Q_{G,in}$  = feed-gas flowrate ( $\text{m}^3\text{s}^{-1}$ ),  $Q_{G,out}$  = off-gas flowrate ( $\text{m}^3\text{s}^{-1}$ ), and  $C_L$  =

residual ozone concentration in the liquid phase ( $\text{mgL}^{-1}$ ). When the bubble column is operated in a continuous-flow mode, the amount of the utilized ozone increases along the column height due to the increase in the ozone contact time with the fluid elements passing through the column. In the current study, and as a result of the relatively short liquid depth (1,315 mm), it was reasonable to assume that the increase in the amount of the utilized ozone along the column height was minimal. Therefore, the bubble-column average amount of the utilized ozone was considered for the assessment of the ozone treatment efficiencies. The residual ozone concentration in the liquid phase was measured and found to be insignificant ( $< 1\%$ ) when compared to the amount of the utilized ozone. As a result, for estimating  $\Delta\text{O}_3$ ,  $C_L$  was assumed to equal zero.

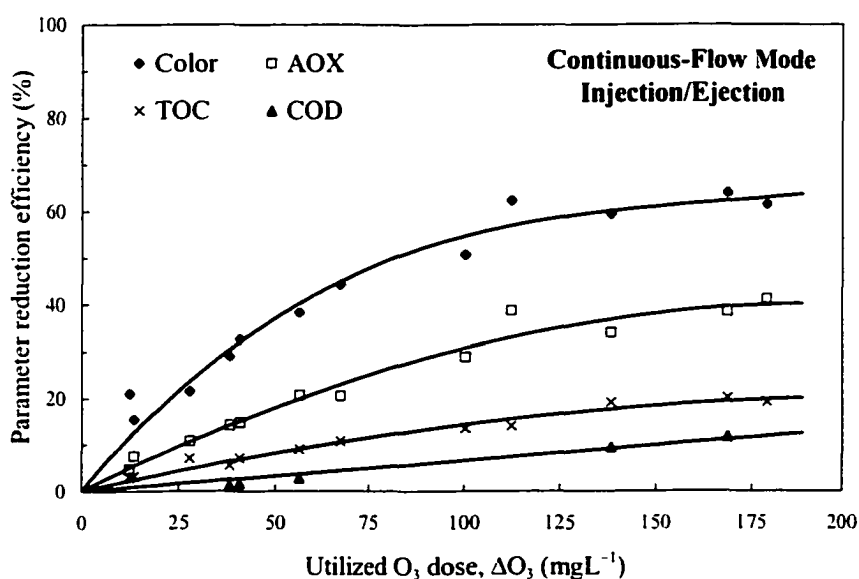


Figure 9.9 The ozonation treatment reduction efficiencies of color, AOX, TOC, and COD.

For the continuous-flow mode, typical reduction efficiencies of color, AOX, TOC, and COD, as functions of  $\Delta\text{O}_3$ , are shown in Figure 9.9. On any parameter reduction performance curve, each data point represents a separate ozonation test that was conducted under certain set of operating conditions that included the feed-gas flowrate, the feed-gas ozone concentration, the liquid flowrate, the gas sparging mode (injection or

ejection), the pH, and the liquid-phase temperature. The solid lines in Figure 9.9 represent the average trends in terms of the induced reduction efficiencies of the parameters under investigation (color, AOX, TOC, and COD) as a result of the ozonation treatment. Interestingly, the ozonation treatment efficiencies were only dependent on the amount of the utilized ozone regardless of the other process variables. The ozonation treatment process was more effective in reducing color and AOX compared to TOC and COD. The maximum reduction efficiencies of color, AOX, TOC, and COD were 64, 41, 20, and 12 %, respectively, at  $\Delta O_3$  of  $180 \text{ mgL}^{-1}$ . These maximum reduction efficiencies are comparable to those observed by Zhou and Smith (1997) under the same  $\Delta O_3$  and in a larger conventional diffuser bubble column (150 mm in diameter and 3960 mm in depth). The higher color and AOX reduction efficiencies, compared to TOC and COD, could be explained by the higher selectivity of ozone towards oxidizing the easily degradable chromophoric (color-causing) and halogenated (AOX-causing) functional groups compared to the ozone selectivity towards reacting with the remaining organic structures. The same phenomenon was observed by Zhou and Smith (1997). As shown in Figure 9.9, as the ozonation treatment proceeded, the ozone induced reduction of color and AOX exhibited two distinct regions.

The two oxidation regions could be defined as follows: (1) during the initial stage of ozonation, higher and rapidly increasing reduction efficiencies occurred, then followed by, (2) gradual reduction in the treatment efficiency. This phenomenon was observed in several studies (Prat and Esplugas, 1989; Heinzle *et al.*, 1992; Zhou and Smith, 1997). Following the initial oxidation stage, the easily oxidizable sites became less available for further ozone oxidation and consequently, the competing reactions between the remaining complex organic structures and ozone became more dominant. As the ozonation proceeded and as the amount of the utilized ozone increased, the rate of increase of color and AOX reduction efficiencies, per increase of the amount of the utilized ozone, decreased.

Figure 9.10 shows the effects of ozonation on the biochemical oxygen demand ( $BOD_5$ ) of the Kraft pulp mill effluent. The solid line in Figure 9.10 represents the

average trend in terms of the induced increase in the  $BOD_5$  of the Kraft pulp mill effluent as a result of the ozonation treatment. As the amount of the utilized ozone increased, the  $BOD_5$  of the pulp mill effluent increased substantially by about 615 % at  $\Delta O_3$  of  $180 \text{ mgL}^{-1}$ . This phenomenon could be related to the simultaneous ozone reactions with the relatively recalcitrant long-chain-high-molecular-weight organic compounds that are not easily aerobically biodegradable and the simple biodegradable organic compounds that are present in the wastewater. The relative proportions of these organic compounds determine the tendency of the wastewater towards changes in its biodegradability (Zhou and Smith, 1997). The final pulp mill effluent, that is biologically treated in an aerated lagoon, is expected to contain larger percentages of the high-molecular-weight organic compounds since the easily biodegradable organic compounds have been oxidized in the biological treatment process. Consequently, the effect of ozonation, on increasing the  $BOD_5$  of the final pulp mill effluent, is expected to be higher as the reactions between ozone and the recalcitrant organic compounds will be dominant. The rate of increase of pulp mill effluent  $BOD_5$  was a function of the initial wastewater  $BOD_5$  and the amount of the utilized ozone.

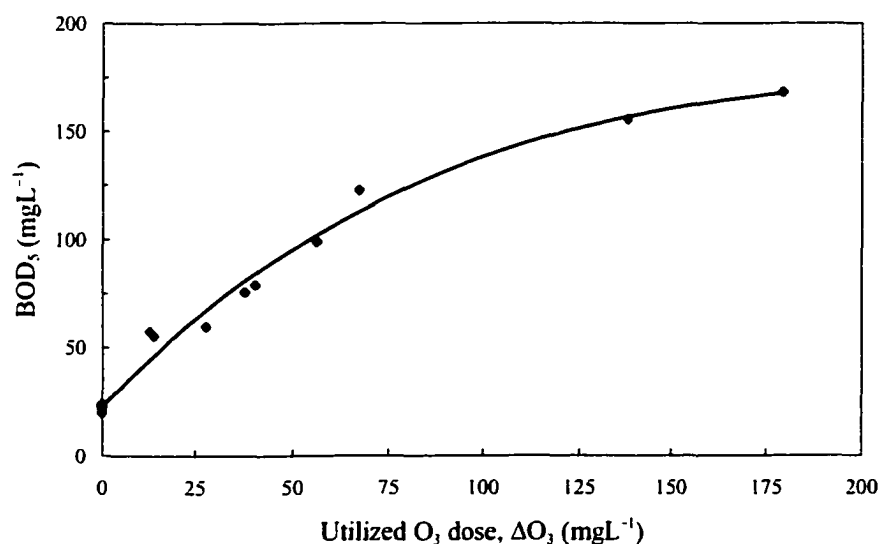


Figure 9.10 The ozonation effects on the biodegradability of pulp mill effluents.

## 9.6 CONCLUSIONS

Using the impinging-jet bubble column as an ozone-contacting unit has led to a significant increase in the mass transfer rates. As a result, the ozone mass transfer in pulp mill effluents was maximized. Excellent predictions of the overall mass transfer coefficients ( $k_La$ 's), in the impinging-jet bubble column, have been achieved through the use of the modified non-isobaric one-phase axial dispersion model (1P-ADM). The 1P-ADM is characterized by its simplicity, reliability, and most importantly, its great potential for practical applications in the design of ozone contactors and the on-line process control.

The ozone treatment was more effective in reducing color and AOX than TOC and COD from the biologically treated Kraft pulp mill effluents. The reduction efficiencies were only dependent on the amount of the utilized ozone regardless of the other process variables. The ozonation process caused a significant increase in the  $BOD_5$  of the pulp mill effluent. Therefore, an additional biological treatment process is required after ozonation to remove the increased amount of the easily biodegradable organic content of the ozonated Kraft pulp mill effluents. As a result, using a combined ozonation-biological treatment system can lead to higher treatment levels of the Kraft pulp mill effluents before being discharged into the receiving environment. The use of the impinging-jet bubble column in treating pulp mill effluents has led to comparable contaminant reduction efficiencies compared to those achieved in larger-scale conventional diffuser bubble columns. As a result, the impinging-jet bubble column has proved to be an efficient and compact contacting unit that can lead to significant decrease in the capital and operating costs of the ozonation treatment facilities.

Ozone gas absorption in highly reactive environments is a dynamic process in which the enhanced overall mass transfer coefficient ( $Ek_La$ ), the enhancement factor ( $E$ ), and the off-gas ozone concentration are affected by the amount of the utilized ozone, the feed-gas flowrate, the liquid flowrate, and the wastewater characteristics. During the course of ozonation, and operating under the same ozonation process variables,  $Ek_La$  and

E will decrease, and the off-gas ozone concentration will increase as a result of the changes in the wastewater characteristics. Good predictions of the off-gas ozone concentrations were achieved by applying the model represented by Equation 9.4. Therefore, the off-gas ozone destruction facilities can be adequately and reliably designed and consequently, optimized operations of the off-gas destruction facilities can be achieved leading to a hazard-free working environment in ozone treatment plants.

## 9.7 REFERENCES

1. APHA-AWWA-WEF, *Standard Methods for the Examination of Water and Wastewater, 19<sup>th</sup> Ed.* American Public Health Association, American Water Works Association, and Water Environment Federation (Washington, DC, USA: American Public Health Association, 1995).
2. Bader, H. and J. Hoigné, "Determination of Ozone in Water by the Indigo Method: A Submitted Standard Method", *Ozone Sci. & Eng.* 4: 169-176 (1982).
3. Bauman, H.D. and L.R. Lutz, "Ozonation of a Kraft Mill Effluent", *Tappi J.* 57(5): 116-119 (1974).
4. Canadian Pulp and Paper Association, *CPPA technical section, H5P Standard Method* (CPPA, 1974).
5. Catros, A., *Hydrodynamics and Mass Transfer in Three-Phase Fluidized Beds with Baffles: Ph.D. Thesis* (London, ON, Canada: University of Western Ontario, 1986).
6. Chen, B.H., N.S. Yang, and A.F. McMillan, "Gas Holdup and Pressure Drop for Air-Water Flow Through Plate Bubble Columns", *Can. J. Chem. Eng.* 64: 387-399 (1986).
7. Danckwerts, P.V., *Gas-Liquid Reactions* (NY, USA: McGraw-Hill, Inc., 1970).
8. Deckwer, W.-D., *Bubble Column Reactors*, Cottrell V. (Trans.), Field R.W. (Ed.) (Chichester, England: John Wiley & Sons Ltd, Inc., 1992).
9. Fitzgerald, S.D. and E.R. Holley, *Research Report No. 144* (Urbana, IL, USA: Water Resources Center, University of Illinois, 1979).
10. Gamal El-Din, M. and D.W. Smith, "Designing Ozone Bubble Columns: A Spreadsheet Approach to Axial Dispersion Model", *Proc. of the IOA/PAG Conf.: Advances in Ozone Technology*, Orlando, FL, USA, 2000.
11. Haberl, R., R. Urban, R. Gehringer, and R. Szinovata, "Treatment of Pulp-Bleaching Wastewaters by Activated Sludge, Precipitation, Ozonation, and Irradiation", *Wat. Sci. & Technol.* 24: 229-239 (1991).
12. Heinzle, E., F. Geiger, M. Fahmy, and O.M. Kut, "Integrated Ozonation-Biotreatment of Pulp Bleaching Wastewaters Containing Chlorinated Phenolic Compounds", *Biotechnol. Prog.* 8(1): 67-77 (1992).

13. Huynh, L.X., C.L. Briens, J.F. Large, A. Catros, J.R. Bernard, and M.A. Bergougnou, "Hydrodynamics and Mass Transfer in an Upward Venturi/Bubble Column Combination", *Can. J. Chem. Eng.* 69: 711-722 (1991).
14. Khan, A.A. *A Study of Intersecting Circular Turbulent Jets, Ms.C. Thesis*, (Edmonton, AB, Canada: University of Alberta, 1989).
15. Lewis, D.A. and J.F. Davidson, "Mass Transfer in a Recirculation Bubble Column", *Chem. Eng. Sci.* 40: 2013-2017 (1985).
16. Mazzei, A.L. and L.J. Bollyky, "Optimizing Mass Transfer Efficiency and Ozone Utilization with High Efficiency Venturi Injectors", *Proc. of the IOA/PAG Conf.*, Toronto, ON, Canada, 1991.
17. Metcalf and Eddy, Inc., *Wastewater Engineering: Treatment, Disposal and Reuse* (NY, USA: McGraw-Hill, Inc., 1991).
18. Oke, N.J., D.W. Smith, and H. Zhou, "An Empirical Analysis of Ozone Decay Kinetics in Natural Waters", *Ozone Sci & Eng.* 20: 361-379 (1998).
19. Prat, V.M. and S. Esplugas, "Ozonation of Bleaching Water of the Paper Industry", *Wat. Res.* 23: 51-55 (1989).
20. Thalasso, F., H. Naveau, and E.-J. Nyns, "Design and Performance of a Bioreactor Equipped with a Venturi Injector for High Gas Transfer Rates", *Chem. Eng. J.* 57: B1-B5 (1995).
21. Unger, D.R. and F. Muzzio, "Laser-Induced Fluorescence Technique for the Quantification of Mixing in Impinging Jets", *AIChE J.* 45: 2477-2486 (1999).
22. Wachsmann, U., N. Rübiger, and A. Vogelpohl, "The Compact Reactor-A Newly Developed Loop Reactor with a High Mass Transfer Performance", *Ger. Chem. Eng.* 7: 39-44 (1984).
23. Wang, K.B. and L.T. Fan, "Mass Transfer in Bubble Columns Packed with Motionless Mixers", *Chem. Eng. Sci.* 33: 945-952 (1978).
24. Witze, P.O., *A Study of Impinging Axisymmetric Turbulent Flows: The Wall Jet, The Radial and Opposing Free Jets: Ph.D. Thesis* (Davis, CA, USA: University of California, Davis, 1974).

25. Zhou, H. and D.W. Smith, "Ozone Mass Transfer in Water and Wastewater Treatment: Experimental Observations Using a 2D-Laser Particle Dynamics Analyzer", *Wat. Res.* 34: 909-921 (2000).
26. Zhou, H. and D.W. Smith, "Process Parameter Development for Ozonation of Kraft Pulp Mill Effluents", *Wat. Sci. & Technol.* 35(2-3): 251-259 (1997).
27. Zhou, H., *Investigation of Ozone Disinfection Kinetics and Contactor Performance Modeling: Ph.D. Thesis* (Edmonton, AB, Canada: University of Alberta, 1995).

## **CHAPTER 10. COMPARING DIFFERENT DESIGNS AND SCALES OF BUBBLE COLUMNS FOR THEIR EFFECTIVENESS IN TREATING KRAFT PULP MILL EFFLUENTS\***

### **10.1 INTRODUCTION**

Kraft pulp mill effluents contain high concentrations of color, AOX, COD, and TOC. Recently, the color and AOX-causing compounds have attracted a large attention due to their high resistance to the conventional biological treatment processes. As a result, the pulp mill final effluent that is discharged into the receiving environment will contain high concentrations of those compounds. Therefore, the interest has shifted to other treatment alternatives in order to comply with the more stringent effluent discharge regulations (Haberl *et al.*, 1991; Zhou and Smith, 1997). Among those treatment alternatives, ozonation has been recognized as one of the highly promising technologies for treating pulp mill effluents due to its high induced reduction efficiencies of color and AOX-causing compounds (Bauman and Lutz, 1974; Nebel *et al.*, 1974; Zhou and Smith, 2000).

Through fast oxidation reactions, ozone can selectively react with the color-causing (chromophoric) and AOX-causing (halogenated) functional groups as a result of their electrophilic nature (Bauman and Lutz, 1974; Nebel *et al.*, 1974). The color reduction efficiency was found to be dependent mainly on the amount of the utilized ozone ( $\Delta O_3$ ) and to some extent on the wastewater initial characteristics in terms of color, COD, pH and dissolved and suspended solids. Zhou and Smith (1997 and 2000) investigated the ozonation effects on reducing color and AOX-causing compounds from a biologically treated Kraft pulp mill wastewater. In the semibatch experiments, maximum reduction efficiencies up to 75 % and 50 % of the color and AOX-causing compounds, respectively, were achieved at a utilized ozone dose of  $125 \text{ mgL}^{-1}$ .

---

A part of this chapter has been accepted for publication. Gamal El-Din, M. and D.W. Smith, *J. Environ. Eng. & Sci.* (August 2001).

Another part of this chapter has been submitted for publication. Gamal El-Din, M. and D.W. Smith, *Ozone Sci. & Eng.* (August 2001).

In the pilot-scale experiments of Zhou and Smith (1997 and 2000), the maximum reduction efficiencies were up to 60 % and 30 % of the color and AOX-causing compounds, respectively, at a utilized ozone dose up to 125 mgL<sup>-1</sup>. As the utilized ozone dose increased to 240 mgL<sup>-1</sup>, the reduction efficiencies of color and AOX-causing compounds increased up to 80 % and 45 %, respectively. The pulp mill wastewater biodegradability can be improved as a result of the conversion of the high-molecular-weight organic compounds to low-molecular-weight organic compounds through the ozone oxidation reactions (Zhou and Smith, 1997). They reported that the pulp mill effluent BOD<sub>5</sub> increased by about 165 % at a utilized ozone dose of 175 mgL<sup>-1</sup> (Zhou and Smith, 1997). Applying a combined ozonation-biological treatment process can help achieving higher treatment levels (Heinzel *et al.*, 1992; Zhou and Smith, 1997). In general, the ozonation treatment induced low reduction efficiencies of the COD and TOC-causing compounds as observed in several studies (Mohammed and Smith, 1992; Zhou and Smith, 1997). The modeling of the induced reduction of color, AOX, TOC, and COD and induced increase of the pulp mill effluent biodegradability, caused by the ozonation process, can lead to more understanding of the effects of the various operating parameters on the performance of the ozonation process. Quantifying the ozonation process parameters and the process treatment efficiencies in various designs of ozonation systems and over a wide range of operating conditions will lead to a reliable and accurate scale-up of the ozonation process.

The experimental results obtained in three different types of ozone contactors were analyzed to study the effects of the ozone contactor design, configuration, operating conditions, and scale-up on the ozonation process reduction efficiencies of the impurities found in Kraft pulp mill effluents. The increase of the biodegradability of this type of wastewater and the dynamics of the ozone gas absorption process were also investigated in two types of ozone contactors. These ozone contactors included: (1) an extra-coarse-bubble diffuser ozone contactor; (2) an impinging-jet ozone contactor; and (3) a fine-bubble diffuser ozone contactor.

## 10.2 EXPERIMENTAL METHODS

### 10.2.1 Extra-Coarse-Bubble Diffuser Ozone Contactor

The ozonation tests were conducted in a semibatch-flow mode in an extra-coarse-bubble diffuser contactor. A detailed schematic of the experimental set-up is shown in Figure 10.1.

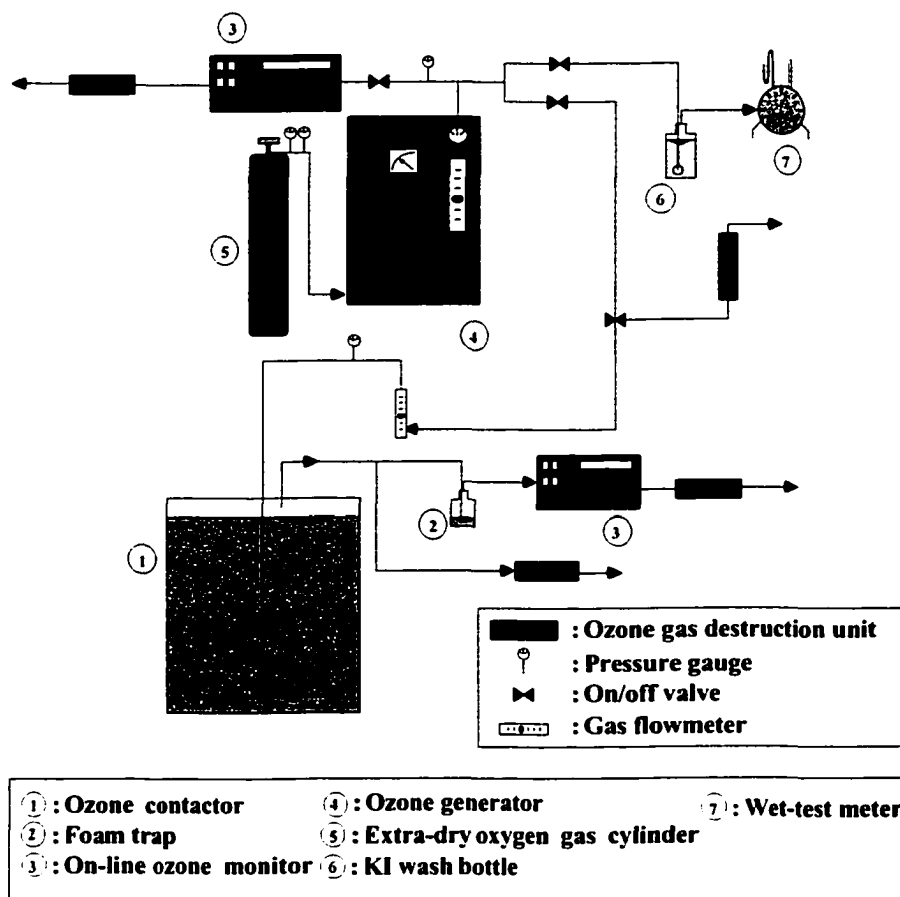


Figure 10.1 Schematic of the experimental set-up of the extra-coarse-bubble diffuser ozone contactor.

The ozone contactor was made from PVC with an inside diameter of 570 mm and a total height of 900 mm. The headspace was restricted to only 6 % of the total reactor volume to shorten the lag-time for the ozone off-gas to travel through the exhaust-gas line to the off-gas ozone monitor. An average volume of  $2.1 \times 10^{-1} \text{ m}^3$  of a Kraft pulp mill

effluent was pumped into the reactor. Ozone gas was generated from extra-dry pure oxygen using a corona discharge ozone generator (model GLS-7, PCI-WEDECO®). The ozone generator was allowed to stabilize for about 1,800 s in order to obtain a stable ozone concentration in the feed gas. The feed gas that contained 4.0 to 8.1 % w/w ozone was sparged into the liquid phase through a set of eight extra-coarse diffusers (95 mm x 15 mm) that were equally spaced over the cross-sectional area of the contactor and elevated about 10 mm from the bottom of the contactor to provide better contact between the gas bubbles and the liquid phase. The feed-gas flowrate ranged from  $2.7 \times 10^{-4}$  to  $3.2 \times 10^{-4} \text{ m}^3 \text{ s}^{-1}$ . Those flowrates corresponded to superficial gas velocities ranging from  $1.0 \times 10^{-3}$  to  $1.2 \times 10^{-3} \text{ ms}^{-1}$ . In order to achieve different utilized ozone doses of up to  $230 \text{ mgL}^{-1}$ , the ozonation time was varied up to 2,820 s. During the ozonation tests, the ozone concentrations in the feed-gas and off-gas were continuously monitored using PCI-WEDECO® ozone monitors (models HC400 and LC, respectively). Those monitors were allowed at least 900 s to stabilize before registering their readings. Periodic calibration of the ozone monitors was conducted using the KI method as described by the Standard Methods for Examination of Water and Wastewater (APHA-AWWA-WEF, 1995). All the materials that came in contact with the dissolved and gaseous ozone during the experiments were made of glass, teflon, stainless steel, or PVC to reduce the possible interference that would result from the reactions between ozone and the experimental set-up components.

## 10.2.2 Impinging-Jet Ozone Contactor

### 10.2.2.1 Continuous-Flow Mode

The ozonation experiments were conducted in a pilot-scale impinging-jet bubble column (see Figure 10.2) in a continuous-flow mode. The bubble column was made from PVC and had an inside diameter of 100 mm and a total height of 1520 mm. The water depth was kept constant at 1315 mm by placing an overflow weir at the top of the column. A ring tube was also installed at the top of the column with a 20 mm-diameter hole facing downward.

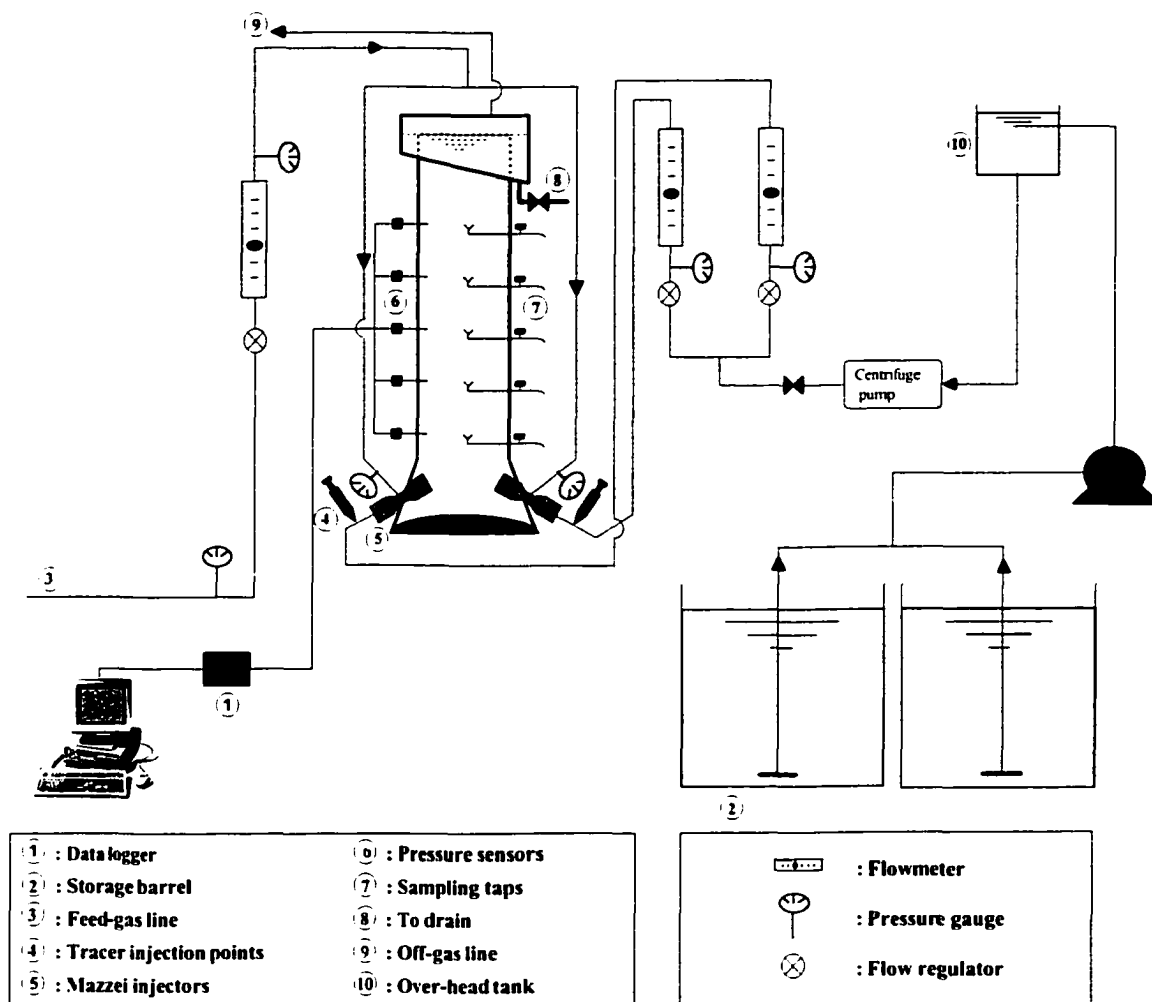


Figure 10.2 Schematic of the experimental set-up of the pilot-scale impinging-jet ozone contactor.

The Kynar Mazzei<sup>®</sup> venturi injectors had an inside diameter of 12.7 mm and were placed 25 mm above the bottom of the column. The injectors were placed at an intersecting angle of 125° and the distance between the centers of the nozzles was 60 mm. The bubble column had an elliptical base to reduce the effect of the backward jet that was created in the ambient fluid as a result of the jet impingement. The sidewalls of the bottom part of the column had a conical shape. With this configuration at the bottom of the column, dead pocketing effects were minimized. Based on the above reactor configuration, it was reasonably assumed that the backmixing along the column height was relatively uniform. The same protocols as described in the previous section, concerning the generation of the ozone gas and the monitoring of the ozone concentrations in the feed and exhaust-gas

lines, were applied during the ozonation experiments conducted in the impinging-jet bubble column. Again, all the materials that came in contact with the dissolved and gaseous ozone during the experiments were made of glass, teflon, stainless steel, or PVC. The ozone contactor was operated in a co-current flow mode under two modes of the gas sparging: (1) positive pressure (i.e., injection) mode; and (2) vacuum or negative pressure (i.e., ejection) mode. At least eight turnovers of the reactor working volume were allowed for the ozonation process to reach isothermal steady-state conditions that was verified by reaching a constant off-gas ozone concentration in the exhaust-gas line. The liquid flowrate ranged from  $6.2 \times 10^{-5}$  to  $2.2 \times 10^{-4} \text{ m}^3\text{s}^{-1}$  leading to an average theoretical hydraulic retention time in the range of 48 to 174 s. During the ozonation experiments, the feed-gas flowrate ranged from  $1.4 \times 10^{-5}$  to  $1.1 \times 10^{-4} \text{ m}^3\text{s}^{-1}$ , the feed-gas ozone concentration ranged from 9.0 to 11.0 % w/w, and the pulp mill effluent temperature ranged from 16.0 to 25.0 °C. The raw pulp mill effluent characteristics were variable over time and the average characteristics of the pulp mill effluent used in the current study are shown in Table 10.1.

Table 10.1 Average characteristics of the raw pulp mill effluent.

Wastewater parameters	Average concentrations				
	Extra-coarse-bubble diffuser ozone contactor	Impinging-jet ozone contactor		Fine-bubble diffuser ozone contactor	
	Semibatch-flow mode	Continuous-flow mode	Semibatch-flow mode	Continuous-flow mode	Semibatch-flow mode
Color (TCU)	1129	1199	1106	1213	1223
AOX ( $\text{mgL}^{-1}$ )	9.6	10.1	11.2	9.1	7.8
COD ( $\text{mgL}^{-1}$ )	671	750	681	607	485
TOC ( $\text{mgL}^{-1}$ )	268	250	240	239	192
BOD <sub>5</sub> ( $\text{mgL}^{-1}$ )	16.5	21.5	18.8	9.1	11.0
pH	7.7	7.7	7.6	7.6	7.6

### 10.2.2.2 Semibatch-Flow Mode

The same operating conditions used in the pulp mill effluent ozonation tests that were operated in the continuous-flow mode, were used in the experiments conducted under semibatch-flow conditions as the liquid-phase was recirculated while the gas-phase was continuously introduced through the injectors' throats. Those experiments were conducted for the purpose of investigating the effects of the ozone contact time ( $t$ ) and the corresponding amount of the utilized ozone ( $\Delta O_3$ ) on the: (1) ozone gas absorption dynamics in terms of the enhanced overall mass transfer coefficient ( $Ek_{1a}$ ) and the enhancement factor ( $E$ ); and (2) the off-gas ozone concentration. Therefore, the ozone contact time was varied from 240 to 2,880 s.

### 10.2.3 Fine-Bubble Diffuser Ozone Contactor

Zhou and Smith (1997) conducted bench-scale and pilot-scale ozonation experiments in a fine-bubble diffuser ozone contactor. They investigated the ozonation treatment efficiencies and the ozone gas absorption dynamics in two different scales of the fine-bubble diffuser ozone contactor and under two different modes of operation: (1) the semibatch-flow mode; and (2) the continuous-flow mode. The liquid phase used in their experiments was Kraft pulp mill effluent that was discharged from an aerated lagoon basin of a Kraft pulp mill. Detailed description of the experimental protocols and the experimental set-up can be found in Zhou and Smith (1997). The raw pulp mill effluent characteristics were variable over time and the average characteristics of the pulp mill effluent used in the study of Zhou and Smith (1997) are shown in Table 10.1.

### 10.2.4 Characterization of the Pulp Mill Wastewater

Before and after ozonation, samples of the pulp mill wastewater were analyzed to determine the ozonation process induced treatment efficiencies. These analyses were performed to determine the color, AOX, COD, TOC, and BOD<sub>5</sub>. The true color was analyzed according to the H5.P method suggested by the Canadian Pulp and Paper

Association (1974). AOX was analyzed using Euroglas AOX analyzer according to the adsorption-pyrolysis- titrimetric method (APHA-AWWA-WEF, 1995). COD was analyzed according to the closed reflux-colorimetric method (APHA-AWWA-WEF, 1995) by employing silver-catalyzed oxidation with potassium dichromate in sulfuric acid. TOC was analyzed according to the combustion-infrared method (APHA-AWWA-WEF, 1995) using a Dohrmann carbon analyzer (model DC-80<sup>®</sup>).

### 10.3 RESULTS AND DISCUSSION

#### 10.3.1 Ozonation Treatment Efficiencies

##### 10.3.1.1 Extra-Coarse-Bubble Diffuser Ozone Contactor

The amount of the utilized ozone ( $\Delta O_3$ ) for a semibatch system is defined as:

$$\Delta O_3 = \int_0^t \frac{(Q_{G,in} C_{G,in} - Q_{G,out} C_{G,out})}{V_L} dt - C_L \quad [10.1]$$

where:  $\Delta O_3$  = amount of the utilized ozone ( $\text{mgL}^{-1}$ ),  $C_{G,in}$  = ozone concentration in the feed gas ( $\text{mgL}^{-1}$ ),  $C_{G,out}$  = ozone concentration in the exhaust gas ( $\text{mgL}^{-1}$ ),  $C_L$  = residual ozone concentration in the liquid phase ( $\text{mgL}^{-1}$ ),  $V_L$  = effective reactor volume ( $\text{m}^3$ ),  $Q_{G,in}$  = feed-gas flowrate ( $\text{m}^3\text{s}^{-1}$ ),  $Q_{G,out}$  = exhaust-gas flowrate ( $\text{m}^3\text{s}^{-1}$ ), and  $t$  = ozone contact time (s). In all the ozonation tests, the residual ozone concentration in the liquid phase was measured and found to be insignificant (< 1 %) compared to the amount of the utilized ozone. As a result, for estimating the utilized ozone doses,  $C_L$  was assumed to equal zero. Typical induced reduction efficiencies of color, AOX, COD, and TOC as functions of the amount of the utilized ozone are shown in Figure 10.3. On any parameter-reduction-efficiency curve, each data point represents a separate ozonation test that was conducted under certain set of operating conditions that included the feed-gas flowrate, the feed-gas ozone concentration, the pH, and the liquid and the gas-phase temperatures. The solid lines in Figure 10.3 represent the average trends in terms of the induced reduction efficiencies of the parameters under investigation (color, AOX, COD, and TOC) as a result of the ozonation treatment. As shown in Figure 10.3, the ozonation

process was more effective in reducing color and AOX compared to COD and TOC. The maximum reduction efficiencies of color, AOX, COD, and TOC were 86, 44, 22, and 15 %, respectively, at  $\Delta O_3$  of  $230 \text{ mgL}^{-1}$ . These observations are consistent with those of Zhou and Smith (1997). An explanation of this phenomenon is that the ozone has a higher selectivity towards oxidizing the easily degradable chromophoric (color-causing) and halogenated (AOX-causing) functional groups compared to the remaining organic structures.

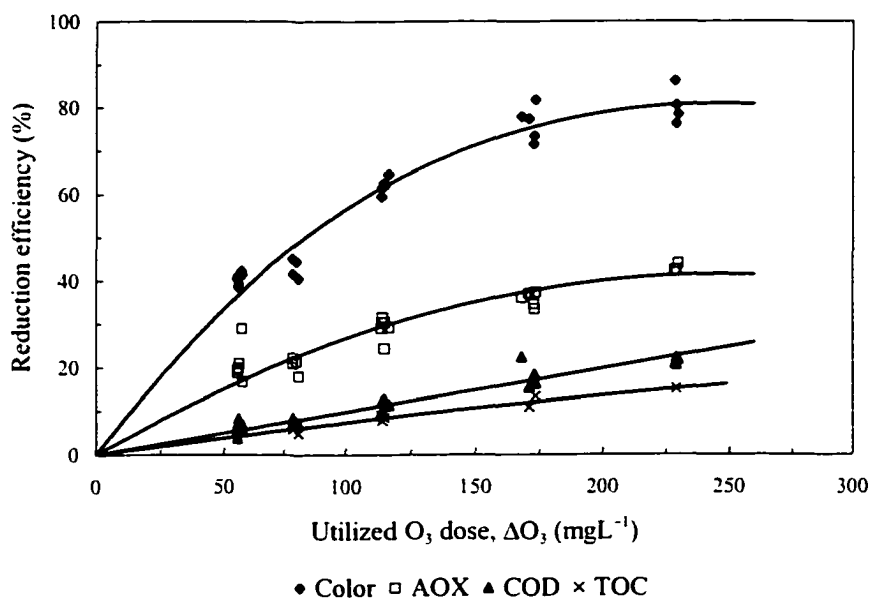


Figure 10.3 Reduction efficiencies of color, AOX, COD, and TOC in the extra-coarse-bubble diffuser ozone contactor.

Figure 10.4 shows the effect of ozonation on the  $BOD_5$  of the Kraft pulp mill wastewater treated in the extra-coarse-bubble diffuser ozone contactor. The solid line in Figure 10.4 represents the average trend in terms of the induced increase in the  $BOD_5$  of the Kraft pulp mill effluent as a result of the ozonation treatment. As the amount of the utilized ozone increased, the  $BOD_5$  of the Kraft pulp mill wastewater increased considerably by about 320 % at  $\Delta O_3$  of  $230 \text{ mgL}^{-1}$ . This phenomenon can be attributed to the reactions of ozone with the relatively recalcitrant long-chain-high-molecular-weight organic compounds that are not easily aerobically biodegradable and with the simple

biodegradable organic compounds that are simultaneously present in the wastewater. The relative proportions of those organic compounds and their reaction rates with ozone determine the level of increase in the biodegradability of the wastewater (Zhou and Smith, 1997). The Kraft pulp mill wastewater that is treated biologically in aerated lagoons is expected to contain larger proportions of the high-molecular-weight organic compounds since most of the easily biodegradable organic compounds have been oxidized in the biological treatment process.

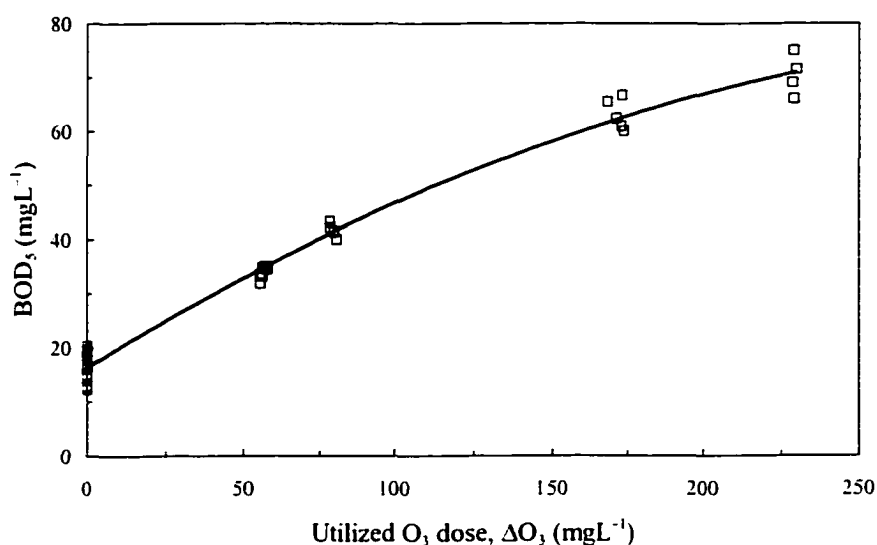


Figure 10.4 The effect of ozonation on the BOD<sub>5</sub> of the pulp mill wastewater treated in the extra-coarse-bubble diffuser ozone contactor.

### 10.3.1.2 Impinging-Jet Ozone Contactor

For a semibatch-flow mode, the amount of the utilized ozone can be determined using Equation 10.1. Meanwhile, the average amount of the utilized ozone ( $\Delta O_3$ ) for a continuous-flow mode is defined as:

$$\Delta O_3 = \left( \frac{Q_{G,in} C_{G,in}}{Q_L} \right) - \left( \frac{Q_{G,out} C_{G,out}}{Q_L} \right) - C_L \quad [10.2]$$

where:  $\Delta O_3$  = average amount of the utilized ozone ( $\text{mgL}^{-1}$ ),  $C_{G,\text{in}}$  = ozone concentration in the feed gas ( $\text{mgL}^{-1}$ ),  $C_{G,\text{out}}$  = ozone concentration in the exhaust gas ( $\text{mgL}^{-1}$ ),  $Q_L$  = liquid flowrate ( $\text{m}^3\text{s}^{-1}$ ),  $Q_{G,\text{in}}$  = feed-gas flowrate ( $\text{m}^3\text{s}^{-1}$ ),  $Q_{G,\text{out}}$  = exhaust-gas flowrate ( $\text{m}^3\text{s}^{-1}$ ), and  $C_L$  = residual ozone concentration in the liquid phase ( $\text{mgL}^{-1}$ ). For a bubble column operating in a continuous-flow mode, the amount of the utilized ozone will increase along the column height as a result of the increase in the contact time between the ozone and the fluid elements flowing through the column. Due to the relatively short liquid depth (1315 mm) inside the impinging-jet ozone contactor, it was assumed that the increase in the amount of the utilized ozone along the column height was negligible.

The reduction efficiencies of each parameter under investigation were pooled together and plotted as function of the amount of the utilized ozone. The data points, representing a wide range of the operating conditions in the injection and the ejection modes, were overlapping suggesting that there was no effect of the gas sparging mode (injection or ejection mode) on the performance of the ozonation process in terms of reducing the concentrations of color, AOX, COD, and TOC. Consequently, the oxidation efficiencies were only dependent on the amount of the utilized ozone regardless of the other process variables. As observed before, the ozonation process was more effective in reducing color and AOX compared to TOC and COD. The maximum reduction efficiencies of color, AOX, COD, and TOC were 82, 72, 34, and 25 %, respectively, at  $\Delta O_3$  of  $473 \text{ mgL}^{-1}$ . At  $\Delta O_3$  of  $180 \text{ mgL}^{-1}$ , the reduction efficiencies of color, AOX, COD, and TOC were 67, 40, 8, and 11 %, respectively. When the ozone contactor was operated in a continuous-flow mode, the maximum reduction efficiencies of color, AOX, COD, and TOC were 64, 41, 12, and 20 %, respectively, at  $\Delta O_3$  of  $180 \text{ mgL}^{-1}$ . For the semibatch and the continuous-flow modes, typical curves of the ozone oxidation performance are shown in Figures 10.5 and 10.6, respectively. The solid lines in Figures 10.5 and 10.6 represent the average trends in terms of the induced reduction efficiencies of the parameters under investigation (color, AOX, COD, and TOC) as a result of the ozonation treatment.

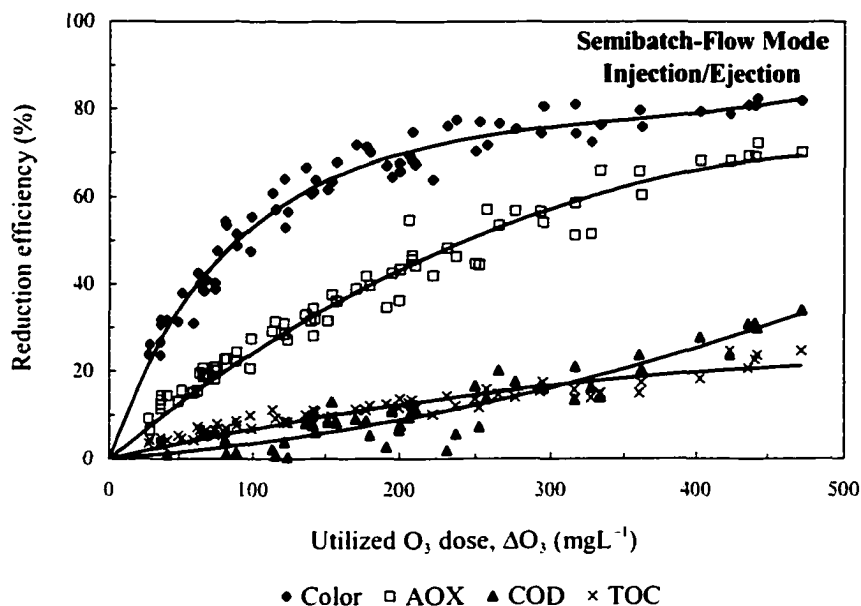


Figure 10.5 Reduction efficiencies of color, AOX, COD, and TOC in the impinging-jet ozone contactor operated in a semibatch-flow mode.

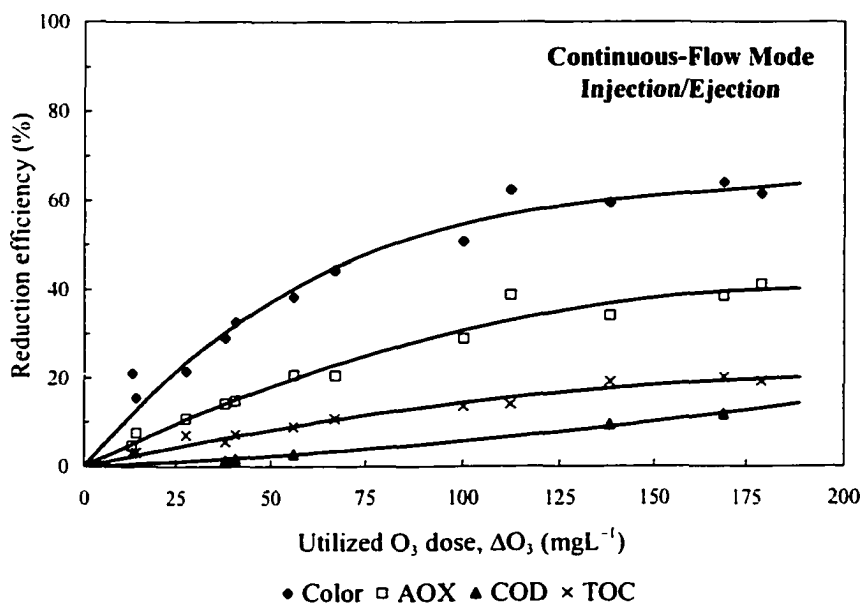


Figure 10.6 Reduction efficiencies of color, AOX, COD, and TOC in the impinging-jet ozone contactor operated in a continuous-flow mode.

As the ozonation process proceeded, the performance curves of the reduction of color and AOX exhibited two distinct regions that could be identified as follows:

- (1) during the initial stage of ozonation, higher and rapidly increasing reduction efficiencies occurred; then followed by
- (2) gradual reduction in the treatment efficiency.

The same phenomenon was reported by several researchers (Prat and Esplugas, 1989; Heinzle *et al.*, 1992; Zhou and Smith, 1997). After the initial oxidation stage, the sites that are easily oxidizable became less available for further oxidation by ozone and as a result, the competing reactions between the remaining complex organic structures and ozone became more dominant.

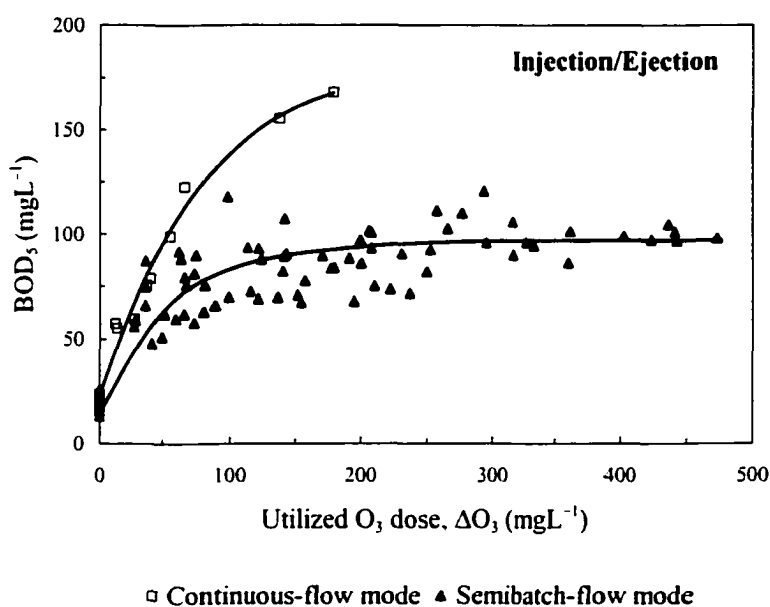


Figure 10.7 The effect of ozonation on the  $BOD_5$  of the pulp mill wastewater treated in the impinging-jet ozone contactor.

Figure 10.7 depicts the effect of ozonation on the  $BOD_5$  of the Kraft pulp mill wastewater treated in the impinging-jet ozone contactor. The solid lines in Figure 10.7 represent the average trends in terms of the induced increase in the  $BOD_5$  of the Kraft pulp mill effluent as a result of the ozonation treatment. Operating the ozone contactor in a continuous-flow mode, and as the amount of the utilized ozone increased, the  $BOD_5$  of the pulp mill wastewater increased considerably by about 615 % at  $\Delta O_3$  of  $180 \text{ mgL}^{-1}$ .

Meanwhile, in the semibatch-flow mode, the  $BOD_5$  of the pulp mill wastewater increased by about 350 % at  $\Delta O_3$  of  $180 \text{ mgL}^{-1}$  and by about 430 % at  $\Delta O_3$  of  $473 \text{ mgL}^{-1}$ . As shown in Figure 10.7 for the continuous and the semibatch-flow modes and during the initial stage of the ozonation process, a fast rate of increase of the  $BOD_5$  per increase of  $\Delta O_3$  occurred. As the ozonation process proceeded, this rate started to decrease and the  $BOD_5$  profile almost reached asymptote at  $\Delta O_3$  of about  $180 \text{ mgL}^{-1}$ .

### 10.3.2 Ozone Gas Absorption Dynamics

A correction factor of 0.9 was used, as suggested by Metcalf and Eddy (1991), to correct  $k_{La}$  that was obtained for a clean-water ozonation system. As a result of the Kraft pulp mill effluents being highly reactive with ozone, the ozone gas absorption process was enhanced by an enhancement factor (E). Measuring the overall mass transfer coefficient ( $k_{La}$ ) and the enhanced overall mass transfer coefficient ( $Ek_{La}$ ) has allowed the determination of the enhancement factor of the ozone gas absorption process ( $E = Ek_{La}/k_{La}$ ). During the ozonation experiments in all the ozone contactors, the residual ozone in the liquid phase was insignificant compared to the amount of the utilized ozone (< 1 %). Therefore, it can be reasonably assumed that at the beginning of the ozonation process, the ozone gas absorption followed the fast or instantaneous-reaction-kinetics regime.

In order to determine  $Ek_{La}$  as a function of the amount of the utilized ozone ( $\Delta O_3$ ), the ozone contactors were operated in a semibatch-flow mode. In the impinging-jet ozone contactor, the gas-phase was continuously fed into the contactor through the injectors' throats while the liquid-phase was recirculated. Several assumptions were considered for the operations of the ozone contactors under semibatch-flow conditions. These assumptions can be found in Gamal El-Din and Smith (2001). Considering an ozone contactor that is operated in a semibatch-flow mode, conducting an ozone mass balance in the gas phase, and assuming that pseudo-steady state conditions prevail at any contact time, the ozone-contactor-average  $Ek_{La}$  can be determined using the model developed by Zhou and Smith (1997) as follows:

$$Ek_L a = \left( \frac{Q_G H}{V_L} \right) \ln \left[ \frac{C_{G.in}}{C_{G.out}} \right] \quad [10.3]$$

where:  $Ek_L a$  = enhanced overall mass transfer coefficient ( $s^{-1}$ ),  $Q_G$  = gas flowrate ( $m^3 s^{-1}$ ),  $C_{G.in}$  = ozone concentration in the feed gas ( $mgL^{-1}$ ),  $C_{G.out}$  = ozone concentration in the exhaust gas ( $mgL^{-1}$ ),  $V_L$  = effective reactor volume ( $m^3$ ), and  $H$  = Henry's constant.  $Ek_L a$  was calculated for each ozonation test using Equation 10.3 and by using the previously determined  $k_L a$ ,  $E$  was then calculated. Negligible accumulation of the ozone concentration in the gas phase was assumed, i.e., pseudo-steady state conditions were assumed for the gas phase as a result of the relatively small time intervals (30 s) over which the gas absorption data were analyzed.

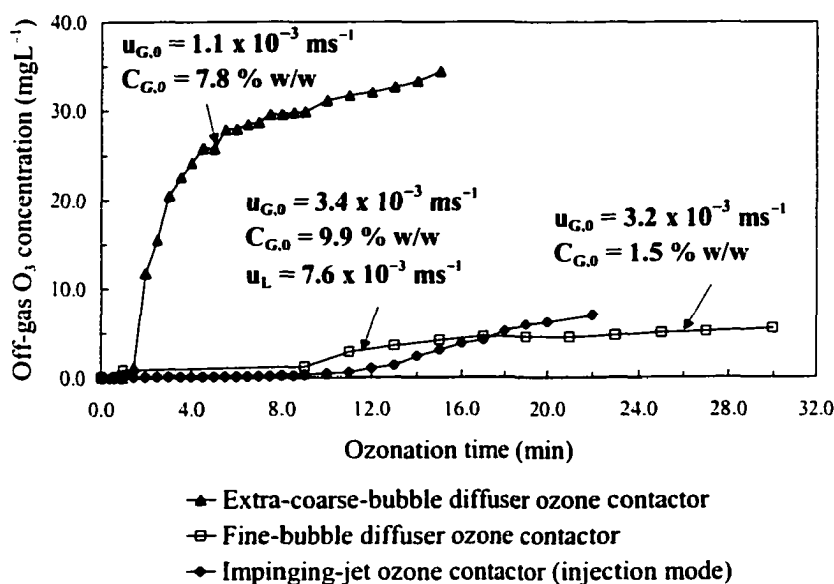


Figure 10.8 The effect of ozonation on the off-gas ozone concentration profiles in three different ozone contactors operated in a semibatch-flow mode.

Figure 10.8 represents a comparison between the fine-bubble diffuser, the extra-coarse-bubble diffuser, and the impinging-jet ozone contactors in terms of the off-gas ozone concentration profiles. The impinging-jet ozone contactor was superior to the other two contactors in terms of its higher mass transfer efficiency due to its lower off-gas

ozone concentrations. Although, the impinging-jet contactor operated at higher feed-gas ozone concentrations and superficial gas velocities compared to the other two ozone contactors. When the impinging-jet ozone contactor was operated in a continuous-flow mode, the off-gas ozone concentrations were dependent on the operating conditions encountered during the ozonation tests.

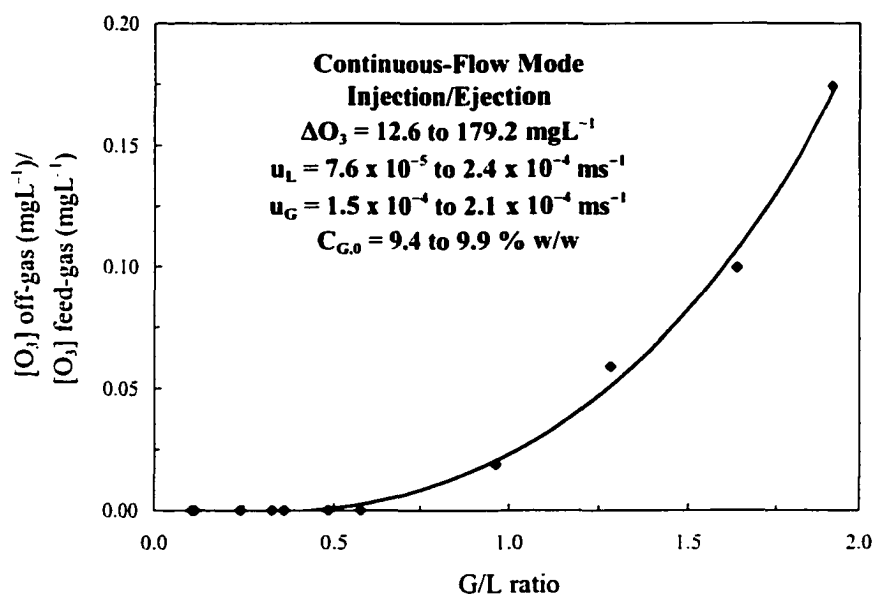


Figure 10.9 The effect of ozonation on the off-gas to the feed-gas ozone concentrations' ratio in the impinging-jet ozone contactor operated in a continuous-flow mode.

The off-gas ozone concentrations were generally low in most of the experimental runs except for those that were conducted at high gas-to-liquid (G/L) flowrate ratios. The ratios of the off-gas to the feed-gas ozone concentrations were pooled for all the ozonation tests that were conducted in the injection and ejection modes and plotted together versus the G/L ratios as shown in Figure 10.9. Interestingly, over the wide range of the operating conditions encountered in the ozonation tests, the ratio of the off-gas to the feed-gas ozone concentrations was only a function of the G/L ratio regardless of the other process variables. The ozonation system exhibited a mass transfer efficiency of 100 % up to G/L ratio of about 0.5 then the mass transfer efficiency started to decrease and

the ratio of the off-gas to the feed-gas ozone concentrations started to increase above zero as G/L ratio increased above 0.5.

Figures 10.10 and 10.11 represent typical  $E$  and  $ESt_G$  values as functions of the amount of the utilized ozone in two types of ozone contactors operated in a semibatch-flow mode. The solid lines in Figures 10.10 and 10.11 represent the general trends in the decrease in  $E$  and  $ESt_G$  as  $\Delta O_3$  increases. In order to compare  $E_{kLa}$ 's obtained in contactors that had different effective reactor volumes,  $E_{kLa}$  was presented in terms of the dimensionless enhanced gas-phase Stanton number ( $ESt_G = E_{kLa}LRT/u_GH$ ). Where  $L$  is the total column height,  $R$  is the universal gas constant,  $T$  is the gas-phase temperature, and  $H$  is the Henry's constant. The operating conditions pertaining to the data presented in Figures 10.10 and 10.11 are the same as those pertaining to the data presented in Figure 10.8 with respect to the extra-coarse-bubble diffuser and the impinging-jet contactors. The enhancement factor ( $E$ ) was higher during the initial stage of the ozonation due to the very rapid ozone reactions with the contaminants that are present in the Kraft pulp mill effluent. As the ozonation progressed,  $E$  and  $ESt_G$  decreased gradually.  $E$  and  $ESt_G$  were significantly higher in the impinging-jet contactor than in the extra-coarse-bubble diffuser contactor. In the impinging-jet contactor, two distinctive regions of this gradual decrease in  $E$  and  $ESt_G$  were observed as shown in Figures 10.10 and 10.11: an initial stage of a very small gradual linear decrease (up to almost  $\Delta O_3 = 100 \text{ mgL}^{-1}$ ); then followed by a second stage of higher gradual decrease following a power-law function. The decrease in the  $E$  and  $ESt_G$  values along the course of ozonation supports the phenomenon of the shift of the ozone gas absorption process from the fast or instantaneous to the intermediate-reaction kinetics regime as the ozonation proceeds. In the impinging-jet ozone contactor, the rates of this gradual decrease in  $ESt_G$  and  $E$  with the increase in the amount of the utilized ozone were much lower, especially at the beginning of the ozonation process, than those observed in the conventional diffuser ozone contactors. This observation along with the low off-gas ozone concentrations produced in the impinging-jet ozone contactor have proved that this ozone contactor can

provide a more efficient contacting technology for treating Kraft pulp mill effluents as compared to the conventional diffuser ozone contactors.

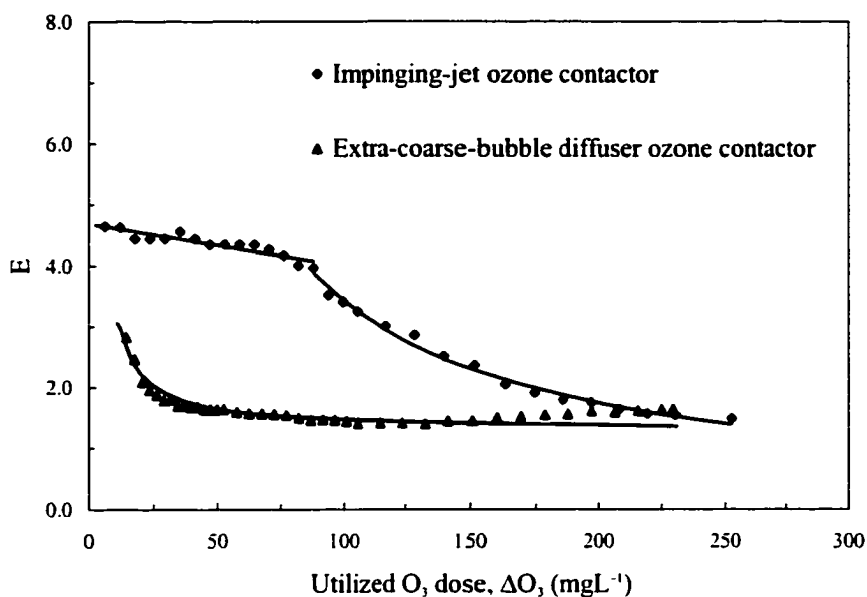


Figure 10.10 The effect of ozonation on the E values in three different ozone contactors operated in a semibatch-flow mode.

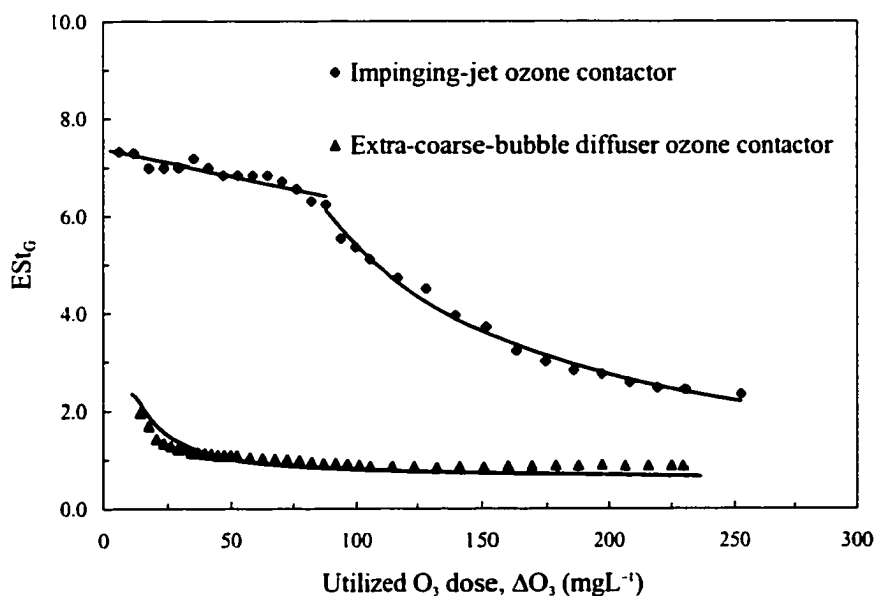


Figure 10.11 The effect of ozonation on the ESt<sub>G</sub> values in three different ozone contactors operated in a semibatch-flow mode.

### 10.3.3 Modeling of the Ozonation Treatment Efficiencies

Figures 10.12 to 10.15 depict typical plots of the  $BOD_5/COD$ , color/COD, AOX/COD, and TOC/COD concentrations' ratios as functions of  $\Delta O_3$ . The solid lines in Figures 10.12 to 10.15 represent the general trends in the change in the  $BOD_5/COD$ , color/COD, AOX/COD, and TOC/COD concentrations' ratios as functions of  $\Delta O_3$ . The relative ratio between the concentrations of the recalcitrant long-chain-high-molecular-weight organic compounds that are not easily aerobically biodegradable and the simple biodegradable organic compounds determines the effectiveness of the ozonation process in increasing the biodegradability of the Kraft pulp mill wastewater. It is more accurate to represent the biodegradability of the wastewater as a ratio of  $BOD_5$  to COD.

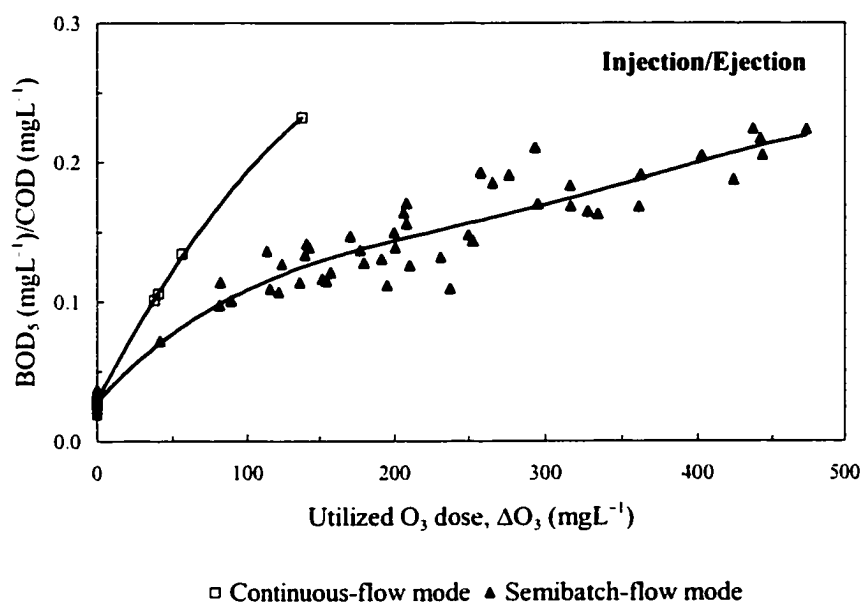


Figure 10.12 The effect of ozonation on the  $BOD_5/COD$  ratio of the treated Kraft pulp mill wastewater in the impinging-jet ozone contactor.

As shown in Figure 10.12, ozonation has caused the biodegradability (represented by  $BOD_5/COD$ ) of the Kraft pulp mill wastewater treated in the impinging-jet ozone contactor to increase from 0.03 to 0.22 at  $\Delta O_3$  up to  $473 \text{ mgL}^{-1}$ . The small ratio of the final  $BOD_5/COD$  indicates the need for further treatment of the Kraft pulp mill

wastewater to increase its biodegradability, and consequently, to remove the increase in the  $BOD_5$  of the wastewater as a result of applying further treatment. One of the promising treatment options that can be investigated is the combination of hydrogen peroxide and ozone treatment followed by a biological treatment process.

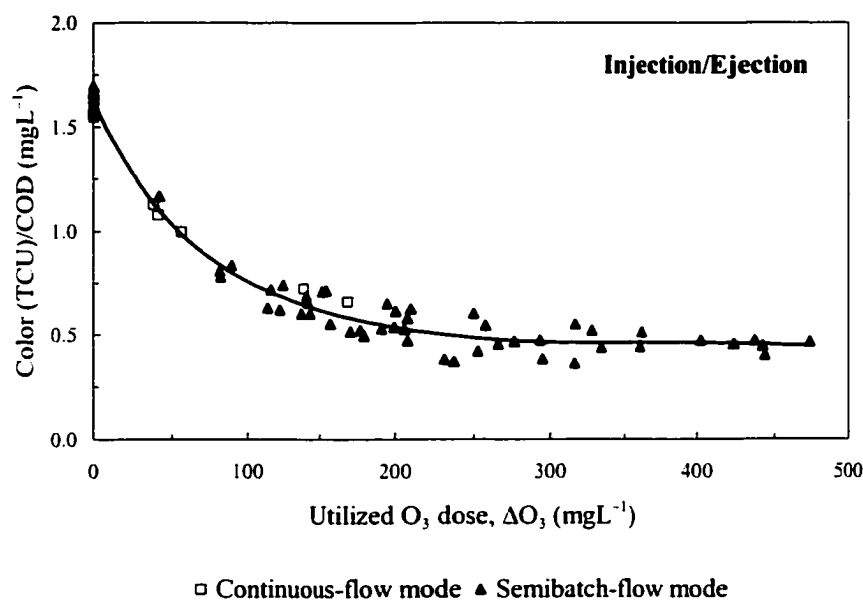


Figure 10.13 The effect of ozonation on the color/COD ratio of the treated Kraft pulp mill wastewater in the impinging-jet ozone contactor.

The color/COD ratios of the Kraft pulp mill wastewater that was treated in the continuous and the semibatch-flow modes under a wide range of operating conditions were pooled together and plotted versus  $\Delta O_3$  as shown in Figure 10.13. There was no effect of the operating mode on the ozonation treatment levels. For the AOX/COD and TOC/COD ratios, as shown in Figures 10.14 and 10.15, the same trend in the reduction of those ratios was observed in the continuous and the semibatch-flow modes except that the initial values (at  $\Delta O_3 = 0$ ) of those ratios were lower in the experiments conducted in the continuous-flow mode. The COD decrease along the course of ozonation was well represented by a linear function that had the same slope for both the continuous and the semibatch-flow modes.

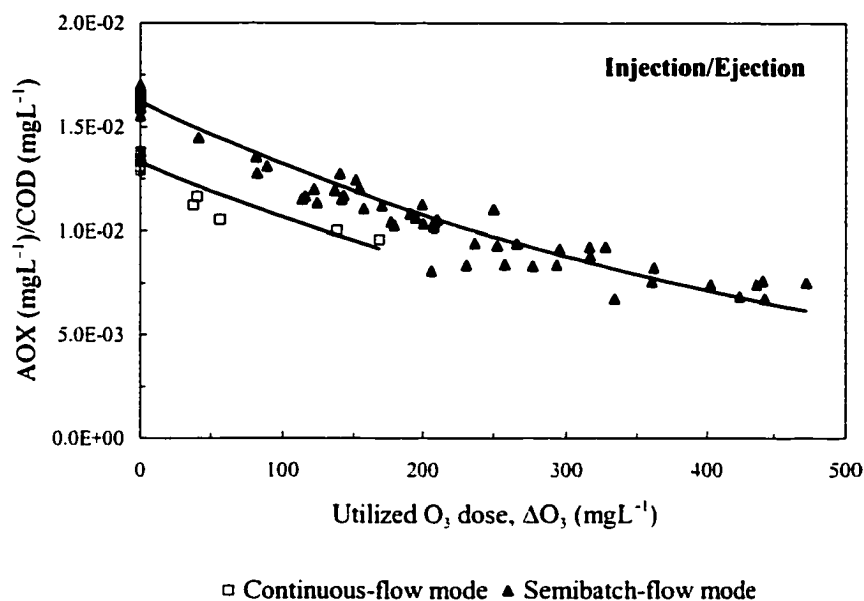


Figure 10.14 The effect of ozonation on the AOX/COD ratio of the treated Kraft pulp mill wastewater in the impinging-jet ozone contactor.

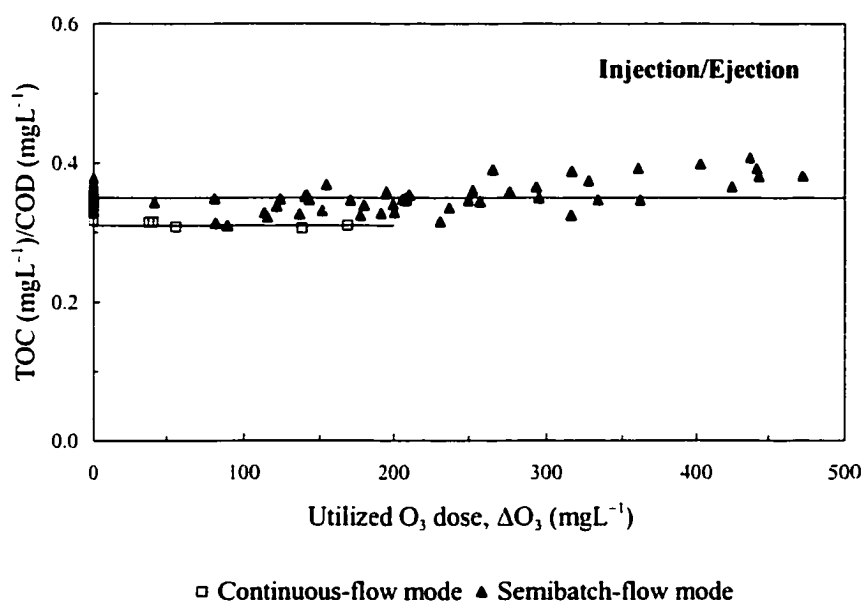


Figure 10.15 The effect of ozonation on the TOC/COD ratio of the treated Kraft pulp mill wastewater in the impinging-jet ozone contactor.

In order to achieve accurate modeling of the ozonation treatment efficiencies in terms of the color, AOX, COD, and TOC induced reduction efficiencies, the ratio of the

initial concentration of the parameter, under investigation, to the initial COD concentration in the pulp mill wastewater can be introduced as another parameter that affects the ozonation treatment levels. This ratio represents the effects of the competing reactions between ozone and the various constituents that are present in the Kraft pulp mill wastewater during the course of ozonation. A general model that can describe the performance of the ozonation treatment can be represented as follows:

$$\log\left(\frac{Y}{Y_0}\right) = a \cdot \Delta O_3 + b \cdot \Delta O_3 \cdot \log\left(\frac{Y_0}{\text{COD}_0}\right) \quad [10.4]$$

This model can be applied to describe the ozonation process reduction efficiencies of color, AOX, and TOC. For COD reduction, the term  $\log\left(\frac{Y_0}{\text{COD}_0}\right)$  reduces to zero. As a result, Equation 10.4 becomes:

$$\log\left(\frac{Y}{Y_0}\right) = a \cdot \Delta O_3 \quad [10.5]$$

where:  $Y$  = final wastewater characteristic parameter concentration (TCU for color, and  $\text{mgL}^{-1}$  for AOX, COD, and TOC),  $Y_0$  = initial wastewater characteristic parameter concentration (TCU for color, and  $\text{mgL}^{-1}$  for AOX, COD, and TOC),  $\Delta O_3$  = amount of the utilized ozone ( $\text{mgL}^{-1}$ ),  $\text{COD}_0$  = initial wastewater COD concentration ( $\text{mgL}^{-1}$ ), and  $a$  and  $b$  are empirical regression constants. Similar models to those represented by Equations 10.5 and 10.6 were developed before by Zhou and Smith (2000).

The experimental data representing the induced reduction efficiencies of color, AOX, COD, and TOC that were obtained in the continuous and the semibatch-flow modes were pooled together and linear regression analyses were performed to obtain the regression constants ( $a$  and  $b$ ) for each parameter under investigation and finally to examine the applicability of the models represented by Equations 10.4 and 10.5 in

predicting the ozone induced reductions of color, AOX, COD, and TOC. The same procedure was performed for the data obtained in the extra-coarse-bubble diffuser ozone contactor.

Table 10.2 Regression parameters for the modeling of the induced reduction efficiencies of color, AOX, COD, and TOC.

Wastewater parameters	Estimated parameters		Multiple r value
	a	b	
<b>Extra-coarse ozone contactor</b>			
Color	-1.88E-03	-6.91E-03	0.95
AOX	-8.15E-03	-3.78E-03	0.89
TOC	-4.35E-04	-2.68E-04	0.97
COD	-4.74E-04	N/A	0.96
<b>Impinging-jet ozone contactor</b>			
Color	-4.06E-03	9.04E-03	0.81
AOX	2.92E-04	8.39E-04	0.98
TOC	8.64E-05	7.87E-04	0.79
COD	-2.79E-04	N/A	0.88

The regression analyses was performed at a 95 % confidence level and the constant parameter was set equal to zero in order to account for the no-treatment condition when the amount of utilized ozone is equal to zero. The regression analyses produced coefficients of correlation (r's) in the range of 0.89 to 0.97 for the data obtained in the extra-coarse-bubble diffuser ozone contactor and in the range of 0.79 to 0.98 for the data obtained in the impinging-jet ozone contactor. The regression parameters obtained for all the wastewater quality parameters representing the Kraft pulp mill wastewater that was treated in the impinging-jet and the extra-coarse-bubble diffuser ozone contactors are shown in Table 10.2.

A Comparison between the predicted and the measured induced ozone reduction efficiencies of the AOX of the Kraft pulp mill wastewater that was treated in the impinging-jet ozone contactor, under various amounts of the utilized ozone, is shown in Figure 10.16

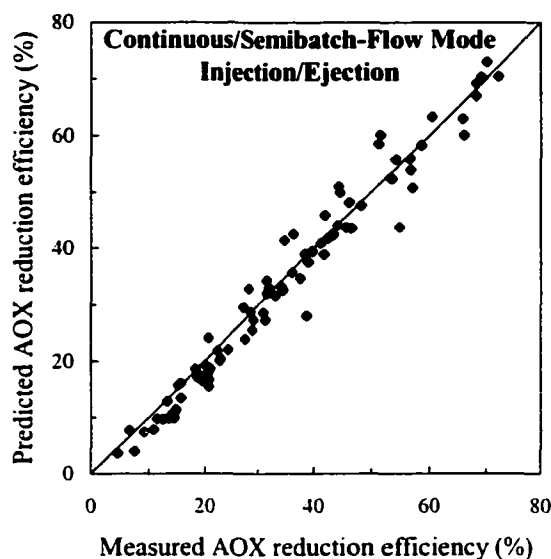


Figure 10.16 A comparison between the predicted and the measured reduction efficiencies of AOX.

#### 10.3.4 Scale-Up of the Ozonation Process

Different ozone contactor designs and configurations should be tested over a wide range of operating conditions in order to achieve proper scale-up of the ozonation process for treating Kraft pulp mill wastewaters. Consequently, relationships can be developed to predict the ozonation treatment levels that can be achieved when scaling up ozone contactors. Zhou and Smith (1997 and 2000) investigated the factors that would influence the scale-up of conventional fine-bubble diffuser ozone contactors. They tested their unit in two operating modes: the semibatch and the continuous-flow modes. Also, two contactor sizes were tested:  $6.0 \times 10^{-2} \text{ m}^3$  and  $4.0 \times 10^{-3} \text{ m}^3$ . Detailed description of their experimental protocols can be found in Zhou and Smith (1997 and 2000). They reported that there was a small scale-up factor associated with the ozonation treatment of Kraft pulp mill wastewaters, although, there was no effect of the mode of operations on the induced reductions of color, AOX, COD, and TOC. Furthermore, a comparison was conducted between the two scales of fine-bubble diffuser ozone contactors used by Zhou

and Smith (1997 and 2000) and the ozone contactors used in the current study in terms of the ozonation treatment levels at a similar  $\Delta O_3$  of  $125 \text{ mgL}^{-1}$ .

Table 10.3 A comparison between three different scales and designs of ozone contactors in terms of the color, AOX, COD, and TOC reduction efficiencies.

<b>Operating conditions</b>	<b>Ozone contactor # (1)</b>	<b>Ozone contactor # (2)</b>	<b>Ozone contactor # (3)</b>	<b>Ozone contactor # (4)</b>
Mode of operations	semibatch	semibatch/ continuous	semibatch	semibatch/ continuous
Gas sparging technique	extra-coarse diffuser	impinging jets	fine diffuser	fine diffuser
Reactor volume ( $\text{m}^3$ )	$2.1 \times 10^{-1}$	$1.7 \times 10^{-2}/$ $1.0 \times 10^{-2}$	$4.0 \times 10^{-3}$	$6.0 \times 10^{-2}/$ $7.0 \times 10^{-2}$
Reactor aspect ratio	1.6	13.2	5.4	22.3/31.3
$\Delta O_3$ ( $\text{mgL}^{-1}$ )	125	125	125	125
<b>Wastewater parameters</b>	<b>% Reduction efficiencies</b>			
Color	65	60	75	63
AOX	31	35	52	32
COD	12	17	20	19
TOC	10	9	17	10

The ozonation induced reduction efficiencies in the four ozone contactors designs are shown in Table 10.3. The results indicated that the scale-up and reactor configuration have exhibited insignificant effects on the ozonation treatment efficiencies. Despite that the impinging-jet ozone contactor, as discussed earlier, has shown to produce lower off-gas ozone concentrations compared to the other ozone contactors that were operated in a semibatch-flow mode. The treatment levels achieved in the impinging-jet and fine-bubble diffuser ozone contactors that were operated in a continuous-flow mode were compared. The two designs of ozone contactors have produced almost identical treatment levels except that the volume of the impinging-jet contactor was one seventh of that of the fine-

diffuser contactor. Consequently, the operating costs of the ozonation process and the ozone off-gas destruction facilities will be greatly reduced when the impinging-jet ozone contactor is used for treating Kraft pulp mill wastewaters.

## 10.4 CONCLUSIONS

Using the venturi injectors for sparging the ozone gas into the liquid phase in the impinging-jet contactor has led to a significant increase in the enhanced overall mass transfer coefficient ( $Ek_{La}$ ) and the enhancement factor ( $E$ ) compared to other designs of ozone contactors. As a result, the off-gas ozone concentrations that were produced from the impinging-jet contactor were substantially lower than those produced from the other contactors.

The ozonation process induced higher reductions in the color and AOX concentrations compared to COD and TOC of the treated Kraft pulp mill effluents. The small ratio of the  $BOD_5/COD$  of the treated wastewater indicates the need for further treatment of this type of wastewater to increase its biodegradability, and consequently, to remove the increase in the  $BOD_5$  of the wastewater as a result of applying further treatment.

The reduction efficiencies of color, AOX, COD, and TOC indicated that the scale-up and reactor configuration have exhibited insignificant effects on the ozonation treatment levels achieved in the three types of ozone contactors examined in this study. This suggests that a small scale-up factor was associated with the ozonation treatment of Kraft pulp mill effluents, especially at large scales, where there was virtually no effect on the ozonation induced reduction efficiencies of color, AOX, COD, and TOC.

The treatment levels achieved in the impinging-jet and fine-bubble diffuser ozone contactors that were operated in a continuous-flow mode were compared and the two designs of ozone contactors were found to produce almost identical treatment levels except that the volume of the impinging-jet contactor was one seventh of that of the fine-diffuser contactor. Based on the above, it is evident that the operating costs of the ozonation process and the ozone off-gas destruction facilities will be greatly reduced when the impinging-jet ozone contactor is used for treating Kraft pulp mill wastewaters.

## 10.5 REFERENCES

1. APHA-AWWA-WEF, *Standard Methods for the Examination of Water and Wastewater, 19<sup>th</sup> Ed.* American Public Health Association, American Water Works Association, and Water Environment Federation (Washington, DC, USA: American Public Health Association, 1995).
2. Bauman, H.D. and L.R. Lutz, "Ozonation of a Kraft Mill Effluent", *Tappi J.* 57(5): 116-119 (1974).
3. Canadian Pulp and Paper Association, *CPPA technical section, H5P Standard Method* (CPPA, 1974).
4. Gamal El-Din, M.G. and D.W. Smith, "Maximizing the Enhanced Ozone Oxidation of Kraft Pulp Mill Effluents in an Impinging-Jet Bubble Column", *Proc. of the IOA/PAG Conf.: Advances in Ozone Technology*, Newport Beach, CA, USA, 2001.
5. Haberl, R., R. Urban, R. Gehringer, and R. Szinovata, "Treatment of Pulp-Bleaching Wastewaters by Activated Sludge, Precipitation, Ozonation, and Irradiation", *Wat. Sci. & Technol.* 24: 229-239 (1991).
6. Heinzle, E., F. Geiger, M. Fahmy, and O.M. Kut, "Integrated Ozonation-Biotreatment of Pulp Bleaching Wastewaters Containing Chlorinated Phenolic Compounds", *Biotechnol. Prog.* 8(1): 67-77 (1992).
7. Metcalf and Eddy, Inc., *Wastewater Engineering: Treatment, Disposal and Reuse* (New York, NY, USA: McGraw-Hill, Inc., 1991).
8. Mohammed, A. and D.W. Smith, "Effects of Ozone on Kraft Process Pulp Mill Wastewater", *Ozone Sci. & Eng.* 14: 461-485 (1992).
9. Nebel, C., R.D. Gottschling, and H.J. O'Neil, "Ozone Decolorization of Pulp and Paper Secondary Wastewaters", *Proc. of First Int. Symp. Ozone for Water and Wastewater Treatments*, 1974.
10. Prat, V.M. and S. Esplugas, "Ozonation of Bleaching Water of the Paper Industry", *Wat. Res.* 23: 51-55 (1989).
11. Zhou, H. and D.W. Smith, "Process Parameter Development for Ozonation of Kraft Pulp Mill Effluents", *Wat. Sci. & Technol.* 35(2-3): 251-259 (1997).

12. Zhou, H. and D.W. Smith, "Ozonation Dynamics and its Implication for Off-Gas Ozone Control in Treating Pulp Mill Wastewaters" *Ozone Sci. & Eng.* 22: 31-51 (2000).

**CHAPTER 11. MEASUREMENTS OF THE SIZE, RISE VELOCITY, AND  
SPECIFIC INTERFACIAL AREA OF BUBBLES IN AN IMPINGING-JET  
BUBBLE COLUMN\***

### 11.1 INTRODUCTION

Gas hold-up ( $\varepsilon_G$ ) is one of the important variables that characterize the hydrodynamics of the gas-liquid flow, i.e., two-phase flow, in bubble columns. It is defined as the fraction of the dispersed volume occupied by the gas bubbles.  $\varepsilon_G$  can affect the performance of bubble columns in two ways: (1) it provides the fractional volume of the gas phase and therefore, its residence time inside the reactor; and (2) in conjunction with the knowledge of the Sauter mean (i.e., volume-to-surface area mean) bubble diameter, it allows the determination of the gas bubbles' specific interfacial area (Jamialahmadi and Müller-Steinhagen, 1992). Gas hold-up, Sauter mean diameter, and gas bubbles' specific interfacial area are interrelated through the following relationship:

$$a = \frac{A}{V} = \frac{6\varepsilon_G}{d_S} \quad [11.1]$$

where:  $a$  = mean gas bubbles' specific interfacial area ( $m^{-1}$ ),  $A$  = mean gas bubbles' surface area ( $m^2$ ),  $V$  = volume of the dispersed phases ( $m^3$ ),  $\varepsilon_G$  = gas hold-up ( $m^3 m^{-3}$ ), and  $d_S$  = Sauter mean bubble diameter ( $m$ ). Since the overall mass transfer coefficient ( $k_L a$ ) can be measured experimentally and with the knowledge of  $a$ , the local mass transfer coefficient ( $k_L$ ) could be determined for the gas-liquid flow in bubble columns.

The use of computational fluid dynamics (CFD) has grown over the past decade since it can offer detailed predictions of the behaviour and the characteristics of multiphase flows such as gas-liquid flow in bubble columns. CFD can lead to significant improvements in the area of scale-up of bubble columns. In order to achieve successful application of CFD in the scale-up process, a better understanding of the fundamentals of the gas-liquid flow phenomena has to be provided.

---

A version of this chapter has been submitted for publication. Gamal El-Din, M. and D.W. Smith, *J. Environ. Eng. & Sci.* (August, 2001).

Gas-liquid flows are complex in their nature and their behaviour can vary substantially depending on the design, configuration, and operating conditions of the bubble columns. It is very hard to conduct experimental measurements inside gas-liquid flows because of their sensitive nature to any disturbances caused by intrusive measuring devices such as electric probes (Mudde *et al.*, 1998). As a result, the use of non-intrusive measurement techniques such as laser Doppler anemometry (LDA) and phase Doppler anemometry (PDA) can provide great tools for characterizing and better understanding of the local rather than the global flow phenomena in gas-liquid flows (Mudde *et al.*, 1998).

Several studies have been conducted for measuring the size of gas bubbles in air-water systems by using a photographic technique (Akita and Yoshida, 1974; Yamashita *et al.*, 1978; Roustan *et al.*, 1996). They observed that, especially at higher gas throughputs, the bubbles were not spherical but could be approximated by oblate ellipsoids. Yamashita *et al.* (1978) measured the  $d_s$  of the ellipsoidal bubbles using a photographic study. Alternatively, and assuming that the bubbles are perfect spheres, they measured the  $d_s$  of the bubbles using an electric probe. Interestingly, and at low gas throughputs, they observed that the two measures of the mean  $d_s$  were almost identical. Also, from their photographic measurements, they observed that  $d_B$  was almost equal to  $d_s$ .

In the current study, a 2-D laser particle dynamics analyzer, that utilizes phase Doppler anemometry (PDA) and laser Doppler anemometry (LDA), was used to obtain simultaneous measurements of: (1) the gas bubble size; (2) the gas bubble size distributions; (3) the gas-phase axial and radial velocity distributions; and (4) the gas-phase turbulence intensities in the axial and radial directions in an impinging-jet bubble column. Two types of liquids were tested: clean deionized water and Kraft pulp mill effluent. The Kraft pulp mill effluent was ozonated using a wide range of utilized ozone doses to investigate its effects on pulp mill effluent characteristics. Of primary interest was its surface active agents (SAA) content and the resulting effect on the surface tension and consequently, on the bubble size ( $d_B$  and  $d_s$ ), the gas hold-up ( $\epsilon_G$ ), and the gas bubbles' specific interfacial area ( $a$ ). The gas and liquid flowrates were varied in order to

determine their effects on the bubble size, the gas bubbles' specific interfacial area, and the gas hold-up.

## 11.2 MEASUREMENT METHODS

### 11.2.1 Particle Dynamics Analyzer

#### 11.2.1.1 Operating Principle

The operating principle of the particle dynamics analyzer can be explained through the use of a simple fringe model. An optical system is used to split a continuous laser beam into two parallel beams. As the two beams pass through a spherical lens, they get reflected and consequently they intersect at the focal point of the lens. Two sets of plane parallel interference fringes are produced, at the intersection point of the laser beams, in the Y-Z and X-Z planes. The spacing between the fringes depends on the intersecting angle and the laser wavelength.

#### 11.2.1.2 Principle of the Bubble Rise Velocity Measurement

The laser Doppler anemometry (LDA) is utilized for measuring the velocity of the bubbles in a gas-liquid flow. As the bubbles rise inside the column and pass through the interference fringes, that are formed in an ellipsoidal volume or referred to as the probe or measurement volume, they will cause a scattering of light in different directions. The scattered light, received by the receiving optics, will have another frequency as a result of the Doppler effect. The Doppler burst is detected by a high-speed photo-multiplier and converted into an electronic signal that will have a frequency proportional to the bubble rise velocity. Therefore, the measurement of those frequencies will allow the determination of the bubble rise velocity. The frequency of the scattered light will carry no information of the sign of the velocity of the bubble. To overcome this velocity sign ambiguity, a small frequency shift is introduced in the transmitting optics to one of the crossing laser beams. As a result, the fringe pattern is no longer stationary but moves perpendicularly to the fringe plane and the light intensity at any point will be modulated at the shift frequency. A bubble moving in the probe volume will scatter light such that

the difference between the modulation frequency and the shift frequency is proportional to the velocity. Therefore, for a bubble moving in the opposite direction to the fringe movement, the modulation frequency will increase. Meanwhile, for a bubble moving in the same direction of the fringe movement, the modulation frequency will decrease. In order to achieve that, a 40 MHz frequency shift was applied via the use of a Bragg cell.

#### 11.2.1.3 Principle of the Bubble Size and Concentration Measurements

The laser Doppler anemometry (LDA) and phase Doppler anemometry (PDA) are utilized for measuring the size and concentration of the bubbles in a gas-liquid flow. As the bubbles pass through the probe volume, they scatter light. The scattered light will contain information about the bubble size. The PDA operating principle can be explained using a fringe model of the phase shift. Considering the interference fringes in the probe volume to be light rays, they are reflected and refracted by the transparent gas bubbles as they pass through the probe volume. A set of two detectors are located at separate locations and will observe alternately light and dark fringes at the same frequency with a relative phase proportional to the spacing between the detectors divided by the spacing between the projected fringes. The spacing between the projected fringes at the location of the detectors is inversely proportional to the effective focal length of the bubble that is proportional to the bubble diameter ( $d_B$ ). Therefore, the measured phase shift is proportional to  $d_B$  of the bubble passing through the probe volume. In order to obtain an exact and accurate linear relationship between  $d_B$  and the phase shift, a specific scattering pattern has to be dominant. The refractive index of water is larger than that of air. Therefore, a  $70^\circ$  scattering angle in a forward scattering mode provides the highest signal levels and an excellent linear relationship between the phase shift and the bubble diameter for measuring the size of an air bubble moving in water (DANTEC, 1989).

The concentration of the bubbles ( $C_B$ ) can be determined based on the knowledge of the arrival rate and the velocity of the rising bubble as well as the cross-sectional area of the probe volume. The cross-sectional area of the probe volume is a function of the laser power, the electronic sensitivity, and the size of the bubble passing through the laser

beam. For a bubble to be detected, the light level must be above a fixed detection threshold. Large bubbles can pass near the edge of the probe volume and still be detected as a result of their ability to scatter more light than small bubbles. Consequently, the concentrations obtained by the PDA will be biased towards large bubbles. This ambiguity in concentration determination is resolved by using the residence time of the bubble as a weighting factor for the bubble size distribution.

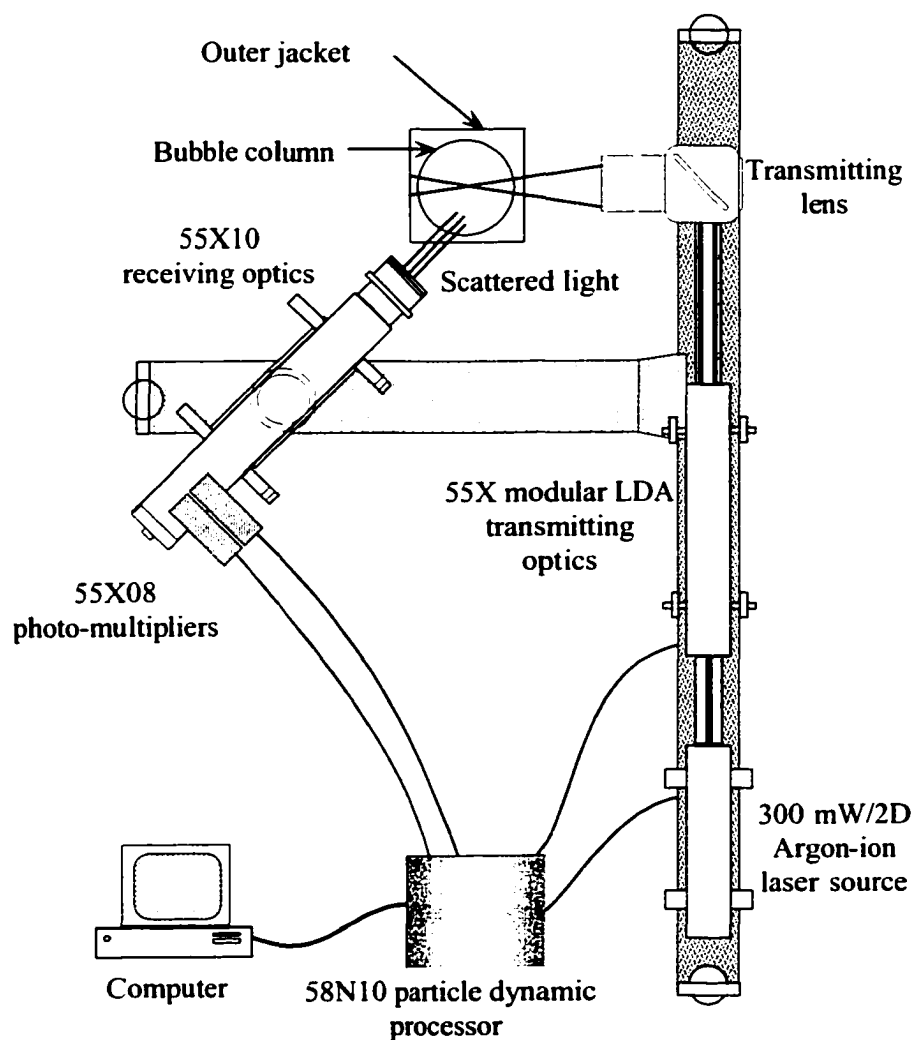


Figure 11.1 Components of the particle dynamics analyzer set-up (adapted from Shawwa, 1998).

#### 11.2.1.4 PDA System Configuration and Operational Settings Adjustment

A 2-D DANTEC<sup>®</sup> laser particle dynamics analyzer was used in the current study. It consisted of (1) 55X modular LDA transmitting optics; (2) 57X10 receiving optics; (3) 55X08 photo-multipliers; and (4) 58N10 processor. The set-up of the PDA system is shown in Figure 11.1. The configuration and operational settings used in the current study are presented in Table 11.1. Those settings were chosen after investigating a wide range of PDA operational configurations and settings to match the velocity and bubble size measurements with those obtained in a photographic study. Therefore, the information obtained from the photographic study helped in adjusting the transmitting and receiving optics configuration and the electronics' operational settings to obtain accurate and reliable results.

#### 11.2.2 Digital Photographic Measurements of the Bubble Size and the Bubble Rise Velocity

Measurements of the bubble size and the bubble rise velocity were conducted using a Canon Powershot G1<sup>®</sup> digital camera. The same operating conditions and the location of measurements that were to be used during the PDA measurements were applied in the photographic study. The camera was leveled and mounted on a stable tripod. An adequate source of light was used and the lens of the camera was focused on a fixed vertical line at the center of the column before the photographic images were recorded. The video photographic study provided rough estimates of the bubble rise velocity by selecting a swarm of bubbles and recording the time it took them to rise over a certain distance along the column height. The rate of video capture was 15 frames per second and the resolution was adjusted to 320/240 pixels. The video images were downloaded and viewed using digital video software. The shutter speed was adjusted to 1/1000 s during the capture of still digital images and the resolution was adjusted to 2048/1536 pixels. Measurements of the bubble size were conducted by selecting a number of individual bubbles that were sharply focused allowing for the shapes and sizes of the bubbles to be obtained.

Table 11.1 PDA system configuration and operational settings.

<b>Laser specifications</b>	
Argon-Ion Laser Power (mW)	300
Bragg Cell Frequency Shift (MHz)	40
U-velocity Laser beam wavelength, $\lambda$ (nm)	514.5
V-velocity Laser beam wavelength, $\lambda$ (nm)	488.0
<b>Electronics set-up</b>	
Signal bandwidth (MHz)	0.12
Validation level during DI water experiments (dB)	0
Validation level during Kraft pulp mill effluent experiments (dB)	-3
Spherical validation	no
Gain	high
<b>Transmitting optics set-up</b>	
Front lens focal length (mm)	600
Laser beam spacing (mm)	12
Fringe spacing, $\delta_{r,x}$ ( $\mu\text{m}$ )	25.726
Fringe spacing, $\delta_{r,v}$ ( $\mu\text{m}$ )	24.401
Number of fringes	8
Measurement volume dimensions, $\delta_x \times \delta_y \times \delta_z$ (mm x mm x mm)	0.2159 x 0.2159 x 28.804
Frequency shift sign	positive
Polarization angle (degree)	0
Polarization orientation w.r.t. scattering plane	parallel
Gaussian beam diameter (mm)	0.82
Beam expansion ratio	1.85
Beam collimation ratio	1.20
<b>Receiving optics set-up</b>	
Front lens focal length (mm)	600
Polarization angle (degree)	0
Polarization orientation w.r.t. scattering plane	parallel
Scattering angle (degree)	70
Scattering mode	Forward reflection
Direction of fringe motion	positive
Fringe direction angle (degree)	0
Angle adjustment (mm)	0

The size measurements were corrected using the proper scale factor that was obtained by mounting a measuring tape of a known scale in the area where the photographic images were recorded. The photographic study was conducted only for the clean deionized water due to the difficulties encountered in obtaining high-quality images when Kraft pulp mill was used as the test liquid. This was a result of the high color content of the effluent.

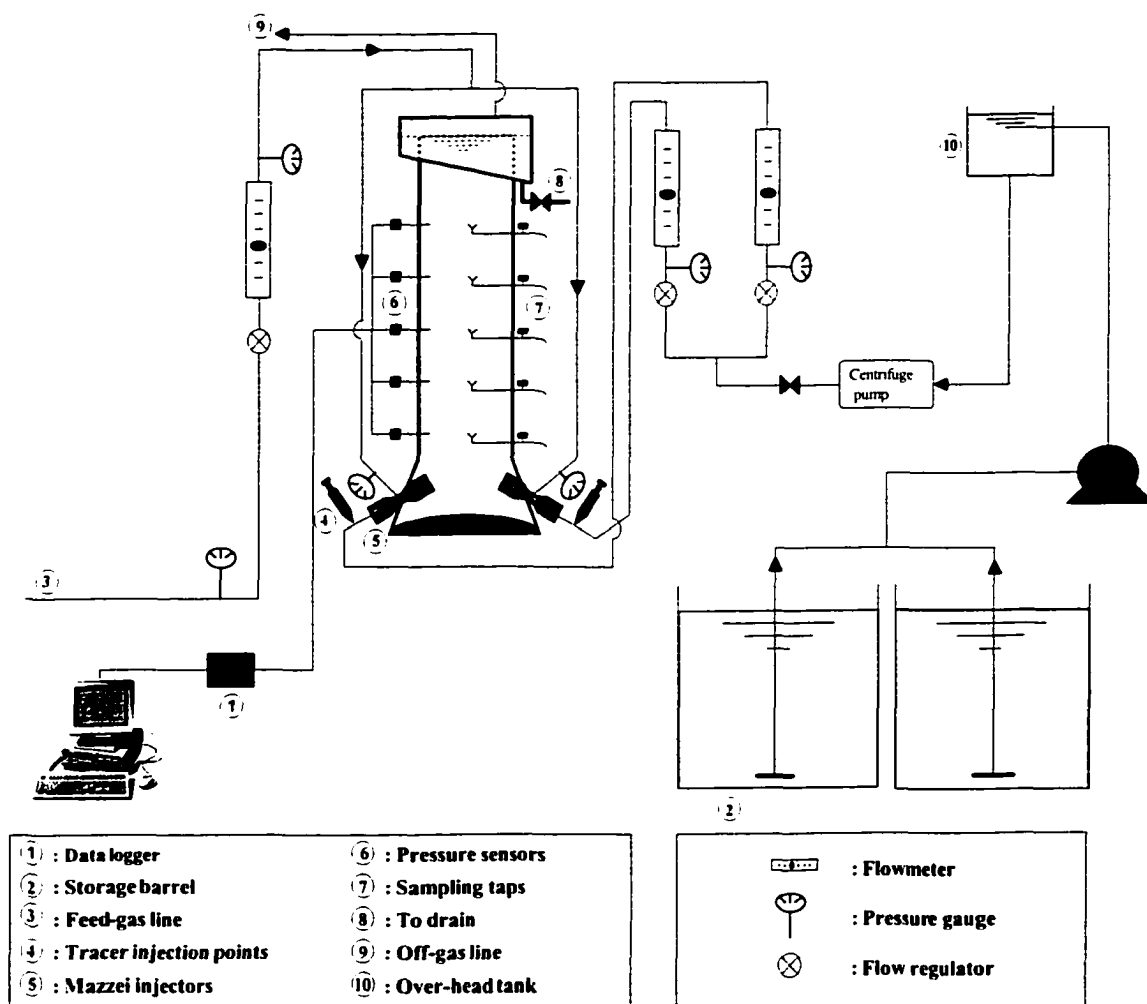


Figure 11.2 Schematic of the experimental set-up of the pilot-scale impinging-jet bubble column.

### 11.2.3 Experimental Set-Up for the Photographic and the PDA Studies

During the photographic and the PDA studies, the measurements were conducted in a pilot-scale impinging-jet bubble column (see Figure 11.2). A detailed description of the

different components of the pilot-scale set-up can be found in Gamal El-Din and Smith (2001). The bubble column was made from clear acrylic and had an inside diameter of 100 mm and a total height of 1,520 mm. The column was surrounded by a 150 mm x 150 mm clear acrylic jacket that had flat surfaces and the gap between the column and the jacket was filled with clean deionized water. The outer jacket was used to minimize the distortions caused by the curved surface of the column (Mudde *et al.*, 1997).

Extra dry air was used as the gas phase and the bubble column was operated for a period of time that was at least eight theoretical reactor hydraulic retention times before measurements were taken to allow the system to reach an isothermal steady-state condition. The pilot-scale bubble column was operated under a wide range of liquid and feed-gas flowrates. During the experiments, the liquid flowrate ranged from  $6.0 \times 10^{-5}$  to  $2.2 \times 10^{-4} \text{ m}^3\text{s}^{-1}$  and the feed-gas flowrate ranged from  $8.2 \times 10^{-6}$  to  $1.0 \times 10^{-4} \text{ m}^3\text{s}^{-1}$ . During the PDA and the photographic studies, measurements were conducted at a point located at the middle of the column height and at a distance equal to  $1/3$  of the column diameter from the column wall.

#### 11.2.4 Experimental Set-Up for the Ozonation of Kraft Pulp Mill Effluent

The Kraft pulp mill effluent was withdrawn from a stilling basin that followed a two-stage aerated lagoon treatment. The average characteristics of the raw pulp mill effluent are shown in Table 11.2.

Table 11.2 Kraft pulp mill effluent average characteristics.

Raw pulp mill effluent parameters	Average concentrations
Colour (TCU)	1129
AOX ( $\text{mgL}^{-1}$ )	9.6
COD ( $\text{mgL}^{-1}$ )	671
TOC ( $\text{mgL}^{-1}$ )	268
BOD <sub>5</sub> ( $\text{mgL}^{-1}$ )	16.5
pH	7.7

The ozonation tests were conducted in a semibatch-flow mode. A detailed schematic of the experimental set-up is shown in Figure 11.3. The ozone contactor was made from PVC with an inside diameter of 570 mm and a total height of 900 mm. The headspace was restricted to only 6 % of the total reactor volume to shorten the lag-time for the ozone off-gas to travel in the exhaust line to the ozone off-gas monitor. An average volume of  $2.1 \times 10^{-1} \text{ m}^3$  of Kraft pulp mill effluent was pumped into the reactor. Ozone gas was generated from extra-dry pure oxygen using a corona discharge ozone generator (model GLS-7, PCI-WEDECO®). The ozone generator was allowed to stabilize for about 1,800 s in order to obtain a stable ozone concentration.

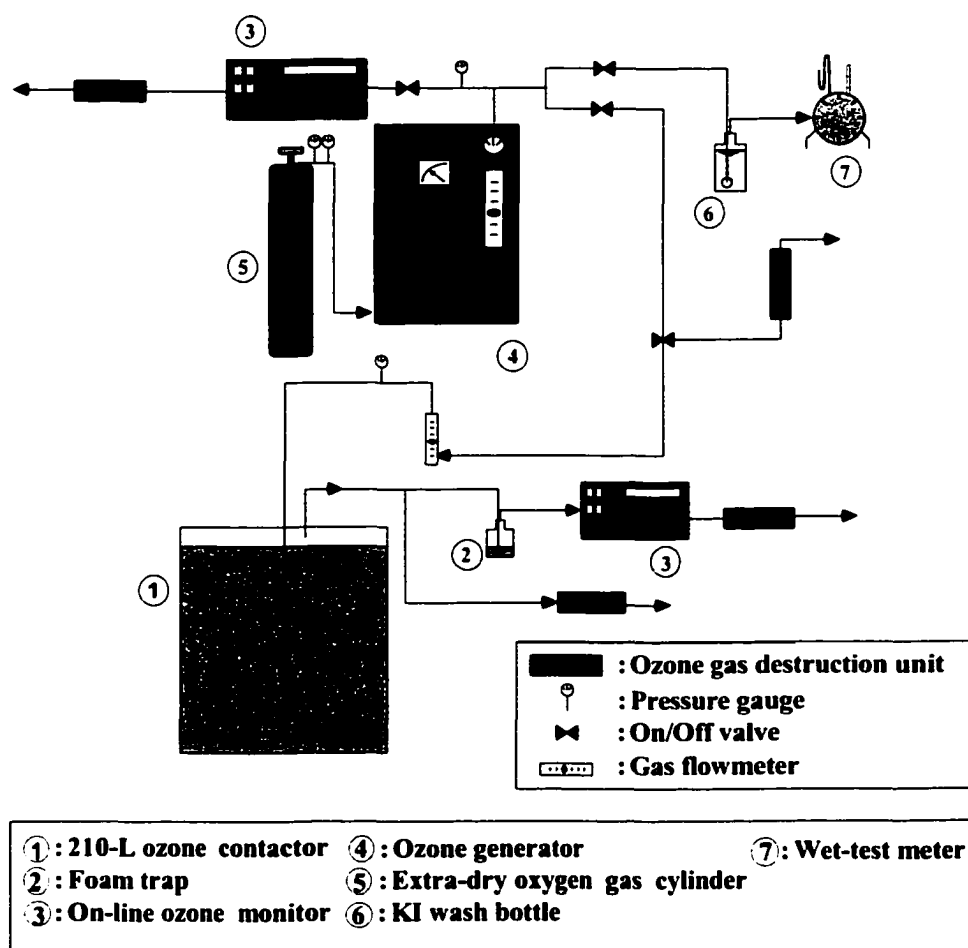


Figure 11.3 Schematic of the ozonation system set-up.

The feed gas that contained 4.4 to 8.3 % w/w ozone was sparged into the liquid phase through a set of eight extra-coarse diffusers (95 mm x 15 mm) equally spaced over the cross-sectional area of the contactor and elevated about 10 mm from the bottom of the contactor to provide better contact between the gas bubbles and the liquid phase. During the ozonation tests, the feed-gas flowrate ranged from  $2.7 \times 10^{-4}$  to  $3.3 \times 10^{-4} \text{ m}^3\text{s}^{-1}$  and the ozone concentrations in the feed gas and off gas were continuously monitored using PCI-WEDECO® ozone monitors (models HC400 and LC, respectively). The monitors were allowed at least 900 s to stabilize before registering their readings. Periodic calibration of the ozone monitors was conducted using the KI method (APHA-AWWA-WEF, 1995). The amount of the utilized ozone ranged from 0 to  $300 \text{ mgL}^{-1}$ .

### 11.3 RESULTS AND DISCUSSION

#### 11.3.1 Digital Photographic Measurements

The rise velocity of bubble swarms was measured to be in the range of  $2.4 \times 10^{-1}$  to  $3.0 \times 10^{-1} \text{ ms}^{-1}$ . Similar ranges of bubble rise velocity were obtained by several researchers who investigated the hydrodynamics of gas bubbles in air-water systems (Kaštánek *et al.*, 1993). The photographic images revealed that the majority of the bubbles had an oblate ellipsoidal shape as shown in Figures 11.4 to 11.6. Therefore, the bubble diameter ( $d_B$ ) was calculated as the arithmetic mean of the maximum and minimum diameters of the bubbles. The angle between the major axis of the bubble and the horizontal direction was defined as  $\phi$  and it was generally  $\leq 90^\circ$  (see Figure 11.7). The maximum diameter was measured along the major axis of the bubble while the minimum diameter was measured along the minor axis of the bubble as shown in Figure 11.7.

For all operating conditions, the mean  $d_B$  ranged from about  $1,400 \mu\text{m}$  to  $2,200 \mu\text{m}$  and an increase in  $u_G$  caused  $d_B$  to increase while an increase in  $u_L$  caused  $d_B$  to decrease. Yamashita *et al.* (1978) observed in their photographic study of the gas bubbles in an air-water system that although most of the bubbles were oblate ellipsoids rather than

spheroids,  $d_S$  and  $d_B$  were almost identical. Therefore, it can be reasonably assumed that  $d_B$  obtained in the current photographic study is an indicator of, if not equal to,  $d_S$ .

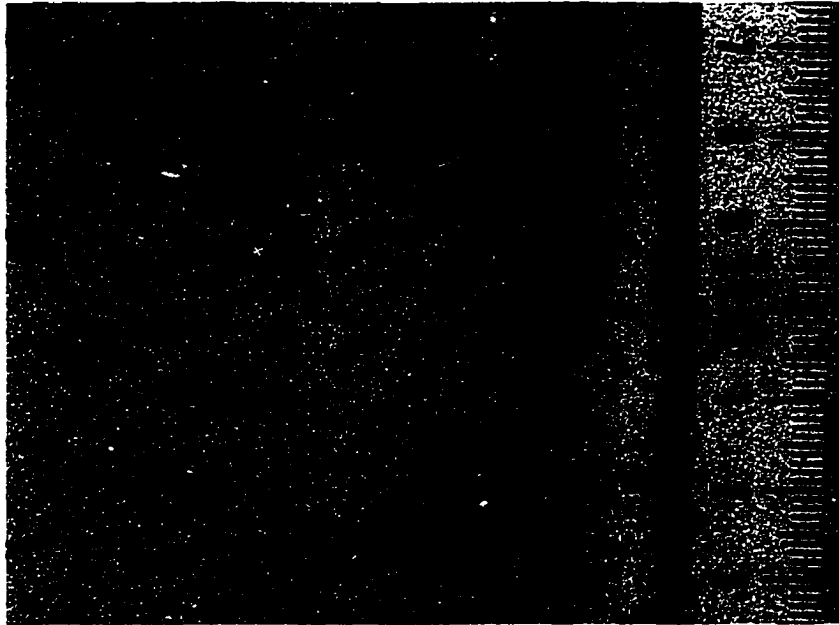


Figure 11.4 A digital image of the air bubbles at  $u_L = 7.7 \times 10^{-3} \text{ ms}^{-1}$  and  $u_G = 1.0 \times 10^{-3} \text{ ms}^{-1}$ .

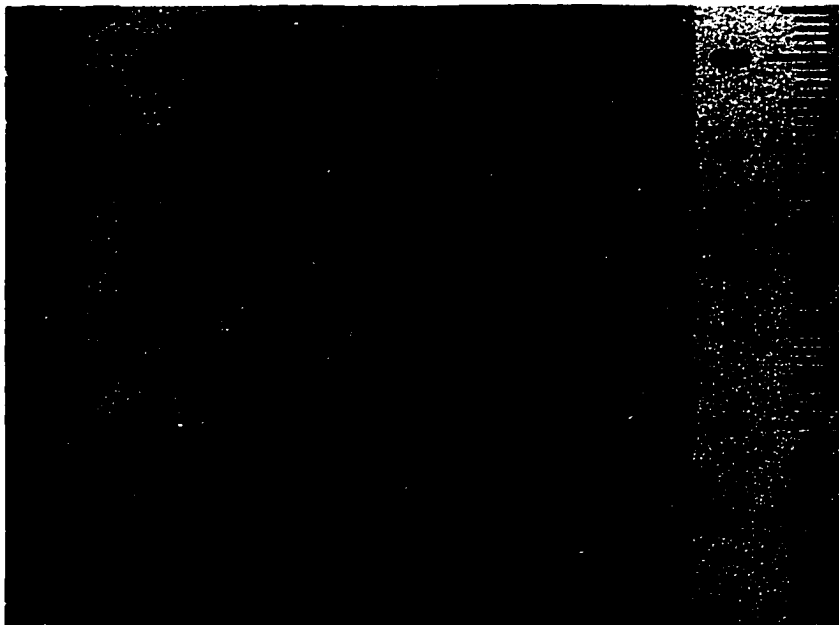


Figure 11.5 A digital image of the air bubbles at  $u_L = 7.7 \times 10^{-3} \text{ ms}^{-1}$  and  $u_G = 7.8 \times 10^{-3} \text{ ms}^{-1}$ .

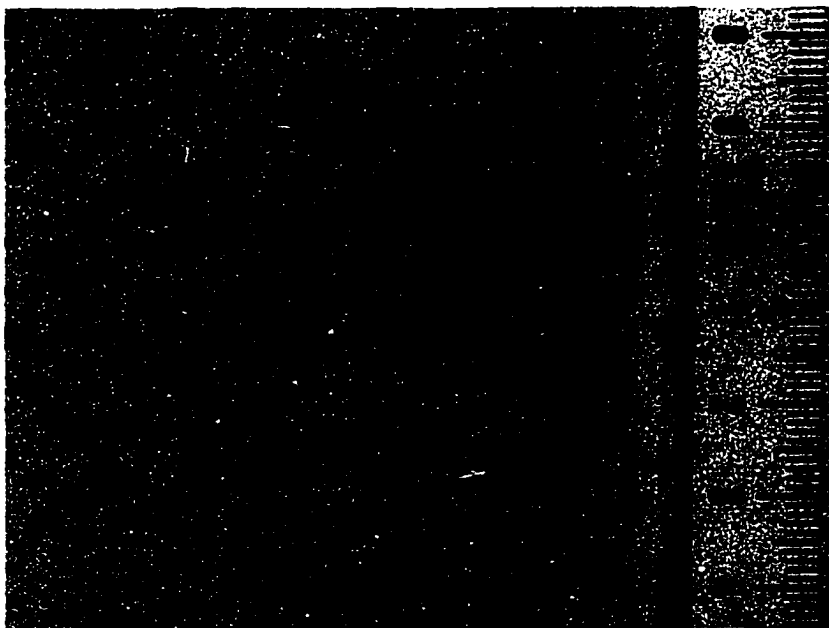


Figure 11.6 A digital image of the air bubbles at  $u_L = 1.9 \times 10^{-2} \text{ ms}^{-1}$  and  $u_G = 8.7 \times 10^{-4} \text{ ms}^{-1}$ .

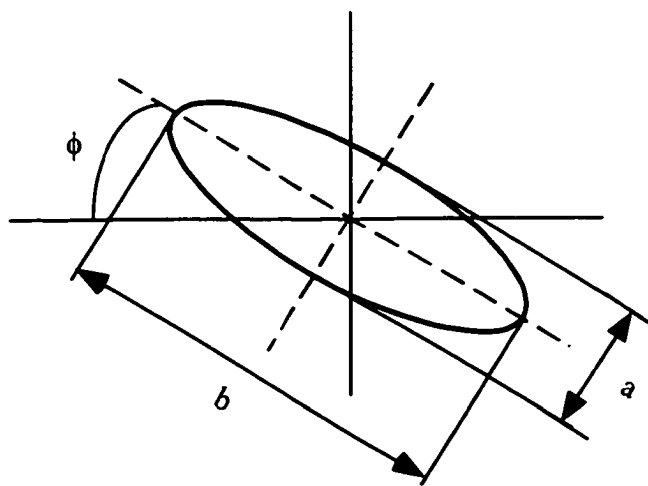


Figure 11.7 Definition of angle  $\phi$ .

### 11.3.2 Particle Dynamics Analyzer Measurements

#### 11.3.2.1 Deionized Water

Figure 11.8 depicts the effects of the superficial gas and liquid velocities ( $u_G$  and  $u_L$ , respectively) on the count mean and Sauter mean bubble diameters ( $d_B$  and  $d_S$ ,

respectively). The gas phase was sparged under positive pressure, i.e., in the injection mode. The values of  $u_L$  and  $u_G$  reported in this study were calculated as follows:

$u_L$  = liquid flowrate/cross-sectional area of the straight section of the impinging-jet bubble column; and

$u_G$  = feed-gas flowrate/ cross-sectional area of the straight section of the impinging-jet bubble column.

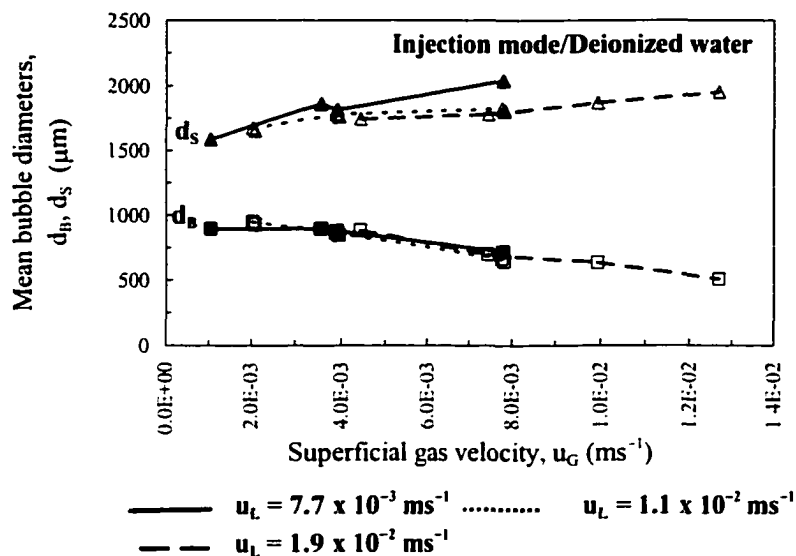
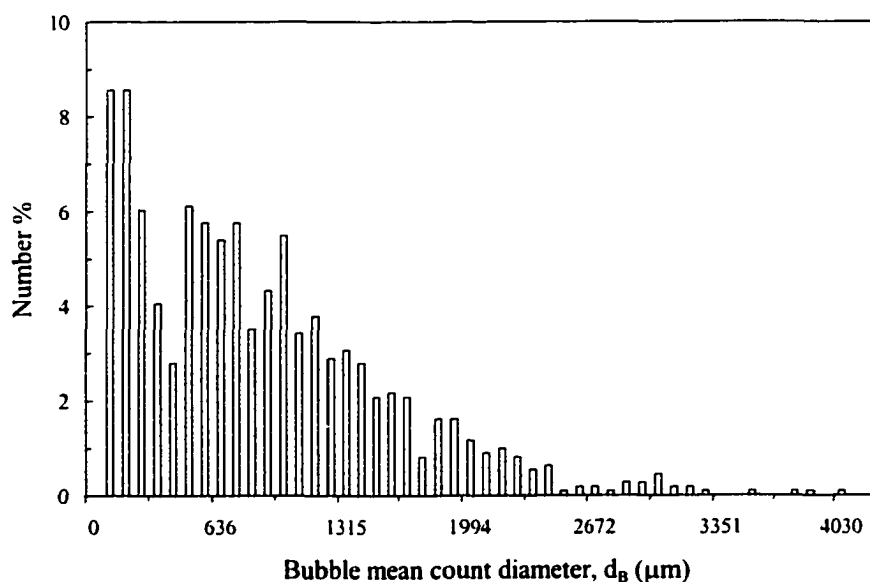


Figure 11.8 Effects of  $u_G$  and  $u_L$  on  $d_B$  and  $d_S$  in deionized water.

As shown in Figure 11.8, at  $u_G \leq 4.0 \times 10^{-3} \text{ms}^{-1}$  and as  $u_L$  increased, the rate of decrease in  $d_B$  per increase in  $u_G$  was lower than that at  $u_G \geq 4.0 \times 10^{-3} \text{ms}^{-1}$ . At  $u_G \geq 4.0 \times 10^{-3} \text{ms}^{-1}$ , the rate of decrease in  $d_B$  per increase in  $u_G$  was almost the same for different  $u_L$ 's. A similar phenomenon was observed by Zhou and Smith (2000). Meanwhile, as  $u_L$  increased,  $d_S$  decreased. Alternatively, as  $u_G$  increased,  $d_S$  increased almost proportionally as observed before in the study of Unno and Inoue (1980) that involved measurements of the sizes of bubbles produced from an orifice mixer that was placed at the bottom of a bubble column. In the impinging-jet bubble column, it was observed that as  $u_L$  increased, the turbulence intensity and turbulent shear stresses increased. Consequently, this resulted in higher shearing of the large gas bubbles into smaller bubbles. Therefore, the mean  $d_B$

and  $d_s$  decreased and they were smaller than those observed before in the studies of Zhou and Smith (2000) and Roustan *et al.* (1996) that were conducted in conventional bubble columns. As indicated earlier by the photographic study, most of the bubbles were ellipsoids rather than spheroids. Therefore, the value of  $d_B$ , obtained in the PDA study, was dependent on the local curvature of the scattering surface of the bubble and the orientation of the bubble with respect to the optical measurement volume. The same observation was reported before by Stanley and Nikitopoulos (1996) when they investigated the effects of the hydrodynamics of an upward gas-liquid jet on the bubble size. Therefore, the value of  $d_B$ , obtained in the PDA study, is not a true measure of the actual count mean bubble diameter of an oblate ellipsoidal bubble. The value of  $d_B$ , obtained in the PDA study, ranged from 500 to 950  $\mu\text{m}$ . Under similar operating conditions to those used in the photographic study, the value of  $d_s$ , obtained in the PDA study, ranged from 1,585 to 2,040  $\mu\text{m}$ . These values were in good agreement with those obtained in the photographic study. Similar trends were observed when the gas phase was sparged under vacuum or negative pressure, i.e., in the ejection mode.



**Figure 11.9** A typical plot of the count-based bubble size distribution in deionized water at high  $u_G$  and low  $u_L$ .

Figures 11.9 to 11.11 present typical plots of the count bubble size distributions in terms of the number %, volume %, and surface area %, respectively, in one of the tests (TR8) conducted in the injection mode. TR8 was conducted at  $u_L$  of  $7.7 \times 10^{-3}$  and  $u_G$  of  $3.9 \times 10^{-3} \text{ ms}^{-1}$ . Under the above operating conditions,  $d_B$  was equal to  $874 \mu\text{m}$ . The count-based size distribution was skewed to the side of small bubbles as compared to a normal distribution and it could be represented by a gamma or log-normal density function. The same phenomenon was reported by Varley (1995) who studied the bubble size characteristics in an aeration tank using a submerged gas-liquid jet.

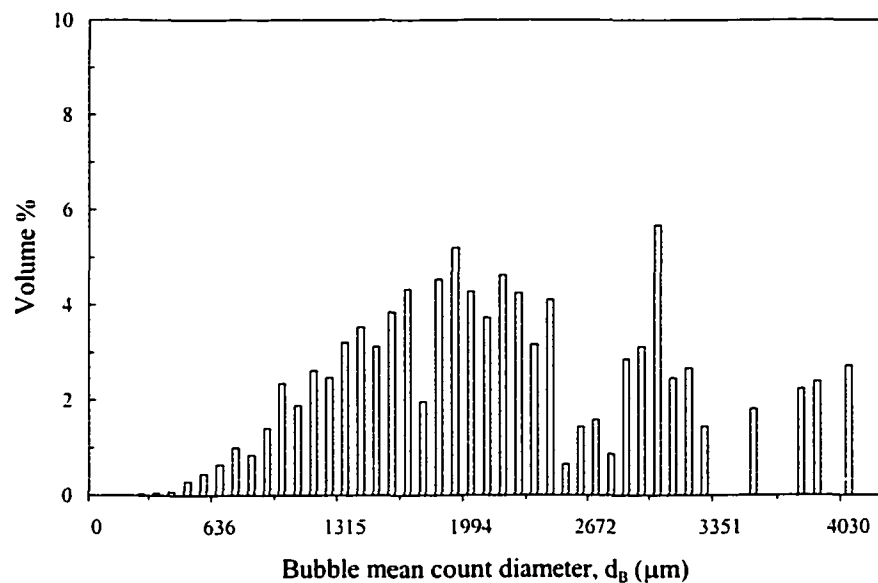


Figure 11.10 A typical plot of the volume-based bubble size distribution in deionized water at high  $u_G$  and low  $u_L$ .

The volume-based size distribution was skewed to the side of large bubbles as compared to a normal distribution and it could be represented by a gamma or log-normal density function. The same phenomenon was reported before in the study of Zhou and Smith (2000) that involved PDA measurements of bubble sizes in a conventional fine-diffuser bubble column. The difference in skews between the count and volume-based size distributions could be explained by the larger contribution of large bubbles to the overall fractional gas volume in the dispersed flow compared to small bubbles. The

surface area-based size distribution was slightly skewed to the side of small bubbles suggesting that small bubbles contributed larger surface area compared to large bubbles. Similar observations were obtained in the experiments conducted in the ejection mode.

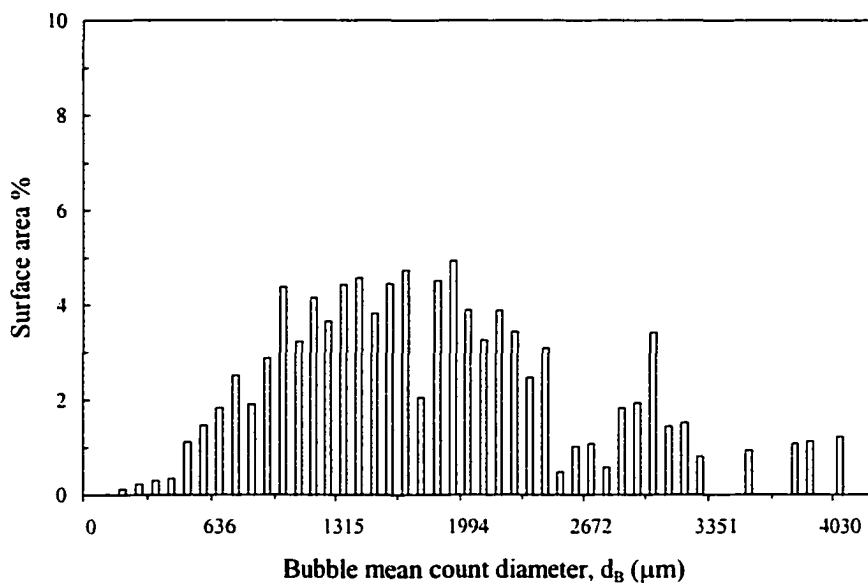


Figure 11.11 A typical plot of the surface area-based bubble size distribution in deionized water at high  $u_G$  and low  $u_L$ .

Figure 11.12 presents a typical plot of the count bubble size distributions in terms of the number % in one of the tests (TR56) conducted in the injection mode. TR56 was conducted at  $u_L$  of  $7.7 \times 10^{-3}$  and  $u_G$  of  $1.0 \times 10^{-3} \text{ ms}^{-1}$ . In TR56, the mean  $d_B$  was equal to 892  $\mu\text{m}$ .  $u_G$  was higher in TR56 than in TR8. As a result and compared to TR8, the count-based size distribution was skewed to the side of small bubbles but to a lesser extent, the distribution had a shape close to that of a skewed normal distribution, the peak of the distribution was higher, and  $d_B$  was higher.

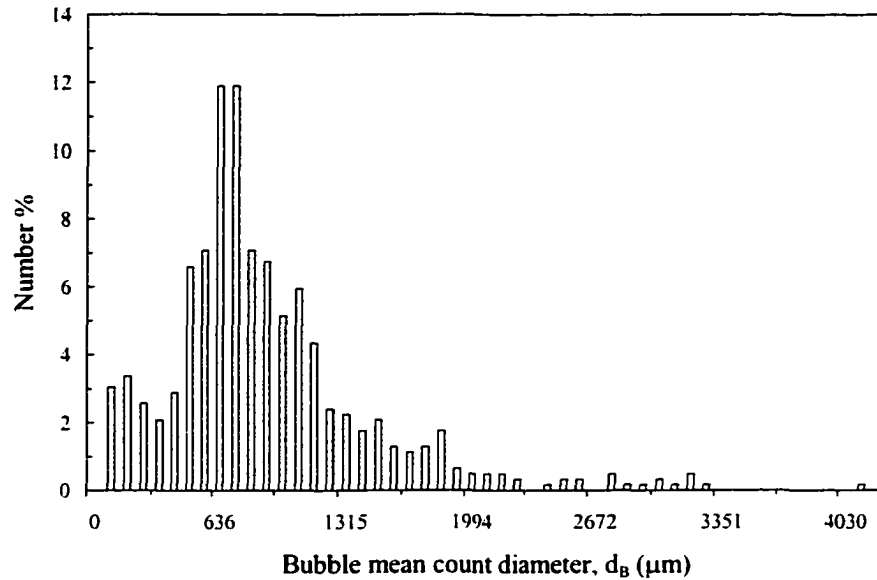


Figure 11.12 A typical plot of the count-based bubble size distribution in deionized water at low  $u_G$  and low  $u_L$ .

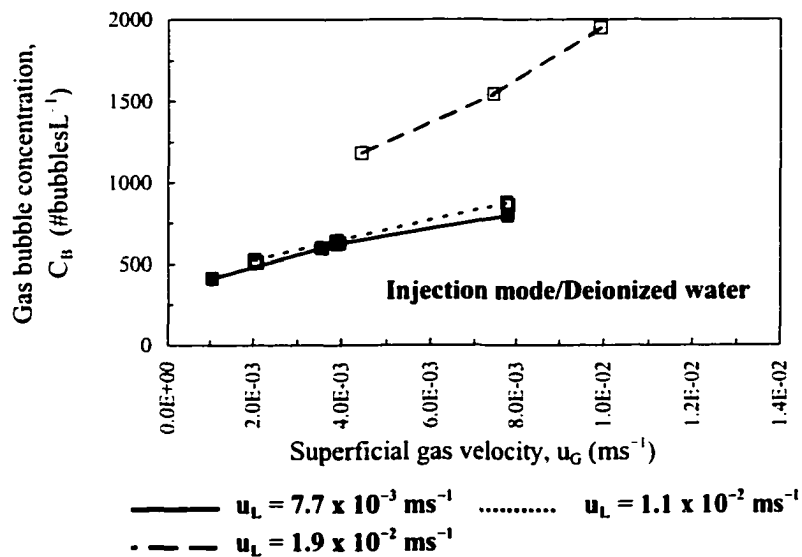


Figure 11.13 Effects of  $u_G$  and  $u_L$  on  $C_B$  in deionized water.

The effects of  $u_G$  and  $u_L$  on the concentration of the bubbles ( $C_B$ ) are shown in Figure 11.13.  $C_B$  increased almost proportionally with the increase in  $u_G$  and  $u_L$ . The rate of increase in  $C_B$  per increase in  $u_L$  was higher than the rate of increase in  $C_B$  per increase

in  $u_G$ . This could have been a result of a high shearing of the large gas bubbles caused by the increase in  $u_L$ . Similar trends were observed during the experiments conducted in the ejection mode.

During the experiments conducted in the injection mode and as shown in Figure 11.14, it was observed that the gas-phase turbulence % in the axial direction (i.e., the root mean square (RMS) velocity divided by the mean axial velocity) increased almost linearly as  $u_G$  increased. Meanwhile as  $u_L$  increased from  $7.7 \times 10^{-3}$  to  $1.9 \times 10^{-2} \text{ ms}^{-1}$  and at  $u_G \leq 4.5 \times 10^{-3} \text{ ms}^{-1}$ , the turbulence % in the axial direction generally increased. Although the turbulence intensity in the liquid phase was not measured, it was expected that since the turbulence levels in the gas phase were high, the liquid phase would as well exhibit high levels of turbulence. The increase in turbulence % could be a result of the gas-liquid flow being in the bubbly flow regime due to the low  $u_G$  encountered in this range of operating conditions.

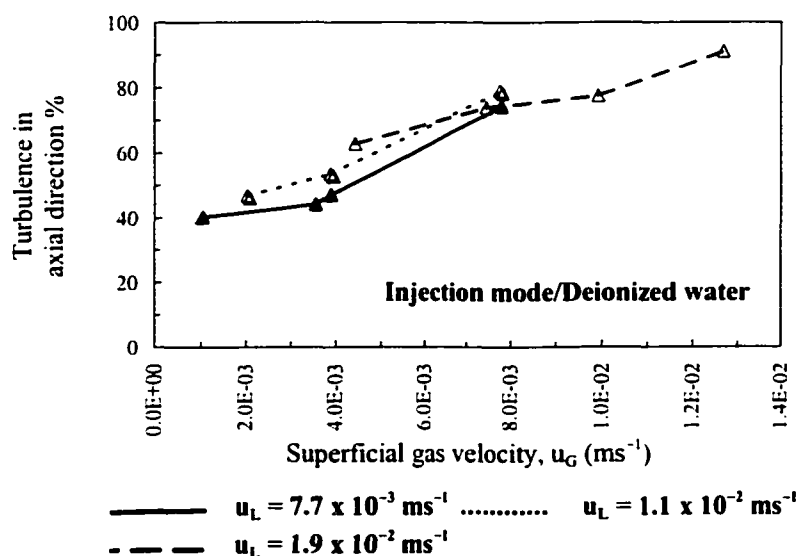


Figure 11.14 Effects of  $u_G$  and  $u_L$  on the gas-phase axial turbulence % in deionized water.

The latter phenomenon could be a result of the decrease in the Sauter mean diameter of the bubbles, and consequently, that could have caused an increase in the entrainment of the surrounding liquid by the rising gas bubbles that carried the entrained liquid upwards. Therefore, the circulation flow pattern could have increased and caused more turbulence in the dispersed flow. At  $u_G \geq 4.5 \times 10^{-3} \text{ ms}^{-1}$ , the turbulence % in the axial direction decreased gradually as  $u_L$  increased. This could be a result of the gas-liquid flow approaching a homogeneous bubbly flow regime that is usually characterized by its high bubble concentration. Also, a somewhat uniform bubble rise velocity distribution was observed. This could have led to the rising of the bubbles without much of mutual bubble interferences, thus, leading to somewhat uniform degrees of axial and radial distributions of gas hold-up and a low degree of turbulence in the axial direction. Similar phenomenon was reported by (Kaštánek *et al.*, 1993). The gas sparging mode had no effect on the dependency of turbulence % on  $u_G$  and  $u_L$ .

Figure 11.15 depicts typical plots of the probability density distributions of the axial bubble rise velocity ( $u$ ) as well as the radial velocity ( $v$ ) for two different tests (TR8 and TR10) that were conducted in the injection mode (i.e., the gas phase was sparged under positive pressure). TR8 was conducted at  $u_L$  of  $7.7 \times 10^{-3}$  and  $u_G$  of  $3.9 \times 10^{-3} \text{ ms}^{-1}$  while, TR10 was conducted at  $u_L$  of  $1.9 \times 10^{-2}$  and  $u_G$  of  $4.4 \times 10^{-3} \text{ ms}^{-1}$ . The velocity profiles were normally distributed as shown in Figure 11.15. The mean radial velocity ( $v$ ) was  $1.2 \times 10^{-3}$  and  $1.1 \times 10^{-3} \text{ ms}^{-1}$  in TR8 and TR10, respectively. The radial velocity profiles confirmed the existence of a circular flow pattern in the bubble column as suggested before by Deckwer (1992). The circular flow pattern is a result of the liquid phase dispersion caused by the entrainment of the surrounding liquid by the rising gas bubbles that carry the entrained liquid upwards (Deckwer, 1992). The mean axial bubble rise velocity ( $u$ ) was  $3.1 \times 10^{-1}$  and  $2.9 \times 10^{-1} \text{ ms}^{-1}$  in TR8 and TR10, respectively. Since  $u_G$  was almost constant between the two runs and as  $u_L$  increased,  $u$  decreased and the spread of the profile was narrowed. In the impinging-jet bubble column, it was observed that as  $u_L$  increased, the gas-phase axial turbulence % increased (at  $u_G \leq 4.5 \times 10^{-3} \text{ ms}^{-1}$ ) causing the turbulent shear stresses to increase considerably. Consequently, this resulted in higher shearing of the large gas bubbles into smaller bubbles, i.e., smaller  $d_B$  and as a

result,  $u$  decreased. Similar trends were observed during the experiments conducted in the ejection mode.

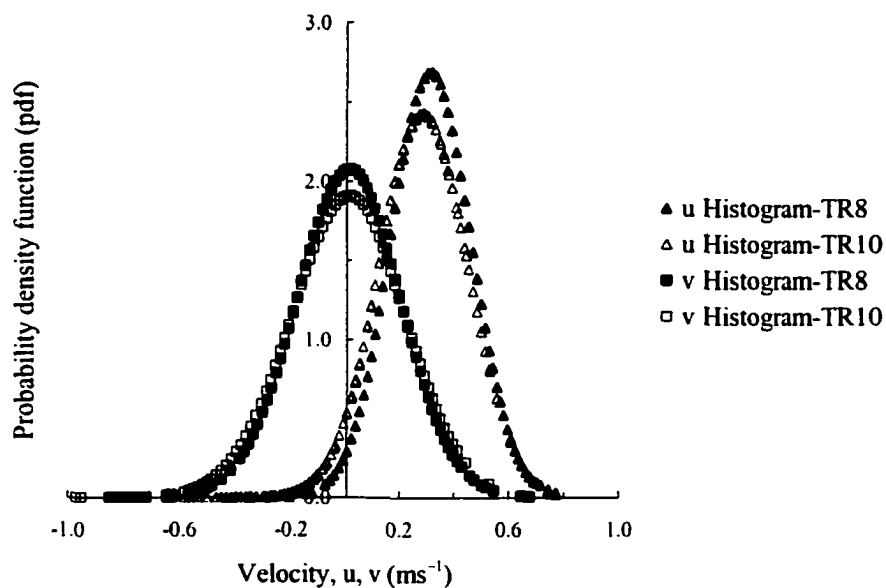


Figure 11.15 Typical probability density distributions of the gas-phase  $u$  and  $v$  in deionized water.

Figure 11.16 depicts the effects of  $u_G$  and  $u_L$  on the bubble rise velocity ( $u$ ) during the experiments conducted in the injection mode. As  $u_G$  increased up to about  $4.0 \times 10^{-3} \text{ ms}^{-1}$ , changes in  $u_L$  had no effect on  $u$ . This could be explained by the gas-liquid flow being in the bubbly flow regime as discussed earlier. Then, as  $u_L$  increased and at  $u_G > 4.0 \times 10^{-3} \text{ ms}^{-1}$ ,  $u$  started to decrease gradually until it reached asymptote at  $u_G$  of about  $1.0 \times 10^{-2} \text{ ms}^{-1}$  as a result of the gas-liquid flow approaching a homogeneous bubbly flow regime. Similar observations were reported by Deckwer (1992). When the experiments were conducted in the ejection mode, similar trends of the dependency of  $u$  on  $u_G$  and  $u_L$  were observed.

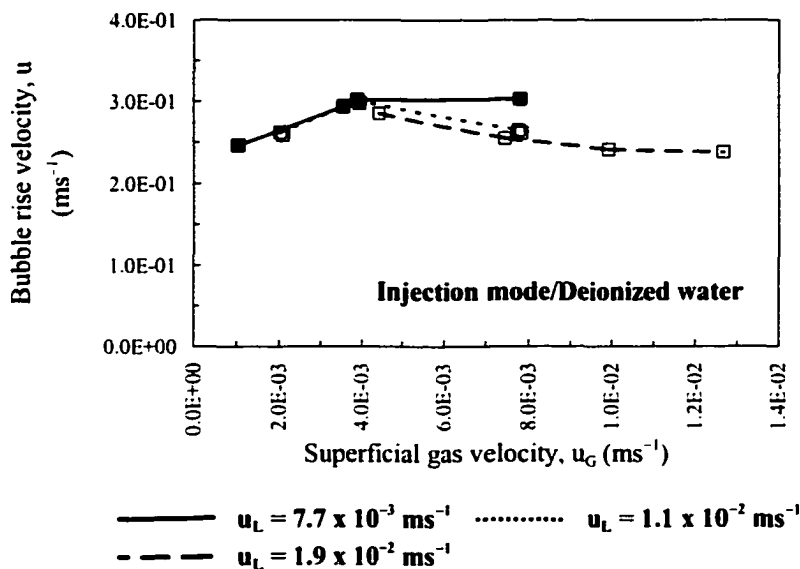


Figure 11.16 Effects of  $u_G$  and  $u_L$  on  $u$  in deionized water.

Figure 11.17 presents the effects of  $u_G$  and  $u_L$  on the gas hold-up ( $\epsilon_G$ ). The gas hold-up was estimated based on the bubble concentration ( $C_B$ ) and the count mean bubble diameter ( $d_B$ ) measurements. As shown in Figure 11.17,  $\epsilon_G$  increased proportionally with the increase in  $u_G$  as reported before by several researchers (Deckwer, 1992; Kaštánek *et al.*, 1993; Roustan *et al.*, 1996; Zhou and Smith, 2000). This phenomenon was a result of the decreased bubble size as  $u_G$  and  $u_L$  increased, and thus, leading to a longer bubble residence time in the bubble column. Also, as  $u_L$  increased, an increase in  $\epsilon_G$  occurred due to the smaller bubble size that resulted from the increase in the shearing of the large gas bubbles into smaller bubbles.

As shown in Figure 11.18, an increase in  $u_G$  and  $u_L$  led to a proportional increase in the gas bubbles' specific interfacial area ( $a$ ). This could be a result of the increase in  $\epsilon_G$  as  $u_G$  and  $u_L$  increased. The same phenomenon was reported by (Zhou and Smith, 2000). Once more, there was no observed effect of the gas sparging mode on the dependency of  $\epsilon_G$  and  $a$  on  $u_G$  and  $u_L$ .

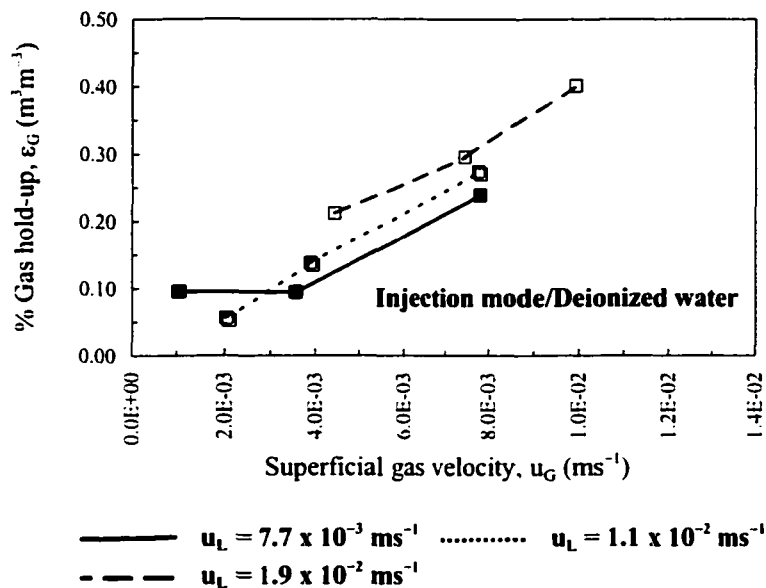


Figure 11.17 Effects of  $u_G$  and  $u_L$  on  $\epsilon_G$  in deionized water.

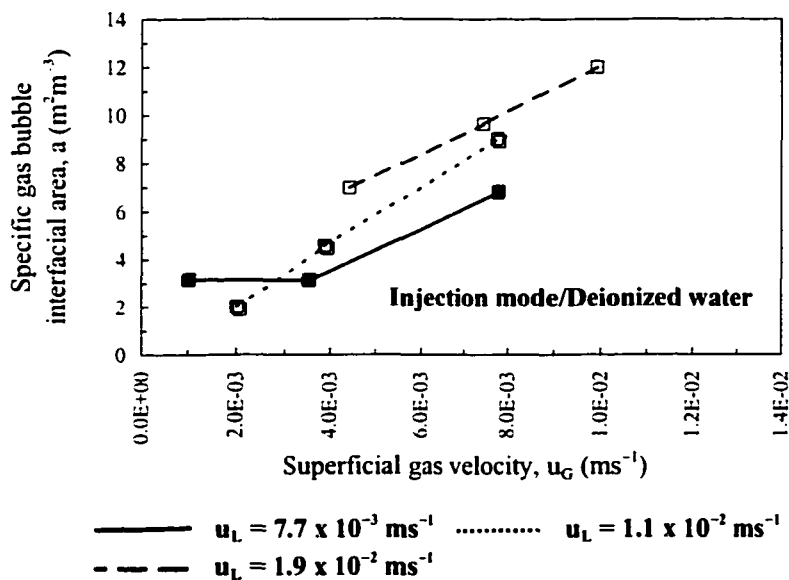


Figure 11.18 Effects of  $u_G$  and  $u_L$  on  $a$  in deionized water.

### 11.3.2.2 Kraft pulp mill effluent

Kraft pulp mill effluents contains surfactants, or referred to as surface active agents (SAA's), and other organic and inorganic compounds that can affect the liquid viscosity

and the bubble surface tension. These effects depend on the type, concentration, and chemical structure of such compounds. The organic compounds can be divided into two main groups (Voigt and Schügerl, 1979): polar organic compounds with low molecular weight; and polar organic compounds with high molecular weight. The SSA's tend to accumulate at the gas-liquid interface with their hydrophobic groups positioned towards the gas phase (Zhou and Smith, 2000). As a result, the surface tension at the interface will be lower than the surface tension in the bulk liquid. Therefore, the surface tension gradient across the liquid film, surrounding the gas bubble, will be higher than that in the bulk liquid leading to a decrease in the size of the gas bubbles. Also, the SAA's can cause damping of the turbulence intensity at the gas-liquid interface and that will lead to a suppression of the coalescence of the mutually contacting gas bubbles (Kaštánek *et al.*, 1993). The coalescence suppressing effect is smallest during the bubble formation and increases as the contact time between the gas phase and the liquid phase increases (Voigt and Schügerl, 1979). The higher the molecular weight of the polar organic compounds, the stronger the suppression of the coalescence but the longer it takes the coalescence suppressing effect to increase as the age of the bubble increases inside the bubble column.

In contrast to the SAA's, the inorganic (i.e., salt) compounds exhibit a different effect on the coalescence suppression (Voigt and Schügerl, 1979). In inorganic solutions, the concentration of the salt compounds in the bulk liquid is the same as that at the gas-liquid interface. This is a result of the liquid phase immediately forming a liquid film around the gas bubble following the bubble formation, therefore, the gradient in the salt concentration between the bulk liquid and at the gas-liquid interface begins to decrease over time. As a result, the salt compounds have their maximum coalescence suppressing effect at the initial stage of the bubble formation and this effect starts to decrease as the age of the gas bubble inside the bubble column increases (Voigt and Schügerl, 1979).

Regarding the effects of the superficial gas and liquid velocities ( $u_G$  and  $u_L$ , respectively) on the count mean bubble diameter ( $d_B$ ), the Sauter mean bubble diameter ( $d_S$ ), the gas bubble concentration ( $C_B$ ), the gas-phase axial turbulence intensity, the gas

bubble rise velocity ( $u$ ), the gas hold-up ( $\epsilon_G$ ), and the gas bubbles' specific interfacial area ( $a$ ), similar trends of those effects were observed when the PDA measurements were conducted during the aeration of the raw Kraft pulp mill effluent as well as the ozonated effluent.

The effects of  $u_G$  and  $u_L$  on  $d_B$  and  $d_S$  during the aeration of raw Kraft pulp mill effluents (i.e.,  $\Delta O_3 = 0.0 \text{ mgL}^{-1}$ ) are shown in Figure 11.19. As  $u_G$  increased, the Sauter mean diameter increased at a rate similar to that observed during the aeration experiments conducted in the deionized water. Also, as  $u_L$  increased,  $d_S$  decreased at a rate similar to that observed in the deionized water. Interestingly, during the aeration of the raw Kraft pulp mill effluent, and as  $u_G$  increased,  $d_B$  increased slightly then it started decreasing. This phenomenon could be a result of the low coalescence suppressing effect of the SAA's due to the short gas bubble residence time in the column that resulted from the increase in the bubble rise velocity ( $u$ ) as  $u_G$  increased up to  $4.0 \times 10^{-3} \text{ ms}^{-1}$ .

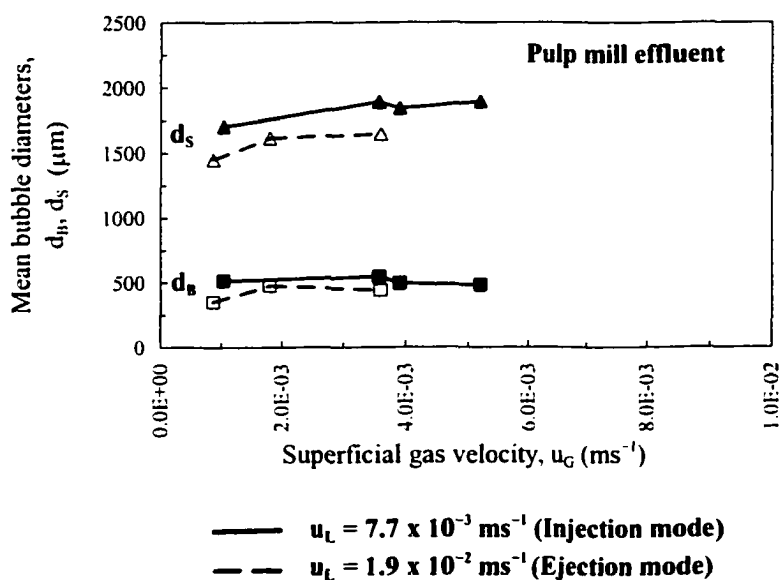


Figure 11.19 Effects of  $u_G$  and  $u_L$  on  $d_B$  and  $d_S$  in raw Kraft pulp mill effluent.

As observed during the aeration of the deionized water and at  $u_G > 4.0 \times 10^{-3} \text{ ms}^{-1}$ ,  $u$  started to decrease and that led to an increase in the gas bubble residence time.

Consequently that might have caused an increase in the coalescence suppressing effect of the SAA's, and as a result,  $d_B$  started decreasing. Alternatively, during the aeration of the ozonated Kraft pulp mill effluents, the effect of  $u_G$  on  $d_B$  was similar to that observed in the deionized water. Generally, the effect of increasing  $u_L$  on decreasing  $d_B$ , during the aeration of the raw and the ozonated Kraft pulp mill effluents, was higher than that observed during the aeration of deionized water. This effect gradually decreased as the amount of the utilized ozone ( $\Delta O_3$ ) increased, possibly due to the increase in the partial or complete oxidation and/or destruction of the surfactants and the inorganic compounds that were present in the raw Kraft pulp mill effluent. The measured  $d_B$  and  $d_S$  in the raw and ozonated Kraft pulp mill effluents were smaller than those obtained in conventional diffuser bubble columns that were tested in the study of Zhou and Smith (2000).

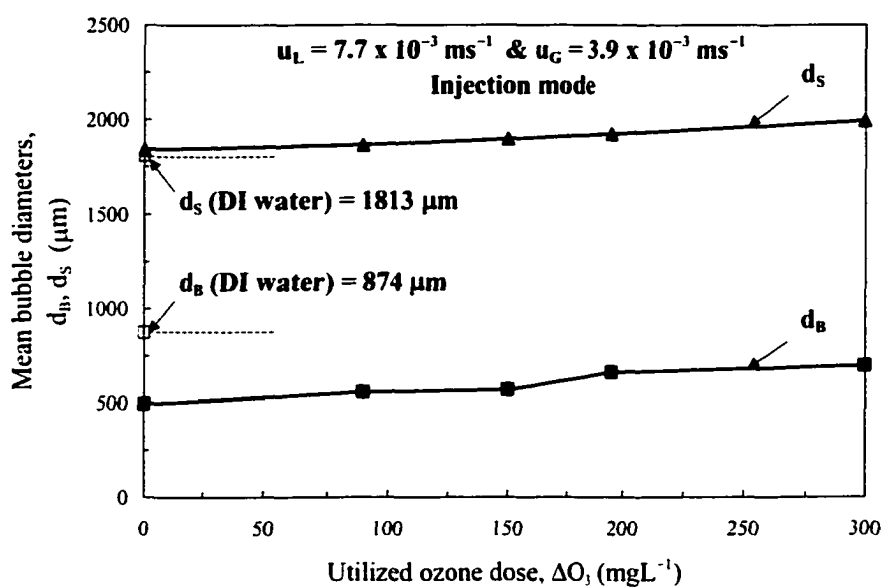


Figure 11.20 Effects of  $\Delta O_3$  on  $d_B$  and  $d_S$  in Kraft pulp mill effluent.

The effects of  $\Delta O_3$  on  $d_B$  and  $d_S$ , for one set of  $u_G$  and  $u_L$  in the injection mode, are presented in Figure 11.20. As  $\Delta O_3$  increased from 0 to 300 mgL<sup>-1</sup>,  $d_S$  increased by almost 8 % (from 1,840 to 1,990  $\mu\text{m}$ ) and  $d_B$  increased by almost 41 % (from 495 to 700  $\mu\text{m}$ ). As shown in Figure 11.20,  $d_S$  was virtually identical in both the deionized water and the

raw Kraft pulp mill effluent. Meanwhile,  $d_B$  in the deionized water was almost two times larger than that in the raw Kraft pulp mill effluent.

The rate of increase in  $C_B$  per increase in  $u_G$  was doubled and the rate of increase in  $C_B$  per increase in  $u_L$  was almost identical in the raw Kraft pulp mill effluent compared to the deionized water. The effects of  $u_G$  and  $u_L$  on  $C_B$  are shown in Figure 11.21. Generally, based on the PDA measurement and visual observations, the gas-liquid flow during the aeration of Kraft pulp mill effluent could be characterized as a homogeneous bubbly flow and the degree of homogeneity decreased as  $\Delta O_3$  increased. Under similar operating conditions, the higher homogeneity of the bubbly flow in the raw Kraft pulp mill effluent compared to the deionized water could be a result of the lower  $d_B$  and  $d_S$ , and the higher  $C_B$  observed in the raw Kraft pulp mill effluent. As a result of the lower  $d_B$  in the raw Kraft pulp mill effluent and under the same operating conditions, the bubble rise velocity ( $u$ ) decreased by about 50 % compared to that in the deionized water. Therefore, lower  $d_B$  and  $d_S$ , higher  $C_B$ , and lower  $u$  caused the gas hold-up ( $\epsilon_G$ ) and the gas bubbles' specific interfacial area ( $a$ ) to increase and they were about four times higher than those in the deionized water.

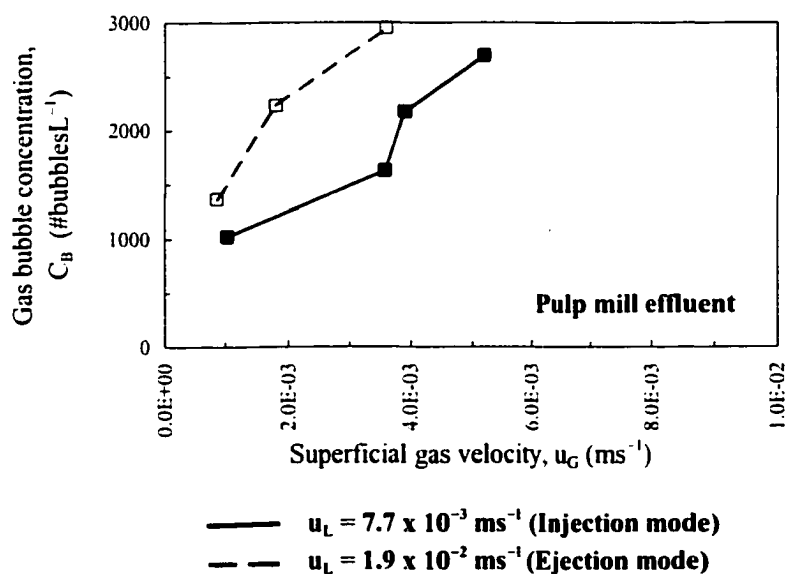


Figure 11.21 Effects of  $u_G$  and  $u_L$  on  $C_B$  in raw Kraft pulp mill effluent.

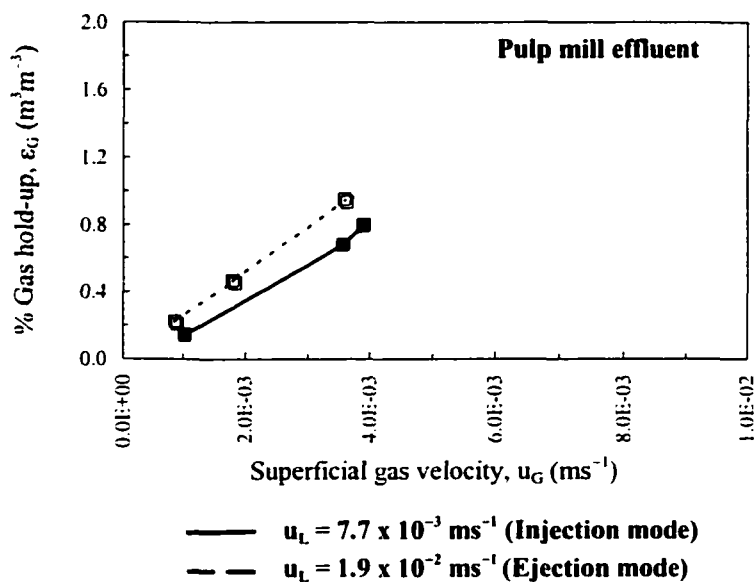


Figure 11.22 Effects of  $u_G$  and  $u_L$  on  $\epsilon_G$  in raw Kraft pulp mill effluent.

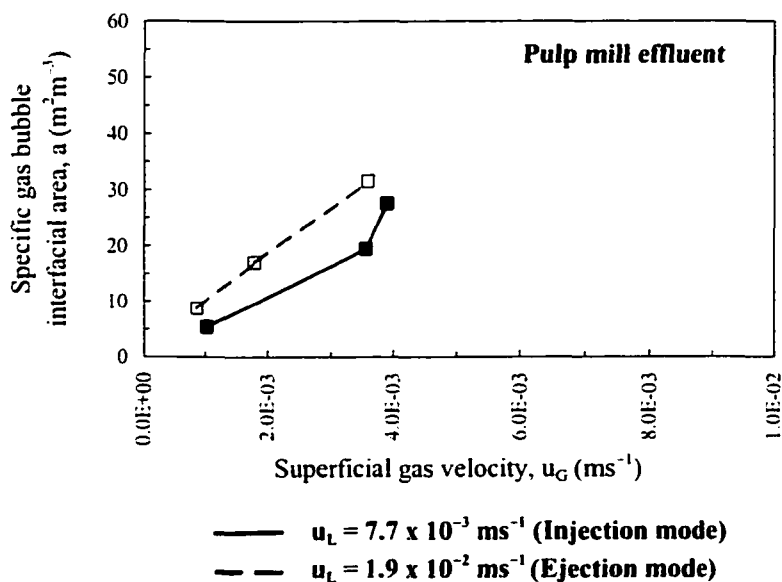


Figure 11.23 Effects of  $u_G$  and  $u_L$  on  $a$  in raw Kraft pulp mill effluent.

The effects of  $u_G$  and  $u_L$  on  $\epsilon_G$  and  $a$  are shown in Figures 11.22 and 11.23, respectively. Under the same operating conditions, the rates of increase in  $\epsilon_G$  and  $a$  per increase in  $u_G$  were almost four times higher in the raw Kraft pulp mill effluent compared to the deionized water. In the raw Kraft pulp mill effluent, at low superficial liquid

velocity ( $u_L$ ) and at either low or high superficial gas velocity ( $u_G$ ), the count-based bubble size distributions exhibited different trends from those observed in the deionized water. Figure 11.24 depicts the count-based bubble size distribution in a test (TR28) that was conducted at low  $u_G$  ( $1.0 \times 10^{-3} \text{ ms}^{-1}$ ) and low  $u_L$  ( $7.7 \times 10^{-3} \text{ ms}^{-1}$ ). Figure 11.25 depicts the count-based bubble size distribution in a test (TR52) that was conducted at high  $u_G$  ( $3.6 \times 10^{-3} \text{ ms}^{-1}$ ) and low  $u_L$  ( $7.7 \times 10^{-3} \text{ ms}^{-1}$ ). The measured  $d_B$  was equal to 516 and 549  $\mu\text{m}$ , in TR28 and TR52, respectively. The distributions were somewhat bimodal and skewed to the side of small bubbles as compared to a normal distribution. Under the same  $u_L$ , an increase in  $u_G$  caused a shift of the low peak towards the side of large bubbles and a decrease in the magnitude of the high peak. Interestingly, at low  $u_G$  and as  $u_L$  increased, the low peak observed before at low  $u_L$ , diminished possibly due to the shearing of the large gas bubbles into smaller bubbles, and consequently, the mean  $d_B$  decreased. This phenomenon is presented in Figure 11.26. As  $u_L$  increased from  $7.7 \times 10^{-3}$  (in TR28) to  $1.9 \times 10^{-2} \text{ ms}^{-1}$  (in TR37) and at almost similar  $u_G$  ( $1.0 \times 10^{-3} \text{ ms}^{-1}$  in TR28 and  $8.6 \times 10^{-4} \text{ ms}^{-1}$  in TR37), the mean  $d_B$  decreased from 516 to 351  $\mu\text{m}$ .

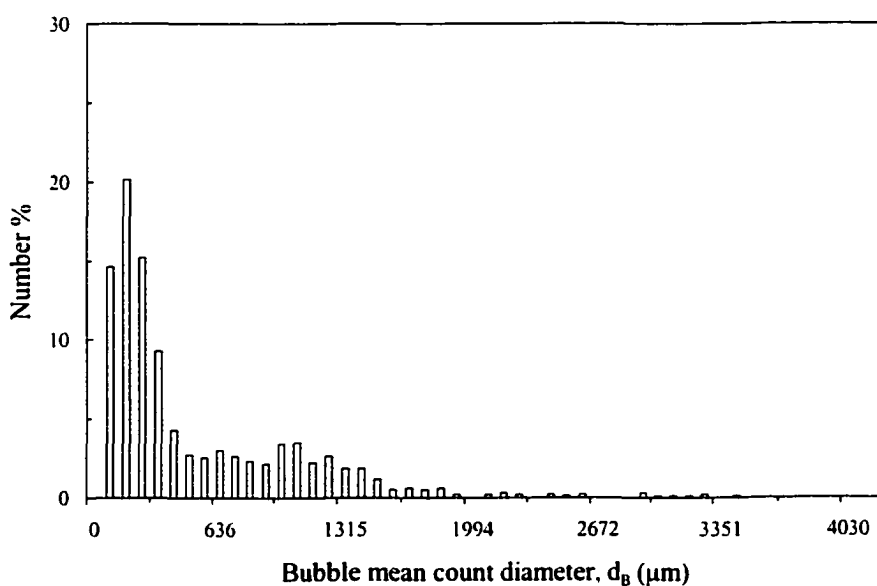


Figure 11.24 A typical plot of the count-based bubble size distribution in raw Kraft pulp mill effluent at low  $u_G$  and low  $u_L$ .

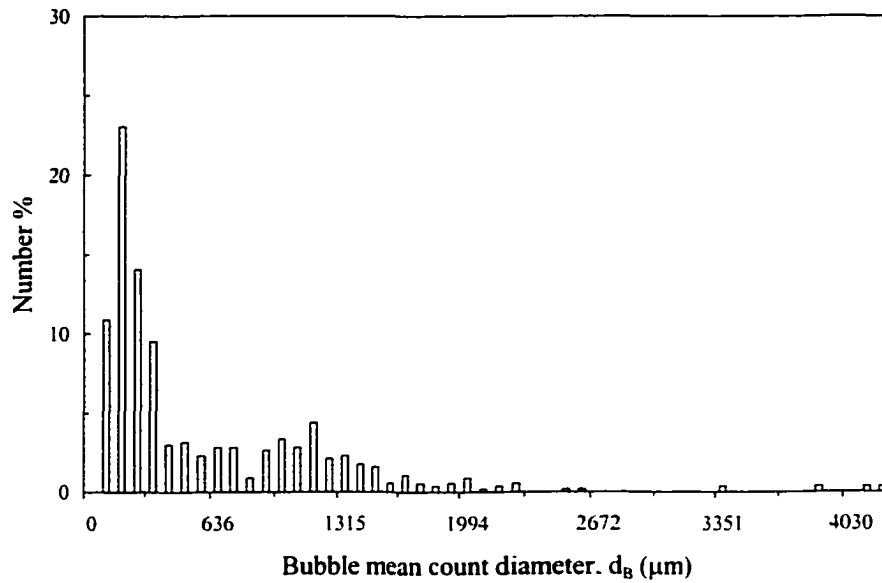


Figure 11.25 A typical plot of the count-based bubble size distribution in raw Kraft pulp mill effluent at high  $u_G$  and low  $u_L$ .

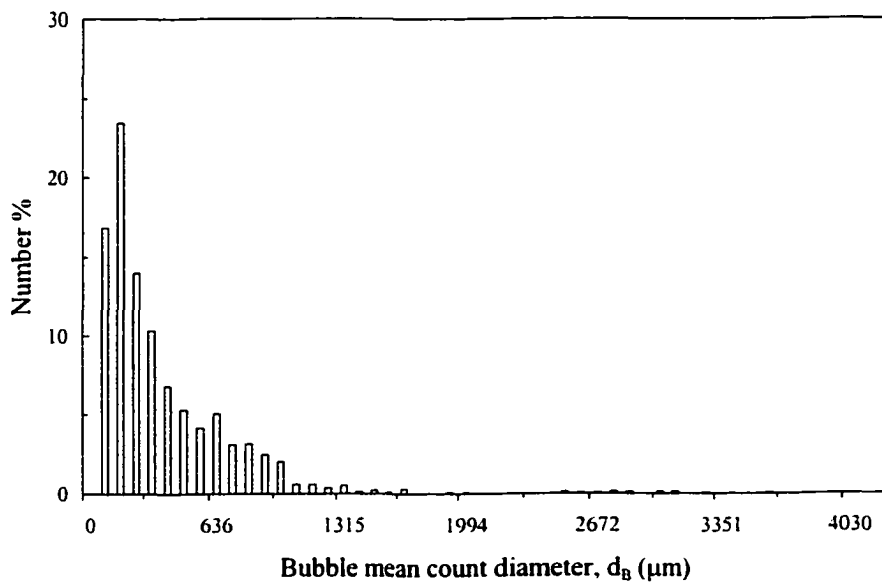


Figure 11.26 A typical plot of the count-based bubble size distribution in raw Kraft pulp mill effluent at low  $u_G$  and high  $u_L$ .

## 11.4 CONCLUSIONS

The two-phase (i.e., gas-liquid) flows are sensitive to any disturbances caused by intrusive measuring devices such as electric probes. Therefore, the 2-D laser and phase Doppler anemometry and the digital photographic measurement techniques provided great non-intrusive tools for characterization and better understanding of the gas bubbles in the impinging-jet bubble column. The digital photographic study provided valuable information on the shape and size of the gas bubbles as well as rough estimates of the bubble rise velocity that aided in optimizing the particle dynamics analyzer configuration and operational settings during the PDA study.

The PDA provided rapid and accurate simultaneous measurements of the bubble size, bubble rise velocity, bubble size distribution, and turbulence intensities in an impinging-jet bubble column that utilized two venturi injectors to create turbulent gas-liquid jets in the ambient fluid.

The intersecting of the gas-liquid jets caused an increase in the turbulence produced in the ambient fluid and as a result the count mean bubble diameter and the Sauter mean bubble diameter decreased and they were smaller than those obtained in conventional bubble columns. This has led to a significant increase in the gas bubbles' specific interfacial area compared to that in conventional bubble columns.

The count mean bubble and Sauter mean bubble diameters were found to be dependent on the superficial gas and liquid velocities. As  $u_L$  increased,  $d_s$  decreased slightly. During the aeration of the deionized water and increasing  $u_G$  caused a slight decrease in  $d_B$ . Meanwhile,  $d_B$  increased slightly then it started decreasing as  $u_G$  increased during the aeration of the raw Kraft pulp mill effluent. During the aeration of ozonated Kraft pulp mill effluent and as  $u_G$  increased,  $d_B$  decreased. The count and the Sauter mean bubble diameters were smaller in the raw Kraft pulp mill effluent compared to those in the deionized water. This has led to a significant increase in the gas bubbles' specific interfacial area and the gas hold-up compared to those in the deionized water. As the raw

**Kraft pulp mill effluent was ozonated and the amount of utilized ozone increased, the count mean and Sauter mean bubble diameters increased.**

**The bubble size distributions exhibited different trends depending on the type of the test liquid and on the operating conditions in terms of the superficial gas and liquid velocities. Generally, those distributions could be well described using normal, gamma, or log-normal density functions.**

**The measurements of the gas hold-up and the gas bubbles' specific interfacial area obtained in the current study provided valuable information that will lead to a better understanding of the mass transfer process in clean environments such as deionized water as well as in highly reactive environments such as Kraft pulp mill effluents.**

## 11.5 REFERENCES

1. APHA-AWWA-WEF, *Standard Methods for the Examination of Water and Wastewater, 19<sup>th</sup> Ed.* American Public Health Association, American Water Works Association, and Water Environment Federation (Washington, DC, USA: American Public Health Association, 1995).
2. Akita, K. and F. Yoshida, "Bubble Size, Interfacial Area, and Liquid-Phase Coefficient in Bubble Columns", *Ind. Eng. Chem., Proc. Des. Develop.* 3: 84-91 (1974).
3. DANTEC, *Particle dynamics analyzer: Users manual*, DANTEC (1989).
4. Deckwer, W.-D., *Bubble Column Reactors*, Cottrell V. (Trans.), Field R.W. (Ed.) (Chichester, England: John Wiley & Sons Ltd, Inc., 1992).
5. Gamal El-Din, M. and D.W. Smith, "Modeling the Ozonation Process in an Impinging-Jet Bubble Column", *Proc. 7<sup>th</sup> Environ. Eng. Specialty Conf., 29<sup>th</sup> Annual CSCE Conf.*, Victoria, BC, Canada, 2001.
6. Jamialahmadi, M. and H. Müller-Steinhagen, "Effect of Superficial Gas Velocity on Bubble Size, Terminal Bubble Rise Velocity and Gas Hold-Up in Bubble Columns", *Develop. Chem. Eng.* 1: 16-31 (1992).
7. Kaštanek, J., J. Zahradník, J. Kratochvíl, and J. Čermák, *Chemical Reactors for Gas-Liquid Systems* (Chichester, England: Ellis Horwood, 1993).
8. Mudde, R.F., J.S. Groen, and H.E.A. Van Den Akker, "Application of LDA to Bubbly Flows", *Nuc. Eng. & Des.* 184: 329-338 (1998).
9. Mudde, R.F., J.S. Groen, and H.E.A. Van Den Akker, "Liquid Velocity Field in a Bubble Column: LDA Experiments", *Chem. Eng. Sci.* 52: 4217-4224 (1997).
10. Roustan, M., R.Y. Wang, and D. Wolbert, "Modeling Hydrodynamics and Mass Transfer Parameters in a Continuous Ozone Bubble Column", *Ozone Sci. & Eng.* 18: 99-115 (1996).
11. Shawwa, A.R., *Rational Approach for Dissolved Air Floatation Contact Zone Modeling: Ph.D. Thesis* (Edmonton, AB, Canada: University of Alberta, 1998).
12. Stanley, K.N. and D.E. Nikitopoulos, "Bubble Measurements in a Gas-Liquid Jet", *Chem. Eng. Comm.* 143: 1-22 (1996).

13. Unno, H. and I. Inoue, "Size Reduction of Bubbles by Orifice Mixer", Chem. Eng. Sci. 35: 1571-1579 (1980).
14. Varley, J., "Submerged Gas-Liquid Jets: Bubble Size Prediction", Chem. Eng. Sci. 50: 901-905 (1995).
15. Voigt, J. and K. Schügerl, "Absorption of Oxygen in Counter-Current Multistage Bubble Columns-I", Chem. Eng. Sci. 34: 1221-1229 (1979).
16. Yamashita, F., Y. Mori, and S. Fujita, "Sizes and Size Distributions of Bubbles in a Bubble Column-Comparison between the Two Point Electric Probe Method and the Photographic Method", J. Chem. Eng. Japan 12: 5-9 (1978).
17. Zhou, H. and D.W. Smith, "Ozone Mass Transfer in Water and Wastewater Treatment: Experimental Observations Using a 2D-Laser Particle Dynamics Analyzer", Wat. Res. 34: 909-921 (2000).

## **CHAPTER 12. GENERAL CONCLUSIONS AND RECOMMENDATIONS**

### **12.1 GENERAL OVERVIEW**

When designing ozone bubble columns, two major sources of uncertainties usually exist: (1) the measurement techniques and the estimation methods of the various operating parameters; and (2) the application of the pertinent design model. The performance of ozone contactors is controlled by the combined effects of the hydrodynamics, ozone mass transfer, and ozone reactions with the constituents present in the liquid phase. Although great advancements in the area of ozone treatment have been achieved, there is still a great demand for more efficient and compact designs of ozone contactors that can provide higher treatment levels in more compact contactors. If this goal can be achieved, the cost of the ozone treatment process will be significantly lowered. Further more, in order to obtain accurate and reliable modeling of the ozonation process, the development of reliable ozonation process parameters is needed. With the development and estimation of those parameters, a rational design approach that integrates those parameters can be designed for practical use in the design and on-line process control of ozone contactors.

The main scope of this research project was to design a new compact ozone contactor that can provide higher treatment levels than those achieved in the conventional ozone contactor designs. Therefore, an impinging-jet bubble column was designed for ozone treatment applications in the area of water and wastewater treatment. The venturi injectors were utilized to create turbulent gas-liquid jets in the ambient fluid by placing them at an intersecting angle of  $125^\circ$  and the distance between the centers of the nozzles was set equal to 60 mm. The main reason for this particular design was to increase the turbulence produced in the ambient fluid and therefore, increase the ozone mass transfer rates.

A number of models were developed for modeling the hydrodynamics and the overall ozonation process in ozone bubble columns. Transient Back flow cell model

(BFCM) was developed as an alternative approach to describe the hydrodynamics of ozone bubble columns. Transient BFCM, when compared to the traditionally used models such as transient ADM or CFSTR's in-series model, represents a flexible, reliable, accurate, and more importantly simple method to describe the backmixing in the liquid phase in bubble columns. The steady-state two-phase axial dispersion model (2P-ADM) and back flow cell model (BFCM) were developed and applied for modeling the ozonation process in ozone bubble columns. A simple and easy-to-use, yet accurate and reliable design model was developed. This model is a modified non-isobaric steady-state one-phase axial dispersion model (1P-ADM). The 1P-ADM is different from the 2P-ADM in its simple use for practical design and process control of full-scale ozone contactors.

In order to model the ozonation process when applied for treating wastewaters such as Kraft pulp mill effluents, the experimental results obtained in three different types of ozone contactors were analyzed. The scope was to study the effects of the ozone contactor design, configuration, operating conditions, and scale-up on the: (1) ozonation process induced reduction efficiencies of the color, AOX, COD, and TOC from biologically treated Kraft pulp mill effluents; (2) the increase in the biodegradability of this type of wastewater; and (3) the dynamics of the ozone gas absorption process. Those ozone contactors had different designs, scales, and configurations. The types of the ozone contactors included: (1) an extra-coarse-bubble diffuser ozone contactor; (2) an impinging-jet ozone contactor; and (3) a fine-bubble diffuser ozone contactor.

Finally, a 2-D laser particle dynamics analyzer was used to simultaneously measure the bubble size, bubble rise velocity, bubble size distribution, and turbulence intensities in the impinging-jet bubble column. These measurements were conducted in clean deionized water and in a Kraft pulp mill effluent that was ozonated using a wide range of utilized ozone doses. The purpose of ozonation was to investigate the effects on surface tension by changing the pulp mill effluent characteristics, and consequently, on the bubble size, the gas hold-up ( $\epsilon_G$ ), and the gas bubbles' specific interfacial area ( $a$ ).

## 12.2 CONCLUSIONS

Based on the theoretical and experimental studies conducted in this research program, the following main conclusions can be drawn:

1. As compared to the traditionally used transient ADM and transient CFSTR's in-series model, the transient BFCM can adequately describe the backmixing in the liquid phase in bubble columns over a wide range of operating conditions and under any given boundary conditions. Therefore, it has some advantages over the transient ADM and the transient CFSTR's in-series model. These advantages are as follows: (1) the transient BFCM can account for variable backmixing coefficient (i.e., variable  $Pe_L$ ) along the column height or along the length of a contacting chamber while predicting simultaneously the RTD curves at various sampling ports; (2) the transient BFCM has the capability to account for variable cross-sectional area along the column height or along the length of a contacting chamber; (3) the analytical solution of the transient ADM for a tracer pulse-input is only available for small deviations from plug flow conditions (Equation 2.11). Therefore, in order to use the solution of transient ADM for a tracer pulse-input under small deviations from plug flow conditions (Equation 2.11) to describe the backmixing in the liquid phase in will lead to inadequate modeling of the hydrodynamics; and (4) the transient BFCM is easy to formulate and solve using a spreadsheet program even for the cases where the mixing parameters are variable along the column height.
2. The number of cells in-series, as one of the mixing parameters to be considered for the transient BFCM simulations, has to be chosen carefully so that the transient BFCM predictions, of the hydrodynamic behaviour in ozone contactors performance under different operating conditions, are closer to the actual backmixing conditions. The transient BFCM should be expanded to account for the backmixing in the gas phase to allow studying the effect of the gas-phase backmixing on the hydrodynamic performance of ozone bubble columns of small

aspect ratios and full-scale ozone contactors where the gas phase can no longer be considered in the plug flow regime.

3. The steady-state BFCM has proven to provide good predictions of the performance of pilot-scale ozone bubble columns. The model predictions should be further tested for different designs and scales of ozone contactors and under different operating conditions. Also, the model should be further expanded to account for variable mass transfer coefficient along the length of the contactor to account for situations where the mass transfer process is enhanced near the entrance of the contactor rather than along the entire contactor length.
4. The two-phase axial dispersion model (2P-ADM) has been developed for describing the performance of ozone bubble columns. Two cases of the model have been developed: (1) the axial dispersion was considered for the liquid and gas phases; and (2) the axial dispersion was considered only in the liquid phase. The main advantage of applying those comprehensive models is to be able to compare between their predictions when used to model the performance of ozone bubble columns. Those models' predictions may vary depending on the bubble column configuration and design as well as the operating conditions. As an example, regarding the effect of bubble column configuration, columns with small aspect ratios might exhibit large gas-phase backmixing that must be accounted for in the model equations. Therefore, most of the models that are currently applied to describe the performance of such ozone contactors are outdated because they are based on inaccurate assumptions with respect to the prevailing liquid and gas-phase flow regimes.
5. The two-phase axial dispersion model (2P-ADM) has proven to be a powerful, accurate and reliable tool for predicting the performance of ozone contactors for both water and wastewater treatment applications. By applying the 2P-ADM instead of the traditionally applied models such as the plug flow model (PFM) or the continuous-flow stirred-tank-reactors (CFSTR's) in-series model, accurate and

reliable designs of ozone contactors can be achieved. As a result, the operating and capital costs will be minimized and the desired treatment objectives can be met.

6. It should be noted that the current model testing is just an initial testing step. Therefore, further studies need to be conducted for both water and wastewater treatment applications and in different ozone contactors of different configurations, designs, and scales. This will help obtain a large and high-quality data set that can allow for further model testing in order to eliminate any uncertainties in the model predictions.
7. The simple version of the 2P-ADM that neglects the backmixing in the gas phase can be applied without affecting the accuracy of the model predictions in situations such as: (1) bubble columns that have large aspect ratios; and (2) when large bubbles are dominant in the gas-liquid flow as a result of using a gas sparging technique that creates large bubbles.
8. A comparison between the 2P-ADM and the BFCM was conducted to test the variability in their predictions of the performance of ozone contactors operating under water or wastewater treatment conditions. Both models have proven to be sufficient and reliable in their predictions of the performance of ozone bubble columns, however, the BFCM was easier to formulate and solve.
9. For wastewater treatment applications and with all the operating conditions being the same, the ADM and the BFCM predicted that the counter-current and the co-current flow modes would exhibit similar characteristics with respect to the dissolved ozone, gaseous ozone, and superficial gas velocity profiles. Changes in the backmixing coefficient, represented by changes in  $Pe_L$ , had relatively small effect on the dissolved ozone concentration profiles and virtually no effect on the gaseous ozone concentration and superficial gas velocity profiles. On the other hand, changes in the overall mass transfer coefficient ( $k_{La}$ ) had large effects on the

dissolved ozone and gaseous ozone profiles and a very small effect on the superficial gas velocity profiles.

10. The 1P-ADM can be solved analytically while the complete axial dispersion model (2P-ADM) requires an elaborate numerical technique to solve the model's equations. Therefore, describing the analytical solution of the 1P-ADM in terms of a simple spreadsheet program facilitates obtaining the model predictions for any operating conditions represented by the model input parameters entered into the spreadsheet program. Compared to the 2P-ADM predictions of the ozone bubble column performance that was presented in the study of Zhou *et al.* (1994), the 1P-ADM has proven to provide excellent predictions of the performance of ozone bubble columns operating under either water treatment conditions and in both the counter-current and the co-current flow modes. The 1P-ADM also provided good predictions of the performance of ozone bubble columns for the wastewater treatment applications. The 1P-ADM is easy and reliable tool to be used for the design and the process-control of bubble columns' operations.
  
11. The 1P-ADM was applied to model the measured dissolved and gaseous ozone concentration profiles in the impinging-jet bubble column. The dissolved ozone concentration profiles along the bubble column height, can be well estimated using the one-phase axial dispersion model (1P-ADM) through the use of bubble column average parameters with respect to the overall mass transfer coefficient ( $k_L a$ ), liquid-phase backmixing coefficient ( $D_L$ ), and coefficient of the gas-phase ozone molar fraction decrease along the column height ( $a_1$ ). During the ozonation of deionized water, it was found that  $k_L a$  and  $D_L$  were dependent on the liquid and gas superficial velocities and the nature of this dependency varied from the gas injection mode to the gas ejection mode. The gas-phase dimensionless ozone concentration profiles can be well described using an exponential relationship representing the gas-phase ozone molar decrease along the column height. The exponent ( $a_1$ ) was found to be dependent on the process dimensionless variables

( $Pe_L$ ,  $St_L$ ,  $St_G$ , and  $D_a$ ) and the nature of this dependency was different in the injection mode from that in the ejection mode.

12. The use of the venturi injectors for the ozone gas absorption caused an increase in the mass transfer rates due to the contact between the gas and the liquid phases inside the injectors. Placing the injectors at an intersecting angle of  $125^\circ$  at the bottom of the bubble column caused an intersecting of the gas-liquid jets. This arrangement has led to a significant increase in the turbulence intensities in the ambient fluid and consequently, a significant increase in the mass transfer rates was achieved. The impinging-jet bubble column has proven to be a very promising gas-liquid contacting unit, when compared to the traditional bubble column designs due to its compact size that can handle higher liquid and gas flowrates without causing any decrease in the mass transfer efficiency of the bubble column.
13. Using the venturi injectors for sparging the ozone gas into the liquid phase in the impinging-jet contactor has led to a significant increase in the enhanced overall mass transfer coefficient ( $Ek_{La}$ ) and the enhancement factor ( $E$ ) compared to other designs of ozone contactors. As a result, the off-gas ozone concentrations that were produced from the impinging-jet contactor were substantially lower than those produced from the other contactors.
14. The ozonation process induced higher reductions in the color and AOX concentrations compared to COD and TOC of the treated Kraft pulp mill effluents. The small ratio of the  $BOD_5/COD$  of the treated wastewater indicates the need for further treatment of this type of wastewater to increase its biodegradability, and consequently, to remove the increase in the  $BOD_5$  of the wastewater as a result of applying further treatment.
15. The reduction efficiencies of color, AOX, COD, and TOC indicated that the scale-up and reactor configuration have exhibited insignificant effects on the ozonation treatment levels achieved in the three types of ozone contactors examined in this

study. This suggests that a small scale-up factor was associated with the ozonation treatment of Kraft pulp mill effluents, especially at large scales, where there was virtually no effect on the ozonation induced reduction efficiencies of color, AOX, COD, and TOC.

16. The treatment levels achieved in the impinging-jet and fine-bubble diffuser ozone contactors that were operated in a continuous-flow mode were compared and the two designs of ozone contactors were found to produce almost identical treatment levels except that the volume of the impinging-jet contactor was one seventh of that of the fine-diffuser contactor. Based on the above, it is evident that the operating costs of the ozonation process and the ozone off-gas destruction facilities will be greatly reduced when the impinging-jet ozone contactor is used for treating Kraft pulp mill wastewaters.
17. Therefore, the 2-D laser and phase Doppler anemometry and the digital photographic measurement techniques provided great non-intrusive tools for characterization and better understanding of the gas bubbles in the impinging-jet bubble column. The digital photographic study provided valuable information on the shape and size of the gas bubbles as well as rough estimates of the bubble rise velocity that aided in optimizing the particle dynamics analyzer configuration and operational settings during the PDA study.
18. The PDA provided rapid and accurate simultaneous measurements of the bubble size, bubble rise velocity, bubble size distribution, and turbulence intensities in an impinging-jet bubble column that utilized two venturi injectors to create turbulent gas-liquid jets in the ambient fluid.
19. The count mean bubble and Sauter mean bubble diameters were dependent on the superficial gas and liquid velocities.

20. The count and Sauter mean bubble diameters were smaller in the raw Kraft pulp mill effluent compared to those in the deionized water. This has led to a significant increase in the gas bubbles' specific interfacial area and the gas hold-up compared to those in the deionized water. As the raw Kraft pulp mill effluent was ozonated and the amount of the utilized ozone increased, the count mean and the Sauter mean bubble diameters increased.
21. The bubble size distributions exhibited different trends depending on the type of the test liquid and on the operating conditions in terms of the superficial gas and liquid velocities. Generally, those distributions could be well described using normal, gamma, or log-normal density functions.
22. The measurements of the gas hold-up and gas bubbles' specific interfacial area obtained in the current study provided valuable information that will lead to a better understanding of the mass transfer process in clean environments such as deionized water as well as in highly reactive environments such as Kraft pulp mill effluents.

### 12.3 RECOMMENDATIONS

In this study, different models have developed for describing the performance of ozone bubble columns and a new design of ozone bubble columns has been proposed. Based on the achieved goals and the drawn conclusions, several recommendations have to be addressed in further future research:

1. Additional testing of the models needs to be conducted in pilot-scale as well as full-scale ozone contactors to verify their applicability for describing the performance of the ozonation process in a wide range of scales and designs of ozone contactors over a wide range of operating conditions.
2. The models should be expanded to account for variable process parameters along the length of the contactor as it is usually the case in full-scale ozone contactors.

3. The models should be tested for their ability to describe the performance of ozonation systems when designed for disinfection purposes.
4. Additional studies need to be conducted to characterize the mass transfer efficiency of the impinging-jet ozone bubble column when used to treat various types of wastewaters such as different waste streams generated from the pulp and paper industry.
5. Additional PDA measurements should be carried out at different locations along the column height to examine the variability of the characteristics of the gas bubbles along the column height.
6. Different injector diameters and intersecting angles should be investigated to examine their effects on the performance of the bubble column. Also, the effect of the distance between the injector exit points should be investigated.
7. The impinging-jet bubble column should be tested for treating different types of wastewaters by utilizing ozone in conjunction with other advanced oxidants such as hydrogen peroxide, UV, fenton reagents, etc.

**APPENDIX A. CURRICULUM VITAE**

## **CURRICULUM VITAE**

**Full Name:** Mohamed Gamal El-Din  
**Citizenship:** Canadian  
**Postal Address:** Department of Civil and Environmental Engineering  
304 Environmental Engineering Building  
University of Alberta  
Edmonton, Alberta  
Canada T6G 2M8  
Telephone #: (780)492-5124  
Fax #: (780)492-8289  
**E-mail:** [mgamalel-din@civil.ualberta.ca](mailto:mgamalel-din@civil.ualberta.ca)

## **UNIVERSITY EDUCATION**

Ph.D. (Environmental Engineering) 1995-Current: Dissertation title “Theoretical Analysis and Experimental Verification of the Performance of Ozone Bubble Columns”. Department of Civil and Environmental Engineering, University of Alberta, Edmonton, Alberta, Canada.

MS (Environmental Engineering) 1994-1995: Course based. Department of Civil and Environmental Engineering, Wayne State University, Detroit, MI, USA.

B.Sc. with Honours (Civil Engineering) 1986-1991: Faculty of Engineering, Cairo University, Cairo, Egypt.

## **RESEARCH INTEREST**

**My research interests include:**

- ◆ **Advanced oxidation processes (AOP's),**
- ◆ **Application of phase Doppler anemometry to multi-phase flows,**
- ◆ **Hydrodynamics modeling,**
- ◆ **Gas mass transfer in water and wastewater,**
- ◆ **Ozone treatment of industrial wastewater,**
- ◆ **Numerical modeling of treatment processes, and**
- ◆ **Water quality modeling.**

## **WORK EXPERIENCE**

**Assistant Professor (July 2001-Current), Department of Civil and Environmental Engineering, University of Alberta, Edmonton, Alberta, Canada.**

**Research Assistant (September 1995-June 2001), Department of Civil and Environmental Engineering, University of Alberta, Edmonton, Alberta, Canada.**

**Research Assistant (January 1994-August 1995), Department of Civil and Environmental Engineering, Wayne State University, Detroit, Michigan, USA.**

**Structural Designer Engineer (August 1991-December 1993), ELOSEILY Consulting Office, Cairo, Egypt.**

## **PUBLICATIONS**

### **REFEREED JOURNAL PAPERS**

Gamal El-Din, M. and D.W. Smith, "Development of Transient Backflow Cell Model (BFCM) for Bubble Columns", *Ozone Sci. & Eng.* 23(4): 313-326 (2001).

Gamal El-Din, M. and D.W. Smith, "Ozone Mass Transfer in Water Treatment: Hydrodynamics and Mass Transfer Modeling of Ozone Bubble Columns", *Wat. Sci. & Technol.: Wat. Suppl.* 1(2): 123-130 (2001).

Smith, D.W. and M. Gamal El-Din, "Theoretical Analysis and Experimental Verification of Ozone Mass Transfer in Bubble Columns", *Environ. Technol.* (Accepted, May 2001)

Gamal El-Din, M. and D.W. Smith, "Designing Ozone Bubble Columns: A Spreadsheet Approach to Axial Dispersion Model", *Ozone Sci. & Eng.* (Accepted, June 2001).

Gamal El-Din, M. and D.W. Smith, "Maximizing the Enhanced Ozone Oxidation of Kraft Pulp Mill Effluents in an Impinging-Jet Bubble Column", *Ozone Sci. & Eng.* (Accepted, July. 2001).

Gamal El-Din, M. and D.W. Smith, "Ozonation of Kraft Pulp Mill Effluent: Process Dynamics", *J. Environ. Eng. & Sci.* (Accepted, August 2001).

### **SUBMITTED JOURNAL PAPERS**

Gamal El-Din, M. and D.W. Smith, "Measurements of the Size, Rise Velocity, and Specific Interfacial Area of Bubbles in an Impinging-Jet Bubble Column", *J. Environ. Eng. & Sci.* (submitted for publication, August 2001).

Gamal El-Din, M. and D.W. Smith, "Comparing Different Designs and Scales of Bubble Columns for Their Effectiveness in Treating Kraft Pulp Mill Effluents", *Ozone Sci. & Eng.* (submitted for publication, August 2001).

Gamal El-Din, M. and D.W. Smith, "Mass Transfer Analysis in Ozone Bubble Columns", *J. Environ. Eng. & Sci.* (submitted for publication, July 2001).

Gamal El-Din, M. and D.W. Smith, "Development of Design Parameters of an Impinging-Jet Bubble Column", *Wat. Res.* (submitted for publication, March 2001).

#### REFEREED PAPERS IN CONFERENCE PROCEEDINGS

Gamal El-Din, M. and D.W. Smith, "Comparing Different Designs and Scales of Bubble Columns for Their Effectiveness in Treating Kraft Pulp Mill Effluents". In: *Advances in Ozone Technology, Proc. of IOA/15<sup>th</sup> World Congress*, London, England (2001).

Smith, D.W. and M. Gamal El-Din, "Modeling the Hydrodynamics and Mass Transfer in an Impinging-Jet Bubble Column". In: *Advances in Ozone Technology, Proc. of IOA/15<sup>th</sup> World Congress*, London, England (2001).

Gamal El-Din, M. and D.W. Smith, "Ozonation of Kraft Pulp Mill Effluent: Process Dynamics and Scale-Up". In: *Proc. 7<sup>th</sup> Environmental Engineering Specialty Conf., 29<sup>th</sup> Annual CSCE Conf.*, Victoria, British Columbia, Canada (2001).

Gamal El-Din, M. and D.W. Smith, "Modeling the Ozonation Process in an Impinging-Jet Bubble Column". In: *Proc. 7<sup>th</sup> Environmental Engineering Specialty Conf., 29<sup>th</sup> Annual CSCE Conf.*, Victoria, British Columbia, Canada (2001).

Gamal El-Din, M. and D.W. Smith, "Maximizing the Enhanced Ozone Oxidation of Kraft Pulp Mill Effluents in an Impinging-Jet Bubble Column". In: *Advances in Ozone Technology, Proc. of IOA/PAG Conf.*, Newport Beach, California, USA (2001).

Gamal El-Din, M. and D.W. Smith, "Designing Ozone Bubble Columns: A Spreadsheet Approach to Axial Dispersion Model". In: *Advances in Ozone Technology, Proc. of IOA/PAG Conf.*, Orlando, Florida, USA (2000).

Gamal El-Din, M. and D.W. Smith, "Ozone Mass Transfer in Water Treatment: Hydrodynamics and Mass transfer Modeling of Ozone Bubble Columns". In: *Proc. of the Water Supply and Water Quality Conf.*, Kraków, Poland, pp. 623-635 (2000).

Gamal El-Din, M. and D.W. Smith, "Rational Approach to Hydrodynamic Modeling of an Ozone Jet-Bubble Column". In: *Proc. 6<sup>th</sup> Environmental Engineering Specialty Conf., 28<sup>th</sup> Annual CSCE Conf.*, London, Ontario, Canada, pp. 327-335 (2000).

#### CONFERENCE/WORKSHOP PAPER AND POSTER PRESENTATIONS

Gamal El-Din, M. and D.W. Smith, "Theoretical Analysis and Experimental Verification of the Ozonation Process in Bubble Columns". Oral presentation, In: *7<sup>th</sup> Int. Conf. on Advanced Oxidation Technologies for Water and Air Remediation*, Niagara Falls, Ontario, Canada, (2001).

Smith, D.W. and M. Gamal El-Din, "Testing the Applicability of One-Phase Axial Dispersion Model to Describe the Performance of Ozone Bubble Columns". Oral presentation, In: *Sustainable Forest Management Network Student Workshop*, Edmonton, Alberta, Canada, (2000).

Gamal El-Din, M. and D.W. Smith, "Comparing ADM and BFCM for Modeling Ozone Bubble Columns with Constant Dimensionless Operating Parameters". Oral presentation, In: *6<sup>th</sup> Int. Conf. on Advanced Oxidation Technologies for Water and Air Remediation*, London, Ontario, Canada, (2000).

Gamal El-Din, M. and D.W. Smith, "Hydrodynamics Modeling of Ozone Jet-Bubble Columns". Poster presentation, In: *Paper Week Int. Conf.*, Montreal, Quebec, Canada, (2000).

Gamal El-Din, M. and D.W. Smith, "Maximizing Enhanced Ozonation of Pulp Mill Effluents". Poster presentation, In: *Paper Week Int. Conf.*, Montreal, Quebec, Canada, (2000).

Gamal El-Din, M. and D.W. Smith, "Maximizing Enhanced Oxidation of Pulp Mill Effluents". Poster presentation, In: *Sustainable Forest Management Network Conf., Science and Practice: Sustaining the Boreal Forest*, Edmonton, Alberta, Canada, (1999).

## TECHNICAL REPORTS

Gamal El-Din, M. and Smith, D.W. "Maximizing Enhanced Ozone Oxidation of Pulp Mill Effluents". Sustainable Forest Management Network, 2000-26, ISBN 1-55261-086-1.

## AWARDS/RECOGNITIONS

July 1991: Awarded an Honours Degree as a result of maintaining a minimum grade of "Very Good" throughout the 5-year undergraduate program at Cairo University.

## PROFESSIONAL MEMBERSHIP AND CONTRIBUTIONS

- ◆ Technical reviewer for the journal of Ozone Sci. & Eng.
- ◆ Current member of the Canadian Society for Civil Engineering (CSCE), International Association on Water Quality (IAWQ), American Water Works Association (AWWA), International Ozone Association (IOA), and Egyptian Syndicate of Civil Engineers.